UNIVERSITÀ
DELLA CALABRIA

Department of Civil Engineering

Doctoral Thesis in

Sciences and Engineering for the Environment, Construction and Energy

Cycle XXXIII (2017-2020)

Academic/Scientific Sector

ICAR/08 – Structural Mechanics

ANALYSIS OF FRACTURE PHENOMENA IN CONCRETE STRUCTURES BY MEANS OF COHESIVE MODELING TECHNIQUES

Course Coordinator

Ch.mo Prof. Salvatore CRITELLI

CRITELLI SALVATORE
02.02.2021 12:03:01
UTC

Scientific Supervisors

Ch.mo Prof. Fabrizio GRECO

GRECO FABRIZIO
02.02.2021
10:27:16 UTC

Ch.mo Prof. Paolo NEVONE BLASI

NEVONE BLASI PAOLO
02.02.2021 10:25:56
UTC

Author

Ing. Umberto DE MAIO

Abstract

Still today, the fracture phenomenon in cementitious materials is a research topic widely investigated by numerous researchers in materials and structural engineering, since it involves many theoretical and practical aspects concerning both strength and durability properties of common concrete structures. Indeed, cracking is one of the main causes of the severe deterioration of concrete structures, usually leading to an unacceptable reduction of their serviceability time. The fracture processes, including onset, propagation, and coalescence of multiple cracks, arise in the structural members because of the low tensile strength of concrete, which is ultimately related to the existence of voids or undetected defects in the material microstructure. Such cracking processes significantly affect the global mechanical behavior of the concrete structures and may facilitate the ingress of corrosive media; therefore, in the scientific community there is a strong interest in reducing cracks width to a minimum or in preventing cracking altogether. In the technical literature, several simplified numerical models, based on either linear-elastic or elastic-plastic fracture mechanics, are proposed to predict the fracture mechanisms during any stage of the lifetime of concrete structures. However, the application of these models is

somehow limited, due to their incapacity to capture the complex inelastic mechanical behavior of reinforced concrete members, involving multiple concrete cracking and steel yielding and their mutual interaction under the combined action of axial and bending loadings.

This thesis aims to develop a sophisticated numerical fracture model to predict the cracking processes in quasi-brittle materials like concrete, and the main failure mechanisms of the reinforced concrete structures in a comprehensive manner. The proposed methodology relies on a diffuse interface model (DIM), based on an inter-element cohesive fracture approach, where cohesive elements are inserted along all the internal mesh boundaries to simulate multiple cracks initiation, propagation and coalescence in concrete. Such a model, is used in combination with an embedded truss model (ETM) for steel reinforcing bars in the failure analysis of reinforced concrete structures. In particular, truss elements equipped with an elastoplastic constitutive behavior are suitably connected to the concrete mesh via a bond-slip interface, in order to capture the interaction with the surrounding concrete layers as well as with the neighboring propagating cracks.

The proposed fracture model takes advantage of a novel micromechanics-based calibration technique, developed and proposed in this thesis, to control and/or reduce the well-known mesh dependency issues of the diffuse cohesive approach, related to the artificial compliance in the elastic regime. In this way,

the initial stiffness parameters of the cohesive element employed in the diffuse interface model are suitably calibrated by means of a rigorous micromechanical approach, based on the concept of representative volume element. In particular, by performing several micromechanical analyses two charts have been constructed which provide the dimensionless normal and tangential stiffness parameters as functions of both the Poisson's ratio of the bulk and the admitted reduction in the overall Young's modulus after the insertion of the cohesive interfaces.

The proposed fracture model has been firstly validated by performing numerical analysis in plain concrete elements, and secondly, employed to analyze the failure mechanisms in externally strengthened reinforced concrete beams.

In particular, several numerical simulations, involving pre-notched concrete beams subjected to mode-I loading conditions, have been performed to investigate the capability of the diffuse interface model to predict self-similar crack propagation and to assess the mesh-induced artificial toughening effects, also introducing two new fracture models for comparison purpose. Moreover, sensitivity analyses with respect to the mesh size and the mesh orientation have been performed to investigate the mesh dependency properties of the proposed fracture model. Further validation of the proposed diffuse interface model has been provided for plain concrete structures subjected to general mixed-mode loading conditions. The role of the mode-II inelastic pa-

rameters (i.e. critical tangential stress and mode-II fracture energy) on the nonlinear behavior of the embedded cohesive interfaces is investigated in a deeper manner. In particular, two sensitivity analyses have been performed by independently varying the mode-II inelastic parameters required by the traction-separation law adopted in the proposed concrete fracture model, in order to quantify the above-mentioned artificial toughening effects associated with mode-II crack propagation. Moreover, comparisons with numerical and experimental results, with reference to mode-I and mixed-mode fracture tests, have been reported, highlighting the effectiveness of the adopted diffuse interface model (DIM) in predicting the failure response in a reliable manner.

Subsequently, the integrated fracture approach is successfully employed to predict the nonlinear response of (eventually strengthened) reinforced concrete beams subjected to general loading conditions. Firstly, the failure analysis of reinforced concrete (RC) beams has been performed to assess the capability of the integrated fracture model to capture multiple crack initiation and propagation. Detailed stress analysis of the tensile reinforcement bars has been also reported to verify the capability of the embedded truss model (ETM) of capturing the tension stiffening effect. Secondly, the well-known concrete cover separation phenomenon has been predicted by performing complete failure simulations of FRP-strengthened RC elements. To this end, a single interface model (SIM) has been incorporated in the proposed

fracture model to capture the mechanical interaction between the concrete element and the externally bonded reinforced system and to predict eventually debonding phenomena in concrete/FRP plate interface. Suitable comparisons with available experimental results have clearly shown the reliability and the effectiveness (in terms of numerical accuracy) of the adopted fracture approach, especially in the crack pattern prediction. Finally, the proposed integrated numerical model is used to predict the structural response of ultra high-performance fiber-reinforced concrete (UHPFRC) structures enhanced with embedded nanomaterials. In this case, the cohesive elements are equipped with a mixed-mode traction-separation law suitably calibrated to account for the toughening effect of the nano-reinforcement. The main numerical outcomes, presented in terms of both global structural response and final crack pattern, show the ability of the proposed approach to predict the load-carrying capacity of such structures, as well as to highlight the role of the embedded nano-reinforcement in the crack width control.

Sommario

Ancora oggi il fenomeno della frattura nei materiali cementizi è un argomento di ricerca ampiamente studiato da numerosi ricercatori nel campo dell'ingegneria strutturale e dei materiali, poiché tale fenomeno coinvolge diversi aspetti sia teorici che pratici riguardanti la resistenza e la durabilità degli usuali manufatti in calcestruzzo. Infatti, la fessurazione è una delle cause più importanti del deterioramento delle strutture in calcestruzzo, spesso comportando un'inaccettabile riduzione della loro vita utile. I processi di frattura, che includono l'innesco, la propagazione e la coalescenza di fessure multiple, si verificano negli elementi strutturali a causa della bassa resistenza a trazione del calcestruzzo, la quale è strettamente connessa all'esistenza di vuoti o difetti non rilevati nella microstruttura del materiale. Questi processi di fessurazione influenzano fortemente il comportamento meccanico globale delle strutture in calcestruzzo e possono facilitare l'ingresso di materiale corrosivo; pertanto nella

comunità scientifica c'è un forte interesse nel prevenire l'instaurarsi delle fessure, e/o ridurre al minimo la loro ampiezza. Nella letteratura tecnica vengono proposti diversi modelli numerici semplificati, basati sulla meccanica della frattura elastica lineare o elastico-plastica, al fine di prevedere i meccanismi di frattura durante ogni fase della vita utile delle strutture in calcestruzzo. Tuttavia, l'applicazione di questi modelli è in qualche modo limitata a causa della loro incapacità di catturare il complesso comportamento meccanico anelastico degli elementi in cemento armato, che coinvolge fessurazioni multiple del calcestruzzo, lo snervamento dell'acciaio e la loro reciproca interazione sotto l'azione combinata di carichi assiali e flessionali.

Questa tesi ha l'obiettivo di sviluppare un modello numerico di frattura sofisticato per prevedere, in modo completo ed esaustivo, i processi di fessurazione nei materiali con comportamento meccanico quasi fragile come il calcestruzzo, oltre che i principali meccanismi di collasso delle strutture in calcestruzzo armato. La metodologia proposta si fonda su un modello ad interfaccia diffusa (DIM), a sua volta basato su un approccio di frattura coesiva inter-elemento, in cui elementi coesivi sono inseriti lungo tutti i bordi della mesh computazionale per simulare l'innesco, la propagazione e la coalescenza di fessure multiple nel calcestruzzo. Tale modello viene utilizzato insieme ad un modello costituito da elementi di tipo "asta" incorporati (Embedded Truss Model, ETM) per tenere conto delle barre di rinforzo nelle analisi a col-

lasso delle strutture in cemento armato. In particolare, gli elementi asta, dotati di comportamento costitutivo elastoplastico, sono opportunamente collegati alla mesh del calcestruzzo tramite un'interfaccia di tipo "bond-slip", in grado di cogliere l'interazione con gli strati di calcestruzzo circostanti e con le fessure vicine.

Il modello di frattura proposto sfrutta i vantaggi di una nuova tecnica di calibrazione basata sulla micromeccanica, sviluppata e proposta in questa tesi, per controllare e/o ridurre i ben noti problemi di dipendenza dalla mesh dell'approccio coesivo diffuso, relativi all'effetto artificiale di cedevolezza nella fase elastica. In questo modo, i parametri di rigidezza iniziali degli elementi coesivi impiegati nel modello ad interfaccia diffusa vengono correttamente calibrati mediante un rigoroso approccio micromeccanico, basato sul concetto di elemento volumetrico rappresentativo. In particolare, eseguendo diverse analisi micromeccaniche sono stati costruiti due abachi che forniscono i parametri adimensionali di rigidezza normale e tangenziale in funzione sia del coefficiente di Poisson della fase solida che della riduzione del modulo di Young ammessa dopo l'inserimento delle interfacce coesive.

Il modello di frattura proposto è stato prima validato eseguendo analisi numeriche in elementi in calcestruzzo semplice e poi utilizzato per analizzare i meccanismi di collasso nelle travi in calcestruzzo armato, anche rinforzate esternamente con materiali compositi.

In particolare, sono state eseguite diverse simulazioni numeriche, con riferimento a travi in calcestruzzo pre-intagliate soggette a condizioni di carico di modo I, al fine studiare la capacità del modello ad interfaccia diffusa di prevedere la propagazione della fessura, oltre che di gli effetti artificiali di tenacità indotti dalla mesh, introducendo anche due nuovi modelli di frattura a scopo di confronto. Inoltre, sono state eseguite analisi di sensitività rispetto alla dimensione e all'orientamento della mesh al fine di indagare le proprietà di dipendenza della mesh del modello di frattura proposto.

Un'ulteriore validazione del modello ad interfaccia diffusa è stata fornita per le strutture in calcestruzzo non armato sottoposte a condizioni di carico di modo misto. Il ruolo dei parametri anelastici di modo II (cioè la tensione tangenziale critica e l'energia di frattura di modo II) nel comportamento non lineare delle interfacce coesive incorporate viene studiato in modo più approfondito. In particolare, sono state eseguite due analisi di sensibilità variando indipendentemente i parametri anelastici di modo II richiesti dalla legge di trazione-separazione adottata nel modello di frattura del calcestruzzo proposto, al fine di quantificare i sopra citati effetti artificiali di tenacità associati alla propagazione della fessura in modo II.

Inoltre, sono stati riportati dei confronti con risultati numerici e sperimentali, con riferimento a prove di frattura in modo I

e in modo misto, evidenziando l'efficacia del modello ad interfaccia diffusa (DIM) nel prevedere in modo affidabile la risposta non lineare della risposta a collasso.

Successivamente, l'approccio di frattura integrato è stato impiegato con successo per prevedere la risposta non lineare delle travi in calcestruzzo armato rinforzate soggetta a condizioni di carico generali. In primo luogo, è stata eseguita l'analisi al collasso di travi in calcestruzzo armato per valutare la capacità del modello di frattura integrato di catturare l'innesco e la propagazione di fessure multiple. È stata inoltre riportata un'analisi dettagliata delle tensioni nelle barre di rinforzo a trazione al fine di verificare la capacità del modello ad aste incorporate (ETM) nel cogliere l'effetto del "tension stiffening".

In secondo luogo, è stato simulato il ben noto fenomeno del distacco del copriferro nelle travi in calcestruzzo armato eseguendo simulazioni al collasso di elementi in calcestruzzo armato rinforzati con sistemi FRP. A tal fine, nel modello di frattura proposto è stato incorporato un modello ad interfaccia singola (SIM) per descrivere l'interazione meccanica tra l'elemento in calcestruzzo e il sistema di rinforzo incollato esternamente e per prevedere eventuali fenomeni di delaminazione lungo l'interfaccia tra il calcestruzzo di supporto e la piastra in FRP. I confronti con alcuni risultati sperimentali disponibili in letteratura hanno mostrato chiaramente l'affidabilità e l'efficacia (in termini di accuratezza numerica) dell'approccio di frattura adottato, specialmente nella previsione del quadro fessurativo.

Infine, il modello numerico proposto è stato utilizzato per prevedere la risposta strutturale di elementi in calcestruzzo fibrorinforzato ad alte prestazioni (Ultra High-Performance Fiber-Reinforced Concrete, UHPFRC) migliorati con nanomateriali dispersi nella matrice cementizia. In questo caso, gli elementi coesivi sono dotati di una legge trazione-separazione di modo misto opportunamente calibrata per tenere conto dell'effetto tenacizzante del nano-rinforzo. I principali risultati numerici, presentati sia in termini di risposta strutturale globale che di quadro fessurativo finale, mostrano la capacità dell'approccio proposto nel prevedere la capacità portante di tali strutture, nonché nell'evidenziare il ruolo del nano-rinforzo nel controllo dell'ampiezza delle fessure.

Notations

$\bar{\boldsymbol{C}}$	Homogenized moduli tensor
$\bar{\boldsymbol{C}}^{(\mathrm{UT})}, \bar{\boldsymbol{C}}^{(\mathrm{G})}, \bar{\boldsymbol{C}}^{(\mathrm{LD})}$	Homogenized moduli tensor for uniform traction (UT), general (G) and linear displacement (LD) boundary conditions
$\bar{\boldsymbol{C}}^{\mathrm{iso}}$	Isotropic moduli tensor closest to $\bar{\boldsymbol{C}}$
$\left\langle \bar{\boldsymbol{C}} \right\rangle_{\phi}$	Angularly averaged homogenized moduli tensor
CDIM	Controlled diffuse interface model
d	Scalar damage function
DIM	Diffuse interface model
E	Young's modulus of the bulk
e_E	Percentage variation of the overall Young's modulus
e_C	Percentage deviation of the homogenized moduli
e_P	Percentage deviation with respect to the mean peak load
ETM	Embedded truss model
f_c	Concrete compressive strength
G	Tangential modulus of the bulk
$\bar{G}$	Overall tangential modulus
$\bar{G}_{2\mathrm{D}}$	Homogenized planar shear modulus
$G_{\mathrm{I}}, G_{\mathrm{II}}$	Modal components of the energy release rate
$G_{\mathrm{I}c}, G_{\mathrm{II}c}$	Mode-I and mode-II fracture energies

i_a	Anisotropy index
i_c	Compliance index
$\boldsymbol{K}$	Second-order secant interfacial constitutive tensor
$\boldsymbol{K}_0$	Second-order elastic interfacial constitutive tensor
K_n, K_s	Normal and tangential interfacial cohesive stiffness parameters
K_n^0, K_s^0	Normal and tangential interfacial elastic stiffness parameters
$\bar{K}_{2D}$	Homogenized planar bulk modulus
l_c^p	Projected crack length
l_c^t	True crack length
L_{mesh}	Mesh size
L_{RVE}	RVE size
$P^{\max}$	Peak load
$\boldsymbol{Q}$	Proper orthogonal transformation tensor
R_E	Reduction of the Young's modulus
R_G	Reduction of the tangential modulus
R_ν	Reduction of the Poisson's ratio
RVE	Representative volume element
s	Slip at the concrete/steel interface
SIM	Single interface model
$\boldsymbol{t}_{\text{coh}}$	Cohesive traction vector
$t_n^{\text{coh}}, t_s^{\text{coh}}$	Normal and tangential components of the cohesive traction vector
$[\![\boldsymbol{u}]\!]$	Displacement jump between the crack faces
α	Dimensionless cohesive softening parameter
β	Tangential-to-normal displacement jump ratio
γ	Mesh topology factor
Γ_d^h	Internal mesh boundaries
δ_m	Mixed-mode displacement jump

δ_m^0	Effective displacement jump at damage onset
δ_m^f	Effective displacement jump at total decohesion
$\delta_m^{\max}$	Maximum effective displacement jump during deformation history
$\delta_m^{\max,\text{old}}$	Maximum effective displacement jump at the previous simulation step
δ_n, δ_s	Normal and tangential components of the displacement jump
δ_n^0, δ_s^0	Normal and tangential displacement jumps at damage onset in pure mode-I and mode-II, respectively
ζ	Cohesive zone model parameter
$\bar{\boldsymbol{\varepsilon}}$	Prescribed macro-strain tensor
η	Crack tortuosity ratio
κ	Dimensionless interfacial normal stiffness
ν	Poisson's ratio of the bulk
$\bar{\nu}$	Overall Poisson's ratio
ξ	Tangential-to-normal stiffness ratio of the interface
ρ	Dimensionless RVE size
σ	Normal stress component
$\bar{\boldsymbol{\sigma}}$	Macro-stress tensor
$\sigma_{\max}$	Normal critical interface stress
τ	Shear stress component
τ_b	Steel/concrete bond stress
$\tau_{b,\max}$	Maximum tangential stress of the bond-slip relation
$\tau_{b,f}$	Friction strength of the bond-slip relation
$\tau_{\max}$	Tangential critical interface stress
Φ_d	Dissipated fracture energy

List of Figures

List of Tables

Contents

Introduction

Most construction materials subjected to mechanical loading and particular environmental conditions are often affected by the well-known fracture phenomenon (Issa, 1999; Ceroni and Pecce, 2007; Arici, 2011). It is a typical damage process understood as the total or partial detachment of an originally intact part of body or structure, which occurs locally by means of elementary failure mechanisms on a microscopic level and strongly depends on physical and micro-structural properties of the considered material. At the macroscopic scale, such a phenomenon consists in the formation and propagation of single or multiple cracks in the body, whereby complete mechanical failure is finally induced. In the civil engineering field, sudden fracture, technically named

(a) (b)

Figure 1. Catastrophic failure of civil constructions: (a) Morandi bridge in Genova - Italy, and (b) civil building in Tainan - Taiwan.

"brittle fracture", is the most dangerous type of damage which may induce premature and catastrophic collapse of civil constructions as bridge and civil building (Figure 1). In the most of cases, the reasons of these failures are undetected defects in material or components, insufficient dimensioning of the construction compared to the actual load, or the application of materials with deficient strength. Engineering mistakes in this area can have undesirable consequences for the life of people and the environment, therefore, both theoretical and numerical investigations for the assessment and prevention of fracture and damage processes play a decisive role. Therefore, it is necessary to develop accurate and reliable methods and models for the structural analysis of civil constructions, especially at the nonlinear regime, in order to assess their safety and serviceability under several loading conditions. In particular, especially for concrete

structures, a suitable prediction of both deflection and crack patterns under ultimate and service load is necessary to a correct design of the individual structural components. As a matter of fact, cracking phenomena, which arise at all stages in the life of concrete structures, may greatly affect the long-term durability and permeability properties (Wang et al., 1997; Bolander and Le, 1999). An adequate control of cracking requires accurate models for predicting both crack width and crack spacing under general geometric configurations and loading conditions.

Most of the existing models, based on either semi-empirical or analytical approaches, do not have a general applicability, being limited to concrete frame elements subjected to axial or bending loads (Frosch, 1999). Therefore, a comprehensive numerical model accounting for the effect of cracking, also including microcracking, on the overall structural response of concrete elements under both ultimate and service loads appears to be still missing. This is attributable to the fact the most known and well-established constitutive models for concrete are based on a continuum representation for this material, in which both kinematic and static variables (i.e. strains and stresses) possess regular spatial distributions. For a concrete crack analysis to be correct, this hypothesis should be removed.

To this end, the main focus of the present thesis is to develop an advanced computational fracture model able to investigate

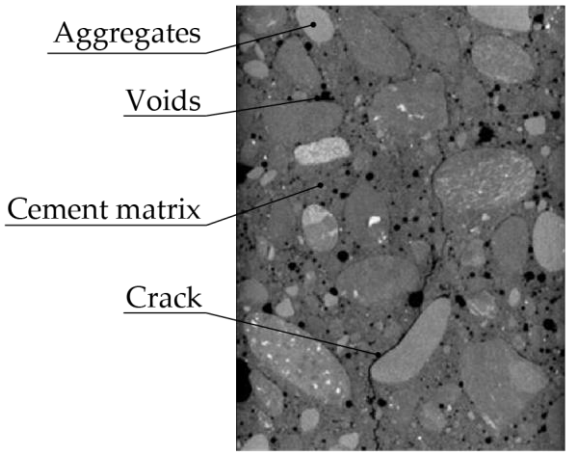

Figure 2. Detail of the concrete microstructure containing a crack.

the fracture phenomena in quasi-brittle materials and, as consequence, to predict the main failure mechanisms in the concrete structures in a unified manner.

Fracture phenomena and failure modes of concrete structures

Concrete, although possessing a low tensile strength, is the most frequently used construction materials in the civil engineering field due to its distinctive characteristics such as notable compressive strength and durability, high-temperature resistance, low-maintenance requirements, and cheapness compared to other materials (Biernacki et al., 2017). It is regarded as a composite material being mainly made of aggregates, cement matrix, and voids containing air or water (Figure 2). However, such a heterogeneity makes concrete as a quasi-brittle material whose

fracture behavior under mechanical loading, is mainly non-linear and characterized, at common spatial scales (i.e. laboratory and building scales), by the development of a fracture process zone (FPZ) before the occurrence of strain localization (Cedolin et al., 1983; Otsuka and Date, 2000). In detail, the concrete fracture behavior is characterized by a gradual transition from an initial diffuse damaged state, in which several micro-cracks grow and interact with each other, to a complete localized damaged state, associated with nucleation and propagation of macroscopic cracks resulting from micro-crack coalescence phenomena (Wittmann and Hu, 1991). These processes play a major role in determining the damage behavior of concrete, influencing its apparent stiffness properties even under relatively low levels of the applied external loads.

To overcome the drawbacks of the concrete material, associated with low tensile strength and significant brittleness (associated with a low energy absorption capacity), it is usually employed in conjunction with steel bars, placed at those locations where the highest tensile stresses appear in the considered structure. Such a reinforcement greatly improves the structural performance of the concrete members, in terms of load-carrying capacity, stiffness, and ductility, but promotes the multiple cracking phenomena (Shardakov et al., 2016). Major cracks can then act as additional channels for penetration of aggressive agents, accelerating the development of deterioration due to chemical

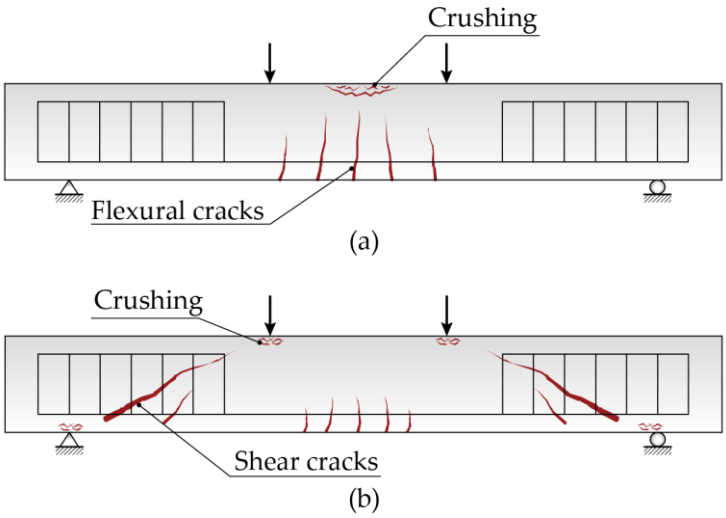

Figure 3. Schematic representation of the failure modes in a reinforced concrete beam: (a) flexural and (b) shear failure mode.

reactions (such as leaching, delayed ettringite formation, and alkali-aggregate reactions), and reinforcement corrosion, as well as the amplification of the freeze/thaw damage effects. Moreover, the corrosion of the steel rebar decreases its effective cross-sectional area and breaks the bond between the rebar and concrete, causing performance degradation of the entire structure (Fu and Chung, 1997; Wang et al., 1997; Zhang et al., 2020).

In these structures, commonly named as reinforced concrete (RC) structures, different failure modes are observed in the experimental tests because of the presence of steel reinforcement, classifiable into two major types: flexural and shear failure.

The former occurs when the acting loads exceed the flexural capacity of the beam mainly guaranteed by the steel rebars. In particular, such a failure usually initiates by the yielding of the

steel reinforcement followed by the concrete crushing at compression side of the structure (Zhan et al., 2015; Yang et al., 2017; Słowik, 2019). The signs of this failure mode are the development of multiple vertical cracks in the middle third of the concrete element, which starting from the tension face extend up to the compression side, leading to a considerable deflection of the structure (see Figure 3a). The flexural failure, being usually of ductile type, is a desired failure mode in the design process of concrete beams. However, when the beam is over-reinforced, the concrete crushing may occur before of the rebars yielding, leading to an undesired brittle failure. This premature failure mode can be prevented either by increasing the compression strength of the structure, introducing, for example, additional steel reinforcement at the compression side, or increasing the height of the concrete section.

The latter failure mode is associated with the development of a diagonal fracture which starts in the proximity of the beam support and propagates towards the load application point (see Figure 3b) (Zararis and Papadakis, 2001). It is a brittle failure mode, which is strongly influenced by the effective span to depth ratio of the concrete element. As a matter of fact, for values less than one of this ratio, i.e. in the case of a deep beam, the loads are directly transferred to the supports, producing a diagonal fracture plane (Wang et al., 2005; Yu and Tan, 2013). Usually, to prevent such a failure mode, a shear reinforcement in form of stirrups is placed in the structure.

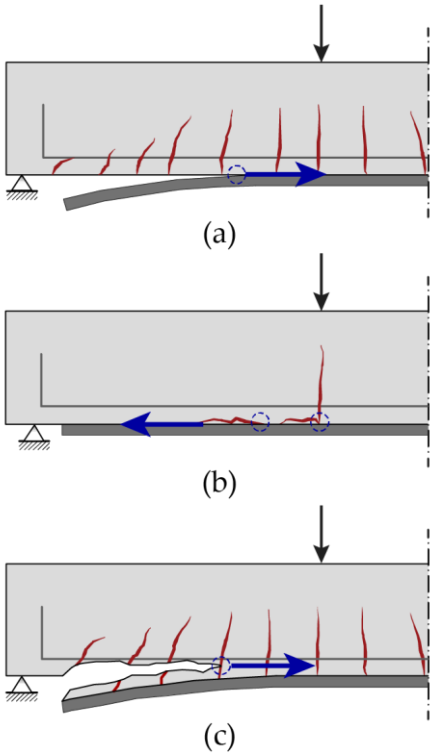

Figure 4. Schematic representation of the main failure modes of an FRP-plated RC beam (the horizontal arrows indicate the direction of crack propagation): a) plate-end interfacial debonding; b) intermediate crack-induced debonding; c) concrete cover separation.

In the last two decades, to improve the flexural strength of existing concrete structures, reinforcement systems based on fiber-reinforced polymer (FRP) have been widely employed, due to the superior mechanical properties of FRP systems over traditional ones (e.g. based on steel plates), such as minimum increase in structural size, excellent resistance to corrosion and fire, very high strength-to-weight ratios, as well as ease of handling and transportation. However, the structural system resulting from

the application of externally bonded FRP composites leads to modify some well-known failure modes of conventional RC structures, i.e. concrete crushing, shear and flexural failure, and to display a number of unique fracture mechanisms, as a result of the great amount of research undertaken in the past decades (see, for instance, (Toutanji et al., 2006) and references herein). These premature failure modes can be reduced to the three modes, i.e. the plate-end and intermediate crack-induced interfacial debonding failures (see Figure 4a and b) and the concrete cover separation failure (see Figure 4c). Such catastrophic failures are strongly associated with the effectiveness of the stress transfer at the FRP-to-concrete interface. As a matter of fact, the bond of this interface is not perfect, and its strength depends on both concrete strength and adhesive thickness. It has been shown that, in high-strength concrete members, failure typically occurs at the adhesive/concrete (AC) interface. In this case, the adhesive plays a notable role, meaning that greater thickness values lead to better stress redistributions and ultimately to greater ultimate load levels (López-González et al., 2012). On the other hand, in low-strength concrete elements, failure occurs in the concrete phase and does not depend on the adhesive thickness. In this case, concrete cover separation is often observed, as reported in many experimental investigations (Fanning and Kelly, 2001; Gao et al., 2004; Maalej and Bian, 2001; Quantrill et al., 1996; Rahimi and Hutchinson, 2001). Such a failure, which is promoted by the nucleation of an inclined crack at the plate end, consists in its

progressive propagation towards the horizontal direction up to the level of the tensile rebars (see Figure 4c).

In the next Section, the previous attempts to investigate the fracture behavior and predict the main failure modes in concrete structures by means of simplified and/or sophisticated computational models are briefly enumerated in order to provide an overview of available methods.

Overview on concrete fracture modeling

With the aim of analyzing fracture in quasi-brittle materials and predicting the main failure modes of concrete structures, many numerical models have been developed and proposed in the technical literature, classifiable in two main groups: discrete and smeared crack models. Discrete crack models assume that damage is lumped into main propagating cracks, whereas smeared crack models capture the damage processes through suitably defined constitutive relations, thus smearing out all the discontinuities over the continuum (Wittmann and Hu, 1991).

In discrete fracture modeling, both linear elastic fracture mechanics (LEFM) and nonlinear fracture mechanics (NLFM) models have been used in the literature for crack analysis in concrete. Since LEFM models assume that the energy dissipation is confined within a vanishing region located in front of a macroscopic crack tip, they have been successfully applied mainly in the case of large concrete structures like dams (Ingraffea, 1990), for which

the extension of the real FPZ can be neglected if compared to the structural size. Another well-known application of LEFM for concrete structures is the prediction of the pull-out test, as confirmed by some recent numerical works (Greco et al., 2015). In more general situations, NLFM models are mandatory to accurately capture the typically experienced size-effects in concrete. As a matter of fact, the real FPZ extension cannot be neglected in small- and medium-sized structures, which are the most common ones in the engineering practice (Bažant, 1984). Among all the NLFM models, cohesive zone models (CZMs) are the most used for concrete and other quasi-brittle materials (Elices et al., 2002).

Within a finite element setting, two main different strategies can be found in the literature for the application of cohesive fracture, i.e. inter-element and intra-element cohesive models. In the first approach, cohesive cracks are constrained to be extended between the finite elements, whereas in the latter, cohesive cracks can propagate across the finite elements.

Inter-element crack propagation is allowed by using specific cohesive interface elements, equipped with a constitutive relation, written in terms of traction-separation law (TSL). Thus, cohesive models have been extensively used in the cases where (single or multiple) crack paths are known a priori, like in debonding problems usually experienced in composite materials (Greco et al., 2002; Greco and Lonetti, 2009). In this case, the interface elements (of the so-called intrinsic type) are inserted prior

to the simulation along these predefined crack paths. On the contrary, in the case of unknown crack paths or patters, usually experienced in concrete structures subjected to general loading conditions, the interface elements (of the so-called extrinsic type) are inserted during the simulation (i.e. on-the-fly) in an adaptive manner, after introducing specific insertion criteria into the model. Several cohesive interface models on this kind have been proposed in the literature to analyze mixed-mode fracture in concrete structures (Bocca et al., 1991; Gerstle and Xie, 1992; Carol et al., 1997; Cendón et al., 2000; Prasad and Krishnamoorthy, 2002; Gálvez et al., 2002b; Yang and Chen, 2005). Inter-element cohesive approaches usually require some remeshing operations, which are associated with high computational costs, being reduced only in the case of local remeshing strategies (Kuutti and Kolari, 2012). Furthermore, due to remapping of the stress and strain states (and, eventually, of the internal variables), remeshing may cause thermodynamically inadmissible artificial healing of previously cracked regions, posing severe uniqueness problems in the case of crack branching.

Intra-element cohesive fracture approaches have been widely used to simulate crack initiation and propagation along unknown crack paths and crack patters without requiring any remeshing. According to these approaches, the propagating discontinuities are embedded by introducing a kinematic enrichment either at the element level, as in the strong discontinuity approach (SDA) (Sancho et al., 2007), or at the node level

(equipped with additional degrees of freedom), as in the partition of unity finite element method (PUFEM) (Gasser and Holzapfel, 2005), the extended finite element method (XFEM) (Moës and Belytschko, 2002), the phantom node method (PNM) (Song et al., 2006), and the cohesive segment method (CSM) (Remmers et al., 2003).

In contrast to discrete fracture models, in smeared crack approaches the fracture energy is distributed over the continuum (Rots, 1988; Oliver, 1989). These approaches, which can be included within the more general framework of continuum damage mechanics (CDM), consider an infinite number of parallel discrete cracks to be continuously distributed over equivalent continua with reduced stiffness and strength in the direction normal to the cracks after the peak strength has been reached.

Smeared crack approaches preserve the continuity features of the displacement solution of the associated boundary value problem (BVP), but the strain softening injected in the constitutive response locally leads to a change in the character of the governing partial differential equations. In particular, in the framework of quasi-static fracture evolution, a loss of ellipticity of the underlying equation system is experienced. This change inevitably leads to the ill-posedness of the BVP, thus rendering such approaches susceptible to localization instabilities (and spurious mesh sensitivities if these continua are approximated by finite element models) (Pijaudier-Cabot and Bažant, 1987). These theo-

retical and numerical difficulties have been tackled in the literature by introducing into the material model some localization limiters, assuring the energy dissipation within a band (i.e. a region with finite width) across the ideal discontinuity line. Different localization limiters have been proposed in the literature, such as crack band models (Červenka et al., 2018; Grassl et al., 2018), fracture energy-based regularization techniques (Comi and Perego, 2001), and the more general and mathematically rigorous nonlocal continuum models, including integral models (Jirásek and Patzák, 2002), strain gradient models (Peerlings et al., 1998), and other enriched continuum models such as micropolar ones (de Borst, 1991; Fantuzzi et al., 2018). These models introduce a material characteristic length scale without a precise physical meaning, in order to restore the well-posedness of the resulting BVP, but may cause the localization bands to exhibit spurious damage diffusion around crack tips.

It is recognized that regularized smeared crack models are reliable models in predicting the load-carrying capacity of quasi-brittle materials in the strain softening regimes without sensible mesh-dependency issues, but they are not able to properly capture crack initiation, growth, coalescence and branching, because essential feature of these phenomena are inevitably lost in the smoothing process. Therefore, they are not suitable for crack analysis in concrete structures, unless special post-processing methods are introduced to extract crack geometries (Matallah et al., 2010).

An interesting numerical method able to overcome the main limitations of the above-discussed approaches is the cohesive finite element method, based on an inter-element discrete fracture representation, by which multiple cracking in quasi-brittle materials is handled in a natural manner. The advantages of this approach over both smeared and intra-element discrete models are twofold. Firstly, it is a very efficient and readily implementable approach for predicting crack initiation and propagation along non-prescribed paths within a standard displacement-type finite element setting, without injecting any enriched kinematics into the solid continuum elements, unlike intra-element fracture techniques. Secondly, it preserves the discrete nature of fracture processes, resulting in a very good capability of capturing the real crack patterns, unlike smeared fracture approaches.

The cohesive finite element method takes inspiration from a series of seminal works about the simulation of intergranular fracture in polycrystalline materials (Maiti et al., 2005; Ortiz and Suresh, 1993; Tijssens et al., 2001; Zavattieri and Espinosa, 2001), in which cohesive interface elements of the intrinsic type were inserted at the grain boundaries prior to the simulation. In (Xu and Needleman, 1994), the cohesive methodology was further extended to model crack propagation along arbitrary paths in homogeneous brittle elastic materials, by inserting cohesive interface elements along all the mesh boundaries. The latter approach, which represents the first application of the cohesive fi-

nite element method in the literature, employed a crossed-triangle quadrilateral mesh for the numerical simulations. The use of a structured triangulation highlighted the well-known mesh dependency issues of inter-element fracture approaches, in terms of lack of spatial convergence for arbitrary crack paths or patterns (Papoulia et al., 2006). Furthermore, it has been largely demonstrated that unstructured meshes with very good isotropic properties (e.g. Delaunay meshes) can reduce such artificial mesh effects, especially in terms of sensitivity to the mesh orientations, even if the question of energy convergence still remains an open issue.

The mesh dependency of the cohesive finite element method is experienced even in the elastic range, mainly due to the artificial compliance increase associated with the insertion of springs with finite stiffness between all the bulk finite elements, according to the adopted intrinsic cohesive formulation. Such a dependency may be alleviated by suitably calibrating the initial cohesive stiffness parameters as functions of the average mesh size, as suggested by many authors (Blal et al., 2012; de Borst et al., 2006; Espinosa and Zavattieri, 2003; Klein et al., 2001; Tomar et al., 2004; Turon et al., 2007).

Concerning concrete structures strengthened with systems based on FRP, extensive research has been performed to predict the main failure mechanisms, i.e. the plate-end and intermediate crack-induced debonding and concrete cover separation failure.

Both empirical and (strength- or fracture mechanics-based) rigorous models have been reported in the literature.

With reference to the most common plate-end debonding, the existing strength models can be classified into two categories: shear capacity models and interfacial stress models (Smith and Teng, 2002a, 2002b). According to the former group, the failure is related to the shear strength of the concrete with no or only partial contribution of the steel shear reinforcement, whereas according to the latter one, the failure requires the evaluation of the normal and tangential interfacial stress at the end of the soffit plate. Besides these simplified models, a large number of sophisticated analytical and numerical approaches have been proposed in the literature to quantitatively predict this type of failure (Buyukozturk et al., 2004; Turon et al., 2006; Obaidat et al., 2010; Pan et al., 2010; Zidani et al., 2015), including some multi-layer formulations in both static and dynamic settings proposed by some of the authors (Bruno et al., 2016). The intermediate crack-induced debonding has received less attention than the plate-end debonding, and most of the existing research works usually adopt simple strength models for FRP/concrete systems, such as bond-slip models derived from direct shear bond tests (Teng et al., 2003). There exist also a few finite element investigations, by which intermediate debonding has been successfully predicted, starting from the stress concentration in the neighborhood of a main flexural crack (Lu et al., 2007; Perera and Bueso-Inchausti,

2010). Once initiated, this failure mechanism evolves as a progressive interfacial slip on both crack sides, leading to a propagating decohesion toward the plate ends.

By contrast, despite of the large number of experimental, analytical and numerical investigations about concrete cover separation failure in FRP-plated concrete structures (Aprile and Feo, 2007; Gao et al., 2004; Radfar et al., 2012; Rahimi and Hutchinson, 2001; Raoof et al., 2000; Yang et al., 2003; Zhang and Teng, 2014), a full understanding of this premature failure is somewhat lacking. In (Gao et al., 2004) it is found that inclined cracks always appear in the concrete at the plate end before the failure load is reached. This means that the final collapse is not directly associated with elastic stress concentrations at the FRP-concrete interface. Many analytical models for cover separation have been developed in the literature, mainly used to estimate the load-carrying capacity of strengthened RC members, but they generally are too inaccurate, often leading to a non-optimal design of the adopted strengthening system. As a matter of fact, closed-form solutions for the analysis of cover separation usually rely on linear elastic models, and thus they cannot handle problems characterized by remarkable material nonlinearities. Among these models, the concrete tooth models have been widely used to analytically predict such a commonly observed failure mode (Raoof et al., 2000). They make use of the theoretical concept of concrete tooth comprised between two adjacent cracks, whose failure under the action of horizontal shear stresses occurs when

the tensile strength at the root of the tooth exceeds the tensile strength of the concrete.

Scope and outline

In the last century, the necessity to have safe civil constructions has encouraged many engineers and researchers to develop simplified and/or sophisticated numerical models able to predict the load-carrying capacity of the considered structure and simulate the damage processes which may occur during the action of the loads. As a fruitful result hereof, a significant number of constitutive models has been put forward in order to describe the mechanical behavior of concrete structures under general loading conditions. Despite these efforts, a comprehensive numerical model, easily implementable in the commercial software, which provides an accurate global structural response, in terms of both loading capacity and crack patterns, with reference to different concrete structures ranging from plain to reinforced concrete, seems to be still missing.

Within this framework, the present thesis aims to develop an integrated finite element fracture model, mainly based on an inter-element cohesive fracture approach, to investigate in a comprehensive manner all the main failure mechanisms, in plain and reinforced concrete structural elements, due to multiple crack initiation, propagation and coalescence.

In Chapter 1 of the present thesis, an extensive overview of the main theoretical and numerical approaches for concrete fracture analysis, is presented after introducing the basic concepts of Fracture Mechanics. Both cohesive and smeared crack models are detailly explained providing numerical examples of their application in the cracking analysis.

In Chapter 2 a novel numerical approach for failure analysis of concrete structures, based on a diffuse cohesive interface fracture approach able to simulate multiple crack onset, propagation and coalescence in quasi-brittle materials like concrete, is presented.

In the first part of Chapter, the theoretical formulation of the diffuse cohesive volumetric finite element method is reported, with reference to the planar elasticity case. The basic concept of this formulation is a variational statement written for a given solid after being discretized in finite elements, whose kinematics is enriched by the presence of cohesive interface elements along its internal boundaries. Typical issues of the diffuse cohesive approach, related to mesh dependency, are investigated in a deep manner, and a new micromechanics-based calibration approach for the stiffness parameters of the cohesive interfaces, employed in the proposed fracture approach, is presented whose aim is to control and/or reduce the mesh-induced artificial compliance in the elastic regime. This approach takes advantage of a numerical homogenization scheme, which is able to extend the analytical results obtained in (Blal et al., 2012; Tomar et al., 2004) to more

general mesh configurations and loading conditions. It is worth noting that the main numerical outcomes of this calibration step are not limited to concrete, but they are directly applicable to any material.

In the second part of the Chapter, the integrated numerical fracture model for failure analysis of concrete structures is widely illustrated, together with computational details. In particular, the proposed model incorporates three submodels in order to investigate all the main damage processes in plain and reinforced structures in a comprehensive manner. As the first submodel, a diffuse interface model (DIM), relying on the cohesive finite element method, is employed to simulate the cracking in concrete. It is obtained by inserting interface elements along all the internal boundaries of the finite element mesh, equipped with a mixed-mode intrinsic traction-separation law. This approach allows the cohesive interfaces to permeate the whole discretized body as a part of the material characterization, and ultimately leads to the prediction of crack paths or patterns in both plain and reinforced concrete without requiring additional crack initiation criteria which are external to the constitutive model of the material, neither adaptive meshing operations at the tip of advancing cracks. In order to obtain a correct prediction of the damage mechanisms in the reinforced concrete analysis, an embedded truss model (ETM), equipped with a bond-slip relation, is developed as the second submodel. It able to adequately capture the effects of the interaction between the reinforcing bars

and the surrounding cracking concrete. Moreover, the integrated fracture model is able to predict eventually debonding phenomena in strengthened concrete structures, by means of a thirdly introduced submodel, i.e. a single interface model (SIM), in which additional mixed-mode cohesive elements are inserted in the existing interface, i.e. between concrete and reinforcement system in the case of FRP-plated RC beams.

Chapter 3 is devoted to numerical calibration and validation of the diffuse interface model, involving concrete specimens under general loading conditions.

In the first part of the Chapter, according to the adopted intrinsic cohesive formulation, the elastic stiffness parameters are numerically determined using the micromechanical approach described in Section 2.1.3, in order to obtain invisible cohesive interfaces. Specifically, two charts for the calibration of both the dimensionless cohesive stiffness and the tangential-to-normal stiffness ratio are provided. In order to assess the general validity of the proposed calibration approach, a further investigation of both compliance and anisotropy levels for the resulting overall homogenized moduli tensor is given.

In the second part of the Chapter, numerical simulations are performed to validate the diffuse interface model, with reference to plain concrete elements subjected to mode I and mixed mode loading conditions. Two additional fracture approaches, are specifically introduced to highlight the mesh influence on the overall strength properties and related crack paths, as predicted by

the proposed DIM methodology. Moreover, to assess the degree of mesh dependency associated with the proposed model, two sensitivity analyses with respect to both mesh size and mesh orientation are performed. Special attention has been devoted to the influence of mode-II cohesive parameters on the global structural response, especially in the predicted damage pattern. Additionally, suitable comparisons with the experimental outcomes has been reported Section 3.2.4 and 3.3.3, thus confirming the reliability of the proposed model for the numerical simulation of crack propagation in concrete and other quasi-brittle materials under general loading conditions.

In Chapter 4, the proposed integrated fracture model is used to analyze failure in different reinforced concrete structures. In particular, numerical simulations are performed to predict the global structural response, in terms of loading capacity and crack patterns, of typical reinforced concrete beams. The simulations also provided a detailed stress analysis of the tensile reinforcement bars validating the capability of the adopted bond-slip approach of capturing the tension stiffening effect.

The integrated numerical model is also employed to simulate the concrete cover separation failure of FRP-plated reinforced concrete (RC) beams. Such application has been chosen to assess the predictive capabilities of proposed numerical approach in terms of both peak and residual load-carrying capacities of retrofitted RC structures, usually involving combined failure modes.

The Chapter ends with a numerical application to nano-enhanced ultra high-performance fiber-reinforced concrete (UHPFRC) element. In this case, a trilinear softening model is chosen for the constitutive beahvior of embedded cohesive interface, in order to capture all the microscopic fracture mechanisms, including cement paste micro-cracking, matrix/aggregate debonding and fiber pull-out. The numerical outcomes, obtained by the numerical analysis of steel bar-reinforced nano-enhanced UHPFRC structures, have demonstrated the reliability and the accuracy of the proposed model in predicting both the strengthening and toughening effects of embedded nanomaterials, in terms of global load-deflection responses and associated crack patterns.

Finally, some concluding remarks are given, together with some future perspectives of this work.

1

Theoretical and numerical approaches for concrete fracture analysis

The fracture phenomena in concrete and other quasi-brittle materials has been the subject of intensive investigation for nearly a century. The complexities associated with the behavior of fractured bodies led the researchers in the past to rely on theoretical approaches, based on Linear-Elastic Fracture Mechanics (LEFM), to understand and simulate the fracture process in various materials. However, these approaches, although providing still basic concepts of recent fracture models today, are not able

to capture complex fracture phenomena affected by factors such as strain softening, ductility, micro-cracking, and bond-slip. With the discovery of the finite element method (FEM), several numerical fracture models, based on continuum and discrete damage mechanics, are elaborated to offer a better analysis of the complex fracture behavior of materials. These models, overcoming the drawbacks of the above-mentioned simplify theoretical approaches and are potentially capable of providing an accurate solution of the stress and strain field during the fracture process, as well as different aspects of the fracture phenomena.

In this Chapter, a background is provided with respect to the fracture mechanics and a few numerical fracture models.

1.1 Basics of fracture mechanics

Fracture mechanics is a discipline that investigates the mechanical behavior of cracked solids. Generally, the fracture process is an irreversible process of rupture due to the nucleation and growth of cracks and strongly depends on a wide variety of factors, including the microstructure of crystalline or amorphous solid, macroscopic effects, as well as, the boundary conditions and the surrounding environment. To predict this phenomenon, in which a high stress concentration is localized near the crack tip, it is necessary to use the principles of fracture mechanics. In the literature, Linear-Elastic Fracture Mechanics (LEFM) and Elastic-Plastic Fracture Mechanics (EPFM) are the main theories

used to analyze the fracture behavior in cracked solids. The first theory investigates the cracking problem in brittle materials where the inelastic deformation and the nonlinear effects are limited to a small area, which can be neglected in comparison to the crack size or the component dimensions. However, in many construction materials, when the stress exceeds the yield stress of material, a small plastic zone arises. It causes a redistribution of the strain and stress fields leading to a blunting of the crack tip. The latter theory, also called ductile fracture mechanics, overcomes the drawbacks of LEFM and it is used to determine the crack problem solution in materials where the extent of inelastic deformation is quite pronounced. In this section, a thorough description of the above-mentioned fracture theories will be presented.

1.1.1 Linear-Elastic Fracture Mechanics in cracked solids

Linear-Elastic Fracture Mechanics is a theory dealing with the behavior of elastic solids with sharp cracks subjected to a certain loading condition. LEFM is applicable to any materials whose deformation behavior can be assumed to be linear-elastic and, as long as the extension of the inelastic region, that arises in the immediate neighborhood of the crack tip due to the high stress concentration, is rather small compared to the crack or body sizes. If these conditions are satisfied, LEFM is a very accurate theory (Bažant and Planas, 1998a).

The study of cracked bodies began around 1913 with the stress analysis, performed by Inglis, of a uniformly stressed elliptical cavity (Inglis, 1913) and observed that, as the ellipse approaches a crack line, the stress at the vertex of the ellipse tends to infinity. But the study had a turning point with the pioneering works of Griffith (Griffith, 1921). In particular, Griffith analyzed the rupture phenomena in solids starting with an isolated crack in an elastic body subjected to an applied stress and proposed, considering the fundamental energy theorems of classical mechanics and thermodynamics, a criterion for crack propagation based on the principle of energy balance, i.e. the crack will propagate if the energy available to extend the crack by a unit surface area is equal to the energy required to do so. The implications drawn from these works are still useful for the most analytical and numerical fracture models developed to date. Griffith's theory has been completed in its essential aspects by Irwin and Rice. Asymptotic expressions of the stress field to calculate the quantity of energy available for fracture ahead of the crack tip in linear-elastic bodies, are proposed by Irwin (Irwin, 1957), while Rice in the mid-1960, considering a non-linear elastic behavior around the crack tip, proposed an alternative method to measure the amount of the required energy to fracture by means of a contour or line integral that encloses the crack front (Rice, 1968a, 1968b).

In the following Sections, a schematic vision of the evolution of the fracture theories in isotropic elastic materials, considering

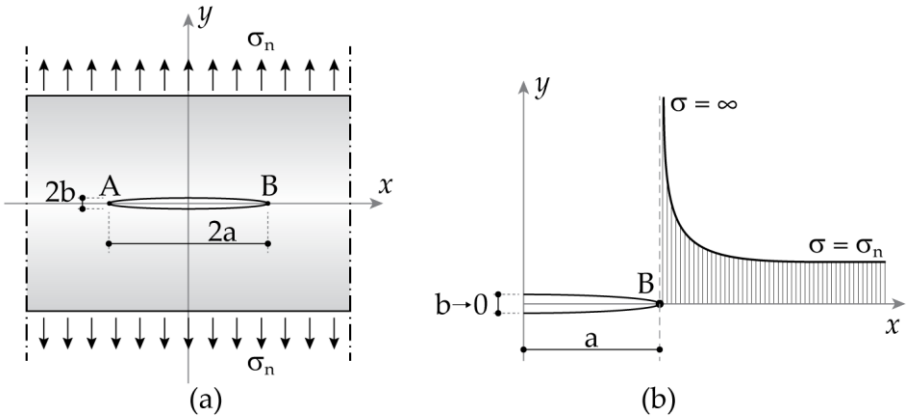

Figure 1.1. Inglis stress analysis: a) crack configuration in an infinite plate subjected to uniform stress; b) crack tip stress field.

small displacements and infinitesimal deformations, is presented.

1.1.1.1 Griffith's crack theory

The fundamental results of the Inglis stress analysis are here summarized. In order to analyze the modifying effect of a crack on the distribution of stress in a linear-elastic solid, we consider an infinity plate containing an elliptical cavity with semi-axes 2a and 2b subjected to a nominal stress σ_n uniformly applied along the Y-axis, as shown in Figure 1.1a. Considering stress-free boundary of the hole and tiny semi-axes size compared to the plate dimension, the solution of stress problem is relative to an exercise of linear elasticity theory. Starting with the equation of the ellipse,

$$\frac{x^2}{a^2}+\frac{y^2}{b^2}=1\,, \tag{2.1}$$

the minimum radius of curvature in terms of semi-axes is:

$$\rho = \frac{b^2}{a}. \tag{2.2}$$

By the solution of elastic stress distribution problem, derived by Inglis (Inglis, 1913), the resultant maximum axial stress, at the end of the ellipse, is:

$$\sigma_{\max} = \sigma_n \left(1 + \frac{2a}{b} \right) = \sigma_n \left(1 + 2\sqrt{\frac{a}{\rho}} \right), \tag{2.3}$$

The ratio between the maximum axial stress and the driving stress σ_n is the *elastic stress-concentration factor*:

$$\frac{\sigma_{\max}}{\sigma_n} = \frac{2a}{b} = 2\sqrt{\frac{a}{\rho}} = K \quad \Rightarrow \quad \sigma_{\max} = K\sigma_n. \tag{2.4}$$

It is worth noting that such factor depends on the hole shape rather than its size. Indeed, as illustrated in Figure 1.1b, over a very sharp hole, i.e. if $\rho \to 0$, the $\sigma_{\max}$ shows a singularity ($\sigma_{\max} \to \infty$) and it is meaningless. Instead, in presence of a circular hole, i.e. equal semi-axes $a = b$, the stress-concentration factor is equal to $K = 3$ and the stress in point B is a well-defined value $\sigma_{\max} = 3\sigma_n$. Therefore, the stress-concentration factor is a fundamental parameter to analyze the stress at a point in proximity of a notch and if it is a sufficiently high value, such a discontinuity can be a source for a crack onset.

The results of the Inglis elastic stress analysis have been a fundamental input to the Griffith crack theory. Griffith, around

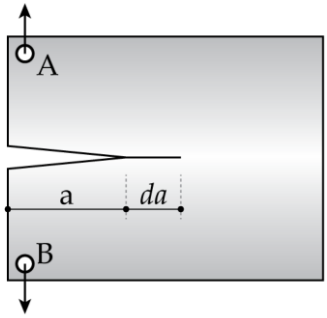

Figure 1.2. Cracked elastic body with an incremental crack extension.

1920, noted that the strength criterion is useless if the stress at the tip crack is an infinite value, regardless of how small the load, and therefore proposed an energy-based failure criterion to the crack advancement that overcome the limits of Inglis prediction but making use of his linear elastic solution.

Griffith considered a conservative reversible thermodynamic system consisting of an elastic body, with unit width, containing a plane-crack surface of length a and subjected to a tensile load in the direction of the y-axis, applied at point A and B of the outer boundaries of body, as depicted in Figure 1.2. The aim was to find the configuration that minimizes the potential energy of the system, in which the crack would be in a state of equilibrium and therefore on the brink of an advancement. The starting point was the expression of the total potential energy U, considering the terms that undergo a change by virtue of a crack virtual extension da (Griffith, 1921):

$$U = U_E - U_A + U_\gamma , \tag{2.5}$$

where, the first two terms of the right member, U_E and U_A,represent mechanical energies, while the last term U_γ is a surface energy. Specifically, the U_E is the strain potential energy stored in the elastic body, U_A is the decrease in elastic energy due to the presence of the crack and the free energy necessary to create the new crack elastic-surface is denoted as U_γ. The energy equilibrium condition is achieved by balancing the terms of the mechanical and surface energy over the virtual crack advancement da. As the crack extends, an increase of the surface energy and, at the same time, a decrease of the mechanical energy contributions occurs. In other words, the crack advancement is favorite by the mechanical energy terms and impeded by the surface energy term. The energy equilibrium condition of (2.5) is defined by the first-order derivative with respect to the virtual crack length, i.e.:

$$\frac{dU}{da} = 0 . \tag{2.6}$$

Subsequently, in order to compute the strain energy release rate during the crack propagation, Griffith applied its energy-balance theory to the case of a large plate containing an infinitely narrow elliptical cavity ($\rho \to 0$), shown in Figure 1.1a, previous analyzed by Inglis, considering an elastic and isotropic material according with Hooke's law. By making explicit the terms of the total potential energy expression (2.5) we obtain that:

$$U = \frac{\sigma_n^2}{2E'} V - \frac{\sigma_n^2}{E'} B\pi a^2 + 2(2aB\gamma_s) , \tag{2.7}$$

where V and B are the volume and width of the body, γ_s is the free surface energy per unit area, and E' is to the reduced Young's modulus, equal to E or $E/(1-\upsilon^2)$ if a plane stress or plane strain conditions are assumed respectively, with υ being the Poisson's ratio. By means of the energy-balance condition, according to (2.6), the critical crack length and the energy release rate are equal to, respectively:

$$a = \frac{2\gamma_s E'}{\pi\sigma_n^2}, \tag{2.8}$$

$$2\gamma_s = \frac{\sigma_n^2 \pi a}{E'}. \tag{2.9}$$

Rearranging the (2.9) a fundamental parameter K_I of Linear-Elastic Fracture Mechanics (Irwin, 1957), called *stress-intensity factor*, is obtained:

$$\sigma_n\sqrt{\pi a} = \sqrt{2\gamma_s E'} \;\Rightarrow\; K_I = \sigma_n\sqrt{\pi a}\,. \tag{2.10}$$

Such a parameter, different from the stress-concentration factor K, which represents only the ratio between the actual and nominal stress at a geometric discontinuity, defines the amplitude of the crack-tip singularity and its critical value is a material property known as fracture toughness (Barsom and Rolfe, 1999). This material property can be determined by means of standardized experimental test, involving specimens having an initial crack, according to the international documents as ASTM 1820 in USA, or ISO 12135 in Europe.

1.1.1.2 Strain-energy release rate

The energy-balance concept proposed by Griffith has introduced a new energy quantity, called strain-energy release rate G, i.e. the potential energy amount Π, provided by the loading system and internal energy elastically stored during crack propagation da, available for infinitesimal crack extensions:

$$G = -\frac{d(U_E - U_A)}{da} = -\frac{d\Pi}{da}. \tag{2.11}$$

When such energy achieves the energy needed to the formation of a new surface, that is the critical fracture energy of material denotes as G_c, the crack advancement occurs. As explain in the previous Section, Griffith evaluate the strain-energy release rate, for a plate subjected to a uniform tensile stress field and containing a crack, equal to $G = \sigma_n^2 \pi a / E' = 2\gamma_s$ and, consequently a fracture stress can be found:

$$\sigma_n = \sqrt{\frac{E'G}{\pi a}}. \tag{2.12}$$

Combining the equations (2.10) and (2.12) an important relationship between the global quantity G and the stress-intensity factor K_I, which instead expresses the strength of the local elastic stress field around the crack tip, is obtained:

$$G = \frac{K_I}{E'}. \tag{2.13}$$

This equation shows that the Irwin' theory based on stress approach and the Griffith' theory based on an energy-balance approach are equivalent.

The condition (2.12) implies that $G = R$, i.e. the strain-energy release rate is equal to the material crack resistance R (assumed by Griffith equal to $2\gamma_s$ only for brittle materials), before relatively slow crack advancement occurs. Consequently, the fracture parameter G_c establishes the crack propagation when $G \geq G_c$. In addition, the fracture stress σ_c can be predicted using the equation (2.12) when the crack is unstable, hence:

$$\sigma_c = \sqrt{\frac{E' G_c}{\pi a}} . \tag{2.14}$$

The Griffith energy-balance approach to crack growth is based on the conservation of energy in the entire body by means of the equation (2.5). The crack growth is considered unstable when the system energy at equilibrium is maximum and stable when it is minimum. A sufficient condition for crack stability is:

$$\frac{d^2U}{da^2}\begin{cases} < 0 \ : \text{ unstable fracture} \\ = 0 \ : \text{ equilibrium} \\ > 0 \ : \text{ stable fracture} \end{cases} . \tag{2.15}$$

1.1.1.3 The J-Integral

The J-Integral, introduced by Rice (Rice, 1968a), is one of most important equations in the fracture mechanics to express the energy release rate G and it could also be applied very suc-

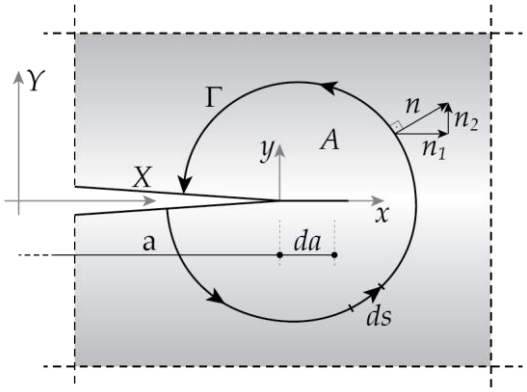

Figure 1.3. Definition of J-Integral around the crack tip.

cessfully at inelastic material behavior. The basic concept proposed by Rice is that the change of potential energy during infinitesimal crack propagation can be expressed with the help of a path-independent line integral.

We consider an arbitrary domain A in the neighborhood of crack tip enclosed by a contour Γ, which runs from the lower to the upper crack face in a mathematically positive sense, with the outward unit normal vector n_j, as depicted in Figure 1.3. On the contour Γ acts a stress field $t_i = \sigma_{ij} n_j$ keep constant during the crack advancement da, while no volume forces act onto the body. During the crack advancement, along its initial direction, the domain A is displaced along with it and all variables field change with the crack length. Because of this, besides the fixed coordinates (X, Y), a new moving system ($x = X - a$, $y = Y$) attached to the crack tip is introduced, so that the total derivate is read as:

$$\frac{d(\cdot)}{da} = \frac{\partial(\cdot)}{\partial a} + \frac{\partial(\cdot)}{\partial X}\frac{\partial X}{\partial a} = \frac{\partial(\cdot)}{\partial a} - \frac{\partial(\cdot)}{\partial x}. \tag{2.16}$$

Now, according to the equation (2.11), we differentiate the potential energy of system, which is a function of the displacement field u_i, with respect to da as follows:

$$\begin{aligned} -\frac{d\Pi(u_i)}{da} &= \frac{d}{da}\left(\int_\Gamma t_i u_i ds - \int_A U_E dA\right) \\ &= \int_A \frac{\partial U_E}{\partial x} dA - \int_\Gamma t_i \frac{\partial u_i}{\partial x} ds + \left[-\int_A \frac{\partial U_E}{\partial a} dA + \int_\Gamma t_i \frac{\partial u_i}{\partial a} ds \right] \end{aligned}. \tag{2.17}$$

Using the following relation concerning the elastic strain-energy potential derivative:

$$\frac{\partial U_E}{\partial a} = \frac{\partial U_E}{\partial \varepsilon_{ij}}\frac{\partial \varepsilon_{ij}}{\partial a} = \sigma_{ij}\frac{\partial u_{i,j}}{\partial a}, \tag{2.18}$$

and converting, by the Gauss's divergence theorem, the line integral into an area integral and involving the equilibrium equations $\sigma_{ij,j} = 0$ the term in brackets of equation (2.17) vanishes. In addition, the first integral of equation (2.17), by means of the Gauss' theorem, can also be converted using the arc length ds along Γ as follows:

$$\int_A \frac{\partial U_E}{\partial x} dA = \int_\Gamma U_E n_1 ds = \int_\Gamma U_E dy. \tag{2.19}$$

Therefore, for the case of a two dimensional plane elastic problem, the energy release rate G can be calculated through a line integral along a curve Γ, which is denoted as J-Integral:

$$G = -\frac{d\Pi}{da} = J \equiv \int_{\Gamma}\left[U_E dy - t_i \frac{\partial u_i}{\partial x} ds\right]. \qquad (2.20)$$

It is worth noting that, to calculate the elastic energy potential we would have to consider the entire system, instead the above-illustrated mathematical proof considers any domain, due to the fact that the J-Integral is independent of the choice of area A and integration path Γ.

1.1.2 Elastic-plastic fracture mechanics in cracked bodies

Many solid materials containing defects during a loading process exhibit some inelasticity in the form of plasticity, creep or phase change in the neighborhood of the crack tip. In this case, due to the stress concentration at the crack tip, the yield stress of material is exceeded at low external load level, developing a small plastic zone. As consequence, the sharp crack becomes increasingly blunted with the increases load and crack opening. The size of plastic zone, that increases as the load increases, could extend, depending on the material and geometric properties, over a wide region or even over the entire solid, until a crack onset takes place. In this zone, due to the fact that the local stresses are limited to the material yield strength, the linear-elastic fracture theory, previously introduced, results to be inaccurate to predict the field equations and the fracture parameters, and, in particular, the stress-intensity factors, which are valid for materials with linear-elastic behavior, are meaningless. However, the dimension of the plastic zone could be a corrective parameter to

evaluate the effective stress-intensity factor, thus accounting for the plasticity effects around the crack tip. The determination of such a plastic zone size, which is small compared to the dimensions of structure or crack length according to the assumption of *small scale yielding*, has been widely investigated by Irwin (Irwin, 1958) and Dugdale (Dugdale, 1960). The purpose was to evaluate an approximation of the fracture zone extension directly ahead of the crack tip, and then, to modify the Griffith's energy-balance equations. In addition, in the elastic-plastic fracture a new local measure of the plastic strains around the crack tip, called *crack tip opening displacement* (CTOD), is introduced by Wells and other authors (Wells, 1965; Burdekin and Stone, 1966) and respect with the well-known fracture parameters it is an experimentally motivated quantity.

In the following Sections a recap of the elastic-plastic theories, including an approximate calculation of the plastic zone, is presented.

1.1.2.1 Approximate size of the crack-tip plastic zone

An approximated estimate of the plastic zone extension can be obtained by means of an elastic-plastic analysis. The aim of the analysis is find the locus of points in which the elastic stress field satisfies the yielding criterion, as long as, the radius of plastic zone r_p stays considerably smaller than the validity radius r_K of the elastic field solution ($r_K \approx 0.02-0.10a$); in other words, the required assumption is a very small plastic zone.

Considering a simple case of a material with perfectly plastic behavior with a yielding stress σ_y, the expressions of the singular principal stresses obtained by the Westergaard semi-inverse method (Westergaard, 1934, 1937) are:

$$\begin{aligned}\sigma_1 &= \frac{K_I}{\sqrt{2\pi r}}\cos\frac{\theta}{2}\left(1+\sin\frac{\theta}{2}\right)\\ \sigma_2 &= \frac{K_I}{\sqrt{2\pi r}}\cos\frac{\theta}{2}\left(1-\sin\frac{\theta}{2}\right)\end{aligned}, \tag{2.21}$$

where θ is the angle between the x axis and the crack direction. By inserting them into the well-known von Mises yield criterion (von Mises, 1913) the plastic zone radius, is obtained as:

$$\begin{aligned} r_p(\theta) &= \frac{1}{4\pi}\left(\frac{K_I}{\sigma_y}\right)^2\left(\frac{3}{2}\sin^2\theta+1+\cos\theta\right) && \text{for plane stress}\\ r_p(\theta) &= \frac{1}{4\pi}\left(\frac{K_I}{\sigma_y}\right)^2\left(\frac{3}{2}\sin^2\theta+(1-2\upsilon)^2(1+\cos\theta)\right) && \text{for plane strain}\end{aligned}. \tag{2.22}$$

Considering a crack advancement along the x axis ($\theta = 0$) the plastic zone radius is:

$$r_p(\theta) = \frac{1}{2\pi}\left(\frac{K_I}{\sigma_y}\right)^2 \quad \begin{cases}1 & \text{for plane stress}\\ (1-2\upsilon)^2 & \text{for plane strain}\end{cases}. \tag{2.23}$$

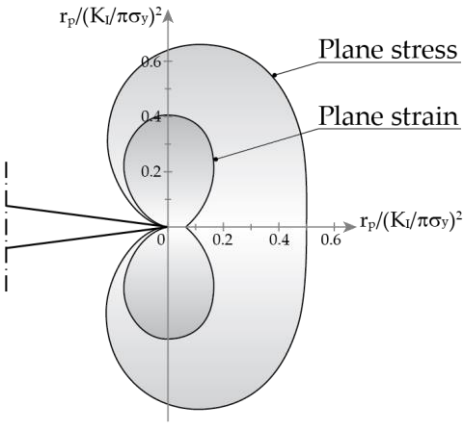

Figure 1.4. Approximate estimation of the crack-tip plastic zones under plane stress and plane strain condition and $\nu = 1/3$.

Figure 1.4 shows the shape of the plastic zone for plane stress and plane strain considering $\nu = 1/3$, and, it worth noting that, the plane stress zone is approximately 9 times much larger than plane strain zone due to the higher constraint for plane strain.

1.1.2.2 Irwin's elastic-plastic model

A simplified model to determine the plastic zone size in the neighborhood of the crack tip under small-scale yielding, for an elastic-perfectly plastic material under plane stress condition, is proposed by Irwin (Irwin, 1960). The elastic stress distribution σ_y, reported in Figure 1.5, indicates that $\sigma_y \to \infty$ as $r \to 0$, but the σ_y stress is limited to yielding stress of material, therefore the $\sigma_y \to \infty$ occurs mathematically, not physically. Using the equation (2.23) for plane stress condition, r_p is determined by imposing the condition $\sigma_y = \sigma_{ys}$. It is clearly visible that, the stress

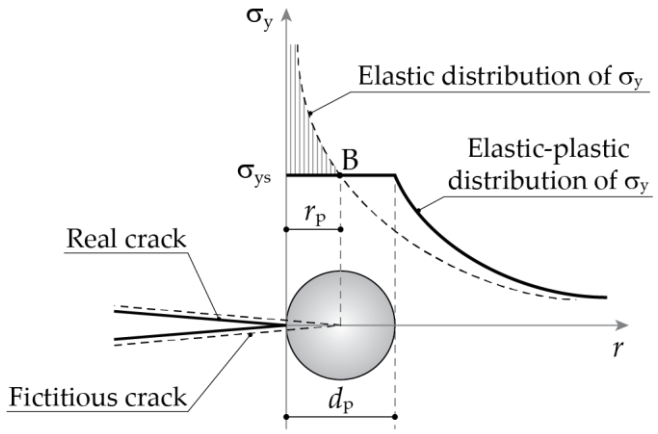

Figure 1.5. Correction of the stress distribution σ_y ahead of a crack tip according to the Irwin model.

equilibrium condition along the y axis is violated because the stress distribution inside the plastic zone is forced to be constant and equal to the yielding stress of material σ_{ys}. Irwin proposed that, due to the re-distribution along the x axis of the elastic stress inside the shaded area depicted in Figure 1.5, a plastic zone size larger than r_p is necessary to satisfy the stress equilibrium. Indeed, the shaded area under the σ_y curve up to the point B is:

$$\int_0^{r_p} \frac{K_I}{\sqrt{2\pi x}} dx = 2\sigma_{ys} r_p \,, \tag{2.24}$$

and the area defined by the yielding stress of material is equal to $\sigma_{ys} r_p$, therefore in order to satisfy the stress equilibrium along y direction the length of plastic zone ahead of the crack tip must be equal to $d_p = 2r_p$, and it is given by:

$$d_p = \frac{1}{\pi}\left(\frac{K_I}{\sigma_{ys}}\right)^2. \tag{2.25}$$

For plane strain condition the stress required to achieve the yielding increases by a factor of $\sqrt{3}$, leading to a plastic zone length equal to:

$$d_p = \frac{1}{3\pi}\left(\frac{K_I}{\sigma_{ys}}\right)^2. \tag{2.26}$$

The yielding stress condition, according to the code ASTM Standard E399, is characterized as the plane stress when $d_p = B$ and as plane strain when $d_p < B/25$, where B is the thickness of the element.

1.1.2.3 Dugdale's elastic-plastic model

In order to avoid the complexities of an elastic-plastic analysis, a simplified yielding model to determine the plastic behavior in front of the crack tip is proposed by Dugdale (Dugdale, 1960). An ideally plastic material behavior is assumed inside the plastic zone. The plane stress condition is valid so that the yielding begins at $\sigma_y = \sigma_{ys}$, while for plane strain condition, due to the constraint deformation in multiaxial stress state, a correction factor α_{cf} is used to achieve the yielding stress of material, so that $\sigma_y = \alpha_{cf}\sigma_{ys}$. In this model, also called *yield strip model*, the entire plastic deformation is concentrated on a line (strip) of length d along which, according to the Tresca's yield criterion, the yield stress σ_{ys} prevails. Considering an infinite plate containing a

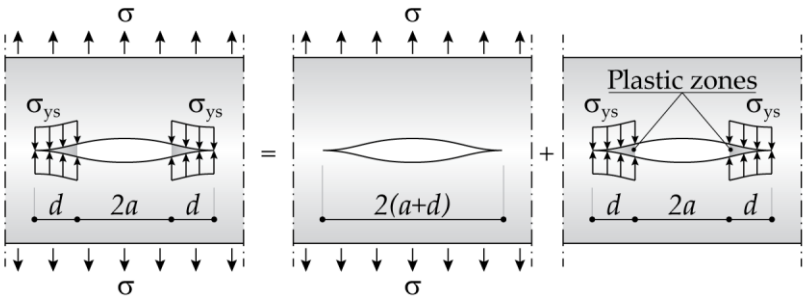

Figure 1.6. Schematic representation of the Dugdale model for a crack subjected to uniaxial tension.

crack length $2a$ and subjected to uniaxial uniform stress in y direction, the model can be imagined as superposition of the two following loading conditions, reported also in Figure 1.6:

1) A crack length $2(a+d)$ in an infinite plane under constant stress σ;
2) A crack length $2(a+d)$ in an infinite plane subjected to a uniform stress distribution equal to σ_{ys} along the plastic zone.

The stress-intensity factor for the problem (1) is given by the linear-elastic solution described in the previous Section, modifying the crack length from the equation (2.10):

$$K_I^{(1)} = \sigma\sqrt{\pi(a+d)}\,. \tag{2.27}$$

Instead, for the load case (2) the stress-intensity factor has been calculated by means of a semi-analytical method based on the *crack weight functions* (Chen, 1989) as follows:

$$K_I^{(2)} = -2\sigma_{ys}\sqrt{\frac{a+d}{\pi}}\arccos\left(\frac{a}{a+d}\right). \tag{2.28}$$

The assumption of no stress singularities at the end of the fictitious crack $|\chi| = \pm(a+d)$ causes the stress-intensity factors of both subproblems to cancel each other out:

$$K_I = K_I^{(1)} + K_I^{(2)} = 0\,. \tag{2.29}$$

From this equation the length of plastic zone d can be deducted as follows:

$$\frac{a}{a+d} = \cos\frac{\pi\sigma}{2\sigma_{ys}} \quad \Rightarrow \quad d = a\left[\left(\cos\frac{\pi\sigma}{2\sigma_{ys}}\right)^{-1} - 1\right]. \tag{2.30}$$

It is worth noting that, no plastic zone appears without load $\sigma = 0$, while an infinite length of d is obtained when the stress approaches the yield stress of material producing a plastic sliding of the entire cross section.

In the case of small yielding, i.e. $\sigma \ll \sigma_{ys}$, the cosine function can be approximated by:

$$\left(\cos\frac{\pi\sigma}{2\sigma_{ys}}\right)^{-1} \approx 1 + \frac{1}{2}\left(\frac{\pi\sigma}{2\sigma_{ys}}\right)^2, \tag{2.31}$$

and using the relation $\sigma\sqrt{\pi a} = K_I$, the plastic zone length is equal to:

$$d = \frac{\pi}{8}\left(\frac{K_I}{\sigma_{ys}}\right)^2. \tag{2.32}$$

The comparison between the plastic zone lengths estimated by Dugdale (equation (2.32)) and Irwin (equation (2.26)) shows that the both models provide similar relations, differing only in the pre-factors $1/\pi = 0.318$ and $\pi/8 = 0.392$ respectively.

1.1.2.4 The Crack Tip Opening Displacement

The above-mentioned simplified elastic-plastic models for brittle materials use the linear-elastic fracture criterion in which the localized plasticity in front of the crack tip is treated as a small deformed area at a small-scale yielding. Otherwise, such a criterion invalidates the elastic solution applicability if a large-scale yielding is considered and the controlling fracture parameter K_I is meaningless. In the latter case, a plastic criterion called *crack tip opening displacement,* based on a local measure of the plastic strains around the crack tip, is proposed by Well (Wells, 1965) and Burdekin and Stone (Burdekin and Stone, 1966). Such a new fracture parameter, denoted as δ_{CTOD}, is the irreversible opening displacement of crack faces that exceeds by far the crack opening due to the purely elastic deformation, and it is observed, in physically sense, when the tip of originally sharp crack undergoes wide stretching and blunting due to the plastic deformation (**Errore. L'origine riferimento non è stata trovata.**). The CTOD criterion states that, in ductile materials, the onset crack starts when the CTOD, exceeds a critical value $\delta_{CTOD,c}$.

Considering the Dugdale's model, the crack opening displacement is identified at the tip of the physical crack at $|x| = \pm a$ and can be expressed as:

$$\delta_{CTOD} = u_2^+ - u_2^- = 2u_2(a), \tag{2.33}$$

where, u_2 is the orthogonal displacement to the plane crack while the u_2^- and u_2^+ are the displacements related to the two crack faces. According to the crack configuration shown in Figure 1.6, the crack opening displacement can be defined by (Rice, 1968c) as follows:

$$\delta = \frac{4\sigma}{E}\sqrt{(a+d)^2 + x^2}, \tag{2.34}$$

and, if $x = a$, then $\delta = \delta_{CTOD}$:

$$\delta_{CTOD} = \frac{4\sigma}{E}\sqrt{(a+d)^2 - a^2} \simeq \frac{4\sigma}{E}\sqrt{2ad}. \tag{2.35}$$

Inserting the length of plastic zone estimated by Dugdale into (2.35) under plane stress condition yields the crack tip opening displacement as:

$$\delta_{CTOD} = \frac{K_I^2}{E\sigma_{ys}}. \tag{2.36}$$

These equations provide similar results differing only in a factor of $2/\pi$. Additionally, the δ_{CTOD} can be related to the strain-energy release rate G considering the (2.13) as follows:

$$\delta_{CTOD} = \frac{4G}{\pi\sigma_{ys}}. \tag{2.37}$$

By an experimental point of view, the determination of δ_{CTOD} in a specimen or in a component is very complicated since measurements directly in the crack tip region are difficult to handle. To avoid such complication the crack mouth opening displacement (CMOD) at the specimen surface is measured and then, by means of geometrical assumption the δ_{CTOD} is extrapolated. The interested reader is referred to the literature (Khor et al., 2016; Machida et al., 1990).

1.2 Computational modeling approaches for cracking analysis

The fracture theories mentioned in the previous Sections, based on the assumption that the fracture process is lumped all into the tip of a sharp crack, neglect a detailed description of the fracture behavior in the neighborhood of the crack tip, i.e. in the so-called fracture process zone (FPZ). However, the real FPZ extension is not negligible in small- and medium-sized structures, which are the most common ones in the engineering practice.

Around 1960s, in some experimental tensile tests, a strain softening behavior with a decrease in the loading carry capacity, i.e. a negative slope in the stress-deformation curve is observed in concrete specimens (Rusch and Hilsdorf, 1963; Evans and Marathe, 1968), due to microcracking and localization of the deformation in a narrow band where energy dissipation occurs. From a computational point of view, especially in the continuum

analysis, the strain softening behavior could introduce some numerical phenomena related to the loss of both stability and uniqueness of the solution, and bifurcation of the equilibrium path. The first to encounter such issues were Rashid (Rashid, 1968) and Scanlon (Scanlon, 1971) during the some concrete cracking analysis in the framework of the finite element method (FEM). In particular, adopting the so-called *damage models* in which the cracking process is simulated through suitably defined constitutive relations, they discovered that the energy dissipated by the fracture decrease with the refinement of the mesh and converges to zero, leading to results strongly dependent on the mesh size. To avoid this spurious mesh sensitivity, suitable regularization approaches must be introduced in the model, thus leading to a correct capturing of damage-induced softening.

In the literature, two models' groups with different softening constitutive laws can be distinguished: cohesive crack models, and smeared crack models. The former models, assume a softening constitutive law, based on a stress-crack opening displacement relation, to simulate the material behavior of the so-called *fictitious crack*, that is the extension of the real crack where the material keeps its ability to transfer the stress. The latter models, instead, introduce a softening stress-strain relation included in a band around the crack in order to describe the fracture process in a wide range of materials.

In the following Sections a description of both above-mentioned models is presented, together with some of the related computational details.

1.2.1 Cohesive crack models

The fundamental idea of the cohesive fracture approach, initially introduced by Barenblatt and Dugdale (Barenblatt, 1959, 1962; Dugdale, 1960) to study brittle fracture, is that the nonlinear fracture process is developed along the extension of the real crack and it is governed by a traction-separation law usually employed for the atomic lattice decohesion. In the literature, several researchers have used cohesive approaches, in the finite element framework, to investigate the fracture phenomena in various materials. For instance, Hillerborg et al. apply the cohesive method to simulate the crack propagation in concrete structures obtaining accurate results also with coarse meshes (Hillerborg et al., 1976). A cohesive finite element formulation based on a boundary integral method is proposed by Petersson to analyze the concrete behavior under mode-I loading condition (Petersson, 1981). The mixed-mode loading condition, instead, is simulated by Ingraffea and Gerstle using a nonlinear algorithm based on stress intensity factors providing results inconsistent respect to the experimental data (Ingraffea and Gerstle, 1984). In addition, Ingraffea et al. show that the bond-slip behavior of reinforcing bars embedded in concrete can be numerically well predicted by cohesive models, using tension-softening interface elements

to modelling the radial secondary cracks (Ingraffea et al., 1984). Several studies on the influence of the size of the tested specimen on the global structural response are carried out using the cohesive approach (Carpinteri, 1989a, 1989b). In particular, using the modified Petersson's cohesive model, a change of the fracture behavior, which range from ductile to brittle, is observed as the structural sizes increase. The large and/or slender structures, with high tensile strength and small fracture toughness, show extremely brittle behavior and a snapback in the equilibrium path, i.e. a positive slope in the softening branch of load-displacement curve, occurs. In addition, in the most of cases, instability problems typical of the model based on LEFM are observed (Carpinteri, 1989c, 1990; Carpinteri and Colombo, 1989). In this context, Planas and Elices developed an asymptotic analysis that allowed an accurate treatment of the cohesive zone for the specimen with very large dimensions (Planas and Elices, 1991). A particular intrinsic potential-based cohesive model is elaborated by Xu and Needleman, in which the cohesive elements are inserted along all boundaries of the discretized computational domain (Xu and Needleman, 1994). However, such an approach inevitably led to mesh dependency issues, in term of lack of spatial convergence for arbitrary crack paths (Papoulia et al., 2006). An alternative numerical procedure, instead, is proposed by Camacho and Ortiz, where bi-dimensional cohesive elements with stress-based extrinsic law are adaptively inserted by duplicating nodes that were previously bonded (Camacho and Ortiz,

1996). A energy-based cohesive model is proposed by Xie and Gerstle for both linear and nonlinear elastic crack propagation problems obtaining an efficient convergence in the mode I and mixed-mode failure analysis (Xie and Gerstle, 1995). The cohesive method is also used by Cendón and other authors, in conjunction with a strong discontinuity approach, to formulate a simple and efficient numerical procedure useful to simulate the fracture behavior under a global mixed-mode loading condition. Their results show that the crack grows with a predominantly local mode I fracture. Subsequent studies were carried out to apply the cohesive fracture modeling in several area, such as dynamic crack growth (Ruiz et al., 2001), viscoelasticity (Rahulkumar et al., 2000), nonhomogeneous materials, and plasticity (Paulino et al., 2017).

The above-mentioned cohesive methods can be divided into two main model groups, i.e. *inter-element* and *intra-element* cohesive models. In the first group, cohesive cracks are constrained to be extended between the finite elements, whereas in the latter, cohesive cracks can propagate across the finite elements. In the subsequent Sections, after a brief introduction of the basic concepts of the cohesive approach, the most important computational methods of type inter- and intra-element, will be illustrated.

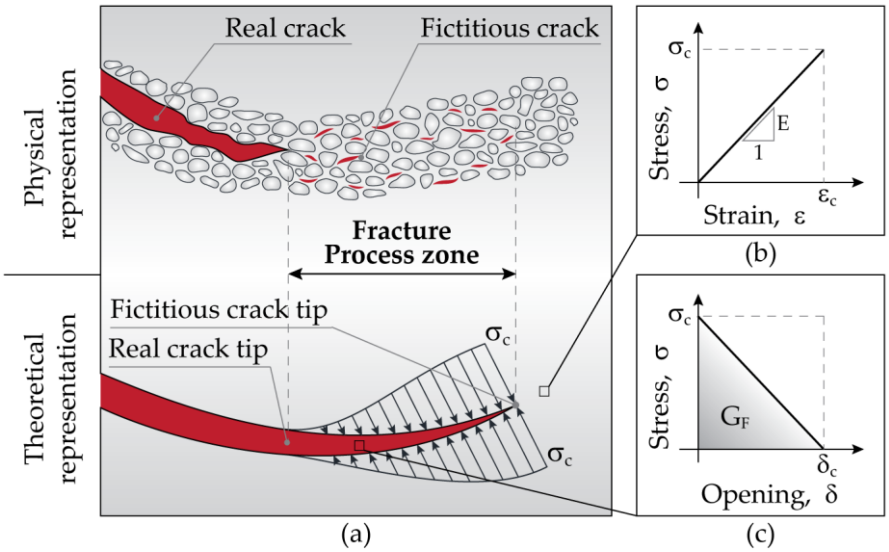

Figure 1.7. Cohesive crack approach: physical and theoretical representation (a), and constitutive laws for undamaged material (b) and fracture process zone (c).

1.2.1.1 Basic concepts of the cohesive approach

The cohesive approach assumes that a fictitious crack, where the material albeit damaged is still able to transfer stresses, begins to form when the principal tensile stress reaches the critical tensile strength of the material (Figure 1.7a). In this zone, called *fracture process zone* (FPZ), the stresses transferred by the material are governed by a traction-separation cohesive law and decrease as the displacement discontinuity increases (Figure 1.7c), while outside of this region, the material behavior is linear-elastic (Figure 1.7b). Such a cohesive function, that describes the interaction force between the two crack faces, represent a real local material

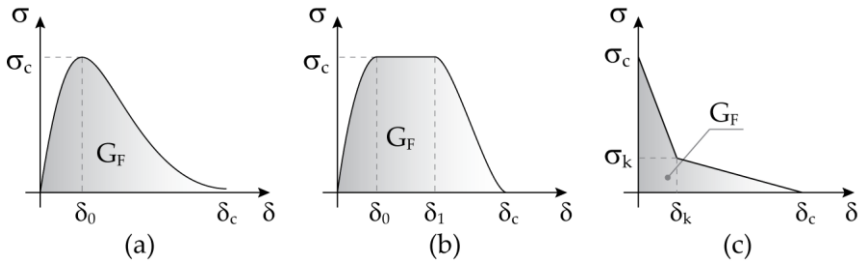

Figure 1.8. Typical shapes of the traction-separation law: fully exponential (a), trapezoidal (b) and bi-linear (c) law.

property and relates the traction force and the opening displacement of the crack. In the literature, several cohesive laws have been proposed, which differ to each other according to various materials and failure mechanisms (Park and Paulino, 2011). However, it does not exist a "natural" cohesive law given a priori, since the cohesive model is a phenomenological model which does not claim to model the real physical fracture process, so that the choice of a separation law is basically free. In Figure 1.8 some typical shapes of traction-separation law are illustrated. They can be collected into two main groups: *intrinsic cohesive laws* (Figure 1.8a, and b), characterized by a linear-elastic branch before the softening branch and usually employed in fracture analysis for which the cohesive elements are inserted prior to the simulation along predefined crack paths, and *extrinsic cohesive law* (Figure 1.8c), without the initial linear-elastic branch, because the cohesive elements are inserted during the simulation (i.e. on the fly) in the area where the critical tensile strength of the material

has already been reached. In particular, the intrinsic cohesive relation starts with a linear-elastic branch in which the stress increases with growing crack opening displacement, up to a maximum value σ_c, called cohesive strength, that is regarded as a material property. After which, a softening branch usually characterized by a decrease in the load-carrying capacity occurs until a critical decohesion opening δ_c is reached, then the material is completely separated and no stress can be transmitted. Integrating the traction-separation law up to the critical opening δ_c, i.e. computing the area under the separation curve, the dissipated fracture energy G_F during the crack propagation is obtained:

$$G_F = \int_0^{\delta_c} \sigma(\delta) d\delta \,. \tag{2.38}$$

A fully exponential law, depicted in Figure 1.8a, based on an energy potential of atomic bonds (Rose et al., 1981), is proposed by Needleman (Needleman, 1990) in a modified form for cohesive zone models in which the dependence of the traction forces on the opening displacement is given by:

$$\sigma(\delta) = \sigma_c \frac{\delta}{\delta_0} \exp\left(-\frac{\delta}{\delta_0}\right). \tag{2.39}$$

After a quasi-linear branch up to the critical strength σ_c the curve decays exponentially. A characteristic feature of this model is that the traction does not approach zero at $\delta = \delta_c$.

In the failure analysis of ductile materials, as metals, an alternative intrinsic cohesive law, illustrated in Figure 1.8b, with a region of constant maximum tension before the softening branch, is proposed by Tvergaard and Hutchinson (Tvergaard and Hutchinson, 1992). Such a trapezoidal law has been obtained by using an additional parameter δ_1, which can be freely chosen, leading to the following formulation for the function $\sigma(\delta)$:

$$\sigma(\delta)=\begin{cases}\sigma_c\left[2\left(\dfrac{\delta}{\delta_0}\right)-\left(\dfrac{\delta}{\delta_0}\right)^2\right] & \text{for } \delta<\delta_0\\ \sigma_c & \text{for } \delta_0<\delta<\delta_1\\ \sigma_c\left[2\left(\dfrac{\delta-\delta_1}{\delta_c-\delta_1}\right)^3-3\left(\dfrac{\delta-\delta_1}{\delta_c-\delta_1}\right)^2+1\right] & \text{for } \delta_1<\delta<\delta_c\end{cases}. \qquad (2.40)$$

In the pioneer work of Petersson on crack propagation analysis in concrete structures, an extrinsic bi-linear traction-separation law, showed in Figure 1.8c, is used to simulate the behavior of cohesive elements inserted in an adaptive manner when a stress criterion was satisfied (Petersson, 1981). The softening stress can be written as:

$$\sigma(\delta)=\begin{cases}\sigma_c-\dfrac{(\sigma_c-\sigma_k)\delta}{\delta_k} & \text{for } \delta<\delta_k\\ \sigma_k-\dfrac{\sigma_k(\delta-\delta_k)}{(\delta_c-\delta_k)} & \text{for } \delta_k<\delta<\delta_c\end{cases}, \qquad (2.41)$$

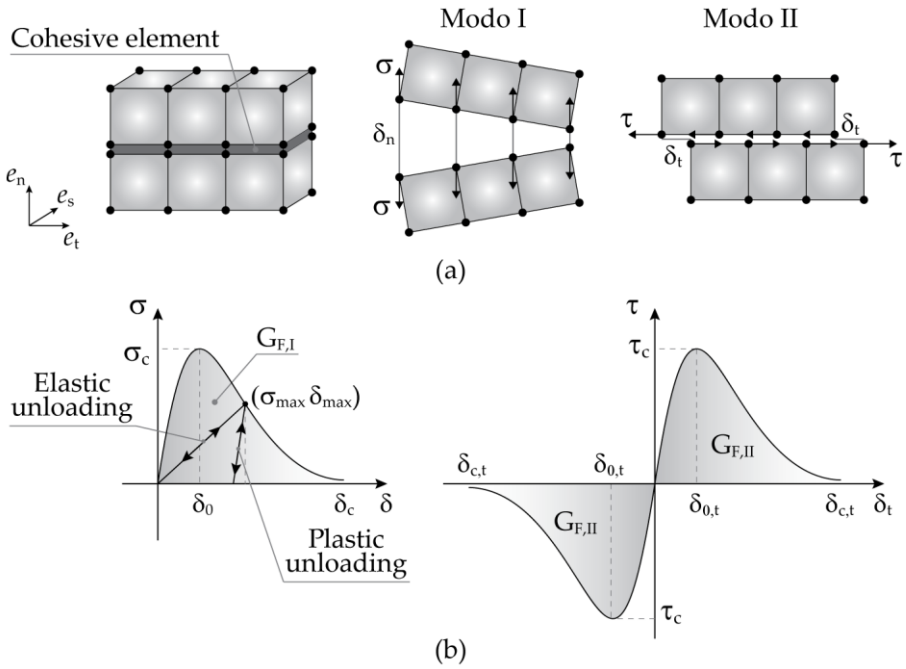

Figure 1.9. 2D finite element realization of cohesive crack model: mode I and mode II loading condition (a) and cohesive law for fracture modes.

where σ_k and δ_k are the kink point coordinates. In order to fit the experimental results, this describing the concrete fracture behavior in a more realistic manner, Petersson proposes $\sigma_k = \sigma_c / 3$ and $\delta_k = 2\delta_c / 9$.

Finally, the essential parameters required by a traction-separation law, needed to implement a cohesive crack model in its simplest form, are the tensile strength and the fracture toughness (or fracture energy) of the tested material, which can be easily obtained by simple experimental tests.

In a general loading condition, the nodes of the damaged interfaces move in the perpendicular direction to the crack (mode I), but also, they can shift to each other in the tangential (mode II) and transversal (mode III) directions to the crack (Figure 1.9a). Thus, the opening displacement vector $\delta = [\delta_n \ \delta_t \ \delta_s]^T$ is defined in the local coordinate system $(\mathbf{e}_n, \mathbf{e}_t, \mathbf{e}_s)$. The cohesive stresses and the opening displacement, in a two-dimensional case, are related by:

$$\begin{matrix} \mathbf{t} = \sigma \mathbf{e}_n + \tau \mathbf{e}_t \\ \boldsymbol{\delta} = \delta_n \mathbf{e}_n + \delta_t \mathbf{e}_t \end{matrix}, \quad \mathbf{t} = f(\boldsymbol{\delta}) \ \text{ or } \ \begin{cases} \sigma = f_n(\delta_n, \delta_t) \\ \tau = f_t(\delta_n, \delta_t) \end{cases}. \tag{2.42}$$

In Figure 1.9b, a typical cohesive law for two-dimensional analysis, which describes both separation modes (I and II), is depicted. It worth noting that, the normal stress is confined by the constraint $\delta \geq 0$, since otherwise a contact of crack faces occurs, producing additional reaction forces to avoid material interpenetration. In the mode-II relation, the tangential stresses change their sign if the direction of the sliding displacement δ_t changes. An alternative method for simulating the local mixed-mode condition and avoiding to consider a cohesive law for each separation mode, is proposed by Ortiz and Pandolfi, based on the introduction of an *effective displacement* δ, relating both normal and tangential local displacements:

$$\delta = \sqrt{(\delta_n)^2 + (\eta \delta_t)^2}, \tag{2.43}$$

whereby, the factor η determines the ratio between shear and tensile stiffness in the cohesive law (Ortiz and Pandolfi, 1999).

The normal and tangential stress functions can be derived from an energy potential Φ_e. For instance, the exponential law (2.39) proposed by Needleman can be obtained by considering the following energy potential:

$$\Phi_e(\delta) = \int_0^{\delta_c} \sigma(\delta) d\delta = G\left[1 - \left(1 + \frac{\delta}{\delta_0}\right)\exp\left(-\frac{\delta}{\delta_0}\right)\right]. \qquad (2.44)$$

By using the expression for the effective displacement δ, the normal and tangential cohesive laws can be extracted as:

$$\sigma = \frac{\partial \Phi_e}{\partial \delta_n} = \frac{t}{\delta}\delta_n, \qquad \tau = \frac{\partial \Phi_e}{\partial \delta_t} = \frac{t}{\delta}\eta^2\delta_t, \qquad (2.45)$$

from which an effective cohesive stress can be defined as:

$$t = \sqrt{(\sigma)^2 + \left(\frac{\tau}{\eta}\right)^2}. \qquad (2.46)$$

The unloading during the irreversible fracture process, is taken into account by the traction-separation law in the numerical analysis. In particular, up to critical tensile strength of the material, the unloading runs elastically on the same curve to the origin. In the softening branch, instead, the unloading and eventually re-loading occur along a different path. If a quasi-brittle material is simulated, the unloading path follows towards the origin, instead, for ductile material the unloading runs parallel to initial elastic slope and a plastic deformation occurs. In both cases, the maximum value of the effective displacement $\delta_{\max}$ over the entire loading history is necessary to be compute, so that:

$$\text{Loading:} \quad \delta = \delta_{\max}$$

$$\text{Unloading:} \quad \delta < \delta_{\max} \begin{cases} \text{elastic}: \; t = a\delta \quad \text{with} \quad a = \dfrac{\partial^2 \Phi_e(0)}{\partial \delta^2} \\ \text{plastic}: \; t = \dfrac{t_{\max}}{\delta_{\max}} \delta \end{cases} . \quad (2.47)$$

The cohesive crack approach is generally used in conjunction with computational techniques to approximate the nonlinear fracture process. Within a finite element setting, two main strategies to investigate failure can be found in the literature, i.e. inter-element and intra-element models. They will be explained in detail in the next Sections.

1.2.1.2 Inter-element cohesive models

In inter-element cohesive models, cracks are constrained to be extended between the finite element of the mesh, and their propagation is allowed by using specific interface elements, equipped with a constitutive relation, written in terms of above-mentioned traction separation law. Such cohesive interface elements can be a priori inserted in the case of known crack path, for example to simulate debonding problems in composite laminates. Instead, in the case of unknown crack paths, these elements are inserted during the simulation, in an adaptive manner. Several cohesive interface models on this kind have been proposed in the literature to analyze mixed-mode fracture in concrete and other quasi-brittle materials (Bocca et al., 1991; Camacho and Ortiz, 1996; Yang and Chen, 2005; Zhang et al., 2007). Here, two of the main inter-element cohesive models will

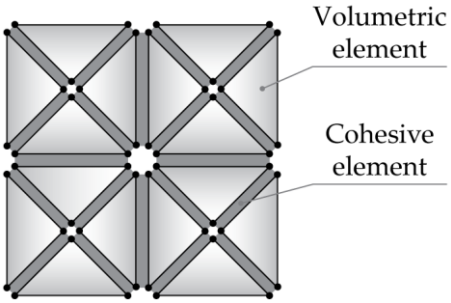

Figure 1.10. Representation of the cohesive/volumetric finite element method.

be explained, also highlighting their advantages and/or potential drawbacks in the failure analysis.

Cohesive/volumetric finite element model proposed by Xu and Needleman. A particular inter-element cohesive model is proposed by Xu and Needleman (Xu and Needleman, 1994) in order to investigate the dynamic crack growth and crack branching phenomena in isotropic elastic solids subjected to tensile loading conditions. The basic idea of the model is to disperse potentially damaging cohesive surfaces over all the discretized body. Thus, a crossed-triangle quadrilateral mesh, in a finite element framework, consisting of volumetric finite elements bordered by cohesive surface elements is involved to perform dynamic crack analysis (**Errore. L'origine riferimento non è stata trovata.**). A constitutive law that relates stress and strain governs the elastic behavior of volumetric bulk elements, while a trac-

tion-displacement jump law is used to describe the nonlinear behavior of a specific set of cohesive surfaces, that are interspersed throughout the continuum.

The equilibrium problem of the discretized body was formulated as a nonlinear boundary value problem (BVP) expressed in the following weak form:

$$\int_V \mathbf{s} : \delta\mathbf{F} dV - \int_{S_{int}} \mathbf{T} \cdot \delta\boldsymbol{\Delta} dS = \int_{S_{ext}} \mathbf{t} \cdot \delta\mathbf{u} dS - \int_V \rho \frac{\partial^2 \mathbf{u}}{\partial t^2} \cdot \delta\mathbf{u} dV , \quad (2.48)$$

where $\mathbf{s}$, $\mathbf{F}$, $\mathbf{t}$ and $\mathbf{T}$ are the nonsymmetric nominal stress tensor, the gradient of deformation, the external load vector and the cohesive traction vector, respectively. The displacement jump across the cohesive surface is denoted as $\boldsymbol{\Delta}$, whilst, V, S_{int}, and S_{ext} are the volume, external surface, and internal cohesive surface, respectively. The symbol ρ represents the density of the material. A constitutive law for isotropic hyper-elastic bulk elements is considered, so that the second Piola-Kirchhoff stress tensor is:

$$\mathbf{S} = \mathbf{s} \cdot \mathbf{F}^{-1} = \frac{\partial W}{\partial \bar{\mathbf{F}}}, \quad (2.49)$$

where W represents the strain energy density. The Lagrangian strain tensor $\bar{\mathbf{F}}$ is given by:

$$\bar{\mathbf{F}} = \frac{1}{2}(\mathbf{F}^{\mathrm{T}} \cdot \mathbf{F} - \mathbf{I}), \quad (2.50)$$

where $\mathbf{I}$ is the identity matrix.

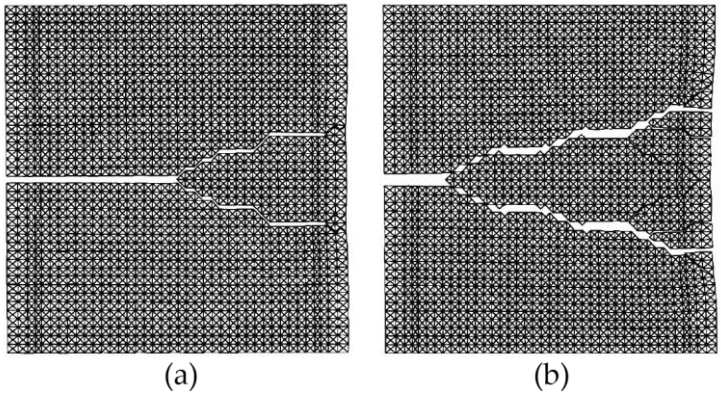

Figure 1.12. Deformed mesh of a block subjected to dynamic loading condition obtained by the volumetric/cohesive finite element method. Pictures taken from (Xu and Needleman, 1994).

Cohesive elements are equipped, instead, with a phenomenological mechanical constitutive relation between the traction and the displacement jump. Fully exponential intrinsic laws (Figure 1.11), used to describe the cohesive forces behavior for each fracture modes (mode I and II), are obtained by the energy potential Φ illustrated in (Xu and Needleman, 1994), so that:

$$\mathbf{T} = \frac{\partial \Phi}{\partial \mathbf{\Delta}}. \tag{2.51}$$

The cohesive/volumetric FE model has been used to perform a dynamic analysis of the wave propagation in a block with and without an initial crack. The specimen is discretized by quadrilateral elements, enriched with diagonal elements at 45°, all surrounded by cohesive surface elements. The effect of varying the impact velocity on the crack branching was investigated. Figure 1.12 shows the crack pattern of the block subjected to symmetric

loading condition with wave speeds equal to 1 ms^{-1} (Figure 1.12a), and 15 ms^{-1} (Figure 1.12b). The main result of the analysis is that the higher the impact velocity the less crack growth there is before branching. Focusing on the crack pattern, we can note that the model is able to capture the crack branching phenomena in an accurate manner, and although the crack can only propagate in parallel and 45° direction respect to the axes, the overall branching angle is noticeably less than 45°, as demonstrated by experimental results. In addition, considering a pre-cracked block, a study of the orientation effect of the cohesive surface elements on the crack path was carried out. Four mesh configurations were built by varying the orientation angle of diagonal elements. The crack pattern of the different configurations with diagonal elements inclined by 15°, 30°, 45°, and 60° respect to the x-axis are depicted in Figure 1.13a, b, c, d, respectively. A zig-zag crack growth is predicted by the configurations with angles of 15° and 30°, even though the meshes and boundary condition are

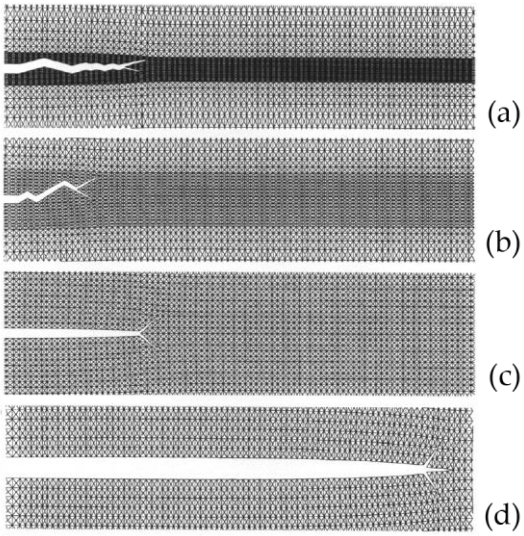

Figure 1.13. Deformed mesh obtained by a mesh orientation sensitivity analysis in (Xu and Needleman, 1994).

symmetric, while a crack propagation in horizontal direction is obtained by the other configurations. It is worth noting that, also the onset of the crack branching phenomena is strongly influenced by the discretization.

The above-discussed diffuse cohesive formulation, consisting of cohesive surface elements inserted along all the mesh boundaries, is one of the first applications of the cohesive approach within the finite element method. In this model, the use of a structured triangulation highlighted the well-known mesh dependency issues of the inter-element fracture approaches, in terms of lack of spatial convergence for arbitrary crack paths or patterns, as showed in Figure 1.13. Furthermore, it has been largely demonstrated that unstructured meshes with very good

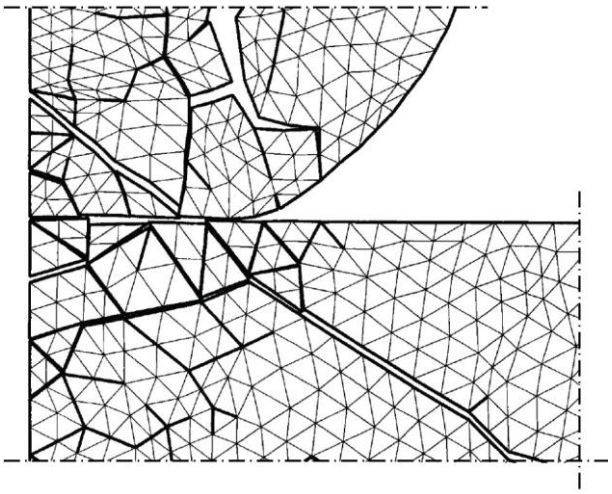

Figure 1.14. Crack phenomena simulated by the adaptive cohesive volumetric finite element model of (Camacho and Ortiz, 1996).

isotropic properties, i.e. Delaunay mesh, can reduce such artificial mesh effects, especially in terms of sensitivity to the mesh orientation, even if the question of energy convergence still remains an open issue.

Adaptive cohesive volumetric finite element model proposed by Camacho and Ortiz. In the inter-element discrete fracture framework, an alternative cohesive volumetric FE model to predict the propagation of dynamic fracture and fragmentation in brittle materials subjected to impact load is developed by Camacho and Ortiz (Camacho and Ortiz, 1996). The proposed model, based on an extrinsic cohesive approach, adaptively create new cohesive surfaces as a brittle fracture criterion is satisfied, duplicating nodes along boundaries of the coherent finite

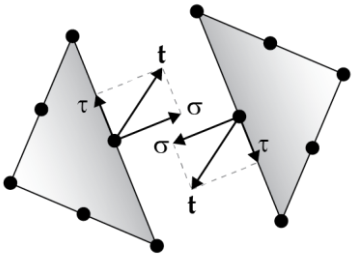

Figure 1.15. Six-node triangular element with representation of the cohesive traction vector and its components.

elements. In this way, the nucleation and propagation of the single or multiple cracks as well as the branching and fragmentation phenomena can be easily simulated (Figure 1.14). An advancing front algorithm to mesh generation is used to discretize the domains of the analyzed body involving six-node triangular elements finite elements (Figure 1.15) and also useful to defining the contact surfaces. Such an algorithm modifies the computational information of boundaries and nodes during the creation of crack surfaces and adds new domains to the system if complete fragmentation occurs. In this model, that also employs a contact/friction algorithm for the self-contact across crack faces, the dynamic equilibrium problem is written in weak form by the virtual work principle at time t_{n+1}, as follows:

$$\int_V \mathbf{P} : \nabla \boldsymbol{\eta} dV - \int_V (\mathbf{f} + \rho \mathbf{a}) \cdot \boldsymbol{\eta} dV - \int_S \mathbf{t} \cdot \boldsymbol{\eta} dS = 0 , \qquad (2.52)$$

where $\mathbf{P}$ and ∇ are the first Piola-Kirchhoff stress and the material deformation gradient, respectively. The body forces, accel-

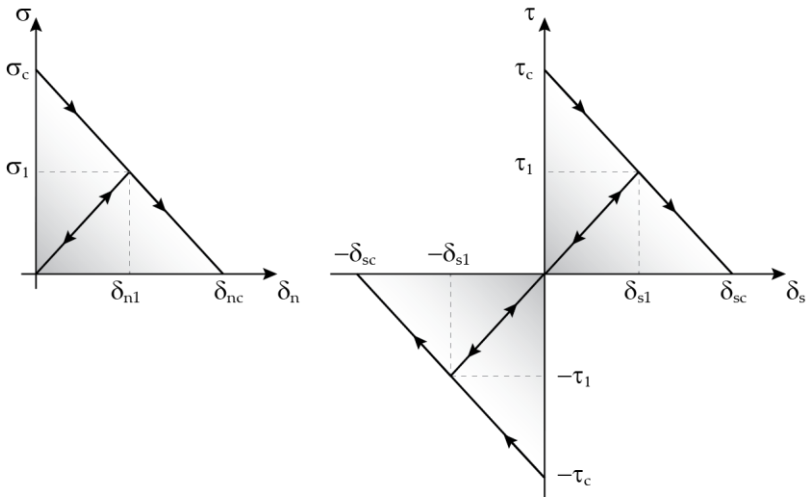

Figure 1.16. Normal and shear cohesive law used in (Camacho and Ortiz, 1996).

erations and boundary traction are denoted as $\mathbf{f}$, $\mathbf{a}$, and $\mathbf{t}$, respectively. The symbol $\boldsymbol{\eta}$ represents an admissible virtual displacement field. The normal σ and tangential τ components of the cohesive traction $\mathbf{t}$, calculated at each load step and at each node of the strain six-node triangular elements (Figure 1.15), are used to verify a mixed-mode fracture criteria proposed by several authors (Margolin, 1984; Dienes, 1986):

$$\begin{aligned} &\sqrt{\sigma^2 + \beta\tau^2} \geq \sigma_{fr} && \text{if } \sigma \geq 0 \\ &\sqrt{\beta}\left\langle |\tau| - \mu|\sigma| \right\rangle \geq \sigma_{fr} && \text{if } \sigma < 0 \end{aligned}, \tag{2.53}$$

where β, μ, and σ_{fr} are the shear stress factor, friction coefficient and the critical fracture stress of the material, respectively. When one of the fracture conditions of (2.53) is satisfied, a new cohesive surface is introduced into the mesh by the interested

nodes duplication. The new cohesive surface elements are equipped with an irreversible extrinsic-type linear softening law for each fracture mode, as depicted in Figure 1.16. The relations between the components of cohesive traction and the displacement jump are the following:

$$\begin{aligned} \sigma &= \sigma_c \left(1 - \frac{\delta_n}{\delta_{nc}}\right) \\ \tau &= \tau_c \left(1 - \frac{|\delta_s|}{\delta_{sc}}\right) \operatorname{sgn}(\delta_s) \end{aligned}, \tag{2.54}$$

where δ_n and δ_s are the normal opening and sliding displacements, respectively. The subscript *c* denotes the critical value of the quantity. As soon as the cohesive stresses reach the corresponding critical values of the material (σ_c and τ_c), they are ramped down linearly as a function of the displacement jump. The critical opening displacement δ_{nc}, can be obtained by the fracture energy, which represents the area under the tensile cohesive law and it can be measured in fracture tests. If unloading occurs, the crack begins to close, and the stresses follow an unloading path towards the origin.

The authors apply the adaptive cohesive model to perform impact fracture analysis involving a hardened steel pellet and an alumina plate. The results of the simulations highlight the computational capabilities of the model to capture complex crack patterns produced by the dynamic fracture progression and frag-

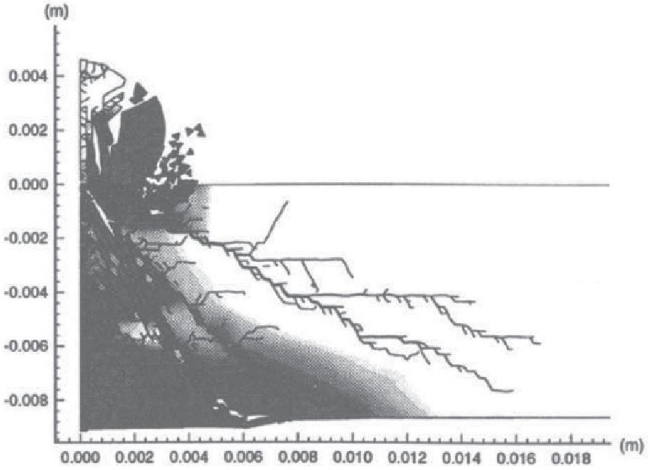

Figure 1.17. Crack pattern obtained by an impact fracture analysis in (Camacho and Ortiz, 1996).

mentation phenomena. In particular, the crack initiation at exterior or interior surface, as well as their propagation through midside and corner nodes, is well simulated by the model (see Figure 1.17). The contact and/or frictional sliding of the crack faces, due to a possible crack closure, is also considered by the contact algorithm implemented in the fracture model. Additionally, typical phenomena of the dynamic fracture, such as crack arrest and crack branching, are predicted in an accurate manner by the model, demonstrating the versatility of the cohesive approach to describe the complex nonlinear mechanical behavior of the material during different fracture phenomena. Such an extrinsic-type cohesive method avoids the mesh dependency issues related to the artificial compliance because the cohesive surface elements are inserted only after that a particular stress criterion is

satisfied. However, the fracture model proposed by Camacho and Ortiz has some limitations. Since cracks can only propagate along the boundaries of the mesh, the predicted path, similar to that obtained by the fracture model proposed by Xu and Needleman, is often jagged and uncoherent with the experimental data. Additionally, the use of a fixed mesh, limits the number of available crack paths with possible distortions of the crack propagation direction and, in some cases, mesh sensitivity issues can occur. As suggested by the authors, these limitations can be overcome by means of suitable remeshing procedures (Kuutti and Kolari, 2012) with a local refinement of the mesh at crack tips in order to increase the number of directions available for the crack propagation and help to prevent premature crack arrest. Furthermore, due to remapping of the stress and strain states, and eventually of the internal variables, such remeshing may cause thermodynamically inadmissible artificial healing of previously cracked regions, posing severe uniqueness problems in the case of the crack branching.

1.2.1.3 Intra-element cohesive models

To model crack initiation and propagation along unknown crack paths without involving any remeshing operations, intra-element cohesive fracture approaches are widely used. Such approaches allow the propagation of the cracks within the finite elements of a given mesh by introducing kinematic enrichment either at the element level, as in the strong discontinuity approach

(SDA), or at the node level, as in the extended finite element method (XFEM). Here, two of the main intra-element fracture models will be explained, highlighting their advantages and/or potential drawbacks in the failure analysis.

Intra-element cohesive model based on the extended finite element method (XFEM).

Recently, the cohesive crack approaches have been implemented in fracture models using alternative finite element frameworks, such as the well-known extended finite element method. The basic concept of the XFEM, is to enrich the approximation space so that it becomes capable of reproducing discontinuities such as cracks or interfaces. In contrast to PUFEM and other generalized FEMs, where the enrichments are usually employed on a global level and over the entire domain, the extended finite element method adopts the same procedure but at local level. Such a method uses the standard finite element mesh, but once the discontinuity takes place, a few degrees of freedom are added to the classic finite element model in selected nodes near to the discontinuity to provide a higher level of accuracy. In this way, the model is able to simulate arbitrary cracks, independently by the mesh, and crack propagation without remeshing procedure.

Considering a discretized domain with a discontinuity, the approximation $\mathbf{u}^h(\mathbf{x})$, used by the XFEM to calculate the displacement field for a point $\mathbf{x}$ locating within the domain, can be

written as the sum of two terms: the classical displacement approximation term related to finite elements without the discontinuity $\mathbf{u}^{\mathrm{FE}}$, and the enriched approximation term for the cracked finite elements $\mathbf{u}^{\mathrm{enr}}$:

$$\mathbf{u}^h(\mathbf{x}) = \mathbf{u}^{\mathrm{FE}} + \mathbf{u}^{\mathrm{enr}} = \sum_{i\in I} N_i(\mathbf{x})\mathbf{u}_i + \sum_{m\in M} N_m(\mathbf{x})\phi(\mathbf{x})\mathbf{a}_m, \quad (2.55)$$

where $\mathbf{u}_i$ is the vector of regular degrees of nodal freedom in the finite element method, and $\mathbf{a}_m$ is the set of degrees of freedom added to enrich the domain of interest. $N_i(\mathbf{x})$ are the classical iso-parametric finite element shape functions, and $\phi(\mathbf{x})$ the enrichment functions defined for the set of nodes included in the influence domain of the discontinuity. I and M are the node-set related to finite elements without the discontinuity and with discontinuity, respectively. In a work of Moës and Belytschko (Moës and Belytschko, 2002), the additional term of the displacement approximation is further divided in two contributions, one related to the finite elements completely cut by the discontinuity and one that describe the approximation displacement field of the element containing the crack tip, thus obtaining the following enriched approximation:

$$\mathbf{u}^h(\mathbf{x}) = \sum_{i\in I} N_i(\mathbf{x})\mathbf{u}_i + \sum_{j\in J} N_j(\mathbf{x})H(f(\mathbf{x}))\mathbf{b}_j + \sum_{k\in K} N_k F(\mathbf{x})\mathbf{c}_k, \quad (2.56)$$

where the Heaviside jump function $H(\cdot)$ is used to enrich the nodes of the elements cut into two parts by the crack. These nodes form the set *J* and are depicted with circles in Figure 1.18.

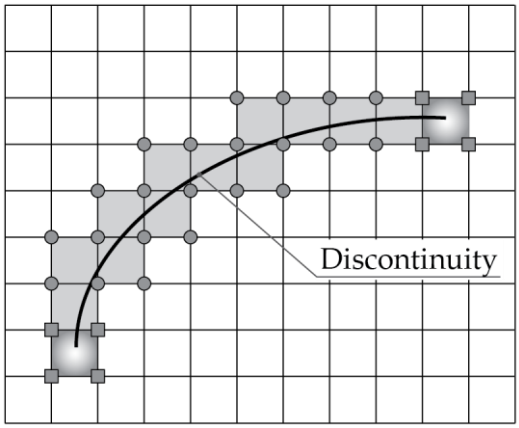

Figure 1.18. Discontinuity within a structured mesh.

The function $f(\mathbf{x})$ is the signed distance function, that identifies the location of the point **x** with respect to the discontinuity, while $F(\mathbf{x})$ is the branch function used to model the displacement field in the elements containing the crack tip. $\mathbf{b}_j$ and $\mathbf{c}_k$, similar to the $\mathbf{a}_m$ in (2.55), represent additional degrees of freedom to model the presence of the crack. The nodes around the tip of the discontinuity, depicted with squares in Figure 1.18, form the set *K*, so that $J \cup K = M$. The most conventional form of branch functions, recently used in a cohesive crack model (Planas and Elices, 1992, 1993; Dolbow et al., 2000) and expressed in the local crack tip polar coordinate system, are defined as:

$$F(r,\theta) \equiv r\sin\left(\frac{\theta}{2}\right) \quad \text{or} \quad r^{3/2}\sin\left(\frac{\theta}{2}\right) \quad \text{or} \quad r^{2}\sin\left(\frac{\theta}{2}\right). \tag{2.57}$$

Introducing the XFEM approximation (2.56) in the equilibrium equation, expressed by mans of a weak form, we obtain the

discrete variational principle weighted with a test function $\mathbf{v}$: find $\mathbf{u}^h \in \Re^h$ (with $\Re^h$ the discrete displacement space) so that:

$$\int_V \boldsymbol{\sigma}(\mathbf{u}^h) : \boldsymbol{\varepsilon}(\mathbf{v}) dV - \int_{S_{int}} \mathbf{t}(\mathbf{u}^h) \cdot \mathbf{w}(\mathbf{v}) dS = \int_{S_{ext}} \mathbf{F} \cdot \mathbf{v} dS \quad \forall \mathbf{v} \in \Re^h, \quad (2.58)$$

where the integration over the volume V, involves the stress tensor $\boldsymbol{\sigma}$ and the function test of the deformation gradient $\boldsymbol{\varepsilon}$, while the integration over internal S_{int} and external S_{ext} surface involve the traction cohesive $\mathbf{t}$ and external load $\mathbf{F}$ vectors, respectively. The symbol $\mathbf{w}$ represent the displacement jump vector along the crack faces.

The fracture process in failure analysis, simulated by an intra-element cohesive model based on XFEM, develops on a discontinuity located in any zone of the discretized domain. Such a discontinuity is introduced in an element when a certain failure criterion is satisfied. Usually, when an equivalent stress exceeds the tensile strength of the material, the crack discontinuity is introduced as a straight line and it is enforced to be geometrically continuous. The actual orientation of this discontinuity is determined by LEFM-based methods such as the principle of local symmetry (Dolbow et al., 2000) and the maximum hoop stress criterion (Erdogan and Sih, 1963). The latter is the most used orientation criterion in this type of analysis and defines the direction of propagation to be along a direction normal to the maximum hoop stress. The angle of crack growth θ is expressed in terms of the external stress intensity factors (SIFs) at the current tip through the formula:

$$\theta = 2\arctan\frac{1}{4}\left(\frac{K_I^{\text{ext}}}{K_{II}^{\text{ext}}} \pm \sqrt{\left(\frac{K_I^{\text{ext}}}{K_{II}^{\text{ext}}}\right)^2 + 8}\right), \tag{2.59}$$

where the sign is chosen so that the hoop stress is positive.

The XFEM combined with the cohesive crack model has been widely used in the literature to simulate crack propagation in several homogeneous and heterogeneous materials. Recently, Gee and coauthors (Gee et al., 2020) have used a valid cohesive-zone XFEM model to predict the structural response, in terms of loading curve and crack path, of a thin rectangular PMMA specimen with an angled initial crack subjected to compression, resulting in a mixed-mode loading condition. The numerically predcited curved crack path is in an excellent agreement with that experimentally found throughout the entire loading history, thus showing the capability of the proposed model to capture, in a very realistic manner, all the main features of mixed-mode crack propagation (see Figure 1.19). The crack pattern has been well predicted by the intra-element fracture models also in concrete fracture analysis. Many numerical results, obtained by several authors (Zi and Belytschko, 2003; de Borst et al., 2004;

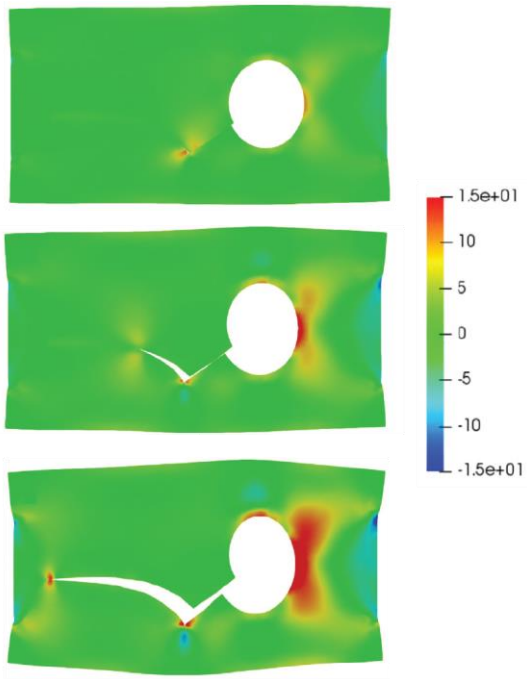

Figure 1.19. Maximum principal stresses of deformed configurations at three different loading steps obtained by cohesive zone XFEM model. Pictures taken from (Gee et al., 2020).

Mergheim et al., 2005) further confirm the accuracy of these models, and demonstrate adequately the effectiveness of the combination of the XFEM and the cohesive crack model in the crack growth simulation in concrete structures. Unlike the above-illustrated inter-element cohesive model, in which the crack is forced to propagate along the boundaries of the finite element, the intra-element approach, by virtue of the extended finite element scheme, is able to inject the discontinuity wherever this crack can be located with respect to the mesh. These models have been proved to provide more reliable numerical results, especially in

the crack path predictions, but usually require a high implementation effort. As a matter of fact, the generalization of XFEM for arbitrary crack propagation problems also required implementation of tracking techniques, such as the level set method (LSM) and the fast marching method (FMM), to re-establish the geometric continuity of the crack line and for determining the location of crack tips (Belytschko et al., 2001; Stolarska et al., 2001).

Embedded finite element method (EFEM) based on a strong discontinuity approach, proposed by Sancho et al.

A simple and successful intra-element cohesive model for the failure analysis of concrete and other quasi-brittle materials, is the embedded cohesive crack model elaborated by Sancho et al. (Sancho et al., 2007). Based on the well-known strong discontinuity approach (SDA) (Simo et al., 1993), in which the displacement jump caused by the geometric discontinuity is embedded in the corresponding finite element displacement field, such a fracture model simulates the crack initiation and propagation processes by means of a simple cohesive crack approach. The typical crack locking problems of the SDA approach, usually caused by the kinematical incompatibility between the cracks in the adjacent elements, are here circumvent by introducing a local crack adaptability algorithm, without resort to the well-known tracking procedures to re-establish the geometric continuity of the crack line (Gasser and Holzapfel, 2006; Jäger et al., 2008).

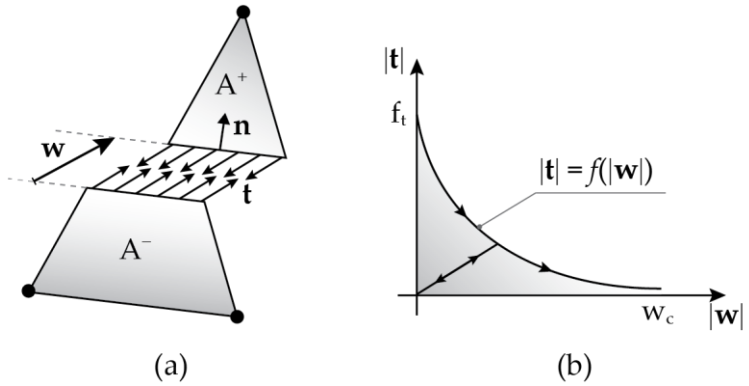

Figure 1.20. Schematic representation of the embedded crack model: notations of a constant stress finite element containing a crack (a) and constitutive cohesive law (b).

The basic concept of the embedded finite element formulation is that, once the principal stress reaches the tensile strength of the material, a straight crack, characterized by a displacement jump vector $\mathbf{w}$, is inserted in the element in the direction normal $\mathbf{n}$ to the maximum principal stress (Figure 1.20a). Thus, the crack modifies the kinematics of the element and the new displacements field, can be written as follows:

$$\mathbf{u}(\mathbf{x}) = \sum_{\alpha \in A^- \cup A^+} N_\alpha(\mathbf{x})\mathbf{u}_\alpha + \left[H(\mathbf{x}) - \sum_{\alpha \in A^+} N_\alpha(\mathbf{x}) \right] \mathbf{w}, \qquad (2.60)$$

where N_α and $\mathbf{u}_\alpha$ are the shape function and nodal displacement associated to the node α, respectively. The Heaviside jump function $H(\mathbf{x})$ has a null value in the region A^- and a value of 1 in the region A^+. In a similar manner, the strain field in the continuum, denoted as ε^c, that determines the stress field of the element on both sides of the crack, is also modified, so that:

$$\varepsilon^c(x) = \underbrace{\sum_{\alpha \in A^- \cup A^+} \left[\mathbf{b}_\alpha(\mathbf{x}) \otimes \mathbf{u}_\alpha \right]^S}_{\varepsilon^a} - \left[\left(\sum_{\alpha \in A^+} \mathbf{b}_\alpha(\mathbf{x}) \right) \otimes \mathbf{w} \right]^S, \quad (2.61)$$

where $\mathbf{b}_\alpha(\mathbf{x})$ is the gradient of the shape function associated to node α. The first summation, according to the finite element method theory, represent the apparent strain ε^a, i.e. the strain field without the discontinuity. The corresponding stress tensor in the element, which follows the hypothesis of elastic bulk material behavior, results to be:

$$\sigma(\mathbf{x}) = \mathbf{E} : \left[\varepsilon^a(\mathbf{x}) - \left[\mathbf{b}^+(\mathbf{x}) \otimes \mathbf{w} \right]^S \right], \quad (2.62)$$

where $\mathbf{E}$ is the tensor of the elastic moduli and $\mathbf{b}^+(\mathbf{x}) = \sum_{\alpha \in A^+} \mathbf{b}_\alpha(\mathbf{x})$. However, along the geometric discontinuity, the stresses are governed by a softening curve according to the adopted cohesive crack approach. This approach is based on a central forces model in which the traction vector $\mathbf{t}$, transmitted across the crack faces, is parallel to the crack displacement jump vector $\mathbf{w}$. The relation between the cohesive traction vector and displacement jump vector (Figure 1.20b) is:

$$\mathbf{t} = f(\tilde{\mathbf{w}}) \frac{\mathbf{w}}{\tilde{\mathbf{w}}}, \quad (2.63)$$

where the variable $\tilde{\mathbf{w}}$ represent the maximum value attained by the effective displacement jump over the entire loading history.

Finally, by prescribing the equilibrium between the traction cohesive vector (2.63) and the stress tensor (2.62) projected in the normal direction $\mathbf{n}$, we obtain:

$$f(\tilde{\mathbf{w}})\frac{\mathbf{w}}{\tilde{\mathbf{w}}} = \left(\mathbf{E} : \left[\varepsilon^a(\mathbf{x}) - \left[\mathbf{b}^+(\mathbf{x}) \otimes \mathbf{w} \right]^S \right] \right) \mathbf{n} \,. \tag{2.64}$$

Once the stress reaches the strength of the material and a straight crack is introduced in the element perpendicular to the principal stress direction, $\mathbf{n}$ is computed as a unit eigenvector of the stress equation. After this, the corresponding vector $\mathbf{b}^+$ is obtained so that the angle between $\mathbf{b}^+$ and $\mathbf{n}$ is the smallest possible. In other words, the geometric discontinuity must be parallel to one of the sides of the triangular finite element.

In the literature, many fracture models based on SDA use crack tracking algorithms to re-establish the geometric continuity of the crack line across the elements. In this model, instead, in order to avoid such types of numerical inconvenience during the simulations and possible crack locking, a simple method, based on a crack adaptability procedure within the element, is introduced. In particular, the model allows the geometric discontinu-

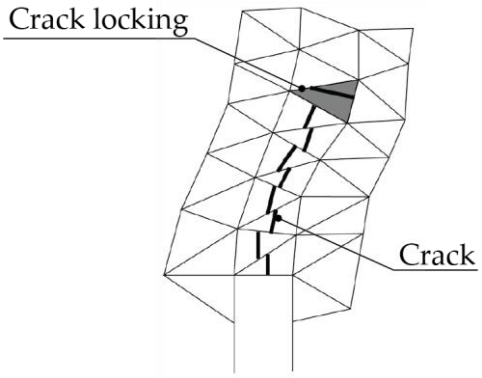

Figure 1.21. Sketch of numerical crack locking phenomena taken from (Sancho et al., 2007).

ity to adapt itself to subsequent variations of the maximum principal stress direction until the effective displacement reached a threshold value (see Figure 1.21). In this way the crack direction is recomputed at each step as if the crack were freshly created.

The embedded crack model is used by the authors for the failure analysis of plain concrete specimens subjected to mode-I and mixed-mode loading conditions (Sancho et al., 2006). The comparisons with experimental results have demonstrated the capability and versatility of the model to predict the global structural response and the crack pattern in an accurate manner without any additional complicated remeshing procedure (see Figure 1.22). In particular, the above-discussed model is able to predict a smoother crack path compared to that jagged obtained by inter-element cohesive models, consequently obtaining a loading curve more consistent with the experimental data. Additionally,

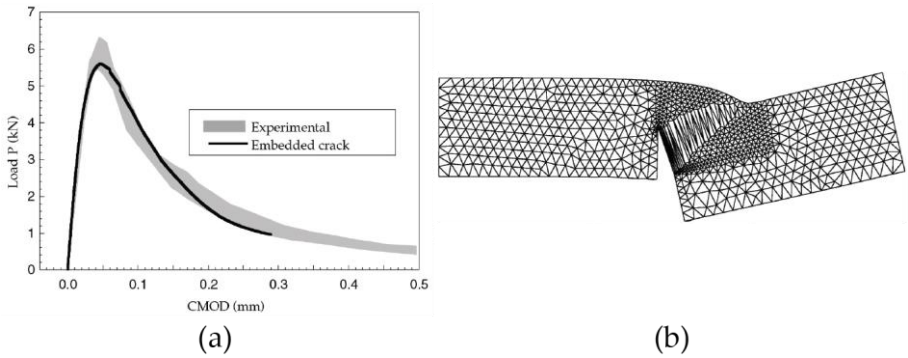

Figure 1.22. Numerical results obtained by the embedded crack model in (Sancho et al., 2006): loading curve (a) and deformed mesh (b).

from a computational point of view, the embedded strong discontinuity model proposed by Sancho et al. does not require a great implementation effort, unlike the X-FEM technique and other sophisticated intra-element approaches.

However, the model would to be tested in more complicated fracture cases, where multiple cracking, crack branching phenomena, and/or coalescence between cracks occur.

1.2.2 Smeared crack models

In contrast to discrete fracture models, in which cracks are modeled as geometric discontinuities, smeared crack models, used almost exclusively in the design practice and that have obtained wide popularity in the finite element analysis, simulate damage processes as a progressive loss of the material integrity due to the propagation and coalescence of micro-cracks and micro-voids (Kachanov, 1986). The smeared crack models (Simo and Ju, 1987a, 1987b; Lemaitre et al., 2002) consider constitutive

relations in which the mechanical effect of the cracking and void growth is introduced with internal state variables which act on the degradation of the elastic stiffness of the material and involve strain softening in order to describes the post-peak gradual decline of stress at increasing strain. Such models can be relatively simple, as the isotropic damage models (Geers et al., 1998; Peerlings et al., 1998; Jirásek, 2004) or more complex as the anisotropic ones (Krajcinovic and Fonseka, 1981; Kuhl and Ramm, 1999; Zhou et al., 2002). However, these models usually adopt different regularization techniques able to prevent the well-known ill-posedness of the associated BVPs, such as those based on strain gradient and micropolar [39] formulations (Peerlings et al., 1998; Leonetti et al., 2019).

In the following Sections the concepts of the continuum damage mechanics, as well as the smeared crack approaches are depicted. In addition, the so-called localization limiters in aid of the continuum damage model, such as crack band models and non-local models, are presented.

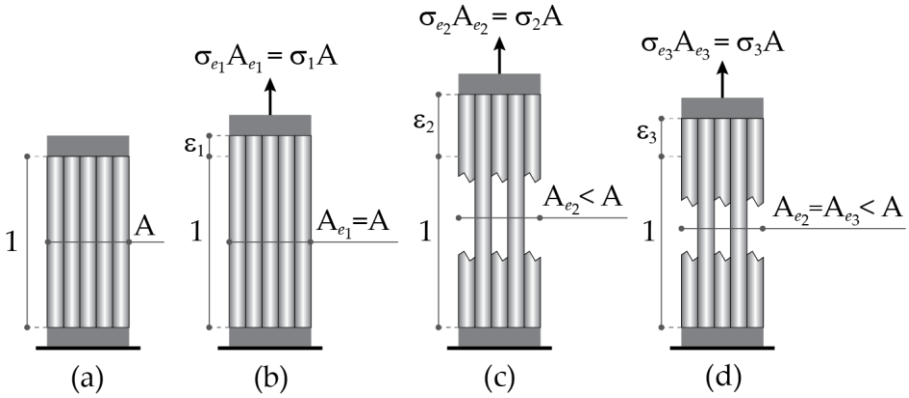

Figure 1.23. Schematic representation of a uniaxial damage model as a bundle of parallel perfectly brittle strips breaking at different strain levels.

1.2.2.1 Basic concepts of continuum damage mechanics

To introduce the basic concepts of the continuum damage mechanics, we analyze the mechanical behavior of a material idealized as set of perfectly brittle strips parallel to the loading direction, as depicted in Figure 1.23a. Initially, all the strips respond elastically, and the entire section maintain the applied load (Figure 1.23b). As the load increases some strips start breaking (Figure 1.23c), and the *effective area* A_e, that is the area of the unbroke strips that can still carry stress, gradually decrease. Now, it is possible to distinguish a nominal stress σ, defined as the force of unit initial area of the cross section, and an *effective stress* σ_e related to the unit effective area. By the equivalence condition $\sigma A = \sigma_e A_e$ we obtain:

$$\sigma = \frac{A_e}{A}\sigma_e , \tag{2.65}$$

in which the ratio A_e / A is a scalar that characterize the integrity of material used in the damage mechanics to define the so-called *damage variable* as follows:

$$D = 1 - \frac{A_e}{A} = \frac{A - A_e}{A} = \frac{A_d}{A}, \tag{2.66}$$

with A_d the damaged area. Therefore, for an intact material, i.e. $A_e = A$, the damage variable is equal to $D = 0$, contrariwise during the degradation process due to the micro-defects propagation, the damage variable asymptotically approaches to the limit value $D = 1$.

Consequently, the nominal stress, governed by Hooke's law, can be expressed as:

$$\sigma = (1 - D) E \varepsilon, \tag{2.67}$$

and the damage process is characterized by the dependence of the D on the applied strain as:

$$D = g(\varepsilon), \tag{2.68}$$

with g a function that describe the stress-strain curve and can be directly identified from a uniaxial tensile test. In the case represented in Figure 1.23d, when the material is first stretched up to a strain level ε_2, inducing a damage $D_2 = g(\varepsilon_2)$ and then a strain decrease occurs until ε_3, the damage area remain constant but the material respond elastically with a reduction of Young's modulus $E_2 = (1 - D_2) E$. In this case, during the unloading and reloading condition, the damage variable must be evaluated from the largest previously reached strain:

$$\kappa = \max_{History}(\varepsilon), \tag{2.69}$$

and the damage evolution law is then replaced by equation:

$$D = g(\kappa). \tag{2.70}$$

Now, we can introduce a new function $f(\varepsilon,\kappa) = \varepsilon - \kappa$ and the loading-unloading conditions can be expressed in the Kuhn-Tucker form as follows:

$$f \le 0, \quad \dot{\kappa} \ge 0, \quad \dot{\kappa} f = 0, \tag{2.71}$$

in which it is imposed that κ can never be smaller than ε, κ cannot decrease and can increase only if the current values of ε and κ are equal. Therefore, $f = 0$ and $\dot{\kappa} > 0$ during damage growth, $f < 0$ and $\dot{\kappa} = 0$ during unloading condition.

The above-explained uniaxial damage test can be extended to general multiaxial stress states by means of an isotropic damage model with a single scalar variable. The fundamental assumptions of the isotropic model are: (i) stiffness degradation is isotropic, i.e. the stiffness moduli, corresponding to different directions, decrease proportionally independently of the loading direction; (ii) the Poisson's ratio is not affected by the damage, i.e., the relative reduction of all stiffness coefficients is the same. Consequently, the damage stiffness tensor is expressed as:

$$\boldsymbol{E}_s = (1 - D)\boldsymbol{E}, \tag{2.72}$$

where $\boldsymbol{E}$ is the elastic stiffness tensor of the intact material and $\boldsymbol{E}_s$ is the secant stiffness that relates the total strain to the total stress, according to the formula:

$$\boldsymbol{\sigma} = \boldsymbol{E}_s \boldsymbol{\varepsilon} = (1-D)\boldsymbol{E}\boldsymbol{\varepsilon}\,. \tag{2.73}$$

Finally, the effective stress tensor is defined as:

$$\boldsymbol{\sigma}_e = \boldsymbol{E}\boldsymbol{\varepsilon}\,, \tag{2.74}$$

and the total multidimensional stress (generalization of (2.65)) can alternatively be written as:

$$\boldsymbol{\sigma} = (1-D)\boldsymbol{\sigma}_e\,. \tag{2.75}$$

As in the uniaxial stress test, we there introduce a loading function f depending on the strain tensor ε, and on a variable κ that controls the evolution of the elastic domains. A state for which $f(\varepsilon,\kappa)<0$ is supposed to be below of the critical damage level. Then, a generalization of Kuhn-Tucker form for the unloading condition can be written as:

$$f(\varepsilon,\kappa) = \tilde{\varepsilon}(\varepsilon) - \kappa\,, \tag{2.76}$$

where the $\tilde{\varepsilon}$ is a scalar measure of the strain level called *equivalent strain*. This damage loading function, similar to the yield function in plasticity, does not depend on σ_e and describe the shape of elastic domains. For instance, a customary definition of equivalent strain for materials as metals is the Euclidean norm of the strain tensor:

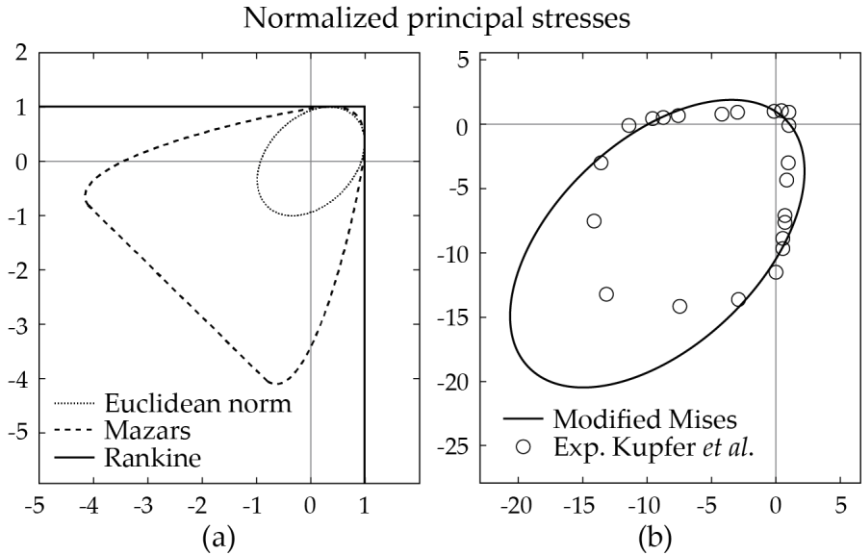

Figure 1.24. Biaxial strength envelopes considering various equivalent strain definitions: comparison between Euclidean norm, Mazars, and Rankine definitions (a); comparison between the predictions of isotropic damage model with modified Mises equivalent strain definition and experimental envelope (Kupfer et al., 1969) (b).

$$\tilde{\varepsilon} = \|\varepsilon\| = \sqrt{\varepsilon : \varepsilon}\,, \tag{2.77}$$

that corresponds to a certain shape of the elastic domains in the stress space, as illustrated in Figure 1.24a (dotted line) considering a Poisson's ratio of $\upsilon = 0.2$. The domains, elliptical and symmetric respect to the origin, shows an equal response under tensile and compressive loading and is suitable for metals only, which possess a symmetric tensile/compressive behavior. Instead, to better describe the mechanical behavior of quasi-brittle materials like concrete, rock and ceramics in which the fracture

process grows mainly if the material is stretched, Mazars considers only the positive part of the normal strain, neglecting the negative one. The equivalent strain definition of Mazars is (Mazars, 1986):

$$\tilde{\varepsilon} = \left\| \langle \varepsilon \rangle \right\| = \sqrt{\langle \varepsilon \rangle : \langle \varepsilon \rangle} = \sqrt{\sum_{i=1}^{3} \left(\langle \varepsilon_i \rangle \right)^2}, \tag{2.78}$$

the symbol $\langle . \rangle$ denoting the positive part operator of McAuley and the corresponding elastic domains is reported in Figure 1.24a (dashed line). In the literature many other equivalent strain definitions are reported such as that according to the maximum principal stress criterion of Rankine (continuous line of Figure 1.24a):

$$\tilde{\varepsilon} = \frac{1}{E} \max_{i=1,2,3} \langle \bar{\sigma}_i \rangle, \tag{2.79}$$

where $\langle \bar{\sigma}_i \rangle$ are the positive parts of principal values of effective stress tensor; or the modified von Mises definition (de Vree et al., 1995) obtained by adding the first invariant of the strain tensor:

$$\tilde{\varepsilon} = \frac{(k-1) I_{1\varepsilon}}{2k(1-2\upsilon)} + \frac{1}{2k} \sqrt{\frac{(k-1)^2}{(1-2\upsilon)^2} I_{1\varepsilon}^2 + \frac{12 k J_{2\varepsilon}}{(1-2\upsilon)^2}}, \tag{2.80}$$

where the $I_{1\varepsilon}$ and $J_{2\varepsilon}$ are the first invariant of the strain tensor and the second invariant of the deviatoric strain tensor, while the k parameter governs the sensitivity to compression relative to that in tension, usually set equal to the ratio between the compressive and tensile uniaxial strength. The corresponding elastic

domains (Figure 1.24b) have ellipsoidal shapes but their centers are shifted from origin along the hydrostatic axis except for the case of the standard von Mises definition with $k=1$, for which it follows $\tilde{\varepsilon} \sim \sqrt{J_{2\varepsilon}}$.

As illustrated in Figure 1.24, the shape of the above-mentioned elastic domains does not completely correspond to the biaxial strength envelope obtained by experiments (Kupfer et al., 1969), showing an underestimate of the material strength when a Mazars equivalent strain definition is considered and an overestimate of the material strength, especially in the biaxial compression region, when the Rankine and modified von Mises damage model are used.

1.2.2.2 Mazars damage model

In the framework of the damage mechanics, a popular and relatively simple concrete damage model, which is also easy to implement and computationally efficient, was proposed by Mazars (Mazars, 1984, 1986). The constitutive equation of model (2.73) is characterized by a damage variable D, with values between 0 and 1, defined as a combination of two damaging modes D_t, and D_c used independently under tensile and compressive condition, respectively, and computed from the same equivalent strain definition (2.78). In the case of general stress states the damage parameter is obtained as a linear combination:

$$D = \alpha_t D_t + \alpha_c D_c, \tag{2.81}$$

where the coefficients α_t and α_c provide the character of the stress state and are evaluated as:

$$\alpha_t = \left(\sum_{i=1}^{3} \frac{\varepsilon_{ti} \left\langle \varepsilon_i \right\rangle}{\tilde{\varepsilon}^2} \right)^{\beta}, \qquad \alpha_c = \left(1 - \sum_{i=1}^{3} \frac{\varepsilon_{ti} \left\langle \varepsilon_i \right\rangle}{\tilde{\varepsilon}^2} \right)^{\beta}, \tag{2.82}$$

where ε_{ti} is the principal strains due to the positive stresses and the exponent β is introduced to improve the damage evolution during the shear loading and in the recent implementation of Mazars model it was set equal to $\beta = 1.06$. With $\alpha_t = 1$ and $\alpha_c = 0$ we have a purely tensile stress state, conversely, with $\alpha_t = 0$ and $\alpha_c = 1$ a purely compressive stress state occurs. The equations of damage evolution are expressed, starting from the equivalent strain at the onset of nonlinearity ε_0, as follows:

$$\begin{aligned} D_t &= 1 - (1 - A_t)\frac{\varepsilon_0}{\tilde{\varepsilon}} - A_t \exp(-B_t(\tilde{\varepsilon} - \varepsilon_0)) \\ D_c &= 1 - (1 - A_c)\frac{\varepsilon_0}{\tilde{\varepsilon}} - A_c \exp(-B_c(\tilde{\varepsilon} - \varepsilon_0)) \end{aligned}, \tag{2.83}$$

with A_t, B_t, A_c, and B_c material parameters related to the softening shape of uniaxial stress-strain curve. They are obtained by tensile and compressive experimental test. The damage equations (2.83) do not have a good accuracy when large strain are applied since the stress level approaches its limit value, and in the case of prevalent compression the compressive stress change sign from negative to positive (see the dotted curve of Figure 1.25). To avoid this complication, the damage variables are set

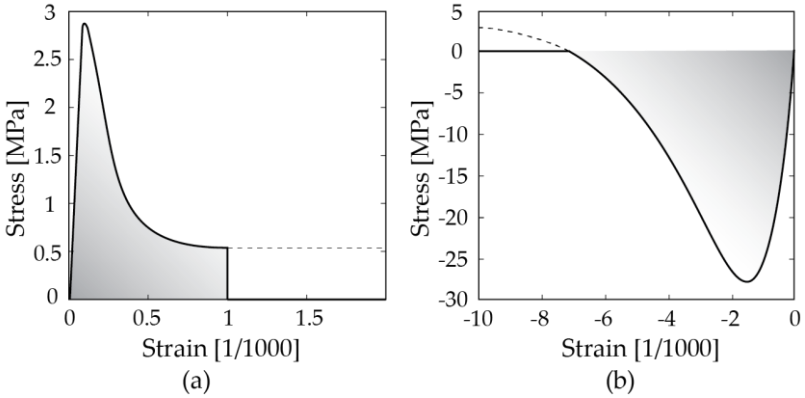

Figure 1.25. Stress strain curves of Mazars damage model for uniaxial tension (a) and uniaxial compression (b).

$D_c = 1$ and $D_t = 1$ when D_c exceed 1 and D_t exceed a certain limit, respectively.

As already reported in Figure 1.24, the elastic domains in the region of biaxial compression not completely correspond to the experimental data of failure envelope in the stress space. To improve the shape of the elastic domains, Mazars revised his damage model considering a multiplicative factor γ in the expression of the equivalent strain:

$$\tilde{\varepsilon} = \gamma \sqrt{\sum_{i=1}^{3} \left(\left\langle \varepsilon_i \right\rangle \right)^2}, \tag{2.84}$$

with

$$\gamma = \frac{\sqrt{\sum_{i=1}^{3} \left\langle \sigma_i^- \right\rangle^2}}{\sum_{i=1}^{3} \left\langle \sigma_i^- \right\rangle^2}, \tag{2.85}$$

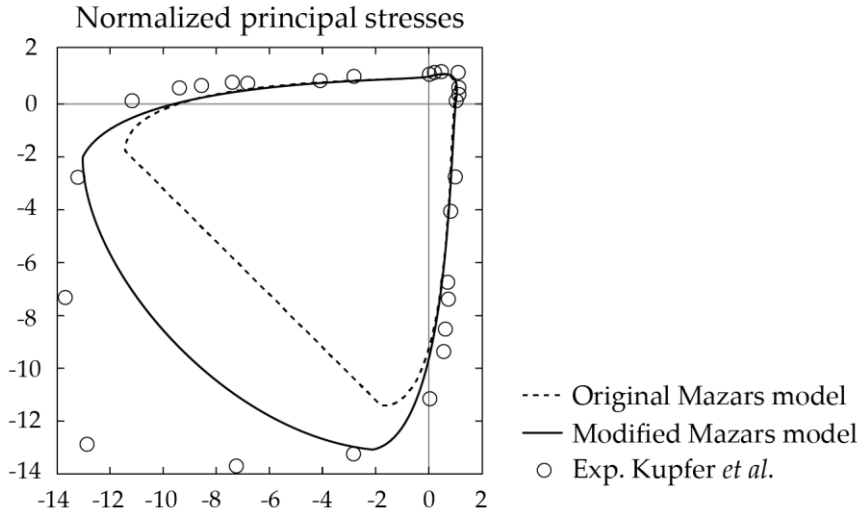

Figure 1.26. Comparison between biaxial failure envelopes predicted by original and modified Mazars damage model, and experimental data of (Kupfer *et al*., 1969)**.**

where $\left\langle \sigma_i^- \right\rangle = -\left\langle -\sigma_i^- \right\rangle$ are the negative parts of the principal stresses. This factor, limited between 0 and 1, is activated only if at least two principal stresses are negative, i.e. only in a biaxial compression condition and it makes the biaxial compressive strength equal to the uniaxial one. With this numerical consideration, the failure envelope becomes more realistic as showed in Figure 1.26.

However, some numerical issues, typical of isotropic damage models, are observed also in the Mazars model. In particular, the model is unable to capture the volumetric dilatancy, observed in the experimental test, in the case of proportional loading path in uniaxial compression and shear test, due to the fact that the ratio

between individual strain components remains constant. In addition, during the unloading phase the permanent strain is not generated and for large strain values in one direction the model completely loses stiffness also in the transverse directions. Nevertheless, the Mazars damage model is a very popular model in the failure analysis of concrete structures, by virtue of its ease of implementation in commercial softwares and its computational efficiency.

1.2.2.3 Strain localization limiters

In concrete structures the material properties cannot be perfectly uniform. If we consider two adjacent sections of a structure, with a certain dimension, their strengths are not identical but one of them must have a critical strength slightly smaller than the other one. Consequently, during a loading phase, as soon as one section reaches the peak strength, further straining yields to softening of this section and to unloading of the other, i.e. the strain *localizes* into one element due to the softening. This leads to the conclusion that the size of the softening zone is dictated by the size of the zone with minimum strength, which can be arbitrarily small.

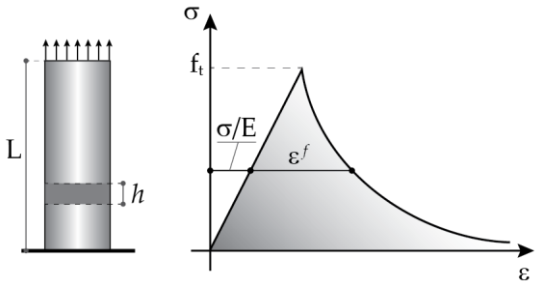

Figure 1.27. Elastic-softening behavior of homogeneous bar.

Now, we consider a homogeneous bar of length L with a linear-elastic mechanical behavior up to its critical strength followed by strain-softening, as depicted in Figure 1.27. The strain in the softening branch can be written as:

$$\varepsilon_s = \frac{\sigma}{E} + \varepsilon^f , \tag{2.86}$$

where E is the Young's modulus, and ε^f is the fracturing strain, graphically represented as illustrated in Figure 1.27. A monotonic increase of strain and an unloading to the origin is further predicted. The area under the stress-strain curve, i.e. the work λ_F required to fully break a unit volume of material is:

$$\lambda_F = \int_0^\infty \sigma d\varepsilon . \tag{2.87}$$

As explained above, a region of bar, of length h, reaches its critical strength so that it continues to stretch, while the remaining part of the bar elastically unloads. The total elongation of the bar is thus:

$$\Delta L = \frac{\sigma}{E}(L-h)+\left(\frac{\sigma}{E}+\varepsilon^f\right)h = \frac{\sigma}{E}L+\varepsilon^f h\,. \tag{2.88}$$

In which we can distinguish the elastic elongation and a fracturing elongation write as follows:

$$\Delta L^f = \varepsilon^f h\,. \tag{2.89}$$

Consequently, the required work to break the entire specimen is only that to break the region with strain softening, so that:

$$W_F = Ah\int_0^\infty \sigma d\varepsilon^f = Ah\lambda_F\,, \tag{2.90}$$

where A is the cross section of the bar. To evaluate the h value, we apply the condition of the second-order complementary work $\delta^2 W$ which must be maximum, and we find that the thermomechanical solution is $h=0$. It follows that, a solution physically unacceptable and contrary to experiment with both inelastic strain and fracture work equal to zero is obtained. From the numerical point of view, this solution implies mathematical problem related to the loss of ellipticity of the governing differential equation and the boundary value problem becomes ill-posed, i.e., it does not have a unique solution with continuous dependence on the given data, thus manifesting a pathological sensitivity of results to the size of finite elements.

Therefore, damage models, based on a continuum formulation with strain softening, must include some conditions that prevent the strain from localizing into a region of measure zero

(Bažant and Belytschko, 1985). The damage models which include these conditions, such as the well-known *crack band model* and the *nonlocal damage models*, will be briefly explained.

Crack band model. The model, originally proposed by Bažant (Bažant, 1976) and developed in full detail for sudden cracking in (Bažant and Cedolin, 1979, 1983), is based on an adjustment of the stress-strain diagram depending on the finite element size. The constitutive law with strain softening must be associated with a width h_c of the crack band, which represents a reference width and it is treated as a material property. The basic concept of this model is to consider a traction-separation law, typical in the discrete fracture models, as the basic constitutive description. At each material point, the stress-strain relation is obtained by the transformation of the traction-separation law considering the width of the numerically simulated process zone which depends on the size of the corresponding finite element. The equation of a softening curve for the cohesive crack model, which involves the displacement jump of the crack opening δ and the stress σ can be written in the general form as:

$$\sigma = f(\delta)\,. \tag{2.91}$$

If the crack opening is smeared over a distance h_c, the resulting fracture strain is:

$$\varepsilon^f = \frac{\delta}{h_c}\,. \tag{2.92}$$

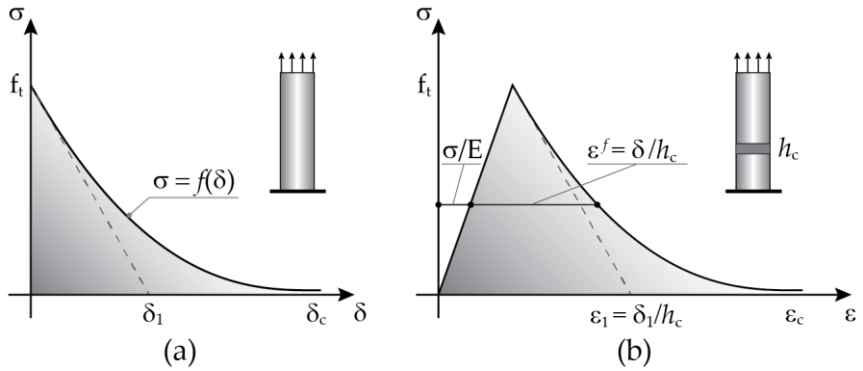

Figure 1.28. Correspondence between the stress-displacement jump softening curve of the cohesive crack model (a) and the stress-strain constitutive curve of the crack band model (b).

As reported in Figure 1.28, there is a correspondence between the softening of the crack band model and the cohesive crack model, in particular the strain in the stress-strain curve can be obtained dividing the crack opening by the width of the crack band. The correspondence is also maintained for the specific fracture energy G, so that:

$$G = \frac{W_F}{A} = h_c \lambda_F \,. \tag{2.93}$$

In a similar manner we can easily obtain the characteristic length in terms of crack band model properties as:

$$l_{ch} = \frac{E}{f_t^2} h_c \lambda_F \,. \tag{2.94}$$

Some difference in the results obtained by both discrete and smeared models, is observed in terms of strain distribution. Ob-

viously, in correspondence of a crack, the fracture strain calculated by the crack band model is smeared over a length of h_c, instead, considering a discrete approach, in which the crack is modeled as a discontinuity, the strain is concentrated in a zone with nil width. However, if h_c is very small respect to the specimen dimensions this difference in the results is negligible.

Therefore, a widely analyzed problem in the literature is to determine the value of h_c in order to obtain acceptable numerical results. In many works about damage mechanics, the value of h_c is taken equal to the size of the finite element. Rots, based on numerical experiments, proposed certain rules for the choice of the equivalent element size for a number of typical situations (Rots, 1988). Červenka, considers reasonable to compute h_c as the size of element projected onto the crack normal and proposed a correction factor of this size (Wittmann et al., 1995).

Nonlocal damage models. As seen above, a local strain softening continuum exhibits spurious damage localization instabilities, in which all damage is localized into a zone of measure zero, leading to spurious mesh sensitivity. To avoid such issues, one must adopt the more general concept of nonlocal continuum, defined as a continuum in which the stress at a point depends on the strains in the neighborhood of that point. The nonlocal models assume that the stresses at a certain point depends not only on the state variables at that point but, in general on the distribution of state variables in a finite region in the proximity of the

point under consideration. The first models date back around 1960s, when Erigen developed the theory of nonlocal elasticity and nonlocal elastoplasticity (Erigen, 1983). Such nonlocal formulations were used, then, as efficient localization limiters by Pijaudier-Cabot and Bažant (Pijaudier-Cabot and Bažant, 1987) with a regularizing effect on problems with strain localization. In the scientific literature, many nonlocal approaches, elaborated for several damage models including smeared crack (Bažant and Lin, 1988; Jirásek and Zimmermann, 1998) or microplane models (Bažant and Ožbolt, 1990; Bažant and Di Luzio, 2004), are present.

From a mathematical point of view, the nonlocal approach consists in replacing a certain variable by its nonlocal counterpart, obtained by a weighted averaging over a region in the neighborhood of each point under consideration. Considering a local field $f(\mathbf{x})$ in a domain V, the corresponding nonlocal field can be written as:

$$\bar{f}(\mathbf{x}) = \int_V \alpha(\mathbf{x},\boldsymbol{s}) f(\boldsymbol{s}) dV(\boldsymbol{s}) \tag{2.95}$$

where $\alpha(\mathbf{x},\boldsymbol{s})$ is a given nonlocal scalar weight function of the distance $r = |\mathbf{x}-\boldsymbol{s}|$ between the "source" point $\boldsymbol{s}$, at which the average is taken, and the "receiver" point $\mathbf{x}$, contributing to that average. In region with uniform strain, such as in the vicinity of boundary, the weight function is usually rescaled:

$$\alpha(\mathbf{x},\boldsymbol{s}) = \frac{\alpha_0\left(\left\|\mathbf{x}-\boldsymbol{s}\right\|\right)}{\int_V \alpha_0\left(\left\|\mathbf{x}-\boldsymbol{s}\right\|\right) dV(s)}, \tag{2.96}$$

where $\alpha_0(r)$ is a monotonically decreasing nonnegative function of the distance $r = |\mathbf{x} - \mathbf{s}|$. The weight function is often taken as the Gauss distribution function:

$$\alpha_0(r) = \exp\left(-\frac{r^2}{2l^2}\right), \tag{2.97}$$

or, according to Bažant and Planas (Bažant and Planas, 1998b), an acceptable function is:

$$\alpha_0(r) = \left(1 - \frac{r^2}{\rho_0^2 l^2}\right)^2, \tag{2.98}$$

where l is a parameter reflecting the internal length of the nonlocal continuum, while ρ_0 is a coefficient equal to $\rho_0 = 0.8178$.

A suitable nonlocal damage formulation that restores well-posedness of the BVP is obtained if the damage variable is computed from the nonlocal equivalent strain. The local equivalent value $.\tilde{\varepsilon}.$ must be replaced by its weighted spatial average:

$$\tilde{\varepsilon}(\mathbf{x}) = \int_V \alpha(\mathbf{x}, \boldsymbol{s})\varepsilon(\boldsymbol{s})dV(\boldsymbol{s}) . \tag{2.99}$$

It is worth noting that the nonlocal equivalent strain is used only to compute the damage variable, instead, to evaluate the effective stress tensor, the strain used in (2.74) is considered as local.

2

A diffuse cohesive model for failure analysis of concrete structures

In this chapter a detailed description of the proposed cohesive fracture model together with computational details is presented. In particular, the first part of chapter is devoted to the theoretical background of the adopted cohesive finite element formulation, and a calibration methodology, based on a numerical micromechanical approach, is proposed for alleviation of the mesh-induced compliance effect typical of the intrinsic cohesive

formulation. The second part of the chapter deal with the description of the proposed ad-hoc numerical model, composed by three different models, useful for investigate in a comprehensive manner all of the main failure mechanisms in the failure analysis of plain and reinforced concrete structures.

2.1 Theoretical background of the diffuse cohesive finite element method

In this Section, the theoretical formulation of the adopted cohesive finite element method is briefly presented, with reference to the planar elasticity case. The extension to the more general three-dimensional case is straightforward but is out of the scopes of the present thesis. The basic concept of this formulation is a variational statement written for a given solid after being discretized in finite elements, whose kinematics is enriched by the presence of cohesive interface elements along its internal boundaries, as shown in Section 2.1.1. Since the resulting BVP is no longer defined at the continuum level, the associated solution turns to be dependent on the adopted finite element mesh. This mesh dependency issues, as already discussed in the Section 1.2.1, cannot be avoided but can be only controlled and/or reduced. To this end, several ad-hoc calibration criteria for the cohesive parameters have been proposed in the literature, as shown in Section 2.1.2, but the achievement of the desired perfect mesh independency still remains an open problem. In this thesis, a novel calibration criterion for the initial stiffness parameters of

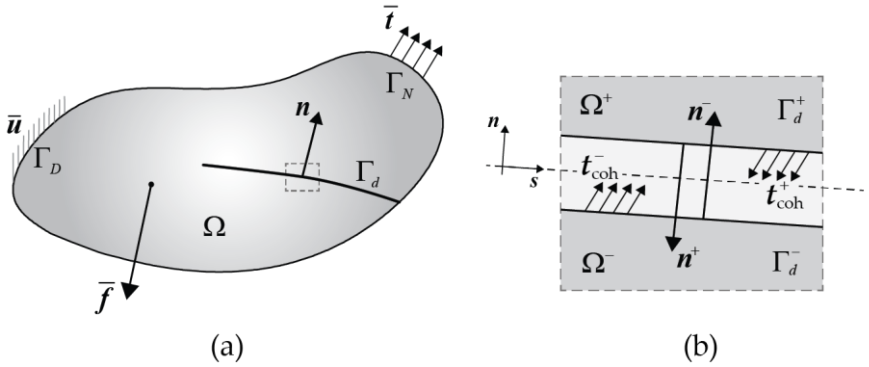

Figure 2.1. Schematic representation of the BVP for a cracked continuum body: (a) schematic representation of the body; (b) crack representation and related notations

the cohesive elements is proposed, based on a rigorous numerical micromechanical approach, explained in Section 2.1.3.

2.1.1 Variational formulation

The theoretical formulation of the adopted cohesive finite element approach is described by considering two different steps. In the first one, the variational formulation for a continuum fractured by a priori known crack is reported. In the second one, the variational formulation is extended to the case of unknown crack locations, involving a discretized computational domain. In the following, both theoretical formulations are presented assuming, without loss of generality, small displacements and negligible inertial forces. The description of the first variational formulation, referred to a general two-dimensional fractured body (Figure 2.1a), starts by considering a domain $\Omega \subset R^2$ bounded by the

piecewise continuous boundary Γ and containing a single discontinuity line Γ_d. The boundary Γ, supposed to be Lipschitz continuous, is subdivided into two subsets Γ_D and Γ_N, where Dirichlet and Neumann boundary conditions are imposed, respectively, with the constraints $\Gamma_D \cup \Gamma_N = \Gamma$ and $\Gamma_D \cap \Gamma_N = \varnothing$. The prescribed displacement on Γ_D and the surface forces on Γ_N are denoted by $\bar{\boldsymbol{u}}$ and $\bar{\boldsymbol{t}}$, respectively. Additionally, the body forces $\bar{\boldsymbol{f}}$ act on the entire volume Ω. The embedded single discontinuity line $.\Gamma_d.$ represents an existing crack lying on a path known a priori, and it is the union of the two, positive and negative, crack faces Γ_d^+ and Γ_d^- (see Figure 2.1b). The adopted cohesive concept implies that the cohesive tractions t_{coh}^+ and $\boldsymbol{t}_{\text{coh}}^-$, assumed to act, respectively, on the positive and negative sides of the given discontinuity, are self-balanced, i.e. $\boldsymbol{t}_{\text{coh}}^- = -\boldsymbol{t}_{\text{coh}}^+$, in order to guarantee the interface equilibrium.

The material response of the bulk phase, assumed to be linearly elastic and isotropic, is described by the following constitutive law:

$$\boldsymbol{\sigma} = \boldsymbol{C}\boldsymbol{\varepsilon}, \tag{2.1}$$

where $\boldsymbol{\varepsilon} = \nabla_s \boldsymbol{u}$ is the symmetric part of the displacement gradient (in the linearized kinematics), and $\boldsymbol{C} = \lambda \boldsymbol{I} \otimes \boldsymbol{I} + 2\mu \boldsymbol{I}^{(4s)}$ denotes the elasticity tensor, λ and μ being the planar Lamè parameters, $\boldsymbol{I}$ the second-order identity tensor, and $\boldsymbol{I}^{(4s)}$ the symmetric fourth-order identity tensor. It follows that the only nonlinearity source is the constitutive behavior of the cohesive crack,

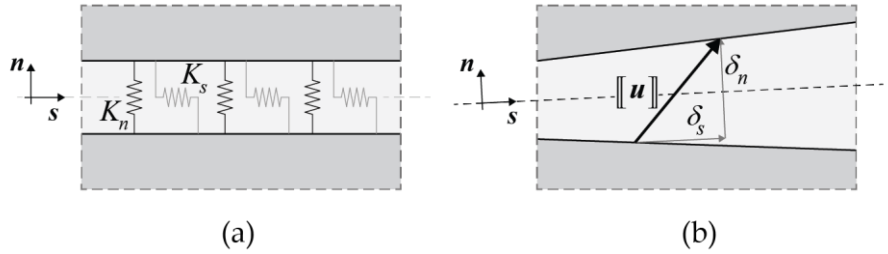

Figure 2.2. Schematic representation of the mixed-mode cohesive interface: (a) normal and tangential distributed nonlinear springs; (b) normal and tangential components of the displacement jump along the interface.

which can be written by a general mixed-mode traction-separation law (TSL) of the type $\boldsymbol{t}_{\text{coh}} = \boldsymbol{t}_{\text{coh}}(\boldsymbol{u})$. The notation $\cdot = (\cdot)^{+} - (\cdot)^{-}$ representing the difference between corresponding values calculated along the crack faces. In the absence of direct cross coupling between normal and tangential modes, the discontinuity, modeled as numerical interface, behave as a bed of nonlinear spring (see Figure 2.2a) acting on the normal and tangential components of the displacement jump, $\delta_n = \boldsymbol{u} \cdot \boldsymbol{n}$ and $\delta_s = \boldsymbol{u} \cdot \boldsymbol{s}$ (see Figure 2.2b), where $\boldsymbol{n}$ and $.\boldsymbol{s}.$ are respectively the unit normal and the tangential to Γ_d^-. Such an interface is characterized by the following constitutive law:

$$\begin{aligned} \boldsymbol{t}_{\text{coh}} &= \boldsymbol{K}\left([\![\boldsymbol{u}]\!]\right)[\![\boldsymbol{u}]\!] \\ \text{with} \quad \boldsymbol{K}\left([\![\boldsymbol{u}]\!]\right) &= K_n\left([\![\boldsymbol{u}]\!]\right)\boldsymbol{n}\otimes\boldsymbol{n} + K_s\left([\![\boldsymbol{u}]\!]\right)\left(\boldsymbol{I} - \boldsymbol{n}\otimes\boldsymbol{n}\right) \end{aligned}, \tag{2.2}$$

where $K_n\left([\![\boldsymbol{u}]\!]\right) \geq 0$ and $K_s\left([\![\boldsymbol{u}]\!]\right) \geq 0$ are the normal and tangential stiffnesses of the interface.

The quasi-static equilibrium problem of such cracked body can be formulated as a nonlinear BVP expressed in the following weak form: Find $\boldsymbol{u} \in U$ such that:

$$\begin{aligned} &\int_{\Omega \setminus \Gamma_d} \boldsymbol{C}\ \nabla_s \boldsymbol{u} : \left(\nabla_s \boldsymbol{v}\right)\ \mathrm{d}\Omega + \int_{\Gamma_d} \boldsymbol{K}\left(\left[\!\left[\boldsymbol{u}\right]\!\right]\right)\left[\!\left[\boldsymbol{u}\right]\!\right] \cdot \left[\!\left[\boldsymbol{v}\right]\!\right]\ \mathrm{d}\Gamma \\ &\quad = \int_{\Omega \setminus \Gamma_d} \overline{\boldsymbol{f}} \cdot \boldsymbol{v}\ \mathrm{d}\Omega + \int_{\Gamma_N} \overline{\boldsymbol{t}} \cdot \boldsymbol{v}\ \mathrm{d}\Gamma \qquad \forall \boldsymbol{v} \in V \end{aligned}, \tag{2.3}$$

the double-dot symbol denotes the scalar product between second-order tensor, whereas, $\boldsymbol{u}$ and $\boldsymbol{v}$ are the (unknown) approximated displacement field and the corresponding arbitrary virtual displacement field, respectively, belonging to the following sets:

$$\begin{aligned} U &= \left\{ \boldsymbol{u} \text{ such that } \boldsymbol{u} \in H^1\left(\Omega \setminus \Gamma_d\right) \text{ and } \boldsymbol{u}\big|_{\Gamma_D} = \overline{\boldsymbol{u}} \right\} \\ V &= \left\{ \boldsymbol{v} \text{ such that } \boldsymbol{v} \in H^1\left(\Omega \setminus \Gamma_d\right) \text{ and } \boldsymbol{v}\big|_{\Gamma_D} = \boldsymbol{0} \right\} \end{aligned}, \tag{2.4}$$

in which $H^1\left(\Omega \setminus \Gamma_d\right)$ is the Sobolev space of degree one defined on the bulk phase, and the backslash symbol standing for the set difference. It is worth noting that the second contribution appearing on the left-hand side of the Equation (2.3) represents the virtual work of the cohesive traction over the discontinuity line Γ_d.

The second step of the theoretical description of the adopted cohesive approach is the derivation of a variational formulation written for a spatially discretized domain. To this purpose, a planar tessellation of Ω is considered, $\Omega^h \subset R^2$, which is not constrained by the presence of the existing discontinuity lines Γ_d,

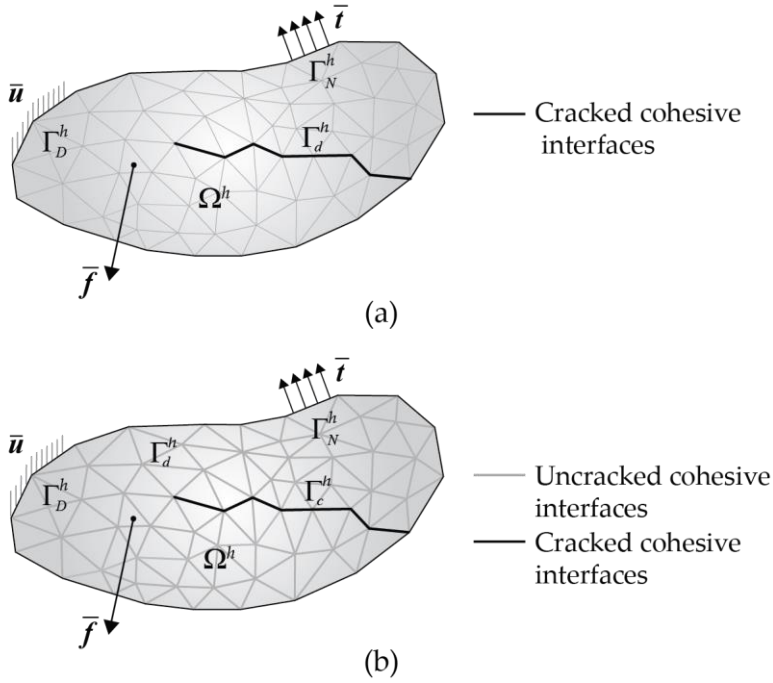

Figure 2.3. Equilibrium problem for a 2D fractured discretized body: (a) cohesive interfaces approximating the exact crack path; (b) cohesive interfaces approximating all the potential crack paths.

but the exact crack path is approximated as a set of cohesive segments Γ_d^h, forced to lie along the internal boundaries of the given tessellation, as depicted in Figure 2.3a. If the real crack path is not known a priori, all of the internal mesh boundaries are regarded as discontinuity lines, and replaced by zero-thickness interfaces Γ_d^h. Such interfaces must be inserted a priori between all the adjacent bulk elements of Ω^h (see Figure 2.3b). The associated boundary value problem expressed in weak form reads as: Find $\boldsymbol{u}^h \in U^h$ such that:

$$\begin{aligned}\int_{\Omega^h\setminus\Gamma_d^h}\boldsymbol{C}\,\nabla_s\boldsymbol{u}^h:\left(\nabla_s\boldsymbol{v}^h\right)\,\mathrm{d}\Omega+\int_{\Gamma_d^h}\boldsymbol{K}\left(\left[\!\left[\boldsymbol{u}^h\right]\!\right]\right)\left[\!\left[\boldsymbol{u}^h\right]\!\right]\cdot\left[\!\left[\boldsymbol{v}^h\right]\!\right]\,\mathrm{d}\Gamma\\ =\int_{\Omega^h\setminus\Gamma_d^h}\overline{\boldsymbol{f}}\cdot\boldsymbol{v}^h\,\mathrm{d}\Omega+\int_{\Gamma_N^h}\overline{\boldsymbol{t}}\cdot\boldsymbol{v}^h\,\mathrm{d}\Gamma\quad\forall\boldsymbol{v}^h\in V^h\end{aligned},\qquad(2.5)$$

where the superscript h refers to the discretized counterparts of the quantities appearing in Equation (2.3). Moreover, if a generic finite element Ω_e^h with boundary Γ_e^h, Ω^h and Γ_d^h have the following definitions:

$$\Omega^h=\bigcup_{e=1}^{n_e}\overline{\Omega}_e^h;\qquad\Gamma_d^h=\left[\bigcup_{e=1}^{n_e}\Gamma_e^h\right]\setminus\Gamma^h,\qquad(2.6)$$

where $\overline{\Omega}_e^h=\Omega_e^h\cup\Gamma_e^h$, with the union operator that acts over all the n_e finite elements of the given tessellation. In this case, Γ_d^h, which is no longer coincident with the real cracks, represents the set of all potential lines for crack propagation. It is denoted as $\Gamma_c^h\subset\Gamma_d^h$ and characterized by a nonlinear behavior. On the other hand, the perfect, i.e. uncracked, interfaces simply behave as linear elastic springs, whose initial stiffness components $K_n^0=K_n\left(\left[\!\left[\boldsymbol{u}^h\right]\!\right]=\boldsymbol{0}\right)$ and $K_s^0=K_s\left(\left[\!\left[\boldsymbol{u}^h\right]\!\right]=\boldsymbol{0}\right)$, do not have a precise physical meaning, but play the role of penalty parameters to enforce the inter-element kinematic compatibility constraint. It is worth noting that the cohesive finite element formulation does not guarantee the spatial convergence to an arbitrary crack path by means of mesh refinements (Xu and Needleman, 1994). Indeed, the total crack length turns to be systematically overestimated regardless of the mesh size, since the (unknown) crack trajectory is forced to be represented as a set of cohesive segments

coinciding with the internal mesh boundaries, whose orientation is restricted to a limited number of predefined angles. However, the use of isotropic tessellations leads to alleviate such mesh dependencies, since no preferential path directions for crack initiation and propagation are introduced into the approximate numerical model.

2.1.2 Investigation of mesh-induced compliance effects

In the cohesive approach described in the previous only a small percentage of cohesive interfaces can be regarded as active when materials with quasi-brittle fracture behavior, where the damage is typically lumped around an existing macro-crack, are considered. In this case, the remaining inactive interfaces are useless and, due to the adoption of an intrinsic cohesive model, negatively affect the mechanical response of the solid by seriously reducing its overall material stiffness. Thus, the insertion along all the internal mesh boundaries of interface elements with finite initial stiffness, inevitably leads to an artificial stiffness reduction also at the elastic range. In the literature, some authors, by using an inter-element fracture approach have observed mesh dependency issues, in terms of lack of spatial convergence for arbitrary crack paths or patterns, when a structured tessellation was used to discretize the computational domain (Papoulia et al., 2006). Such a mesh dependency of the cohesive finite element method is experienced even in the elastic stage and due to the artificial compliance increase associated with the insertion of springs with

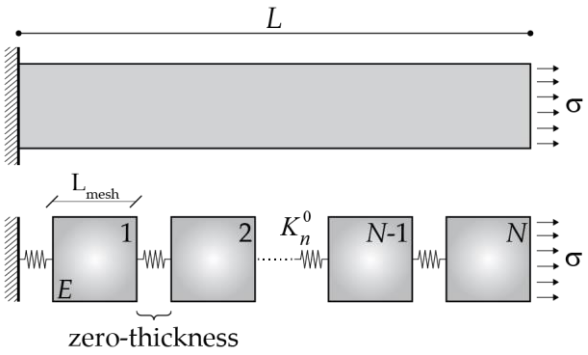

Figure 2.4. Mesh-induced artificial compliance in a 1D example: overall elastic behavior in the normal direction.

finite stiffness between all the bulk finite elements. In several works, suitable calibrations of the initial cohesive stiffness parameters are proposed to alleviate the mesh dependency considering the average mesh size (Klein et al., 2001; Espinosa and Zavattieri, 2003; Tomar et al., 2004; de Borst et al., 2006; Turon et al., 2007; Blal et al., 2012).

As already discussed in (Klein et al., 2001), the longitudinal stiffness reduction induced by the presence of diffuse cohesive interfaces can be qualitatively analyzed by using a simple rectangular specimen length L, subjected to a uniaxial tensile stress σ, as depicted in Figure 2.4. This specimen is discretized into N quadrilateral elements, having the same size equal to $L_{\text{mesh}} = L/N$ and linearly elastic behavior, and N zero-thickness interfaces elements. The total elongations of the bulk elements and the cohesive interfaces are $\Delta L_b = L\sigma/E$ and $\Delta L_c = N\sigma/K_n^0$, respectively, where E and K_n^0 are the Young's modulus of the bulk

material and the initial stiffness of the cohesive interfaces, respectively. It follows that the total uniaxial strain ε of the plate can be computed as $\left(\Delta L_b + \Delta L_c\right)/L = \left(L\sigma/E + N\sigma/K_n^0\right)/L$, leading to the following expression for the overall (or apparent) elastic modulus of the plate:

$$\bar{E} = \frac{\sigma}{\varepsilon} = \frac{1}{\frac{1}{E} + \frac{N}{LK_n^0}}. \tag{2.7}$$

Thus, the material stiffness reduction, due to the presence of undamaged cohesive interfaces, is equal to the ratio between the overall and bulk longitudinal moduli, written as follows:

$$\frac{\bar{E}}{E} = \frac{1}{\frac{1}{E} + \frac{NE}{LK_n^0}} = \frac{1}{1 + \frac{E}{L_{mesh}K_n^0}}. \tag{2.8}$$

By analyzing Equation (2.8), it can be observed that the stiffness reduction can be decreased either by increasing the mesh size L_{mesh}, or increasing the initial normal cohesive stiffness K_n^0. However, both K_n^0 and L_{mesh} must be chosen such that the dimensionless quantity appearing on the right-hand side of Equation (2.8) is not excessively high, to avoid spurious traction oscillations, due to the ill-conditioning of the resulting numerical problem. Such oscillations could eventually lead to an incorrect crack pattern, as already reported in (de Borst et al., 2006).

The resulting induced additional compliance is proportional to the density of cohesive interfaces, i.e. the total length of cohesive edges per unit area in the 2D case, which in turn depends on the adopted finite element size L_{mesh} for a given computational mesh. It follows that, such an increase in the overall compliance causes a divergence of the solution as the mesh is refined due to the varying overall elastic properties. This effect should be made negligible by controlling the initial normal stiffness via a suitably calibration of its value as a function of the adopted mesh size. To this end, rather than fixing directly the value for K_n^0, it is preferable to calibrate the dimensionless normal stiffness $\kappa = K_n^0 L_{\text{mesh}} / E$, which incorporates the mesh size effects, in terms of the imposed reduction for the longitudinal modulus $R_E = \bar{E}/E < 1$. By using Equation (2.8), it follows:

$$\kappa = \frac{R_E}{1 - R_E}. \tag{2.9}$$

Once the parameter κ is computed by using Equation (2.9) for a chosen R_E, the initial normal stiffness K_n^0 of the cohesive interface can be found as a function of the adopted mesh size L_{mesh}.

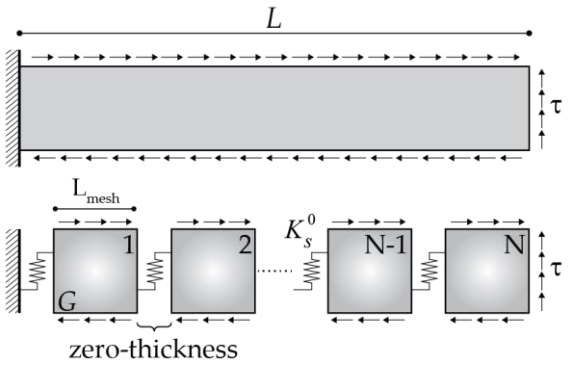

Figure 2.5. Mesh-induced artificial compliance in a 1D example: overall elastic behavior in the tangential direction.

Following the above described procedure, the artificial reduction in the overall tangential stiffness, considering the previously introduced rectangular specimen subjected to a pure shear stress τ (see Figure 2.5), can be easily expressed by the ratio between the overall and bulk tangential moduli as follows:

$$\frac{\bar{G}}{G}=\frac{1}{1+\dfrac{NG}{LK_s^0}}=\frac{1}{1+\dfrac{G}{L_{\text{mesh}}K_s^0}}=\frac{1}{1+\dfrac{G}{L_{\text{mesh}}\xi K_n^0}}=\frac{1}{1+\dfrac{G}{E}\dfrac{1}{\xi K_n^0}}, \quad (2.10)$$

where $\xi = K_s^0 / K_n^0$ is a new dimensionless parameter, i.e. the ratio between the tangential and normal initial stiffness coefficients of the cohesive interface. By imposing a prescribed reduction for the overall tangential modulus $R_G = \bar{G}/G < 1$, which in general can be different from R_E, we can obtain such parameter from Equation (2.10), which in general can be different from R_E:

$$\xi = \frac{1}{2(1+\nu)\kappa}\frac{R_G}{1-R_G}, \quad (2.11)$$

where ν is the Poisson's ratio of the bulk phase. It is useful to highlight that, prescribing the same reduction for both longitudinal and tangential overall moduli, i.e. imposing the restriction $R_E = R_G$, the following result for the parameter ξ is obtained:

$$\xi = \frac{G}{E} = \frac{1}{2\left(1+\nu\right)}, \tag{2.12}$$

implying that the ratio $\xi = K_s^0 / K_n^0$ is uniquely depends on the Poisson's ratio of the bulk phase. Additionally, it is worth noting that the Equations (2.8) and (2.10) can be regarded as inverse rules of mixtures for the overall moduli $\bar{E}$ and $\bar{G}$, respectively, thus providing lower-bounds for these moduli, according to the well-known Reuss approximation applied to a two-phase laminated composite made of bulk and cohesive layers. Obviously, Equations (2.9) and (2.12) can be rigorously applied for calibrating the initial stiffness of the cohesive interfaces only in the unrealistic case in which they are aligned.

In the literature, different semi-empirical lower bounds for the cohesive stiffness ratio κ have been proposed in the literature by several authors in order to obtain "invisible" cohesive interfaces in more general situations. Values of κ larger than 50 are recommended by (Turon et al., 2007) to ensure an apparent loss of stiffness less than 2% in numerical analyses of delamination in composite materials. Furthermore, in (Espinosa and Zavattieri, 2003) is observed that, the speed of the elastic wave propagation

in isotropic materials is not affected by the presence of an internal cohesive interface when the κ parameter is kept $\kappa \geq 10$. Instead, a rigorous calibration criterion, based on energy equivalence condition between a discrete system made of bulk and interface elements arranged in a cross-triangle quadrilateral mesh and its equivalent homogeneous system, under three different (uniaxial, biaxial and pure shear) uniform loading conditions, is firstly introduced by (Tomar et al., 2004). Considering plane stress conditions and assuming $\xi = K_s^0 / K_n^0 = 1$, the following criterion for κ values is obtained:

$$\kappa = \left(1 + \sqrt{2}\right) \frac{R_E}{1 - R_E}, \tag{2.13}$$

which is similar to the Equation (2.9) but predicts greater values for the initial elastic stiffness at fixed R_E, due to the different spatial distribution of cohesive interfaces.

A generalization of the previous criterion (2.13) to the more general 3D case with any type of external loading conditions and mesh topologies, is proposed in (Blal et al., 2012). Such a criterion is based on an analytical micromechanical approach which uses a Hashin-Shtrikman estimate to compute the overall elastic stiffness of a solid with embedded cohesive interfaces. The authors, consider the cohesive interfaces as a collection of uniformly distributed penny-shaped inclusion embedded in a continuous matrix and the overall properties of the resulting composite material are obtained as a closed-form function of bulk properties and

mesh parameters. The two unknown dimensionless stiffness parameters κ and ξ of this composite with isotropic overall constitutive behavior can be evaluated, enforcing the same reduction for both the overall moduli $\bar{E}$ and $\bar{G}$, by means of the following relations:

$$\kappa = \frac{\gamma}{3\left(1-2\nu\right)}\frac{R_E}{1-R_E}, \qquad \xi = 2\frac{1-2\nu}{1+3\nu}, \tag{2.14}$$

such a restriction implies no reduction of the overall Poisson's ratio ν and guarantees the positive definiteness of the overall strain energy, also for hydrostatic loading conditions, as already discussed by some authors (Li et al., 2004).

The dimensionless parameter γ appearing in the first of Equations (2.14) depends on the topology of the given mesh. These relations have been also applied to the case of planar meshes (Blal et al., 2012). In particular, for cross-triangle quadrilateral mesh, with size L_{mesh} coinciding with the side length of the square cell, γ has been found to be equal to $2\left(1+\sqrt{2}\right)$, while for isotropic Delaunay tessellation, it has been calculated by the following formula:

$$\gamma = \frac{32\sqrt{2}}{3\pi\sqrt[4]{3}}, \tag{2.15}$$

obtaining a value of about $\gamma \approx 3.6485$. The Equation (2.15) is obtained considering the L_{mesh} as the edge length of an equivalent regular tessellation made of equilateral triangles (Blal et al., 2012).

Unfortunately, such an approach is only able to estimates the effective properties, and the adopted simplifying hypotheses are usually associated with unacceptable accuracy levels for real situations of practical interest. Therefore, a novel numerical homogenization scheme, described in Section 2.1.3, is proposed in the present thesis, with the aim of increase the accuracy of the prediction obtained from Equation (2.14).

2.1.3 A numerical micromechanical approach for the alleviation of mesh-induced compliance

In order to enhancing the predictions of the existing semi-empirical and analytical methods discussed in Section 2.1.2, here a novel numerical micromechanical approach for the calibration of the initial (elastic) cohesive stiffness parameters is presented. Inspired by the works of some authors (Blal et al., 2012), the proposed approach considers the material as a composite consisting of two phases, i.e. the bulk material and the cohesive interfaces (embedded between the bulk elements), with either random or regular microstructure, depending on the topology of the employed finite element mesh. As a consequence, the overall elastic properties of such an assembly can be obtained by applying a rigorous micromechanical approach, based on the concept of representative volume element (RVE). Without loss of generality, the proposed homogenization framework will be presented in the case of planar elasticity.

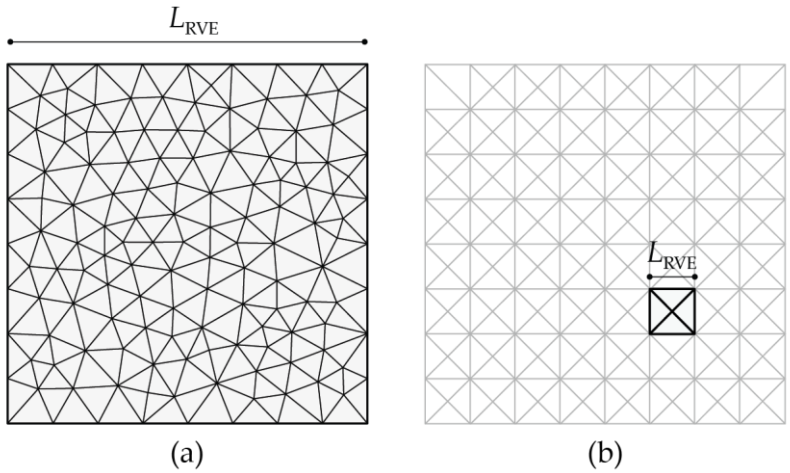

Figure 2.6. Representative volume element (RVE) of a cohesive finite element assembly: (a) RVE with statistically homogeneous and ergodic properties for unstructured meshes; (b) repeating cell (RC) for periodically structured meshes.

In the presence of an unstructured mesh the RVE is chosen as a volume containing a very large (mathematically infinite) set of bulk elements and embedded inter-element cohesive interfaces equipped with statistically homogeneous and ergodic properties (see Figure 2.6a), whereas if a periodically structured mesh, a repeating cell (RC) can be adopted as a clearly defined RVE (see Figure 2.6b). In the former case, the condition $L_{\text{mesh}} \ll L_{\text{RVE}}$ must hold, whereas in the latter case, the RVE size L_{mesh} turns to be coincident with the mesh size.

According to the well-established principle of scale separation, being the main assumption of classical homogenization theory, the overall constitutive response of such a heterogeneous microstructure is based on an equilibrium state which neglects

body forces, so that the microscopic stress field $\boldsymbol{\sigma}$ is divergence-free in the bulk.

According to the average field theory, the macroscopic stress and strain fields, denoted as $\bar{\boldsymbol{\sigma}}$ and $\bar{\boldsymbol{\varepsilon}}$ respectively, can be expressed for a given RVE, denoted by Ω, in terms of microscopic tractions $\boldsymbol{t}=\boldsymbol{\sigma}\boldsymbol{n}$ and displacements $\boldsymbol{u}$ at the RVE boundary Γ as:

$$\bar{\boldsymbol{\sigma}}=\frac{1}{|\Omega|}\int_{\Gamma}\boldsymbol{t}\otimes\boldsymbol{x}\;d\Gamma,\qquad \bar{\boldsymbol{\varepsilon}}=\frac{1}{|\Omega|}\int_{\Gamma}\boldsymbol{u}\otimes_{s}\boldsymbol{n}\;d\Gamma\,, \tag{2.16}$$

where $\boldsymbol{n}$ is the outer normal at $\boldsymbol{x}\in\Gamma$, $\otimes$ and $\otimes_s$ are the tensor product and its symmetric part, respectively, and $|\cdot|$ denotes the Lebesgue measure, defining the conventional area in the two-dimensional Euclidean space R^2. By applying the divergence theorem to Equations (2.16), the alternative following expressions can be derived for the macroscopic stress and strain fields:

$$\bar{\boldsymbol{\sigma}}=\frac{1}{|\Omega|}\int_{\Omega\setminus\Gamma_d}\boldsymbol{\sigma}\;d\Omega,\qquad \bar{\boldsymbol{\varepsilon}}=\frac{1}{|\Omega|}\left(\int_{\Omega\setminus\Gamma_d}\boldsymbol{\varepsilon}\;d\Omega+\int_{\Gamma_d}[\![\boldsymbol{u}]\!]\otimes_{s}\boldsymbol{n}\;d\Gamma\right). \tag{2.17}$$

From the last of Equations (2.17), it follows that the average equivalence for the macroscopic strain field is valid only in the absence of discontinuities. The microscopic displacement field can be additively split in a linear part $\bar{\boldsymbol{\varepsilon}}\boldsymbol{x}$, representing a homogeneous deformation, coinciding with the prescribed macro-strain $\bar{\boldsymbol{\varepsilon}}$ in the adopted strain-driven homogenization scheme, and of a correction part $\boldsymbol{w}(\boldsymbol{x})$ associated with a nonhomogeneous deformation, also referred to as fluctuation field. The integral

kinematic constraint represented by the last of Equations (2.16) can be reformulated in terms of this fluctuation field:

$$\int_{\Gamma} \boldsymbol{w} \otimes_s \boldsymbol{n} \, d\Gamma = \boldsymbol{0} . \tag{2.18}$$

As is well known, Equation (2.18) can be satisfied by three alternative boundary conditions (BCs) on Γ, i.e. linear displacement (LD), periodic fluctuation (PF), and uniform traction (UT) BCs. In the former case, the boundary fluctuation field is assumed zero in a pointwise sense, whereas in the latter case, the boundary tractions are expressed in terms of a uniform (i.e. constant) macro-stress tensor $\bar{\boldsymbol{\sigma}}$. As the constitutive responses of both bulk and interface components are assumed linearly hyperelastic with convex microscopic strain energy densities, denoted respectively by W_b (in 2D, energy per unit area) for the bulk and W_c (in 2D, energy per unit length) for the cohesive interfaces, the homogenization condition can be obtained by solving the following minimization problem:

$$\bar{W}\left(\bar{\boldsymbol{\varepsilon}}\right) = \inf_{\boldsymbol{w} \in A\left(\bar{\boldsymbol{\varepsilon}}\right)} \frac{1}{|\Omega|} \left(\int_{\Omega \setminus \Gamma_d} W_b\left(\boldsymbol{\varepsilon}\left(\boldsymbol{w}\right)\right) d\Omega + \int_{\Gamma_d} W_c\left(\left[\!\left[\boldsymbol{u}\right]\!\right]\left(\boldsymbol{w}\right)\right) d\Gamma \right), \tag{2.19}$$

where $\bar{W}\left(\bar{\boldsymbol{\varepsilon}}\right)$ is the macro-stress potential, assumed to be depending only on $\bar{\boldsymbol{\varepsilon}}$, and $A\left(\bar{\boldsymbol{\varepsilon}}\right)$ denotes the set of admissible fluctuation fields satisfying the above considered three alternative BCs. Hence, the macro-stress $\bar{\boldsymbol{\sigma}}$ and the macroscopic moduli tensor $\bar{\boldsymbol{C}}$ are defined respectively as the first and second derivatives of $\bar{W}\left(\bar{\boldsymbol{\varepsilon}}\right)$ with respect to the macro-strain. Since the minimization problem (2.19) is linear, it follows that:

$$\bar{\boldsymbol{\sigma}} = \frac{1}{|\Omega|}\int_{\Omega\setminus\Gamma_d} \boldsymbol{C}\boldsymbol{\varepsilon}\left(\boldsymbol{u}\right) d\Omega = \bar{\boldsymbol{C}}\bar{\boldsymbol{\varepsilon}}, \quad \text{with } \bar{C}_{ijkl} = \frac{1}{|\Omega|}\int_{\Omega\setminus\Gamma_d} \boldsymbol{C}\boldsymbol{\varepsilon}\left(\boldsymbol{u}^{kl}\right) : \boldsymbol{\varepsilon}\left(\boldsymbol{u}^{ij}\right) d\Omega \quad \left(i,j,k,l = 1,2\right) \tag{2.20}$$

where $\boldsymbol{C}$ is the microscopic moduli tensor of the bulk, and $\boldsymbol{u}^{ij}$ is the solution of the problem (2.19) for a unit prescribed macro-strain $\bar{\boldsymbol{\varepsilon}}^{ij} = \boldsymbol{e}_i \otimes_s \boldsymbol{e}_j$, $\boldsymbol{e}_i$ being the unit vectors parallel to the coordinate axes x_i. In the special case of uniform traction (UT) boundary conditions, the macro-stress tensor $\bar{\boldsymbol{\sigma}}$ is unknown a priori, being understood to be computed for a prescribed macro-strain $\bar{\boldsymbol{\varepsilon}}$, and therefore the integral condition (2.18) can be expressed in a generalized sense by introducing the following weak form:

$$\boldsymbol{\lambda} : \left(\int_{\Gamma} \boldsymbol{w} \otimes_s \boldsymbol{n}\, d\Gamma\right) = 0\,, \tag{2.21}$$

where $\boldsymbol{\lambda}$ is a (constant) second-order tensorial Lagrange multiplier field having the physical meaning of the unknown macro-stress tensor $\bar{\boldsymbol{\sigma}}$ (see (Bruno et al., 2008) for additional details). The generalized constraint (2.21) can be incorporated in a new formulation of the minimization problem (2.19), taking the form of a saddle point problem:

$$\bar{W}\left(\bar{\boldsymbol{\varepsilon}}, \bar{\boldsymbol{\sigma}}\right) = \sup_{\bar{\boldsymbol{\sigma}}\in \mathrm{Sym}} \inf_{\boldsymbol{w}\in A(\bar{\boldsymbol{\varepsilon}})} \frac{1}{|\Omega|}\left(\int_{\Omega\setminus\Gamma_d} W_b\left(\boldsymbol{\varepsilon}\left(\boldsymbol{w}\right)\right) d\Omega + \int_{\Gamma_d} W_c\left(\left[\!\left[\boldsymbol{u}\right]\!\right]\left(\boldsymbol{w}\right)\right) d\Gamma - \bar{\boldsymbol{\sigma}} : \left(\int_{\Gamma} \boldsymbol{w} \otimes_s \boldsymbol{n}\, d\Gamma\right)\right), \tag{2.22}$$

where Sym is the set of all symmetric tensors. It should be noted that the variational formulation (2.22) gives the solution for $\boldsymbol{u}$ except for rigid body motions, which can be suppressed by introducing suitable additional constraints. Considering an RVE with of convex elastic constituents, the following general inequalities involving the homogenized moduli tensor $\bar{\boldsymbol{C}}$ hold:

$$\bar{\boldsymbol{C}}^{(\mathrm{UT})}\bar{\boldsymbol{\varepsilon}}:\bar{\boldsymbol{\varepsilon}} \le \bar{\boldsymbol{C}}^{(\mathrm{G})}\bar{\boldsymbol{\varepsilon}}:\bar{\boldsymbol{\varepsilon}} \le \bar{\boldsymbol{C}}^{(\mathrm{LD})}\bar{\boldsymbol{\varepsilon}}:\bar{\boldsymbol{\varepsilon}}, \tag{2.23}$$

for the same prescribed macrostrain $\bar{\boldsymbol{\varepsilon}}$, meaning that the homogenized moduli tensor $\bar{\boldsymbol{C}}^{(\mathrm{G})}$ obtained for general boundary conditions is always comprised between the lower and upper limit tensors, corresponding to uniform traction (UT) and linear displacement (LD) boundary conditions, respectively. For elastic stiffness calibration purposes, we are interested in the lower bound $\bar{\boldsymbol{C}}^{(\mathrm{UT})}$, being associated with the greatest predicted value of moduli reduction among all of the alternative boundary conditions. In this thesis, the numerically derived homogenized moduli will refer to this type of BCs. In a two-dimensional plane stress or strain setting, the linearly elastic constitutive law can be expressed in the following matrix form:

$$\begin{Bmatrix} \bar{\sigma}_{11} \\ \bar{\sigma}_{22} \\ \bar{\sigma}_{12} \end{Bmatrix} = \begin{bmatrix} \bar{C}_{1111} & \bar{C}_{1122} & \bar{C}_{1112} \\ \bar{C}_{2211} & \bar{C}_{2222} & \bar{C}_{2212} \\ \bar{C}_{1211} & \bar{C}_{1222} & \bar{C}_{1212} \end{bmatrix} \begin{Bmatrix} \bar{\varepsilon}_{11} \\ \bar{\varepsilon}_{22} \\ 2\bar{\varepsilon}_{12} \end{Bmatrix}. \tag{2.24}$$

Due to the assumed major symmetry of the effective elastic tensor $\bar{\boldsymbol{C}}$, to solve for all the six independent components, three

BVPs must be specified, by considering two uniaxial and a shear macro-strain paths in the x_1x_2 plane.

Once the homogenized moduli tensor $\bar{\boldsymbol{C}}$ is derived, representing the overall elastic properties of the discretized continuum with embedded interfaces prior to damage onset, the artificial compliance effect induced by the presence of intrinsic cohesive elements along all the mesh boundaries can be investigated by using a suitable compliance index, defined as follows:

$$i_c = \frac{\left\| \bar{\boldsymbol{C}} - \boldsymbol{C} \right\|}{\left\| \boldsymbol{C} \right\|}, \tag{2.25}$$

where $\boldsymbol{C}$ is the elastic tensor of the bulk phase, and the symbol $\left\| \bullet \right\|$ denoting the conventional Euclidean norm of the enclosed tensor. Such a compliance index represents a measure of the distance between the homogenized moduli tensor and the elasticity tensor of the bulk phase, and therefore the condition $i_c \ll 1$ represents a necessary requirement for the cohesive/bulk aggregate to approximate the original continuum. It is useful to highlight that, the 2D homogenized moduli tensor $\bar{\boldsymbol{C}}$ is anisotropic in general, and the anisotropy level is expected to be dependent on the topology of the adopted computational tessellation as well as on the adopted values for the initial cohesive stiffness parameters K_n^0 and K_s^0, or their dimensionless counterparts κ and ξ, already defined in Section 2.1.2. In order to measure the anisotropy induced by the presence of embedded cohesive interfaces, the following anisotropy index is introduced:

$$i_a = \frac{\left\| \bar{\boldsymbol{C}} - \bar{\boldsymbol{C}}^{\mathrm{iso}} \right\|}{\left\| \bar{\boldsymbol{C}}^{\mathrm{iso}} \right\|}, \tag{2.26}$$

$\bar{\boldsymbol{C}}^{\mathrm{iso}}$ being the closest isotropic moduli tensor to the numerically computed homogenized moduli tensor $\bar{\boldsymbol{C}}$. In order to obtain the invisibility of embedded cohesive interfaces, is also required that the condition $i_a \ll 1$ remains valid for the considered values of K_n^0 and K_s^0. Both the requirements for the indexes (2.25) and (2.26) will be verified a posteriori in the following numerical computations, illustrated in Section 3.1.2.

The isotropic moduli tensor $\bar{\boldsymbol{C}}^{\mathrm{iso}}$ can be determined by solving a particular version of the more general problem of finding the closest approximation of an elasticity tensor with arbitrary material symmetry to an elasticity tensor with given symmetry, which has been largely investigated. Various metrics have been proposed in the literature to determine the distance between two arbitrary elasticity tensors, as reported in (Bruno et al., 2008), but the most widely used is the Euclidean metric, denoted as $d_E\left(\boldsymbol{C}_1, \boldsymbol{C}_2\right) = \left\| \boldsymbol{C}_1 - \boldsymbol{C}_2 \right\|$. Accordingly, a good candidate for such an equivalent isotropic elasticity tensor is the projection of the homogenized moduli tensor $\bar{\boldsymbol{C}}$ onto the class C^{iso} of isotropic elasticity tensors, computed by using the distance d_E, such that:

$$\bar{\boldsymbol{C}}^{iso} = \underset{\bar{\boldsymbol{C}}^* \in C^{\mathrm{iso}}}{\mathrm{Arg\,min}}\, d_E\left(\bar{\boldsymbol{C}}, \bar{\boldsymbol{C}}^*\right). \tag{2.27}$$

Similarly, the closest isotropic homogenized 2D moduli, i.e. the planar bulk modulus $\bar{K}_{2D}$ and shear modulus $\bar{G}_{2D}$ can be obtained by the following double minimization problem:

$$\left(\bar{K}_{2D}, \bar{\mu}_{2D}\right) = \underset{\bar{K}^*_{2D}, \bar{\mu}^*_{2D}}{\text{Arg min}}\, d_E\left(\bar{\boldsymbol{C}}, \bar{\boldsymbol{C}}^*\left(\bar{K}^*_{2D}, \bar{\mu}^*_{2D}\right)\right), \tag{2.28}$$

with respect to the unknowns $\bar{K}^*_{2D}$ and $\bar{G}^*_{2D}$, leading to the following expressions:

$$\begin{aligned} \bar{K}_{2D} &= \frac{1}{2}\left(\bar{C}^{\text{iso}}_{1111} + \bar{C}^{\text{iso}}_{1122}\right) = \frac{1}{4}\left(\bar{C}_{1111} + \bar{C}_{2222} + 2\bar{C}_{1122}\right) \\ \bar{G}_{2D} &= \frac{1}{2}\left(\bar{C}^{\text{iso}}_{1111} - \bar{C}^{\text{iso}}_{1122}\right) = \frac{1}{8}\left(\bar{C}_{1111} + \bar{C}_{2222} - 2\bar{C}_{1122} + 4\bar{C}_{1212}\right) \end{aligned}, \tag{2.29}$$

which shows as such isotropized moduli do not depend on the moduli $\bar{C}_{1112}$ and $\bar{C}_{2212}$, and represent the 2D counterpart of the relations for 3D elasticity reported in (Bruno et al., 2008).
Thus, the planar bulk modulus $\bar{K}_{2D}$ can be expressed as a function of the homogenized Young's modulus $\bar{E}$ and Poisson's ratio $\bar{\nu}$, in this way:

$$\bar{K}_{2D} = \frac{\bar{E}'}{2(1-\bar{\nu}')} \quad \text{with} \quad \bar{E}' = \begin{cases} \bar{E} & \text{plane stress} \\ \dfrac{\bar{E}}{1-\bar{\nu}^2} & \text{plane strain} \end{cases}, \quad \bar{\nu}' = \begin{cases} \bar{\nu} & \text{plane stress} \\ \dfrac{\bar{\nu}}{1-\bar{\nu}} & \text{plane strain} \end{cases}. \tag{2.30}$$

Instead, the planar shear modulus $\bar{G}_{2D}$ is equal to the typical shear modulus $\bar{G}$, considering either in plane-strain or plane-stress elasticity:

$$\bar{G}_{2D} = \bar{G} = \frac{\bar{E}}{2(1+\bar{\nu})}. \tag{2.31}$$

An angular averaging technique is employed to calculate the isotropized overall moduli tensor $\bar{C}^{\text{iso}}_{ijkl}$, leading to perfectly equivalent results as the minimization problem (2.27). Considering the case of planar elasticity, the homogenized (anisotropic) moduli tensor $\bar{C}_{ijkl}$ can be analytically averaged over the single polar angle ϕ, by means of a proper orthogonal transformation with the following matrix representation:

$$\left[\boldsymbol{Q}\right] = \begin{bmatrix} \cos\phi & \sin\phi \\ -\sin\phi & \cos\phi \end{bmatrix}, \tag{2.32}$$

with reference to the 2D setting, the angularly averaged overall moduli tensor $\langle \bar{\boldsymbol{C}} \rangle_{\phi}$ is then:

$$\left\langle \bar{C}_{ijkl} \right\rangle_{\phi} = \frac{1}{2\pi} \sum_{mnpq} \bar{C}_{mnpq} \int_0^{2\pi} Q_{mi} Q_{nj} Q_{pk} Q_{ql} d\phi \qquad \left(m,n,p,q = 1,2\right). \tag{2.33}$$

It can be easily shown that $\langle \bar{\boldsymbol{C}} \rangle_{\phi}$ turns to be isotropic and coincides with the closest isotropic homogenized moduli tensor $\bar{\boldsymbol{C}}^{\text{iso}}$, whose matrix representation in Voigt notation is:

$$\left[\bar{\boldsymbol{C}}^{\text{iso}}\right] = \begin{bmatrix} \bar{C}^{\text{iso}}_{1111} & \bar{C}^{\text{iso}}_{1122} & 0 \\ \bar{C}^{\text{iso}}_{1122} & \bar{C}^{\text{iso}}_{1111} & 0 \\ 0 & 0 & \frac{1}{2}\left(\bar{C}^{\text{iso}}_{1111} - \bar{C}^{\text{iso}}_{1122}\right) \end{bmatrix}. \tag{2.34}$$

Assuming $i_a \ll 1$, i.e. isotropy condition of the homogenized medium, the artificial compliance associated with the embedded cohesive interfaces can be measured by considering $\bar{\boldsymbol{C}}^{\text{iso}}$ rather

than $\bar{\boldsymbol{C}}$. Therefore, instead of the compliance index (2.25), the overall moduli reductions $R_E = \bar{E}/E$ and $R_\nu = \bar{\nu}/\nu$ have been used to calibrate the stiffness parameters of the embedded cohesive interfaces. Chosen the reduction values of the overall moduli, the resulting system of nonlinear equations to be solved in the two unknowns κ and ξ takes the following form:

$$\begin{cases} R_E = R_E\left(\kappa, \xi\right) \\ R_\nu = R_\nu\left(\kappa, \xi\right) \end{cases}. \tag{2.35}$$

Noteworthy results concerning the calibration of the cohesive stiffness parameters with reference to the random mesh configurations will be reported in Section 3.1.1.

2.2 Description of the proposed numerical fracture model for failure analysis of internally and/or externally reinforced concrete structures

Based on the cohesive finite element formulation described in Section 2.1, a novel numerical failure model for concrete structures has been developed, with the aim of analyzing in a unified manner all the nonlinear failures due to both diffuse and localized damage phenomena. Such a model, is able to predict the commonly experienced damage mechanisms (Figure 2.7) in concrete members reinforced with longitudinally and transversely internal steel bars (with reference to the usual reinforced concrete (RC) beams), and/or external strengthening system (with

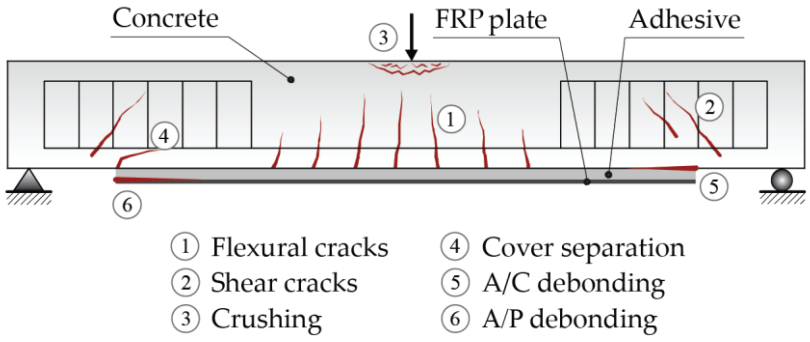

Figure 2.7. Principal failure mechanisms in internally and/or externally reinforced concrete structures.

reference to the latest FRP-plate RC beams). To this end, the proposed model incorporates the three following different models: (i) a diffuse interface model (DIM) for modeling multiple crack initiation and propagation in concrete; (ii) an embedded truss model (ETM) equipped with a bond-slip relation, able to simulate the behavior of steel rebars as well as their interaction with the neighboring concrete layer; and (iii) a single interface model (SIM) for modeling potential crack initiation and propagation along all the existing material interfaces, e.g. adhesive/concrete (A/C) and adhesive/plate (A/P) interfaces. These three models have been implemented within COMSOL Multiphysics®, chosen for all the numerical computations by virtue of its advanced scripting capabilities. In particular, the implementation of the diffuse interface model has been performed by taking advantage of the integrated Physics Builder functionality, which offers a user-friendly graphical interface to extend the built-in finite element library (Comsol AB, 2018).

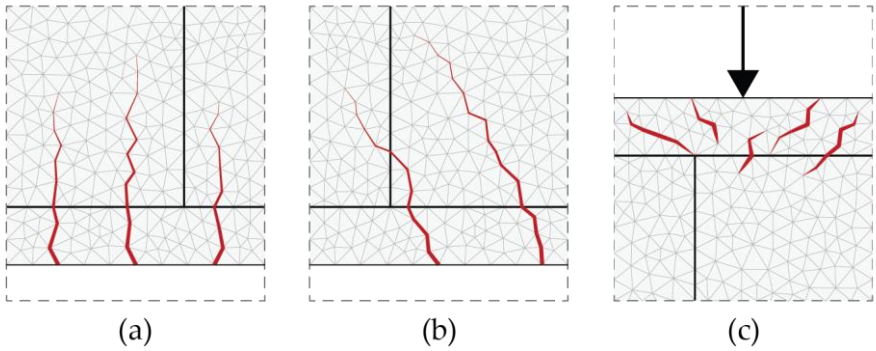

Figure 2.8. Potential crack patterns predicted by the diffuse interface mod-el: (a) flexural cracks; (b) shear cracks; (c) compressive crushing.

2.2.1 Diffuse interface model for concrete cracking

The diffuse interface model (DIM) allows multiple crack initiation and propagation in concrete to be accounted for, based on the cohesive finite element formulation described in Section 2.1. The main advantage of this approach is that no mesh updates are required, unlike in many classical discrete crack approaches, the diffuse damage phenomena being modeled as potential multiple cracking along all the internal mesh boundaries. As a matter of fact, if applied to the strengthened reinforced concrete (RC) structures, remeshing is inevitably tedious and time-consuming, due to the presence of a large number of embedded material discontinuities. The potential crack patterns which can be easily predicted by the present diffuse interface model are depicted in

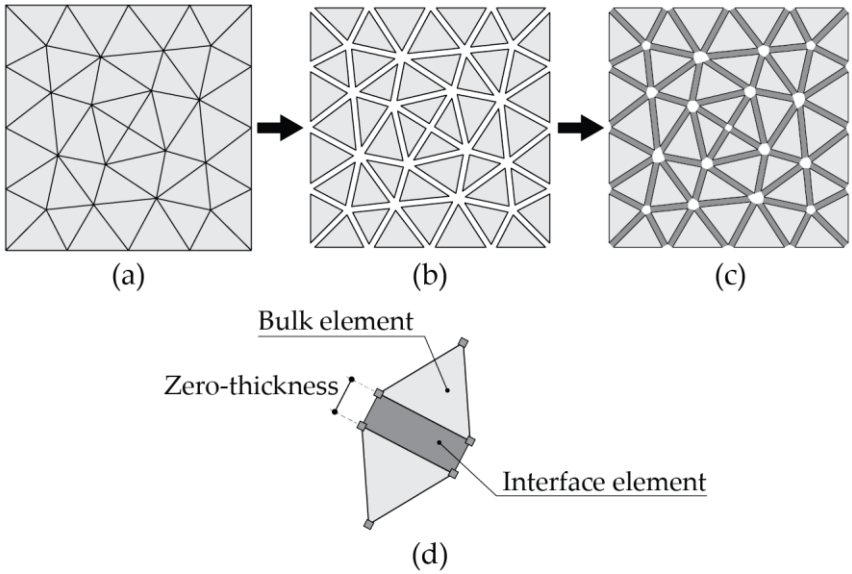

Figure 2.9. Construction of the cohesive/volumetric finite element mesh: (a) generation of a standard isotropic unstructured (i.e. Delaunay) triangulation; (b) separation of the bulk finite elements; (c) insertion of the cohesive interface elements; (d) detail of zero-thickness interface element between two bulk elements.

Figure 2.8. A fundamental preprocessing operation for the adopted inter-element fracture approach is the construction of the cohesive/volumetric finite element mesh. Such an operation, performed in an automatic manner by exploiting the advanced scripting capabilities of the adopted finite element environment, consists of three steps:

1. **Generation of the initial 2D bulk mesh**: three-node triangular elements are arranged according to an unstructured isotropic, i.e. Delaunay, spatial tessellation to alleviate the

mesh-induced effects (see Figure 2.9). Such a mesh is automatically created, by imposing the maximum element size within the region where cohesive elements must be inserted.

2. **Separation of the bulk finite elements**: duplication of every common node shared by each pair of bulk elements (see Figure 2.9b). It follows that a separated node is created at the same location for every pair of adjacent elements. Subsequently, the nodal connectivity is updated by using these duplicated nodes, resulting in a new decoupled mesh configuration, in which each element is no longer connected with its neighboring elements. This step is automatically performed by prescribing an explicit slit condition on the displacement field along the interior mesh boundaries.
3. **Insertion of the cohesive interface elements** (Figure 2.9c). This step consists in the automatic generation of four-node zero-thickness elements between the opposite faces of all the neighboring elements, as depicted, in more detail, in Figure 2.9d, allowing them to be interconnected.

The mechanical behavior of the embedded cohesive interfaces is governed by an uncoupled mixed-mode traction-separation law (TSL), written in the matrix form as follows:

$$\begin{Bmatrix} t_n \\ t_s \end{Bmatrix} = \left(1-d\right) \begin{bmatrix} K_n^0 & 0 \\ 0 & K_s^0 \end{bmatrix} \begin{Bmatrix} \delta_n \\ \delta_s \end{Bmatrix}, \tag{2.36}$$

the subscripts n and s referring to the normal and tangential directions, respectively. It is worth noting that the off-diagonal

stiffness terms are zero in the assumed constitutive law, meaning that the dilatancy effects are totally neglected in the present thesis. The following (effective) mixed-mode separation δ_m is defined to account for mixed-mode initiation and evolution:

$$\delta_m = \sqrt{\langle \delta_n \rangle^2 + \delta_s^2}\,, \tag{2.37}$$

where the symbol $\langle \bullet \rangle$ denotes the Macaulay operator, enforcing the condition that the effective separation is insensitive to a compressive displacement jump. The behavior of cohesive interfaces is governed by the following linear-exponential isotropic damage evolution law, investigated in (Park et al., 2016), involving a single scalar damage variable d:

$$d = \begin{cases} 0 & \text{for } \delta_m^{\max} \le \delta_m^0 \\ 1 - \dfrac{\delta_m^0}{\delta_m^{\max}} \left\{ 1 - \dfrac{1 - \exp\left[-\alpha \left(\dfrac{\delta_m^{\max} - \delta_m^0}{\delta_m^f - \delta_m^0} \right) \right]}{1 - \exp(-\alpha)} \right\} & \text{for } \delta_m^0 < \delta_m^{\max} \le \delta_m^f\,, \\ 1 & \text{for } \delta_m^{\max} > \delta_m^f \end{cases} \tag{2.38}$$

where δ_m^0 and δ_m^f denote the effective displacement jumps at damage initiation and complete decohesion, respectively, and $\delta_m^{\max}$ is a state variable defined as the maximum effective displacement jump over the entire deformation history. The non-dimensional parameter α, ranging in the open interval $(0, \infty)$,

directly influences the rate of damage evolution. For $\alpha \to 0$ a linear softening is attained, whereas for $\alpha \to \infty$ a fully exponential softening is found. This parameter is calibrated for the specific material under examination (set as 5 for concrete in the present thesis).

The mixed-mode crack initiation is governed by the following stress-based quadratic interaction criterion:

$$\left(\frac{\langle t_n \rangle}{\sigma_{\max}} \right)^2 + \left(\frac{t_s}{\tau_{\max}} \right)^2 = 1, \tag{2.39}$$

where $\sigma_{\max}$ and $\tau_{\max}$ denote the normal and tangential critical interface stresses. According to this criterion, a purely compressive stress state does not induce any crack initiation, leading to the following definition for the effective separation δ_m^0, valid only for $\delta_n > 0$, after which the material stiffness of the interface initiates to decrease due to the appearance of damage:

$$\delta_m^0 = \delta_n^0 \delta_s^0 \sqrt{\frac{1+\beta^2}{\left(\delta_s^0\right)^2 + \left(\beta \delta_n^0\right)^2}}, \tag{2.40}$$

where $\delta_n^0 = \sigma_{\max} / K_n^0$, $\delta_s^0 = \tau_{\max} / K_s^0$, and $\beta = \delta_s / \delta_n$ is the ratio between the tangential and normal displacement jumps.

The mixed-mode crack propagation is governed by the following linear power law criterion (also valid only for $\delta_n > 0$), involving the two in-plane modal components G_{I} and G_{II} of the energy release rate:

$$\frac{G_{\mathrm{I}}}{G_{\mathrm{I}c}}+\frac{G_{\mathrm{II}}}{G_{\mathrm{II}c}}=1, \tag{2.41}$$

$G_{\mathrm{I}c}$ and $G_{\mathrm{II}c}$ being the mode-I and mode-II fracture energies, respectively. The energy release rates corresponding to total decohesion are (see [63] for additional details about their derivation):

$$\begin{aligned} G_{\mathrm{I}} &= \frac{K_n^0}{2\left(1+\beta^2\right)}\left(\left(\delta_m^0\right)^2+\frac{2\left(1+\alpha-e^{\alpha}\right)}{\alpha\left(1-e^{\alpha}\right)}\delta_m^0\left(\delta_m^f-\delta_m^0\right)\right) \\ G_{\mathrm{II}} &= \frac{\beta^2 K_s^0}{2\left(1+\beta^2\right)}\left(\left(\delta_m^0\right)^2+\frac{2\left(1+\alpha-e^{\alpha}\right)}{\alpha\left(1-e^{\alpha}\right)}\delta_m^0\left(\delta_m^f-\delta_m^0\right)\right) \end{aligned} \tag{2.42}$$

By inserting Equation (2.42) into Equation (2.41), and solving the equation with respect to δ_m^f, the mixed-mode displacement jump corresponding to total decohesion is obtained as:

$$\delta_m^f=\frac{\alpha\left(1-e^{\alpha}\right)}{2\left(1+\alpha-e^{\alpha}\right)}\left[\frac{2\left(1+\beta^2\right)}{\delta_m^0}\left(\frac{K_n^0}{G_{\mathrm{I}c}}+\frac{\beta^2 K_s^0}{G_{\mathrm{II}c}}\right)^{-1}-\left(1-\frac{2\left(1+\alpha-e^{\alpha}\right)}{\alpha\left(1-e^{\alpha}\right)}\right)\delta_m^0\right] \tag{2.43}$$

When $\delta_n \le 0$, a pure mode-II fracture occurs (i.e. $G_{\mathrm{I}}=0$), and the related crack advancement criterion reads as $G_{\mathrm{II}}=G_{\mathrm{II}c}$. The mode-II energy release rate corresponding to total decohesion is:

$$G_{\mathrm{II}}=\frac{K_s^0}{2}\left(\left(\delta_s^0\right)^2+\frac{2\left(1+\alpha-e^{\alpha}\right)}{\alpha\left(1-e^{\alpha}\right)}\delta_s^0\left(\delta_s^f-\delta_s^0\right)\right). \tag{2.44}$$

Imposing the expression (2.44) equal to $G_{\mathrm{II}c}$, and solving with respect to δ_s^f, the mode-II displacement jump corresponding to total decohesion is found as:

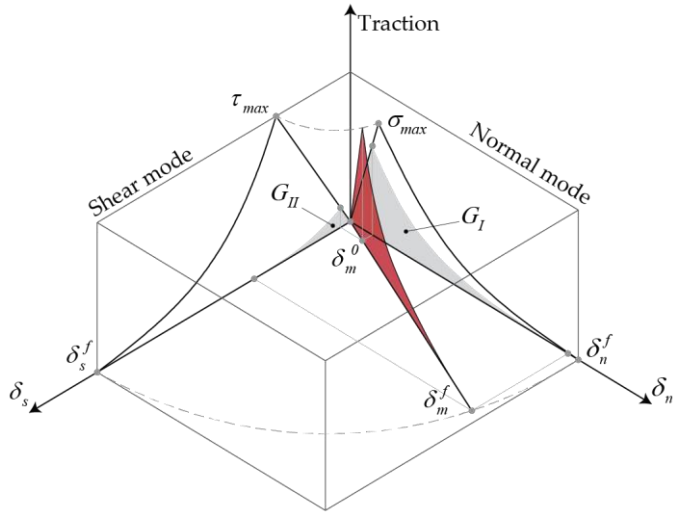

Figure 2.10. Schematic representation of the linear-exponential mixed-mode cohesive traction-separation law.

$$\delta_s^f = \frac{\alpha\left(1-e^{\alpha}\right)}{2\left(1+\alpha-e^{\alpha}\right)}\left[\frac{2G_{IIc}}{K_s^0\delta_s^0}-\left(1-\frac{2\left(1+\alpha-e^{\alpha}\right)}{\alpha\left(1-e^{\alpha}\right)}\right)\delta_s^0\right]. \qquad (2.45)$$

The present interface formulation cannot predict damage under pure compression and does not incorporate any friction model. The proposed cohesive law is accompanied by an additional unilateral contact constraint enforced by a penalty approach, consisting in re-applying the initial normal stiffness K_n^0 when interpenetration is detected. In summary, such a mixed-mode traction-separation law, whose graphic representation is illustrated in Figure 2.10, depends on seven parameters, i.e. K_n^0 and K_s^0, $\sigma_{\max}$ and $\tau_{\max}$, G_{Ic} and G_{IIc}, and α.

2.2.2 Embedded truss model for steel/concrete interaction

In order to obtain a correct prediction of the damage mechanisms in the reinforced concrete analysis, the effect of the interaction between the reinforcing bars and the surrounding cracking concrete should be adequately captured by the adopted modeling approach. Such an effect, commonly referred to as tension stiffening effect, is related to the capacity of undamaged concrete to carry tensile forces between adjacent primary cracks, resulting in a higher overall stiffness compared to that associated with the only steel bars. Tension stiffening is usually included in numerical models by modifying the tensile constitutive behavior of the concrete phase. In reality, tension stiffening is related to the bond stress transferred by the steel/concrete interface between the primary cracks. Additionally, the related crack patterns can be correctly captured (in both 2D and 3D cases) only if the slip between the bars and the surrounding concrete is taken into account. Such a slip behavior plays a notable role in determining the structural response of reinforced elements in the cracked stage, also influencing the distribution of bond stresses along the reinforcement bars, and ultimately, the extent of crack widths and deflections.

In the adopted numerical model for damaging RC structures, the reinforcing bars are modeled as embedded truss model (ETM) elements connected to concrete by means of specific interfaces equipped with a bond stress-slip relation, in order to capture the interaction effect of the re-bars and concrete.

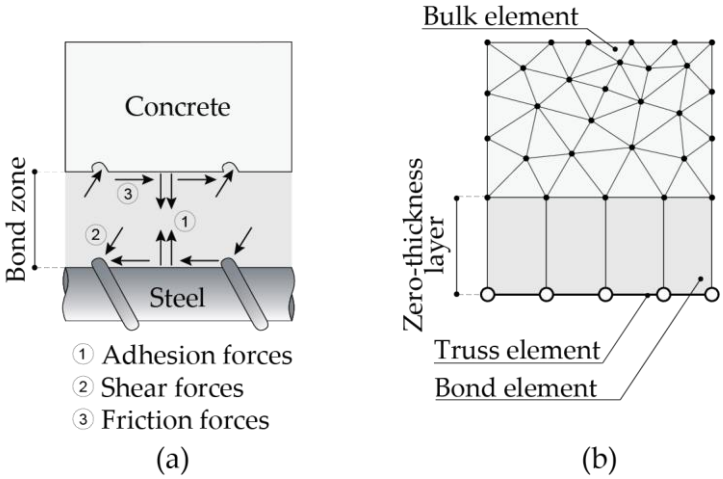

Figure 2.11. Schematic representation of the steel/concrete interaction: (a) detailed representation of the steel/concrete bond zone; (b) bond-layer model.

The adopted embedded truss model allows the steel/concrete bond behavior to be realistically simulated with significantly lower effort than more sophisticated models, based on a detailed representation of the geometry of both rebars and surrounding concrete (see Figure 2.11a). Such a detailed representation should include the ribs of the reinforcement and the concrete lugs, inevitably leading to a high computational cost and to modelling difficulties, associated with the need of very refined computational meshes. The bond between concrete and steel reinforcement is here taken into account by using a simplified model, based on a discrete representation of the bond layer (see Figure 2.11b). The link between rebar and concrete is defined by introducing dedi-

cated zero-thickness nonlinear interface elements, acting as nonlinear tangential spring between truss elements, referred to the reinforcement, and bulk elements for the concrete, defining the bond strength and stiffness as functions of the relative tangential displacement (slip), s, between the two different materials.

The bond behavior for different geometries and boundary conditions is realistically simulated by this approach by a reliable and accurate constitutive model for the surrounding concrete. As the intrinsic cohesive approach, this bond model is of phenomenological type, since it cannot predict the mechanical behavior of the given bimaterial system starting from its adhesion and friction properties, and a calibration based on the rebar type as well as on the mechanical properties of the surrounding concrete is necessary.

The bond-slip relation adopted in the present thesis is the popular relation valid for ribbed bars and good bond conditions, contained in the CEB-FIP Model Code (Fib, 2013), shown in Figure 2.12. Up to the slip $s_1 = 1\,\text{mm}$, at which the peak bond strength $\tau_{\max}$ is achieved, the tangential stress is defined by the relation $\tau = \tau_{\max}\left(s/s_1\right)^{0.4}$, where $\tau_{\max} = 2.5\sqrt{f_c}$ with f_c compressive strength in MPa. After exceeding the slip s_1, the response curve remains constant before decreasing linearly from slip $s_2 = 2\,\text{mm}$ to slip s_3 (coinciding with the clear distance between

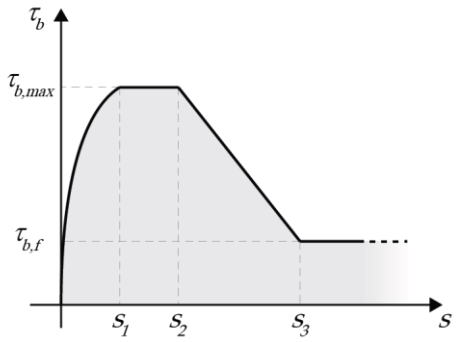

Figure 2.12. Bond-slip relation (taken from the CEB-FIP Model Code) for bond behavior at the concrete/steel interface.

ribs), as the concrete corbels between the ribs are sheared off, after which a constant residual frictional strength $\tau_{\text{res}} = 0.4\tau_{\max}$ is reached. The adopted local bond-slip behavior is able to capture the experimental evidence that the load transfer between reinforcement and concrete is mainly accomplished through bearing of the reinforcing bar lugs on the surrounding concrete at small slip values and through friction at large slip values.

The steel/concrete connection perpendicularly to the rebar direction is assumed to be perfect, meaning that only the displacement jump in the bar direction (i.e. the slip) is considered as an active degree of freedom of the zero-thickness steel/concrete interface element. With reference to a two-dimensional model reduction, ad-hoc two-node truss elements, in which all the distributed steel rebars at a given depth are concentrated, are embedded between planar three-node bulk elements such that the nodes of concrete and steel meshes are superposed to each other. Moreover, the embedded truss elements are equipped with an

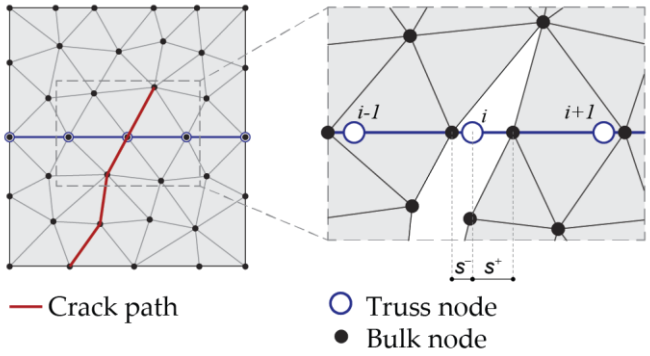

Figure 2.13. Representation of crack propagation across the reinforcing bars.

elastoplastic model with linear hardening to describe the yielding behavior of the steel reinforcement, using a tangent plastic modulus one hundred times smaller than the elastic one.

A fundamental feature of the proposed embedded truss model is that it allows any crack to propagate across the reinforcement steel layer, as shown in Figure 2.13. It follows that, for any truss node, two different slips can be defined for the steel/concrete element pairs across a potential crack path passing through that node. Accordingly, the related crack width can be computed as the sum of such slips (taken as absolute values), denoted as s^- and s^+, as illustrated in Figure 2.13.

2.2.3 Single interface model for debonding phenomena

In the case of reinforced concrete structures externally strengthened with FRP systems, is very important take into account the possible damage phenomena which can occur along

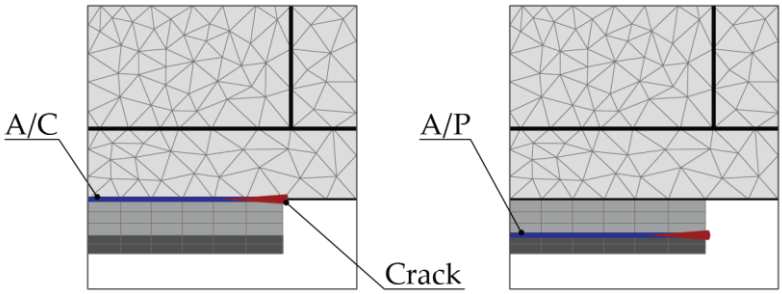

Figure 2.14. Potential crack patterns predicted by the single interface model (cracks are highlighted in red): (a) adhesive/concrete (A/C) interfacial debonding; (b) adhesive/plate (A/P) interfacial debonding.

the material interfaces, i.e. between adhesive and concrete and/or between adhesive and FRP plate.

To this end, in the proposed numerical model such material interfaces are not perfect but are susceptible to be damaged under general loading conditions. Additional mixed-mode cohesive elements are inserted in those locations, able to simulate multiple interfacial debonding initiation and propagation. Cohesive fracture models are chosen as the most straightforward for this type of problems, where predefined weak physical interfaces exist. Coherently with the adopted intrinsic approach, the cohesive interface elements, placed along the prescribed crack paths, are kept active from the beginning of the numerical simulation. The formulation of the adopted cohesive approach has been already described in the Section 2.1, considering in this case an a priori known crack path. The proposed single interface model (SIM) is able to represent both adhesive/concrete (AC) and adhesive/plate (A/P) interfacial debonding, as depicted in Figure 2.14.

3

Numerical calibration and validation of the diffuse interface model in plain concrete

In this chapter both the calibration and validation of the diffuse interface model, described in Section 2.2, are presented, involving plain concrete specimens. In particular, the numerical calibration of the elastic stiffness parameters of the interface elements, using the micromechanical approach described in Section 2.1.3, is reported in Section 3.1. Thereafter, the proposed fracture model has been validated under mode I and mixed-mode loading conditions, whose results are illustrated in Section 3.2 and 3.3

respectively, also providing some comparisons with those obtained by numerical and experimental tests.

3.1 Numerical calibration of the diffuse interface model

In this Section, the elastic stiffness parameters for obtaining invisible cohesive interfaces are numerically determined, using the micromechanical approach described in Section 2.1.3. In detail, two charts for the calibration of both the dimensionless cohesive stiffness $\kappa = K_n^0 L_{\text{mesh}} / E$ and the tangential-to-normal stiffness ratio $\xi = K_s^0 / K_n^0$ are provided in Section 3.1.1. A further investigation of both compliance and anisotropy levels for the resulting overall homogenized moduli tensor is given in Section 3.1.2.

3.1.1 General results on planar random mesh configurations

Concerning the elastic calibration of the diffuse interface model (DIM), described in Section 2.1, here general numerical results obtained by the linear homogenization technique, presented in Section 2.1.3, have been reported, with reference to isotropic unstructured mesh configurations, under uniform traction (UT) boundary conditions and plane stress assumption. Such a type of boundary conditions provides the smallest homogenized moduli among those that satisfy the Hill-Mandel's macro-homogeneity condition, associated with the greatest estimated value for the artificial compliance. Thus, under general boundary conditions, the resulting loss of stiffness induced by the presence of

the interface elements is assured to be always smaller than the prescribed one.

In the following analysis, a circular RVE with diameter $D = L_{\mathrm{RVE}}$ has been considered. Such a type of RVE, despite has not the space-filling property of more commonly used tetragonal and hexagonal RVEs, has been chosen here in order to avoid the introduction of preferential directions for the mesh generation, by virtue of the absence of corners in the original geometry. A Delaunay tessellation, composed by n_e three-node finite elements and embedded four-node elastic interface elements placed along the internal mesh boundaries, according to the insertion procedure described in Section 2.2.1, is employed to discretize the RVE.

The average mesh size L_{mesh}, which represent the edge length of an equivalent equilateral triangulation, can be obtained by the following formula:

$$L_{\mathrm{mesh}} = \sqrt{\frac{4A_{\mathrm{int}}}{n_e\sqrt{3}}}, \tag{2.46}$$

where A_{int} is area containing the interface element, in this case is equal to the area of RVE, i.e. $A_{\mathrm{int}} = \pi D^2 / 4$. To obtain corrected homogenized moduli, the L_{mesh} should be much smaller than L_{RVE} for the homogenized moduli. In order to determine the mesh size L_{mesh} to be used for homogenization purposes, different mesh configurations have been considered, by varying the associated number n_e of finite elements from 110 to 8364. These

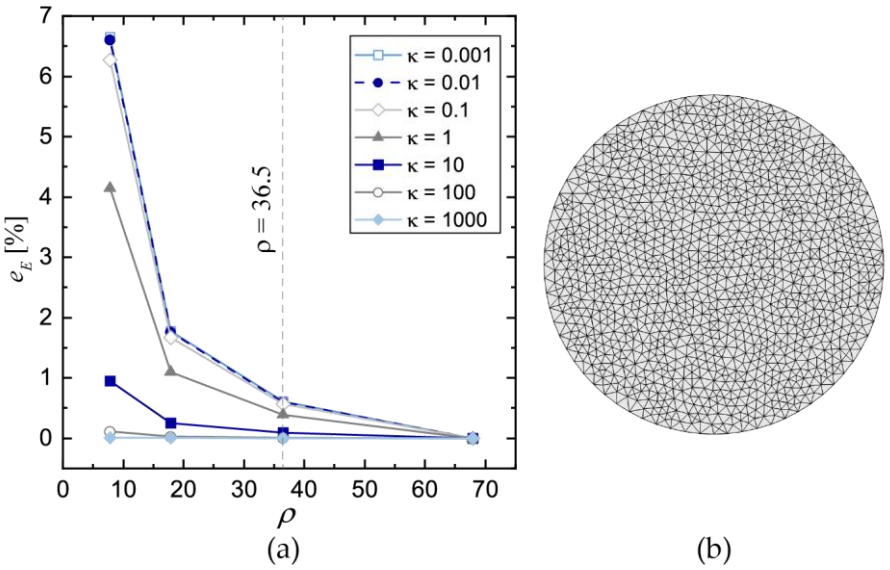

Figure 3.1. Mesh convergence analysis for homogenization purposes: (a) percentage variation of the overall Young's modulus vs dimensionless RVE size; (b) adopted mesh configuration for the calibration of the cohesive interface model (having $\rho = L_{\mathrm{RVE}} / L_{\mathrm{mesh}} = 36.5$).

preliminary numerical computations have been addressed to a concrete-like material with bulk elastic constants $E = 30$ GPa and $\nu = 0.2$, whose cohesive interfaces have been calibrated by preliminarily assigning $\xi = 1$.

The results of the mesh sensitivity analysis in terms of convergence of the overall Young's modulus $\bar{E}$, for different values of κ belonging to a wide range, as a function of the dimensionless parameter $\rho = L_{\mathrm{RVE}} / L_{\mathrm{mesh}}$, which is a suitable measure of the distance between the macro-scale (i.e. the RVE scale) and the micro-scale (i.e. the finite element scale) are reported in Figure 3.1a. The dimensionless parameter $\rho = 36.5$ provides the coarsest mesh

assuring a percentage variation of the overall Young's modulus $\bar{E}$, defined as $e_{\%} = \left(\bar{E} - \bar{E}_{\text{ref}}\right) / \bar{E}_{\text{ref}} \times 100$, smaller than 1% compared to the finest mesh resolution (corresponding to the reference value $\rho_{\text{ref}} = 67.9$), for any considered value of κ. The mesh associated with $\rho = 36.5$, depicted in Figure 3.1b, has been chosen to perform the next numerical homogenization analysis. It has been also verified that this mesh density is sufficient to achieve a numerical accuracy of about 1% on the statistical fluctuations of the results associated with many RVE realizations.

Obtained the RVE size as a function of the adopted mesh size, the calibration of the elastic stiffness parameters of the embedded cohesive interfaces has been performed after solving the system (2.35), for fixed values of R_E and R_ν, in an iterative manner, i.e. by testing different values for the couple $\left(\kappa, \xi\right)$.

From the numerical analysis has been found that no reduction of the overall Poisson's ratio, i.e. $R_\nu = 1$, allows the dependence of R_ν on the normal stiffness parameter κ to be practically neglected, coherently with what predicted by Equation (2.12). It follows that the ratio ξ between the dimensionless tangential and normal stiffness can be regarded as a function of only the Poisson's ratio of the bulk phase, whose numerically derived behavior is shown in Figure 3.2. Moreover, the following closed-

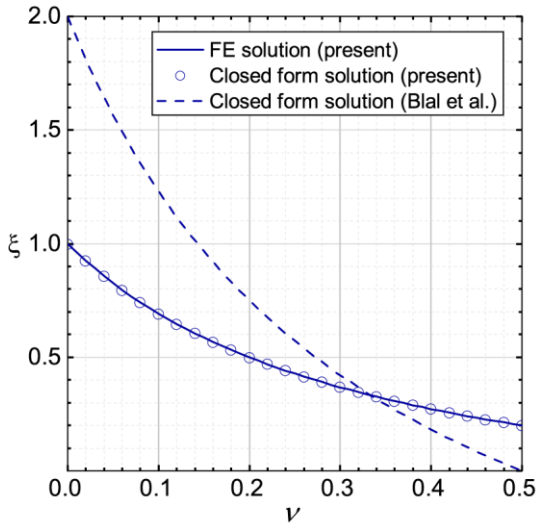

Figure 3.2. Tangential-to-normal stiffness ratio for different values of the Poisson's ratio: comparisons between the present results, in terms of both numerical and closed-form according to Equation (2.47), and those obtained in (Blal et al., 2012).

form solution has been found, also depicted in Figure 3.2, having the best fit of the numerically derived points:

$$\xi = \frac{1-\nu}{1+3\nu}, \tag{2.47}$$

which can be regarded as the 2D counterpart (under plane stress conditions) of the latter of Equations (2.14), which was derived in (Blal et al., 2012) for the 3D case (although also applied to planar elasticity problems). In contrast to what predicted by the latter of Equations (2.14), also reported in Figure 3.2 for comparison purposes, the tangential-to-normal stiffness ratio to be assigned

according the proposed numerical calibration methodology is always smaller than one (this limit value is reached for $\nu = 0$). Additionally, in contrast with the latter of Equations (2.14), in the case of incompressible materials (i.e. $\nu = 0.5$), the present result predicts no vanishing behavior for ξ. By introducing Equation (2.47) in the first of Equations (2.35), it follows that normal stiffness parameters κ can be found as a function of the given Poisson's ratio and the desired reduction R_E, expressed in percent.

A significant chart (Figure 3.3), valid for any isotropic and linearly elastic material with $0 \le \nu < 0.5$ subjected to a plane stress state, has been obtained performing several numerical analyses. In detail, the chart numerically confirms the qualitative behavior of the first of Equations (2.14), characterized by the limits $\lim_{\kappa \to 0} R_E = 1$ and $\lim_{\kappa \to \infty} R_E = 0$, but provides more reliable results in the case of greater Poisson's ratios. Indeed, the first of Equations (2.14) predict an infinite cohesive stiffness for any reduction of the overall moduli, when perfectly incompressible materials are consider. It is worth noting that the most useful part of this chart is the top one, here extracted and reported in the same Figure 3.3, which refers to values of R_E greater than 0.95, i.e. a stiffness reduction of 5%, usually admissible for engineering purposes. The value of κ assuring a reduction R_E of the overall Young's modulus smaller than a given threshold, is the abscissa of the intersection point between the horizontal line passing through this threshold value and the curve associated with the given Poisson's ratio.

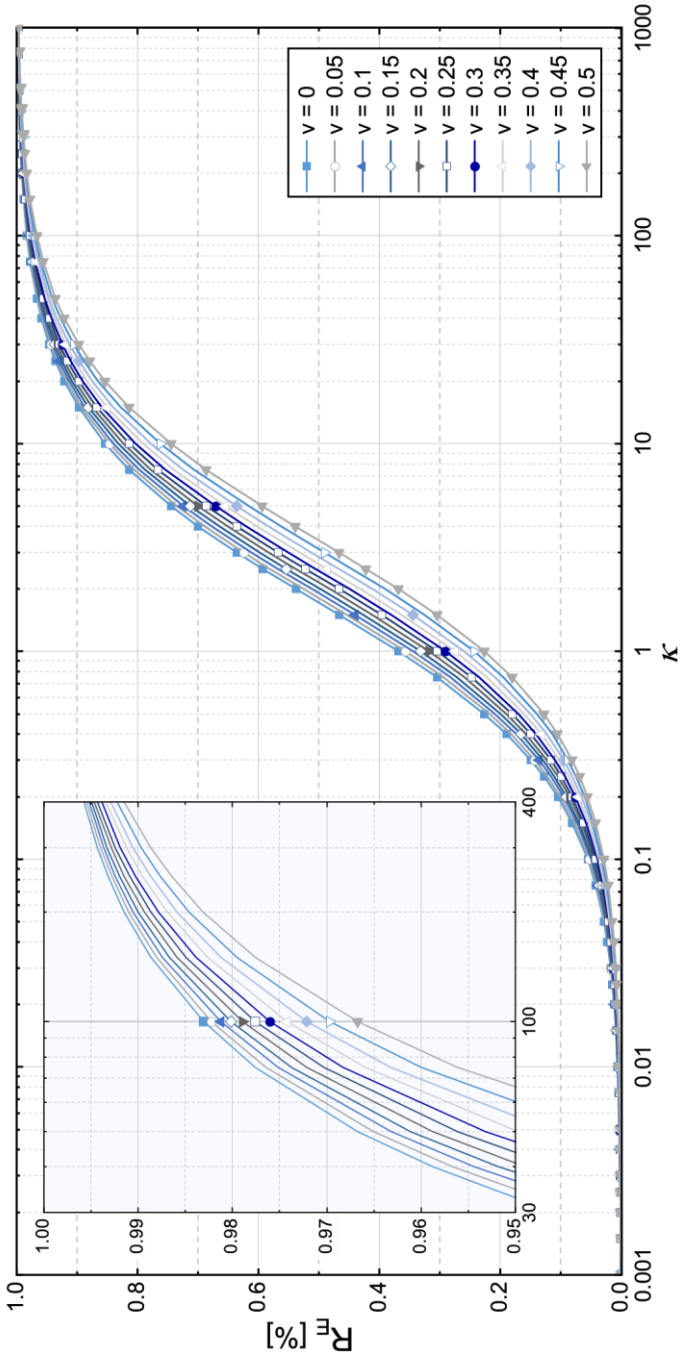

Figure 3.3. Chart of the dimensionless normal stiffness vs Young's modulus reduction for the elastic calibration of the diffuse interface model.

For the particular case of a typical concrete with Poisson's ratio equal to 0.2 and assuming a Young's modulus reduction of 2%, the calibration of the diffuse interface model, performed by using the numerical results reported in Figure 3.2 and Figure 3.3 leads to the following values for the dimensionless parameters governing the elastic response of the cohesive elements: $\xi = 0.500$ and $\kappa = 107.6$.

3.1.2 Numerical investigation of compliance and anisotropy levels

Here, a numerical investigation of both the compliance and anisotropy levels induced by the computational mesh has been performed, in order to assess the general validity of the proposed calibration approach. To this end, the two corresponding indices (2.25) and (2.26), introduced in Section 2.1.3, have been evaluated for different values of both κ and ν within the ranges of variation considered in Section 3.1.1.

As expected, the results of the numerical analysis highlighted that the compliance index i_c is strongly affected by the elastic stiffness of the cohesive interface, providing unacceptable compliance increments (greater than 5%) for values of κ smaller than 20, regardless of the adopted Poisson's ratio (see Table 3.1). Contrarily, the variation of the Poisson's ratio has a limited influence on the i_c, which tends to slightly increase for increasing values of ν at fixed κ. The variation of the anisotropy index i_a within the same ranges of independent variables is reported in Table 3.2.

Table. 3.1. Compliance index as a function of both the Poisson's ratio and dimensionless normal stiffness

		ν										
		0	**0.05**	**0.1**	**0.15**	**0.2**	**0.25**	**0.3**	**0.35**	**0.4**	**0.45**	**0.5**
κ	**0.001**	0.9994	0.9994	0.9995	0.9995	0.9995	0.9996	0.9996	0.9996	0.9996	0.9997	0.9997
	0.002	0.9988	0.9989	0.9989	0.999	0.9991	0.9991	0.9992	0.9992	0.9993	0.9994	0.9994
	0.005	0.9971	0.9972	0.9974	0.9975	0.9977	0.9978	0.998	0.9981	0.9983	0.9984	0.9985
	0.01	0.9942	0.9945	0.9948	0.9951	0.9953	0.9956	0.9959	0.9962	0.9965	0.9968	0.9971
	0.02	0.9884	0.989	0.9896	0.9902	0.9907	0.9913	0.9919	0.9925	0.993	0.9936	0.9942
	0.05	0.9716	0.973	0.9744	0.9758	0.9772	0.9786	0.98	0.9814	0.9828	0.9842	0.9856
	0.1	0.9448	0.9474	0.95	0.9527	0.9553	0.958	0.9607	0.9634	0.9661	0.9689	0.9716
	0.2	0.8954	0.9001	0.9048	0.9096	0.9145	0.9194	0.9244	0.9294	0.9345	0.9397	0.9449
	0.5	0.7741	0.7829	0.7919	0.8012	0.8107	0.8204	0.8303	0.8405	0.851	0.8617	0.8727
	1	0.6316	0.6434	0.6557	0.6685	0.6818	0.6956	0.71	0.725	0.7407	0.7571	0.7743
	2	0.4618	0.4745	0.488	0.5023	0.5174	0.5335	0.5506	0.5689	0.5884	0.6094	0.6318
	5	0.2557	0.2656	0.2762	0.2878	0.3004	0.3141	0.3292	0.3457	0.3641	0.3845	0.4073
	10	0.1467	0.1532	0.1603	0.1682	0.1768	0.1864	0.1971	0.2091	0.2227	0.2381	0.2559
	20	0.0792	0.083	0.0872	0.0919	0.097	0.1028	0.1094	0.1168	0.1253	0.1352	0.1468
	50	0.0333	0.0349	0.0368	0.0389	0.0412	0.0439	0.0468	0.0503	0.0542	0.0589	0.0644
	100	0.0169	0.0178	0.0188	0.0198	0.0211	0.0224	0.024	0.0258	0.0279	0.0303	0.0333
	200	0.0085	0.009	0.0095	0.01	0.0106	0.0113	0.0121	0.0131	0.0141	0.0154	0.0169
	500	0.0034	0.0036	0.0038	0.004	0.0043	0.0046	0.0049	0.0053	0.0057	0.0062	0.0068
	1000	0.0017	0.0018	0.0019	0.002	0.0021	0.0023	0.0025	0.0026	0.0029	0.0031	0.0034

Table 3.2. Anisotropy index as a function of both the Poisson's ratio and dimensionless normal stiffness

		ν										
		0	**0.05**	**0.1**	**0.15**	**0.2**	**0.25**	**0.3**	**0.35**	**0.4**	**0.45**	**0.5**
κ	**0.001**	4.548E-3	4.389E-3	4.217E-3	4.031E-3	3.832E-3	3.620E-3	3.396E-3	3.161E-3	2.918E-3	2.669E-3	2.414E-3
	0.002	4.545E-3	4.386E-3	4.214E-3	4.029E-3	3.830E-3	3.618E-3	3.394E-3	3.160E-3	2.917E-3	2.668E-3	2.413E-3
	0.005	4.537E-3	4.379E-3	4.207E-3	4.023E-3	3.824E-3	3.613E-3	3.390E-3	3.157E-3	2.914E-3	2.665E-3	2.411E-3
	0.01	4.523E-3	4.366E-3	4.196E-3	4.012E-3	3.815E-3	3.605E-3	3.383E-3	3.150E-3	2.909E-3	2.661E-3	2.408E-3
	0.02	4.496E-3	4.342E-3	4.174E-3	3.992E-3	3.797E-3	3.589E-3	3.369E-3	3.138E-3	2.898E-3	2.652E-3	2.400E-3
	0.05	4.417E-3	4.269E-3	4.107E-3	3.932E-3	3.743E-3	3.541E-3	3.327E-3	3.102E-3	2.867E-3	2.626E-3	2.379E-3
	0.1	4.292E-3	4.153E-3	4.002E-3	3.836E-3	3.657E-3	3.464E-3	3.259E-3	3.043E-3	2.817E-3	2.583E-3	2.343E-3
	0.2	4.061E-3	3.940E-3	3.806E-3	3.658E-3	3.496E-3	3.320E-3	3.132E-3	2.932E-3	2.721E-3	2.502E-3	2.276E-3
	0.5	3.497E-3	3.414E-3	3.319E-3	3.210E-3	3.088E-3	2.953E-3	2.804E-3	2.642E-3	2.470E-3	2.287E-3	2.095E-3
	1	2.840E-3	2.793E-3	2.735E-3	2.666E-3	2.585E-3	2.492E-3	2.387E-3	2.269E-3	2.140E-3	2.000E-3	1.850E-3
	2	2.064E-3	2.047E-3	2.024E-3	1.991E-3	1.950E-3	1.900E-3	1.839E-3	1.769E-3	1.689E-3	1.599E-3	1.500E-3
	5	1.134E-3	1.137E-3	1.136E-3	1.132E-3	1.123E-3	1.109E-3	1.090E-3	1.065E-3	1.035E-3	9.986E-4	9.564E-4
	10	6.472E-4	6.525E-4	6.562E-4	6.579E-4	6.573E-4	6.543E-4	6.486E-4	6.401E-4	6.287E-4	6.141E-4	5.963E-4
	20	3.482E-4	3.523E-4	3.557E-4	3.580E-4	3.594E-4	3.595E-4	3.585E-4	3.560E-4	3.522E-4	3.469E-4	3.401E-4
	50	1.459E-4	1.480E-4	1.498E-4	1.512E-4	1.523E-4	1.529E-4	1.530E-4	1.527E-4	1.518E-4	1.505E-4	1.486E-4
	100	7.416E-5	7.527E-5	7.624E-5	7.705E-5	7.767E-5	7.809E-5	7.827E-5	7.823E-5	7.794E-5	7.742E-5	7.666E-5
	200	3.738E-5	3.796E-5	3.847E-5	3.890E-5	3.923E-5	3.947E-5	3.959E-5	3.960E-5	3.950E-5	3.928E-5	3.895E-5
	500	1.503E-5	1.526E-5	1.547E-5	1.565E-5	1.579E-5	1.589E-5	1.595E-5	1.596E-5	1.593E-5	1.585E-5	1.573E-5
	1000	7.525E-6	7.644E-6	7.750E-6	7.839E-6	7.911E-6	7.962E-6	7.992E-6	8.000E-6	7.986E-6	7.949E-6	7.891E-6

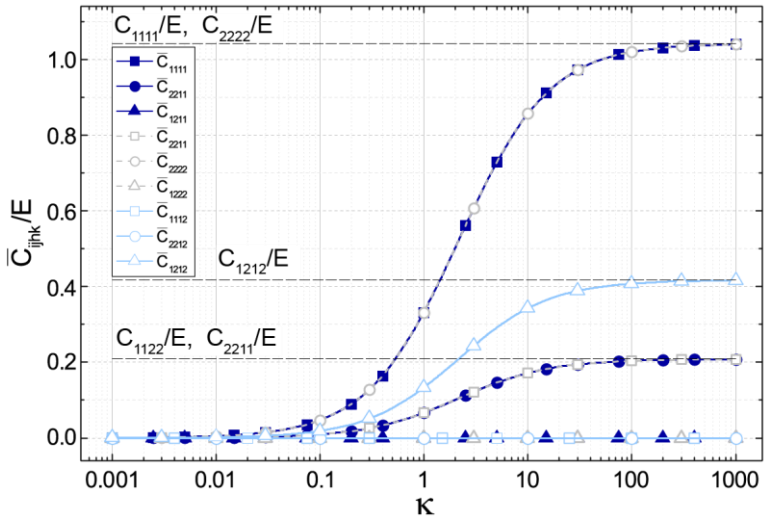

Figure 3.4. Behavior of the (plane stress) homogenized moduli for a cohesive finite element assembly (with $\nu = 0.2$) as a function of the normal stiffness parameter of the embedded interfaces (dashed lines refer to the corresponding bulk moduli).

As expected, for any value of ν, a decrease of the stiffness parameter κ leads to an increase of the mesh-induced anisotropy level, which, however, does not exceed 1%. This value confirms the effectiveness of the proposed micromechanical calibration with respect to the desired isotropy requirement.

The numerical results obtained by this preliminary analysis, reported in Figure 3.2, Figure 3.3, Table 1, and Table 2 are valid for any isotropic material with Poisson's ratio ranging from 0 to 0.5. In the particular case $\nu = 0.2$, which is typical for concrete, further numerical results are presented, aimed at better investigating the mesh-induced effects on the homogenized moduli.

The behavior of the homogenized moduli, normalized with respect to the Young's modulus of the bulk, for the considered cohesive finite element assembly as a function of the normal stiffness parameter of the embedded interfaces, is depicted in Figure 3.4. It can be noted that for any value of κ, the cohesive finite element assembly preserves its isotropy, thus assuring the same loss of stiffness in each direction. This effect is essentially due to the adopted (isotropic) mesh topology, for which the embedded cohesive interfaces are randomly placed without introducing any preferential orientation into the model.

A more detailed investigation of the mesh-induced anisotropy associated with the diffuse interface model is provided by evaluating the effective moduli for several mesh orientations in the x_1x_2 plane. The rotated moduli $\bar{\boldsymbol{C}}^*$ are computed using the Equation (2.32). The percentage deviation of the homogenized moduli with respect to their angularly averaged counterpart, considering each orientation and for different values of the normal stiffness parameter, has been computed by the following formula:

$$e_{\%} = \frac{\bar{C}^*_{ijkl} - \left\langle \bar{C}_{ijkl} \right\rangle_{\phi}}{\left\langle \bar{C}_{ijkl} \right\rangle_{\phi}} \times 100 \tag{2.48}$$

with $\left\langle \bar{C}_{ijkl} \right\rangle_{\phi}$ the angularly averaged overall moduli tensor calculated by means of Equation (2.33). The numerical computed deviations for the principal moduli, reported in Figure 3.5, are always very small (in the worst case less than 0.5%), thus further

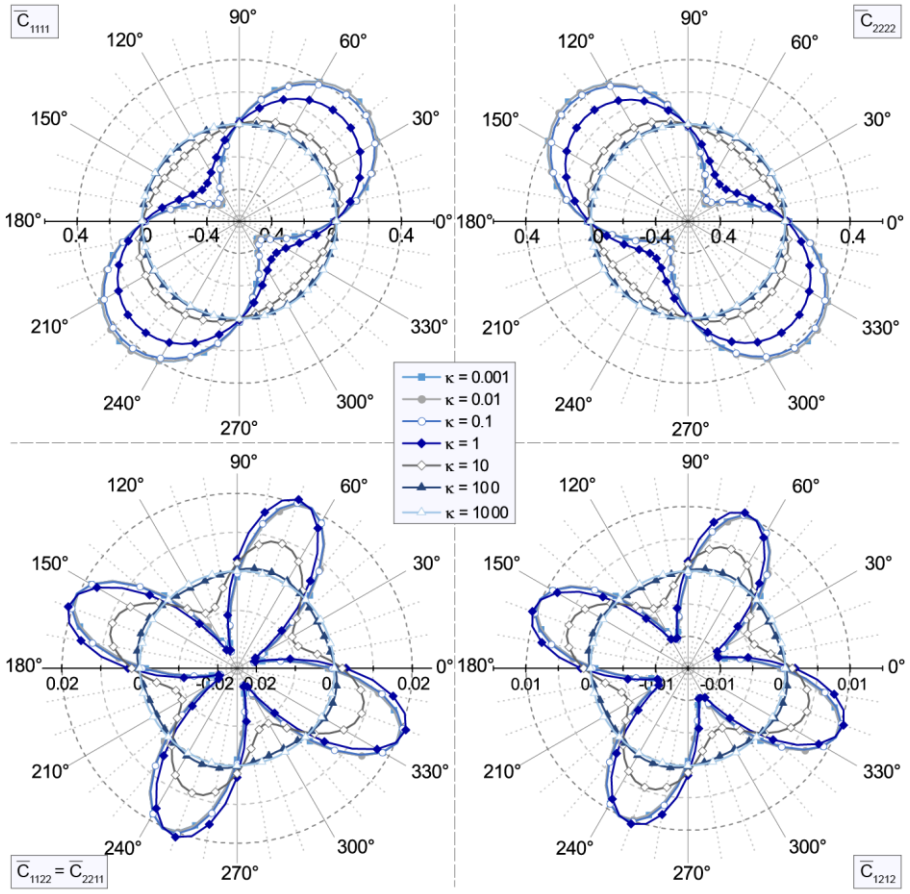

Figure 3.5. Percentage deviation of the homogenized moduli with respect to their angularly averaged counterpart vs mesh orientation for different values of the normal stiffness parameter κ.

confirming the effectiveness of the proposed calibration methodology with respect to the desired isotropy property. As expected, this deviation tends to decrease for increasing values of the stiffness parameter. Interestingly, it can be noted also that the deviation for the macroscopic moduli $\bar{C}_{1122} = \bar{C}_{2211}$ and $\bar{C}_{1212}$ are always

negligible for any value of κ, meaning that, even in the presence of soft embedded elastic interfaces, the shear constitutive response preserves its perfect isotropy. It is worth noting that the present numerical outcomes refer to the (isotropic) Delaunay mesh depicted in Figure 3.1b. However, the adoption of different meshes, without isotropic properties, would probably introduce a more evident dependency of the homogenized moduli on the mesh orientation, but this investigation is outside of the scopes of the present thesis.

3.2 Numerical validation of the diffuse interface model in plain concrete under mode-I loading

The numerical simulations here reported are conducted to validate the diffuse interface model (DIM), described in Chapter 2 and calibrated by using the homogenization technique presented in Section 2.1.3, with reference to plain concrete structures subjected to mode-I loading conditions. In detail, as shown in Section 3.2.1, two additional fracture approaches, named SIM and CDIM, are specifically introduced to highlight the mesh influence on the overall strength properties and related crack paths, as predicted by the proposed DIM methodology. Finally, in Section 3.2.2, two sensitivity analyses with respect to both mesh size and mesh orientation are performed to assess the degree of mesh dependency associated with the proposed model.

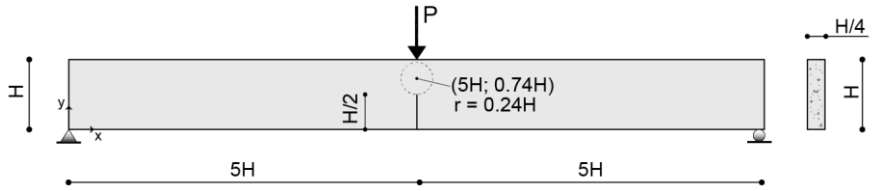

Figure 3.6. Geometric configuration and boundary conditions for the three-point bending test.

Table 3.3. Material parameters for the cohesive interfaces.

K_n^0 [N/mm³]	K_s^0 [N/mm³]	$\sigma_{\max}$ [MPa]	$\tau_{\max}$ [MPa]	G_{Ic} [N/m]	G_{IIc} [N/m]	α
1.185e6	6.306e5	3.33	3.33	124	124	5

3.2.1 Geometric and material properties

The simply supported pre-notched beam subjected to a three-point bending test analyzed in (Petersson, 1981) is considered, whose geometry and boundary conditions, sketched in Figure 3.6, are expressed in terms of the beam height $H = 0.2$ m. A plane stress state is assumed. The bulk material is linearly elastic and isotropic with Young's modulus $E = 30$ GPa and Poisson's ratio $\nu = 0.18$, whereas the inter-element interfaces behave non-linearly according to the mixed-mode traction-separation law (2.36), adopting the following cohesive parameters, listed in Table 3.3: the initial normal and tangential stiffness parameters, K_n^0 and K_s^0, the tensile and shear critical stresses, $\sigma_{\max}$ and $\tau_{\max}$, the mode-I and mode-II fracture energies, G_{Ic} and G_{IIc}, and the non-

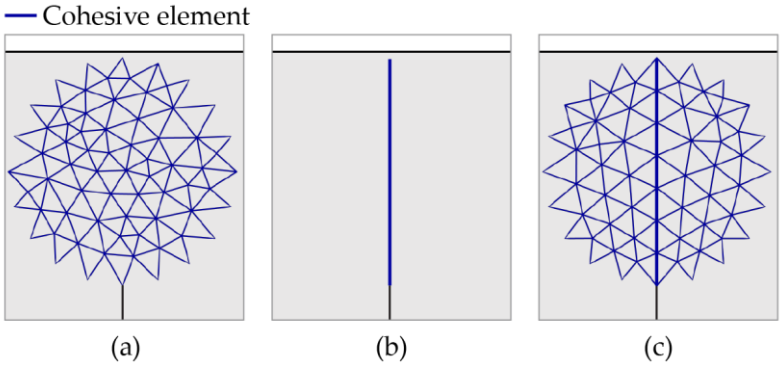

Figure 3.7. Cohesive element distribution in the diffuse interface model (DIM) (a), single interface model (SIM) (b) and controlled diffuse interface model (CDM) (c).

dimensional parameter α appearing in (2.38). In particular, the initial normal and shear stiffness parameters K_n^0 and K_s^0 have been set to assure, for the given mesh size, no reduction of the overall Poisson's ratio, according to the condition (2.47), and a reduction of the overall Young's modulus of 2%, according to the chart reported in Figure 3.3. The corresponding dimensionless stiffness parameters, obtained by graphical linear interpolation, are $\xi = 0.532$ and $\kappa = 104.0$. For this numerical example, the normal and shear critical stresses, $\sigma_{\max}$ and $\tau_{\max}$, are set equal to each other, as well as the mode-I and mode-II fracture energies in order to avoid artificial strengthening and/or toughening effects associated with the activation of local mixed-mode induced by the mesh in the diffuse interface model. In order to reduce the computational cost of the simulations using the proposed diffuse in-

terface model, here simply referred to as DIM simulation, the cohesive elements are inserted only within a predetermined critical region, which is susceptible to be damaged (see Figure 3.7a). Such a region, which is placed ahead of the preexisting notch, has a circular shape with radius $r = 0.24H$, chosen to avoid preferential directions during the generation of the random Delaunay tessellation. A suitable isotropic mesh refinement has been performed within this critical region, by prescribing a maximum element size of 4 mm, which corresponds to an average mesh size of about 2.632 mm.

3.2.2 Assessment of mesh-induced artificial toughening effects

A deeper investigation of the toughening effects induced by the mesh has been performed by comparing the proposed DIM approach, depicted in Figure 3.7a with two comparison models. The first comparison model, termed single interface model (SIM), is characterized by the presence of cohesive elements arranged along the vertical direction, assuring a collinear propagation of the existing notch (see Figure 3.7b). The second comparison model is a controlled diffuse interface model (CDIM). Such a model, used in combination with the SIM configuration, is conceived to gain a deeper insight into the reasons for the mesh-induced artificial toughening effects experienced by the DIM ap-

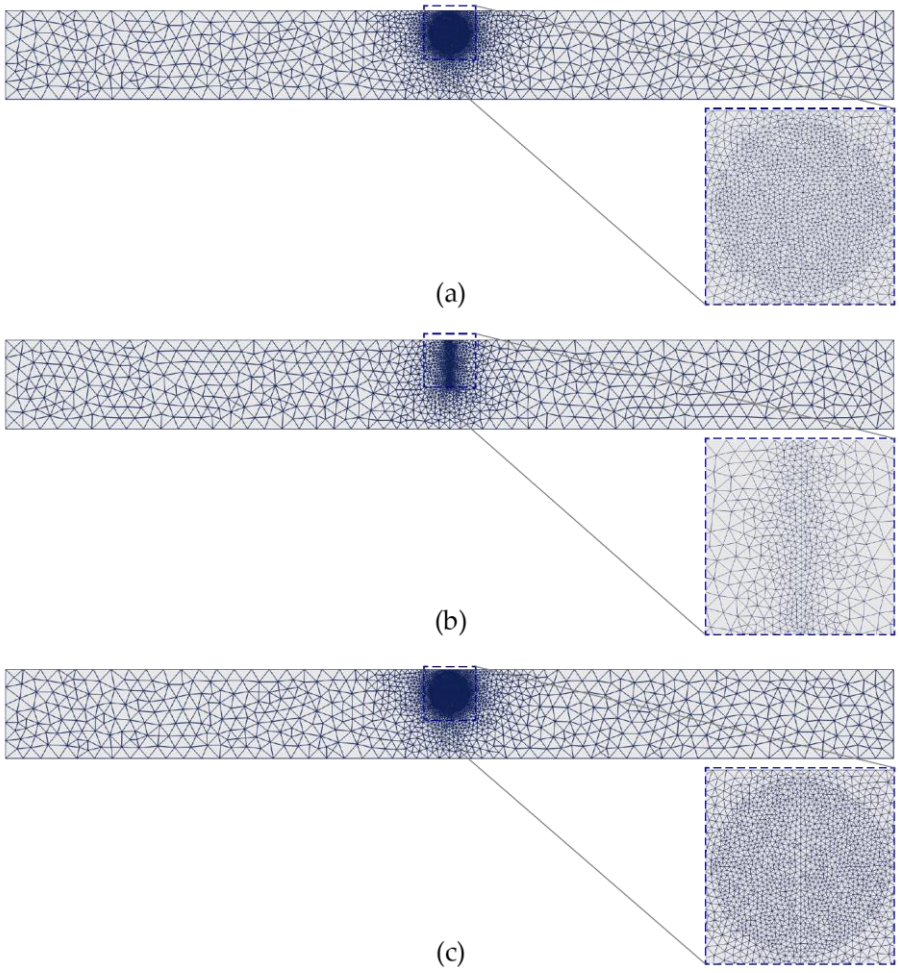

Figure 3.8. Delaunay meshes used for the three-point bending test: (a) DIM; (b) SIM; (c) CDIM.

proach. In the CDIM approach, a given subset of cohesive interface elements is constrained to lie along the symmetry line of the considered circular region (see Figure 3.7c). Such a model is obtained starting from an isotropic Delaunay mesh generated using

an additional control edge aligned with the vertical direction, coinciding with the self-similar growth direction for the preexisting notch.

The unstructured mesh used of both SIM and CDIM are characterized by the same average size of the embedded cohesive elements as in the DIM configuration. The resulting Delaunay meshes for the three above-described models, depicted in Figure 3.8, are composed of three-node plane stress triangular elements for the bulk and four-node zero-thickness for the interface elements placed accordingly with what described in Section 2.2.1. A suitable transition zone has been introduced for all models, to assure a graded mesh coarsening outside the critical region.

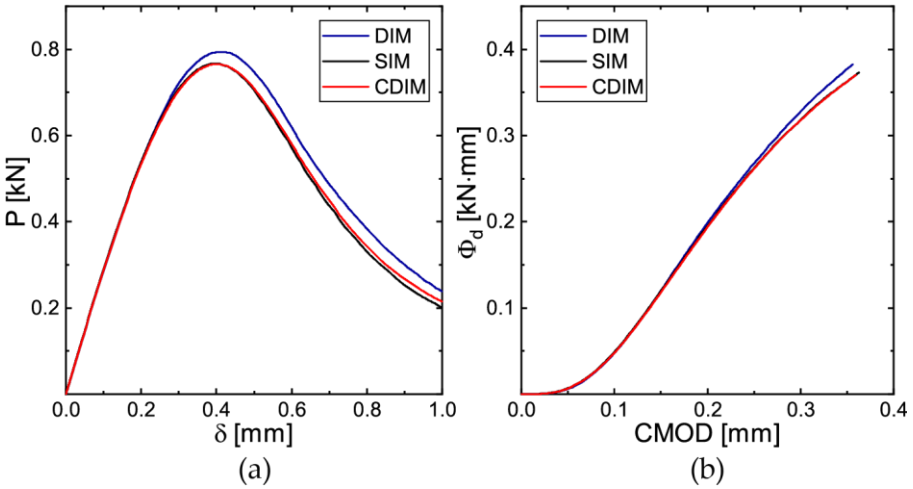

Figure 3.9. Global structural response predicted by DIM, SIM and CDIM approaches: (a) load versus mid-span deflection curve; (b) dissipated fracture energy versus crack mouth opening displacement (CMOD) curve.

Figure 3.9 shows the comparison between these three models, in terms of both load versus mid-span deflection and dissipated fracture energy versus crack mouth opening displacement (CMOD) curves, considering the SIM configuration as the reference. The dissipated fracture energy Φ_d has been computed as the difference between the work of the applied load P and the stored elastic strain energy, both computed at the current displacement δ, according to the following relation:

$$\Phi_d(\delta) = \int_0^{\delta} P(\delta')\mathrm{d}\delta' - \frac{1}{2}P(\delta)\delta \tag{2.49}$$

The first term of the Equation (2.49) being the total energy, graphically represented as the area under the load-displacement

curve $P = P(\delta)$ of Figure 3.9a, and second term being the strain elastic energy stored at the current displacement δ.

The comparison between the three models clearly shows that the DIM predicts a slightly stronger structural response at both peak and post-peak stages with respect to the reference model, due to the artificial toughening effect induced by the mesh (see Figure 3.9a). In particular, the DIM approach leads to a systematic overestimation of the load-carrying capacity predicted by the SIM, at both peak and post-peak regimes, as confirmed by the divergent behaviors of the associated dissipated fracture energy, shown in Figure 3.9b. However, the relative error on the peak load numerically predicted by the diffuse interface model, of about 0.79 kN, with respect to that obtained by the reference one is of only 3.8%, which is acceptable for engineering purposes, thus validating the numerical accuracy of the proposed fracture methodology. Additionally, Figure 3.10 shows that the main crack path predicted by the diffuse interface model, although forced to develop along the inter-element boundaries, is globally in good accordance with that assumed by the reference model, considering self-similar crack propagation. It is worth specifying that, the main crack path is defined as the union of cohesive segments which do not experience any elastic unloading during the entire simulation, i.e. for which $\delta_m = \delta_m^{\max}$ until the final load step, always considering monotonic loading conditions. Moreover, the presence of secondary cracks branching off of the main crack is highlighted.

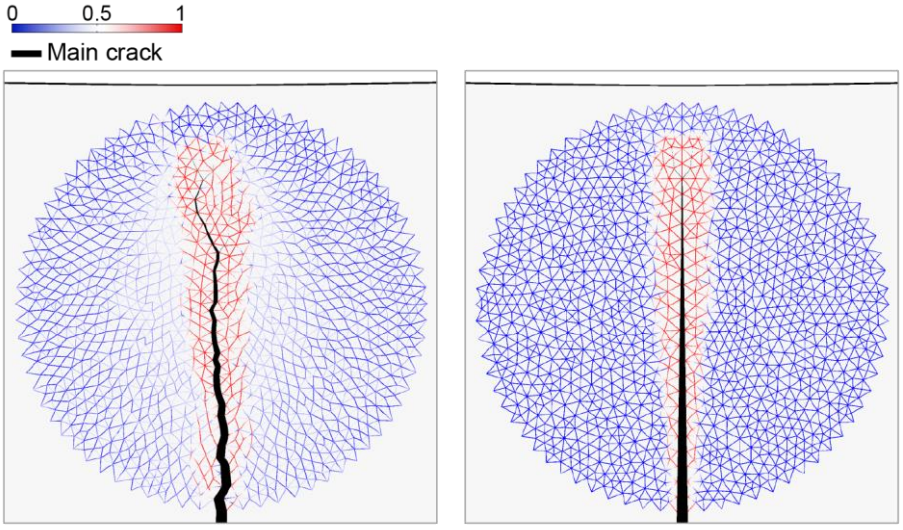

Figure 3.10. Damage variable map and main crack path as predicted by: (a) DIM; (b) CDIM.

To understand if the above-mentioned toughening effect is due to the occurrence of secondary cracking or to the jagged path of the main propagating crack, a comparison with the controlled diffuse interface model (CDIM), is carried out. It is worth noting that, by analyzing again Figure 3.9, the global structural response obtained by means of the CDIM approach is practically coincident with that obtained using the reference SIM configuration, in terms of both load versus mid-span deflection and dissipated fracture energy versus CMOD curves. Furthermore, as can be easily observed in Figure 3.10b, the main crack path predicted by the CDIM configuration is perfectly aligned with that prescribed by the SIM approach owing to the presence of vertical control

edges. However, the appearance of secondary cracks is still experienced, even if localized within a narrower band with respect to the DIM case.

It follows that the nucleation of small secondary cracks in the neighborhood of the main crack tip, as predicted by the present diffuse interface model, has only a negligible influence on the numerically predicted structural behavior, and specifically on the estimated fracture properties. Thus, the toughness increase associated with the DIM configuration is not due to the appearance of such secondary cracks, but rather to the tortuosity of the main crack induced by the randomly placed internal boundaries of the adopted unstructured mesh. More generally, it can be concluded that crack localization phenomena in plain concrete, being accompanied by elastic unloading in the surrounding material, are not sensibly altered by the presence of cohesive elements scattered outside the localization zone. Such a result, rigorously verified for the CDIM configuration (see Figure 3.10b), can be likely extended to the DIM approach, provided that the real crack path is well approximated by the mesh boundaries.

3.2.3 Sensitivity analyses with respect to the mesh size and the mesh orientation

Here, two sensitivity analyses have been performed for the previously mentioned mode-I fracture test in order to investigate the mesh dependency properties of the adopted diffuse interface

model, and the related numerical results are reported in terms of both global structural response and crack path predictions.

The first sensitivity analysis is devoted to the analysis of the mesh size influence on the numerically predicted fracture properties. It can be noted that the mesh size in the direction of crack propagation cannot be freely chosen, but an upper bound for it is needed to ensure that both stress and displacement fields within the fracture process zone (FPZ) are accurately described. However, no theoretical values for the minimum number of elements needed in the FPZ, whose size is denoted as L_{FPZ}, are available in the literature. Only empirical results have been reported about the suggested ratio $N_{\min} = L_{\mathrm{FPZ}}/L_{\mathrm{mesh}}$ to be adopted in the simulations, which typically ranges between 2 and 10 (see, for instance, (Moës and Belytschko, 2002; Turon et al., 2007)). The FPZ size, which is an inherent length scale determined by the material properties, can be expressed in the following form valid for mode-I fracture propagation:

$$L_{\mathrm{FPZ}} = \gamma \frac{G_c E'}{\sigma_c^2} \tag{2.50}$$

where E' is the 2D effective Young modulus, G_c denotes the mode-I fracture energy, σ_c is the normal interfacial strength, and γ is a parameter which depends on the adopted cohesive zone model. If Rice's model is used (Falk et al., 2001), γ is equal to $9\pi/32 \approx 0.88$ and the resulting FPZ size is of about 0.30 m for the considered concrete. Such a value is greater than the considered

beam's height $H = 0.2$ m, so that no additional restrictions are imposed on the admissible mesh size other than the usual ones, classically related to the control of discretization errors in the regions with high stress gradients.

For the beam analyzed in Section 3.2.1, four different meshes have been considered, by progressively dividing in half the maximum element size prescribed within the above-defined circular critical region from 16 to 2 mm. The resulting average element sizes associated with these meshes, indicated respectively as Mesh 1, 2, 3 and 4 in Figure 3.11, are reported in Table 3.4. It is worth noting that Mesh 3 has been already considered for deriving the numerical outcomes presented in Section 3.2.2.

Table 3.4 also shows the cohesive initial stiffness coefficients for the considered meshes, computed according to the calibra-

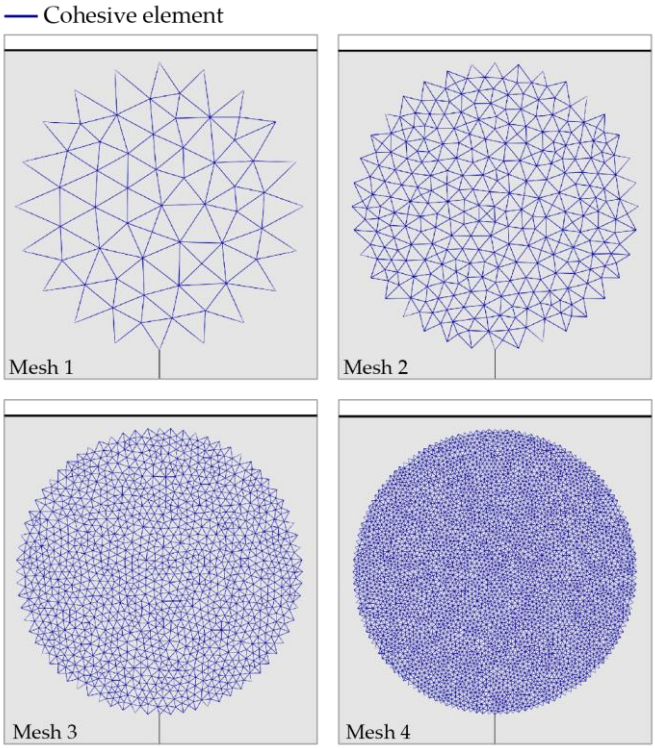

Figure 3.11. Mesh configurations within the critical region for the sensitivity analysis with respect to the mesh size.

Table 3.4. Average element length and elastic stiffness coefficients of the interface elements for different mesh sizes.

Mesh	L_{mesh} [mm]	K_n^0 [N/mm3]	K_s^0 [N/mm3]
1	12.2	2.559e5	1.361e5
2	5.38	5.796e5	3.084e5
3	2.63	1.185e6	6.306e5
4	1.42	2.193e6	1.166e6

tion procedure described in Section 3.1.2. As expected, the increasing of the mesh density leads to greater values of the stiff-

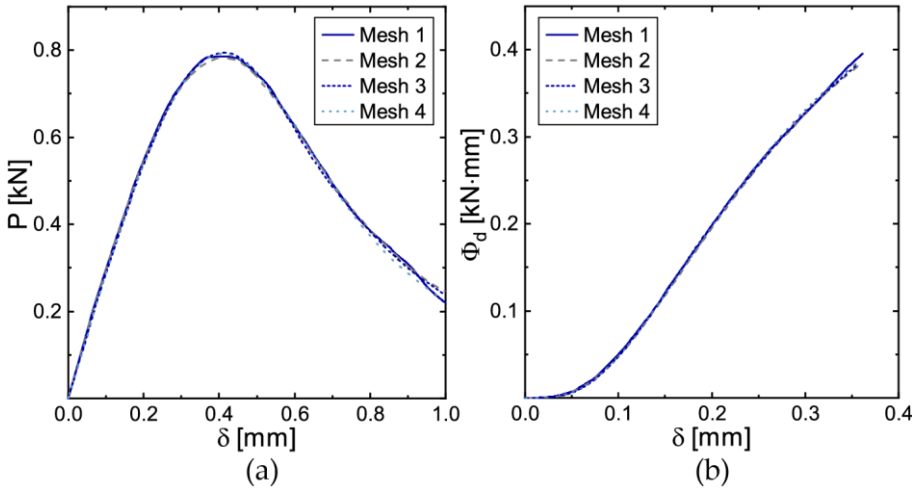

Figure 3.12. Global structural response for different mesh sizes within the cohesive region: (a) load versus mid-span deflection curve; (b) dissipated fracture energy versus crack mouth opening displacement curve.

ness coefficients, in order to assure the same loss of the apparent stiffness.

The results of the sensitivity analysis clearly show that the global response is almost independent of the adopted mesh size, in terms of both load versus mid-span deflection (Figure 3.12a) and dissipated energy versus CMOD (Figure 3.12b) curves. In particular, the maximum value of the percentage relative deviation with respect to the mean peak load $\bar{P}^{\max}$, computed for each mesh as:

$$e_i = \frac{\left| P_i^{\max} - \bar{P}^{\max} \right|}{\bar{P}^{\max}} \times 100 \qquad i = 1,\ldots,4 \tag{2.51}$$

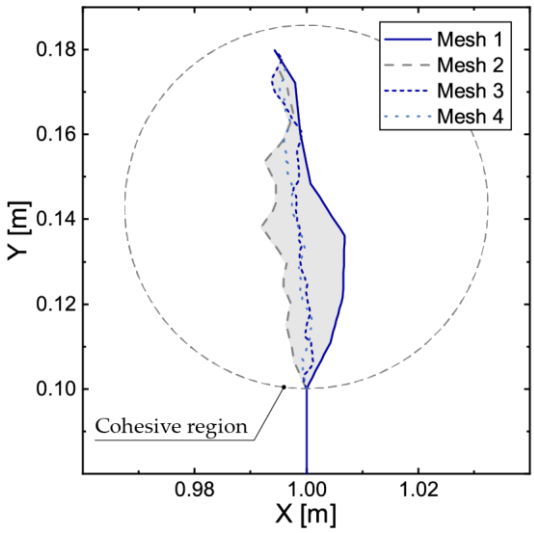

Figure 3.13. Numerically predicted main crack path for different mesh sizes within the cohesive region.

is only of about 0.61%, thus confirming the efficacy of the above calibration in the reduction of mesh dependency issues also in the nonlinear cohesive stage. It is worth noting that the coarsest mesh (i.e. Mesh 1) is associated with some slight oscillations in the numerically predicted structural response, especially in the post-peak region. This fact represents an indication that the adopted spatial discretization is not sufficiently to capture the stress gradients within the ligament ahead the main propagating crack.

Figure 3.13 shows the crack path for the different mesh configuration. A lack of convergence for the predicted crack path is observed, due to the tortuosity induced by the irregularly dis-

Table 3.5. Crack tortuosity ratio for different mesh sizes within the cohesive region.

	Mesh 1	**Mesh 2**	**Mesh 3**	**Mesh 4**
l_c^t [m]	0.0748	0.0818	0.0843	0.0804
l_c^p [m]	0.0721	0.0770	0.0799	0.0771
η	1.037	1.062	1.054	1.042

tributed mesh elements. As the mesh is refined, the crack propagation path becomes more jagged, being forced to pass through a greater number of randomly placed mesh nodes. However, the apparent crack trajectories, obtained by suitably filtering the reported random oscillations, do not deviate too much from the vertical straight line, predicted under self-similar propagation conditions. The artificial crack roughness induced by the mesh can be estimated by the ratio between the true length l_c^t of the irregular crack path and the projected length l_c^p on the vertical direction (i.e. the crack propagation direction in the absence of mesh bias), here referred to as crack tortuosity ratio $\eta > 1$. The values of this ratio obtained for the different meshes, reported in Table 3.5, fall within a restricted range (characterized by a maximum percentage relative deviation of about 1.26%), thus revealing the fractal nature of the approximate discrete crack propagation path. The resulting average crack tortuosity ratio, equal to 1.049, is strictly related to the estimated fractal dimension of crack trajectories for a Delaunay mesh. From a mechanical point

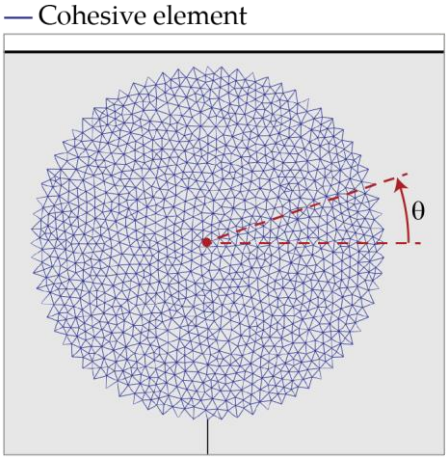

Figure 3.14. Rotating mesh within the critical region for the sensitivity analysis with respect to the mesh orientation.

of view, such a value represents a measure of the artificial toughening effect induced by the mesh. Being close to unity, this value further confirms the reliability of the adopted cohesive approach to predict the overall fracture properties in concrete structures.

The second sensitivity analysis deal with the mesh orientation influence on the predicted fracture properties at fixed mesh size. To this end, several mesh configurations have been considered, by rotating in the counterclockwise sense the discretized circular critical region considered in Section 3.1 around its center through an angle θ ranging between 0° and 360° (see Figure 3.14). A constant angular increment is chosen, such that the position of boundary nodes, which are equally spaced along the circle, is kept unchanged after each rotation. It follows that the parametric analysis does not involve the generation of a new mesh outside the critical region for each considered direction.

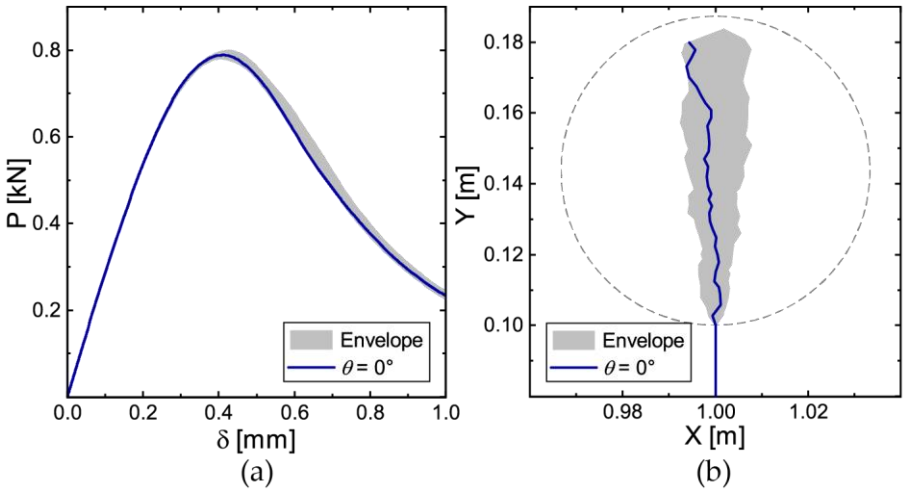

Figure 3.15. Enveloped structural responses for different mesh orientations within the cohesive region: (a) load versus mid-span deflection curves; (b) numerically predicted main crack paths.

In Figure 3.15, the numerical results of the sensitivity analysis, are reported. By analyzing Figure 3.15a, showing the envelope of the load versus mid-span deflection curves, it can be noted that the predicted structural response is almost insensitive to the mesh orientation. In particular, the percentage relative deviations of the peak load, computed according to Equation (2.51) for different mesh orientations, is smaller than 2% (in the worst case), as shown in Table 3.6. A greater dependence on the mesh orientation is experienced by the predicted crack path, as shown in Figure 3.15b. All the numerical crack trajectories are found to lie within a sharp wedge with opening angle of about 14°, symmetrically placed with respect to the self-similar crack propagation (i.e. vertical) direction. The influence of the mesh orientation

Table 3.6. Peak load relative deviation for different mesh orientations within the cohesive region.

θ [°]	0	30	60	90	120	150	180	210	240	270	300	330
$P^{\max}$ [kN]	0.789	0.790	0.788	0.788	0.780	0.794	0.801	0.793	0.790	0.780	0.789	0.785
e [%]	0.01	0.09	0.13	0.14	1.11	0.61	1.54	0.55	0.17	1.09	0.01	0.48

Table 3.7. Crack tortuosity ratio for different mesh orientations within the cohesive region.

θ [°]	0	30	60	90	120	150	180	210	240	270	300	330
l_c^t [m]	0.0843	0.0884	0.0852	0.0850	0.0862	0.0843	0.0832	0.0821	0.0843	0.0824	0.0844	0.0841
l_c^p [m]	0.0799	0.0835	0.0816	0.0803	0.0825	0.0803	0.0794	0.0772	0.0802	0.0794	0.0807	0.0798
η	1.0542	1.0581	1.0436	1.585	1.0454	1.0502	1.0489	1.0632	1.0505	1.0377	1.0463	1.0539

on the artificial toughening effect is further assessed by computing the crack tortuosity ratio for the different rotation angles, as reported in Table 3.7. Also in this case, all the values fall within a little range, characterized by a maximum percentage relative deviation of about 1.25% with respect the orientation averaged value, found equal to 1.051. It follows that the use of Delaunay triangulations within a cohesive finite element approach leads to achieve almost isotropic fracture behaviors, assuring the absence of preferential crack path directions induced by the mesh.

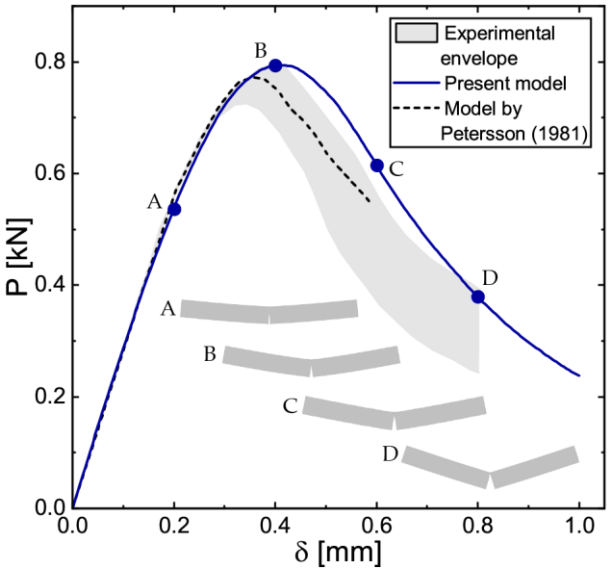

Figure 3.16. Load versus mid-span deflection curve predicted by the proposed model and comparison with experimental and numerical results obtained by (Petersson, 1981).

3.2.4 Comparison with existing experimental and numerical results

In order to assess the effectiveness of the adopted diffuse interface model (DIM) in predicting the failure response in a reliable manner, the numerical results reported in Section 3.2.2 have been compared with both experimental and numerical results obtained in (Petersson, 1981), as shown in Figure 3.16. The numerical model adopted in (Petersson, 1981) is based on a fictitious crack concept incorporated in a finite element framework. There, an extrinsic bilinear cohesive law is employed to describe

the softening behavior, in combination with an additional stress-based crack insertion criterion.

The present linear-exponential intrinsic cohesive model, used within the proposed DIM approach, predicts a slightly stronger structural response with respect to the above-mentioned extrinsic bilinear cohesive model, here taken as the reference (with a percentage relative error on the peak load of only about 2.9%), due to the previously discussed mesh-induced artificial toughening effect. Moreover, the present model is judged as able to predict a global structural response which is also in good agreement with the experimental outcomes, the numerically predicted load versus mid-span deflection curve being very close to the upper limit curve of the experimental envelope.

3.3 Numerical validation of the diffuse interface model in plain concrete under mixed-mode loading

The proposed diffuse interface model is here employed to perform further numerical analysis by considering the more general case of mixed-mode fracture conditions, usually associated with crack paths unknown a priori. The famous mixed-mode test introduced in (Gálvez et al., 2002a) has been considered, involving a small-sized pre-notched concrete beam subjected to unsymmetrical three-point bending. In particular, in Section 3.3.2 has been performed an investigation of the influence of mode-II cohesive parameters, i.e. the tangential critical stress $\tau_{\max}$ and mode-II fracture energy G_{IIc}, on the global structural response,

with special attention to the numerically predicted damage pattern. Additionally, a suitable comparison with the experimental outcomes has been reported Section 3.3.3, thus confirming the reliability of the proposed model for the numerical simulation of mixed-mode crack propagation in concrete and other quasi-brittle materials.

3.3.1 Geometric and material properties

The geometry and boundary conditions of the tested pre-notched concrete specimen, expressed in terms of its height $D = 75$ mm, are sketched in Figure 3.17a. The bulk material is assumed to be linearly elastic, with Young's modulus $E = 38$ GPa and Poisson's ratio $\nu = 0.2$. The cohesive elements, according with the insertion procedure described in Section 2.2.1, have been randomly inserted only within a critical zone susceptible to be damaged, in order to reduce the computational effort of the simulations performed using the proposed DIM approach. In this rectangular zone, a mesh refinement has been performed, by imposing a maximum mesh size of 1 mm, which corresponds to an average length of the interface elements of about 0.744 mm. The resulting enriched Delaunay mesh, reported in Figure 3.17b is composed of three-node triangular elements and four-node zero-thickness interface elements. The simulations by means of the proposed (DIM) and reference (SIM) models have been performed under plane stress and displacement-controlled

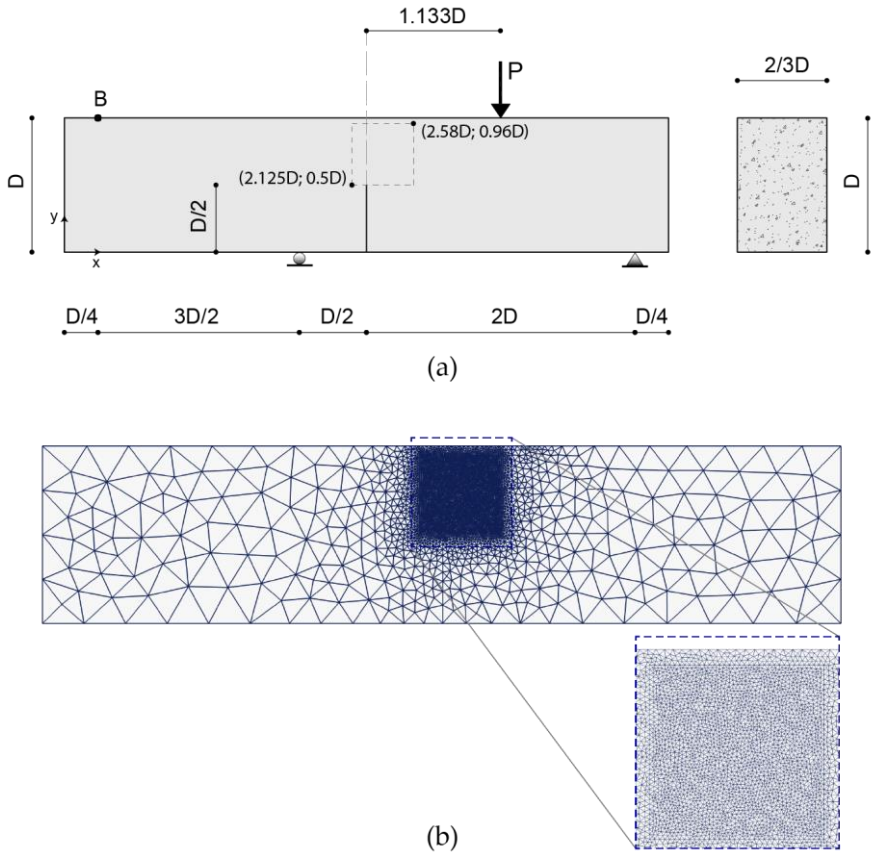

Figure 3.17. Tested small-sized pre-notched concrete beam: (a) geometric configuration and boundary conditions of the tested concrete beam and (b) computational mesh with homogeneous refinement for mixed-mode crack propagation.

quasi-static loading conditions, adopting a displacement increment of 5e−3 mm.

Table 3.8. Material parameters for the cohesive interfaces.

K_n^0 [N/mm³]	K_s^0 [N/mm³]	$\sigma_{\max}$ [MPa]	$\tau_{\max}$ [MPa]	G_{Ic} [N/m]	G_{IIc} [N/m]	α
5.492e6	2.746e6	3.0	3.0	69	69	5

The cohesive parameters required by the adopted mixed-mode traction-separation law, presented in Section 2.2.1, are listed in Table 3.8, where the mode-II inelastic parameters are intended as reference values for the sensitivity analysis reported in next Section 3.3.2. Moreover, the parameters K_n^0 and K_s^0 have been chosen to assure, for the adopted mesh size, no reduction of the overall Poisson's ratio, and a reduction of the overall Young's modulus of 2%. The related dimensionless stiffness parameters are $\xi = 0.5$ and $\kappa = 107.6$, providing the following initial cohesive stiffness values: $K_n^0 = 5.492\text{e}6$ and $K_s^0 = 2.746\text{e}6$.

3.3.2 Sensitivity analyses with respect to the mode-II inelastic cohesive parameters

Several investigations on the influence of the shear fracture parameters on mixed-mode fracture in concrete have demonstrated that when a crack propagates in stable manner under mixed loading, a local mode I crack propagation is usually predominant over mode II (see, for instance, (Gálvez et al., 2002a) and references therein). As a matter of fact, large variations in the mode-II inelastic parameters, i.e. shear strength and fracture energy in mode II, are known to produce very little effects on the

numerical predictions obtained by means of common cohesive approaches.

Nevertheless, the sensitivity of cohesive shear parameters on mixed-mode fracture using a cohesive finite element approach has not been sufficiently investigated. Indeed, the artificial tortuosity of the predicted crack paths caused by the mesh induces unavoidable nonphysical local mixed-mode crack propagation conditions with non-negligible mode-II dissipated energy.

In this Section, two sensitivity analyses have been performed by independently varying the mode-II inelastic parameters required by the traction-separation law adopted in the proposed concrete fracture model, in order to quantify the above-mentioned artificial effects associated with mode-II crack propagation. The first sensitivity analysis has been conducted by assessing the influence of the mode-II fracture energy on the predicted global structural response, by varying it in a wide range. In particular, the following values have been considered, $G_{IIc} = 0.2$, 0.5, 1, 2, 5, 10, 20 and 50 times larger than G_{Ic}, keeping fixed the other material parameters reported in Table 3.8.

Figure 3.18 shows the associated numerically predicted structural response in terms of applied load versus displacement at point B. A slightly increase of the overall strength as the mode-II fracture energy increases is predicted at both peak load and post-peak stages by the proposed model (see Figure 3.18a). This trend is more visible for mode-II toughness values up to $G_{IIc} = 5\, G_{Ic}$. As a matter of fact, starting from the value

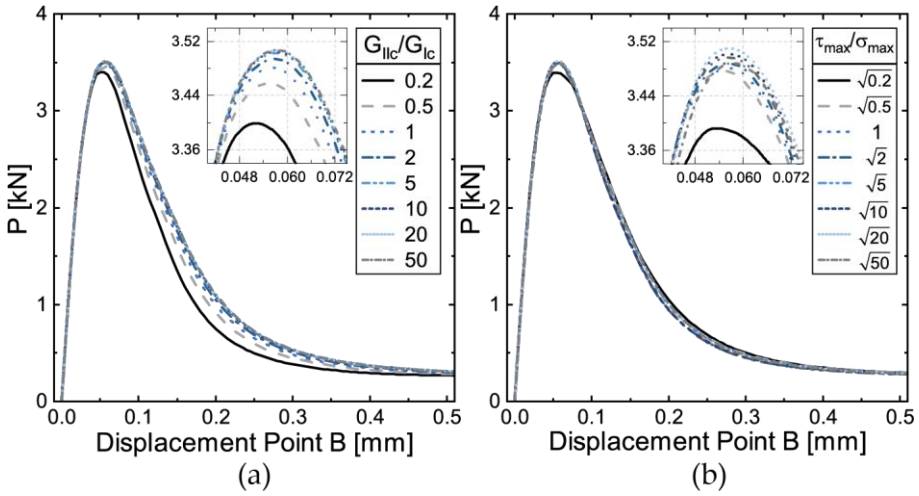

Figure 3.18. Global structural response by varying mode II fracture energy (a) and critical tangential strength (b).

$G_{IIc} = 10G_{Ic}$, the global structural response is almost insensitive to the magnitude of the mode-II fracture energy. By virtue of this independence property, being also consistent with the value suggested in (Gálvez et al., 2002a), such a value has been considered for the numerical simulations reported in Section 3.3.3 and Section 4.

The second sensitivity analysis has been concerned with the influence of the tangential critical stress, while keeping fixed the mode-II fracture energy $G_{IIc} = G_{Ic}$. In particular, the following values have been considered, $\tau_{\max} = \sqrt{0.2}$, $\sqrt{0.5}$, 1, $\sqrt{2}$, $\sqrt{5}$, $\sqrt{10}$, $\sqrt{20}$ and $\sqrt{50}$ times larger than $\sigma_{\max}$. It is worth noting that a more limited range of relative variations is used, being scaled by fixing for the ratio $\tau_{\max}/\sigma_{\max}$ the square roots of the values considered for G_{IIc}/G_{Ic} in the first sensitivity analysis.

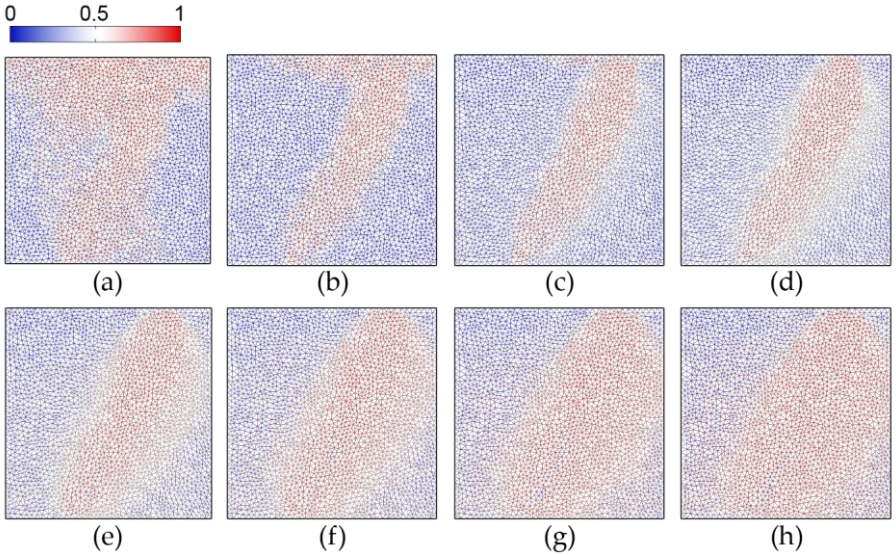

Figure 3.19. Damage variable maps at the point B vertical displacement of 0.2 mm for different values of the ratio τ_{max}/σ_{max} : (a) $\sqrt{0.2}$; (b) $\sqrt{0.5}$; (c) σ_{max} ; (d) $\sqrt{2}$; (e) $\sqrt{5}$; (f) $\sqrt{10}$; (g) $\sqrt{20}$; (h) $\sqrt{50}$ ..

Figure 3.18b shows the related numerical results, in term of load versus point B displacement curves. The predicted global structural response seems to be almost independent of the tangential strength of the cohesive interfaces, except for the value $\tau_{max} = \sqrt{0.2}\sigma_{max}$, associated with a peak load lower than the other values.

By analyzing the numerically predicted damage patterns, a stronger restriction for the admissible values of τ_{max} has been found. The damage variable maps corresponding to the point B vertical displacement value of 0.2 mm for the different tangential critical strengths considered in the present sensitivity analysis

are reported in Figure 3.19. The results confirm that for values of $\tau_{\max}/\sigma_{\max}$ up to 1 (see Figure 3.19a to Figure 3.19c), an artificial anticipation of local concrete crushing occurs at the upper zone, dominated by a compressive stress state, strictly due to the fact that the adopted cohesive interface model does not incorporate any friction model. On the other hand, for $\tau_{\max}/\sigma_{\max}$ greater than or equal to $\sqrt{5}$ (see Figure 3.19e to Figure 3.19h), a pathological bandwidth enlargement of the region characterized by damage localization is experienced. Indeed, if a too much high value is chosen for $\tau_{\max}$, only the cohesive interfaces almost orthogonal to the tensile principal stress direction are allowed to be damaged, as crack initiation is forced to occur in almost pure mode-I. Such a phenomenon has the negative effect of spreading the damage out, ultimately leading to erroneously predicted damage patterns. The most reliable results seem to be found in the case $\tau_{\max}/\sigma_{\max} = \sqrt{2} \approx 1.4$. This value is consistent with the assumption that $\tau_{\max}$ possesses a more precise physical meaning than $G_{\mathrm{II}c}$, representing the cohesion of the material.

3.3.3 Comparison with the experimental results

An additional numerical simulation has been performed by using the following values for the mode-II parameters, i.e. $\tau_{\max} = 1.4\sigma_{\max}$ and $G_{\mathrm{II}c} = 10G_{\mathrm{I}c}$, as suggested in Section 3.3.2, and the related numerical results have been compared with the experimental results obtained in (Gálvez et al., 1998), as shown in Figure 3.20.

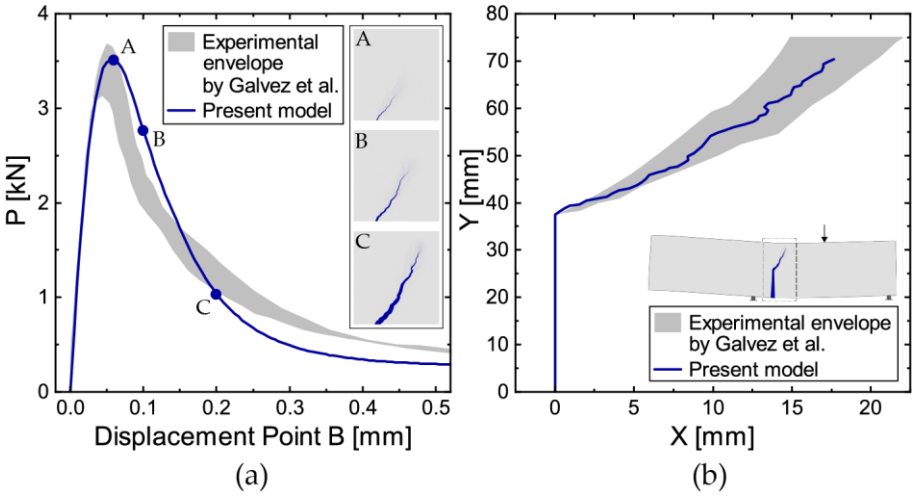

Figure 3.20. Comparisons between numerical and experimental results for the unsymmetrical three-point bending test: (a) load versus point B displacement curve; (b) crack path.

In particular, the predicted loading curve, reported in Figure 3.20a, is in good agreement with the ones obtained by the experimental tests, especially at the peak load. However, small discrepancies are observed in the softening branch, for which the diffuse interface model (DIM) predict an initial slightly stronger structural response probably due to the above-mentioned toughening effect induced by the mesh. In addition, the numerically predicted residual strength is underestimated with respect to the experimental tests, because friction, which has a role in providing the ultimate load-carrying capacity, has not been incorporated into the adopted cohesive traction-separation law. Nevertheless, the proposed fracture model is able to capture a realistic

macro-crack evolution, as can be observed in the deformed crack configurations at points A, B and C reported in Figure 3.20a.

Finally, Figure 3.20b shows the comparison, in terms of crack path, between the present numerical simulation and the experimental tests. It is clearly visible that the crack trajectory predicted by the DIM approach completely lies within the envelope of experimentally measured cracks.

4

Failure analysis of strengthened reinforced concrete (RC) structures

This chapter is devoted to the application of the proposed numerical fracture model, presented in Section 2.2, to the failure analysis of internally and/or externally reinforced concrete structures. In particular, in Section 4.1 the proposed numerical framework, including the DIM and ETM, described respectively in Sections 2.2.1 and 2.2.2, is successfully used to predict the nonlinear response of a reinforced concrete (RC) beam subjected to multiple crack initiation and propagation. Subsequently, the proposed

failure model, integrated with the Single Interface Model (SIM), described in Section 2.2.3, is employed to predict the load-carrying capacity and the related damage patterns of a real-scale RC beams retrofitted with FRP system, involving concrete cover separation failure. Finally, several applications involving plain and steel bar-reinforced nano-enhanced UHPFRC beam are reported in Section 4.3, further demonstrating the effectiveness and versatility of the proposed failure model to investigate the complex fracture process in the different types of concrete structures.

4.1 Numerical application to reinforced concrete elements

The proposed integrated fracture model has been here used to failure analysis of a reinforced concrete beam with reference to the four-point bending test analyzed in (Gao et al., 2004). A useful comparison with the existing experimental results, reported in Section 4.1.2, is carried out in terms of loading curve and crack pattern, showing a good numerical prediction of the global structural response. In order to validate the capability of the adopted bond-slip approach of capturing the tension stiffening effect, a detailed stress analysis of the tensile reinforcement bars has been also reported. Finally, Section 4.1.3 presents a sensitivity analysis with respect to the mesh size, aimed at assessing the reliability of the DIM approach, in terms of the desired mesh-independence property.

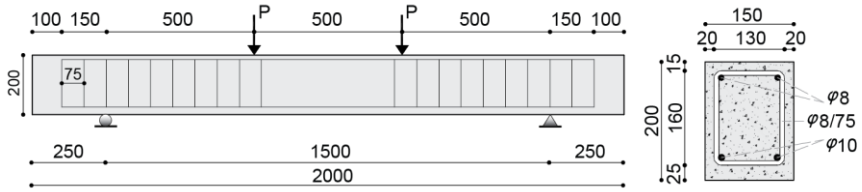

Figure 4.1. Geometric configuration and boundary conditions of the tested RC beam (all dimensions are expressed in mm).

Table 4.1. Main elastic and strength properties of materials.

Material	Young's modulus (GPa)	Poisson's ratio	Yield strength (MPa)	Tensile strength (MPa)	Compressive strength (MPa)
Concrete	31.0	0.20	-	2.1	35.7
Steel	200.0	0.30	460.0	-	-

4.1.1 Geometric and material properties

The geometric configuration as well as loading and boundary conditions of the RC element under consideration are depicted in Figure 4.1, whilst in Table 4.1 are reported the mechanical properties of concrete and steel reinforcing bars. In order to reduce the simulation efforts, only a half beam has been modeled, owing to the symmetry of both geometry and boundary conditions, thus imposing a suitable symmetry condition as reported in Figure 4.2. The computational domain has been meshed by using a Delaunay triangulation, made of three-node elements with prescribed maximum size of 10 mm (and average size of about 7.26 mm). As reported in (Gao et al., 2004) no con-

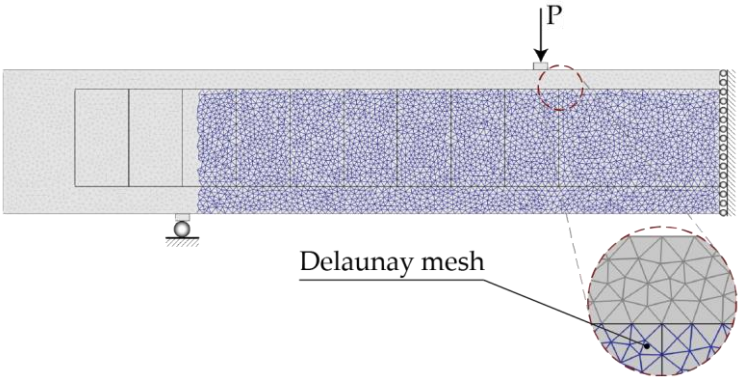

Figure 4.2. Mesh configuration with identification of cohesive interface elements (highlight in blue) for the tested RC beams.

Table 4.2. Material parameters for the cohesive interfaces.

K_n^0 [N/mm³]	K_s^0 [N/mm³]	σ_{max} [MPa]	τ_{max} [MPa]	G_{Ic} [N/m]	G_{IIc} [N/m]	α
4.574e5	2.287e5	2.1	2.94	125	1250	5

crete crushing is observed in the experimental tests, thus the cohesive interfaces have been inserted only in the region dominated by combined tension-shear stresses as shown in Figure 4.2. Furthermore, the cohesive interfaces are not inserted along the existing truss elements, to avoid the occurrence of preferential crack propagation along straight lines, especially at the stirrup level, due to the lack of accuracy by the present 2D model in capturing the actual 3D interactions at the steel/concrete interfaces.

In Table 4.2 are listed the cohesive parameters, useful to calibrate the interface elements. Such parameters are chosen to match the material properties of the considered concrete, except

for the tangential critical stress τ_{max} and the mode-II fracture energy G_{IIc}, not given in (Gao et al., 2004). As already discussed in Section 3.3, these parameters only slightly affect mixed-mode crack growth, whenever they fit into a large range with physical meaning. Coherently with what suggested in Section 3.3.2, the parameter τ_{max} has been set equal to about 1.4 times larger than σ_{max}, this value being consistent with typical cohesion values for concrete material, whilst G_{IIc} has been chosen ten times bigger than G_{Ic}.

All the subsequent simulations have been conducted under plane stress conditions and adopting a displacement control scheme with constant increments of 2e-2 mm for the mixed-span deflection.

4.1.2 Numerical results and comparison with experimental data

The global structural response, in terms of loading curve and failure pattern, of the beam under consideration predicted by the proposed fracture model, is reported in Figure 4.3 and Figure 4.4, respectively.

The loading curve shows a typical trilinear behavior (see Figure 4.3), in which two changes of slope are clearly detected, coinciding with the nucleation of main cracks in concrete (point A) and the yielding of steel reinforcing bars (point C). It is worth noting that after all the primary cracks have been developed by coalescence of several micro-cracks, a crack stabilization phase

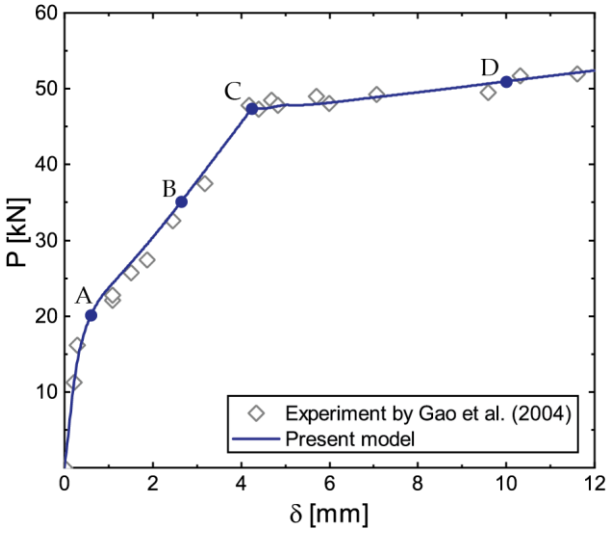

Figure 4.3. Global structural response in terms of the load versus mid-span deflection curve.

begins, coinciding with the linear branch (i.e. at constant reduced stiffness) up to point C. The comparison with the results obtained in (Gao et al., 2004) are also reported in Figure 4.3, showing that the present numerical predictions are in a perfect agreement with the experimental outcomes.

The deformed configurations with representation of the main crack (in black) and damage variable map for the simulation steps A, B, C, and D highlighted in the global structural response of Figure 4.3, are reported in Figure 4.4. It can be easily observed that the main cracks gradually nucleate at the tension face of the beam within the constant bending moment span and, subsequently, they spread to the shear span (see Figure 4.4a). As the controlled mid-span deflection increases, the main cracks

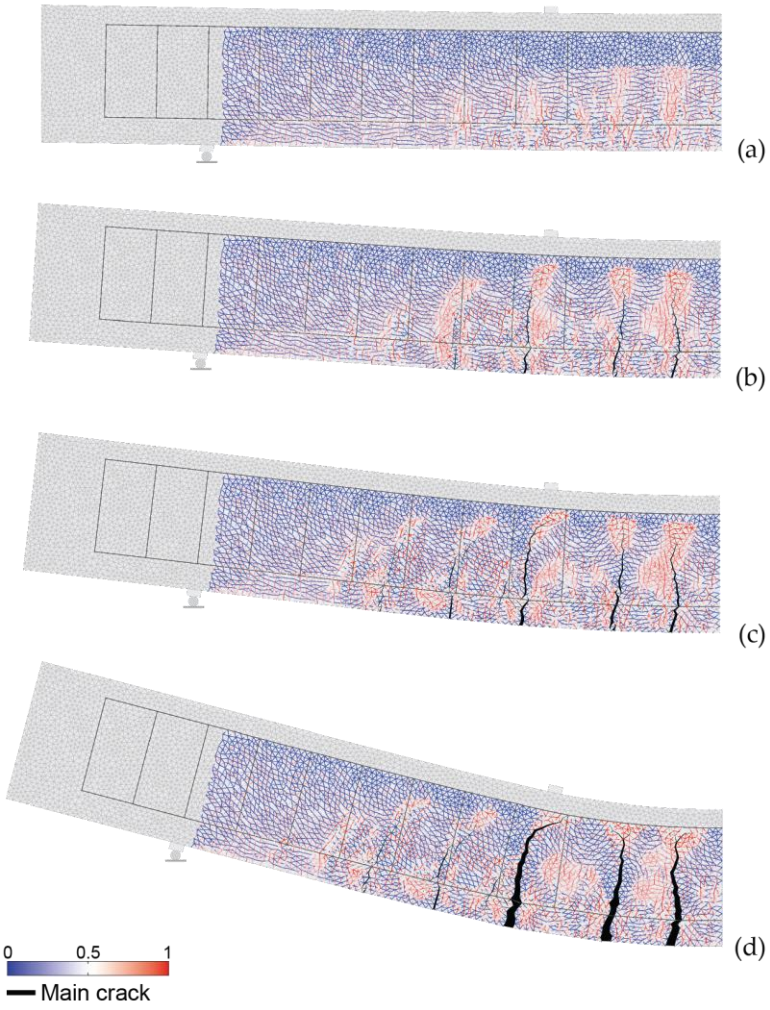

Figure 4.4. Deformed configuration (magnified by a scale factor of 15), damage variable map and main crack pattern for the RC beam at the different simulation steps highlighted in Figure 4.3: a) point A; b) point B; c) point C; d) point D.

gradually propagate in a stable manner (see Figure 4.4b, corresponding to point B of Figure 4.3), associated with the elastic unloading (i.e. reclosing) of adjacent secondary cracks. The distance

between adjacent cracks (also referred to as crack spacing) is almost uniform within the constant bending moment span, showing a clear tendency to increase towards the supports. The deformed shapes of the control beam at first yield point and subsequent hardening of tensile bars, are depicted in Figure 4.4c and Figure 4.4d, respectively.

It is worth noting the importance of the embedded truss model (ETM), described in Section 2.2.2, in capturing the correct tensile cracking behavior. Indeed, the adopted formulation, based on a bond-slip relation between steel and concrete, is able to allow the main cracks to pass across the tensile steel reinforcements, thus avoiding artificial propagation constraints or, even worse, crack arrests. Similarly to the existing smeared crack approaches, the proposed model is able to capture the diffuse damage, as highlighted in the damage maps of the cohesive interface elements in Figure 4.4.

Additionally, the distribution of the longitudinal stress along the tensile steel bars at the simulation steps reported in Figure 4.3, together with the corresponding final crack pattern, are depicted in Figure 4.5. The reported behavior appears to be oscillating, with local peaks in correspondence with the main cracks. A gradual decrease of this stress is reported with increasing distances from the nearest cracks, associated with the development of bond forces at the steel/concrete interface, so that local minima are attained mid-way between adjacent cracks. These results confirm the ability of the adopted bond-slip model is capturing the

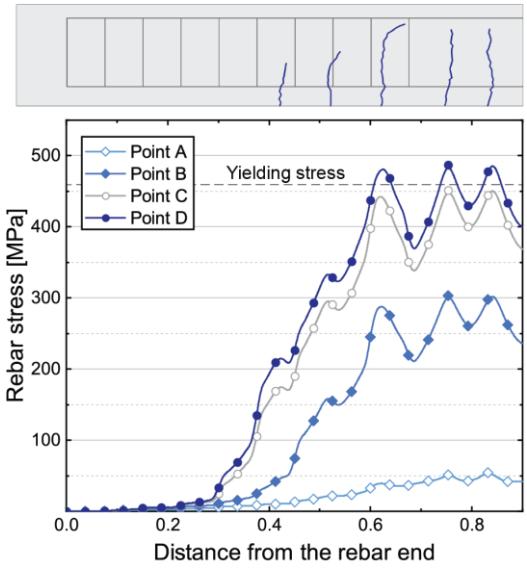

Figure 4.5. Longitudinal stress along the tensile reinforcement bars at the different simulation steps highlighted in Figure 4.3.

well-known tension stiffening effects. Coherently with the predictions of most common tension stiffening models, the first steel yielding is reached in the neighborhood of the primary cracks within the constant moment span (point C).

4.1.3 Sensitivity analysis with respect to the mesh size

Here, a sensitivity analysis has been performed by varying the mesh size, in order to assess the reliability of the previously obtained numerical results. Three distinct mesh configurations have been considered, depicted in Figure 4.6, Mesh 2 being already used to perform the failure analysis in Section 4.1.2. The related average element length and elastic stiffness coefficients

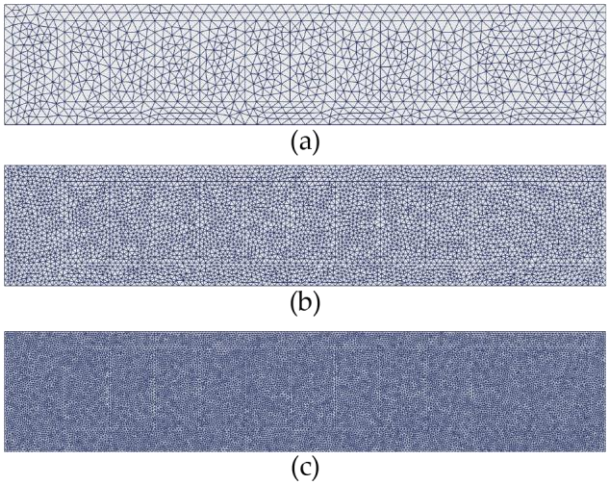

Figure 4.6. Mesh configurations adopted for the sensitivity analysis: (a) Mesh 1; (b) Mesh 2; (c) Mesh 3.

Table 4.3. Average element length and elastic stiffness coefficients of the interface elements for different mesh sizes.

Mesh	L_{mesh} [mm]	K_n^0 [N/mm³]	K_s^0 [N/mm³]
1	14.9	2.237e5	1.118e5
2	7.26	4.574e5	2.287e5
3	3.67	9.041e5	4.520e5

of the embedded interface elements are reported in Table 4.3. The global response of the RC beam, in terms of the load versus mid-span deflection curve, predicted by the proposed model, is almost independent of the adopted mesh size, as shown in Figure 4.7a. As a measure of the mesh dependency, the percentage error on the first yielding loading level is considered, computed with respect to the finest mesh (Mesh 3), taken as the reference one. The maximum value for this error, corresponding to the coarsest

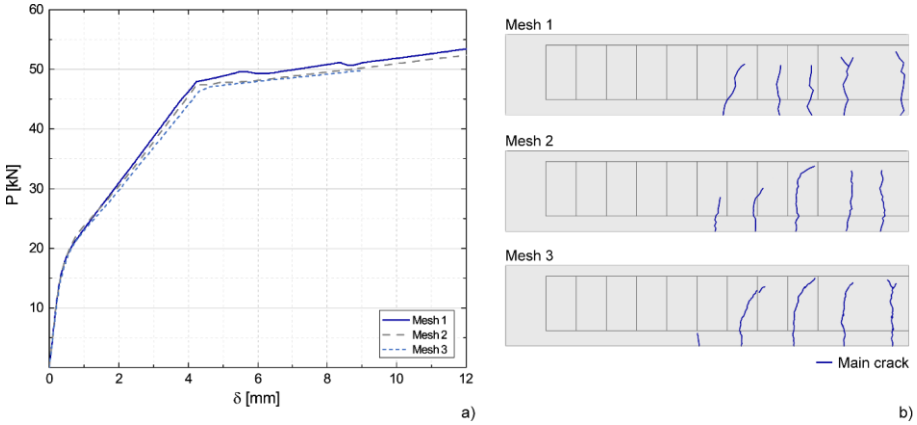

Figure 4.7. Global structural response of the RC beam for the three considered meshes: (a) load versus mid-span deflection curve; (b) Main crack pattern at the displacement $\delta = 9$ mm .

mesh (Mesh 1), is of about 2%, thus confirming the desired mesh-independence property of the proposed numerical fracture model. Incidentally, it is useful to note that some convergence troubles have been experienced by the numerical simulation performed with the finest mesh (Mesh 3), prematurely stopped at a mid-span deflection of about 9 mm. This is due to the occurrence of local snap-back instabilities, whose increased probability is related to the higher number of potential failure locations with respect to the other meshes.

However, a lack of convergence for the crack pattern is observed in Figure 4.7b being an unavoidable feature of the cohesive finite element method. Indeed, the exact location of the main cracks is strongly affected by the randomness of the adopted computational meshes. Interestingly, we note that for Mesh 3, due the presence of a higher number of potential cracks, directly

associated with the greater mesh density, a more uniform spacing between adjacent cracks within the constant moment span is predicted, whose averaged value is found to be of about 125 mm.

4.2 Numerical application to FRP-plated RC elements

The proposed integrated numerical model is here employed to perform numerical failure analysis of FRP-plated reinforced concrete (RC) elements. In particular, the simulation of the well-kwon concrete cover separation is reported in Section 4.2.2, with reference to the four-point bending test reported in (Gao et al., 2004). Such an application has been chosen to assess the predictive capabilities of our numerical approach in terms of both peak and residual load-carrying capacities of retrofitted RC structures, usually involving combined failure modes.

4.2.1 Geometric and material properties

The geometric configuration as well as the loading and boundary conditions of the tested FRP-plated RC beam are depicted in Figure 4.8, whereas in Table 4.4 are listed the principal mechanical properties of the involved material constituents, i.e. concrete, steel, adhesive and FRP plate. The given strengthening system adopts a carbon FRP (CFRP) strip made of four composite layers with overall thickness equal to 0.44 mm, externally bonded to the soffit surface of the beam by using a 2 mm thick epoxy adhesive.

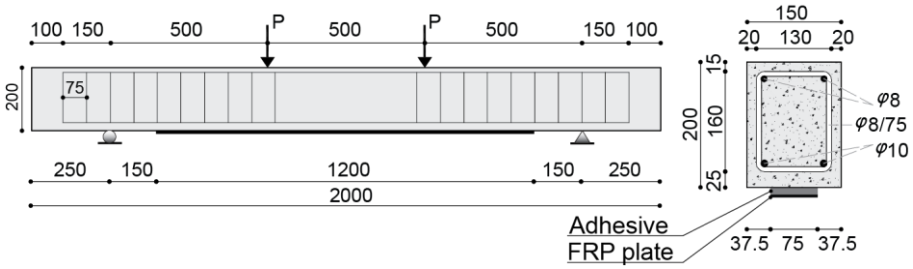

Figure 4.8. Geometric configuration, loading and boundary conditions of the tested FRP-plated RC beam (all dimensions are expressed in mm).

Table 4.4. Main elastic and strength properties of materials.

Material	Young's modulus (GPa)	Poisson's ratio	Yield strength (MPa)	Compressive strength (MPa)	Tensile strength (MPa)
Concrete	31.0	0.20	-	35.7	2.1
Steel	200.0	0.30	460	-	-
CFRP plate	235.0	0.35	-	-	4200
Epoxy resin	1.0	0.35	-	-	-

Due to the symmetric geometric and boundary conditions, and in order to reduce the associated computational effort, only a half beam has been modeled for the subsequent numerical computations. To this end, appropriate boundary conditions have been prescribed to the symmetry line of the specimen. The considered beam has been discretized by using a Delaunay mesh made of three-node triangular elements with prescribed maximum size of 10 mm for the concrete solid phase (resulting in an average size of 7.31 mm), enriched by embedded four-node cohesive interface elements coinciding with the bulk inter-element

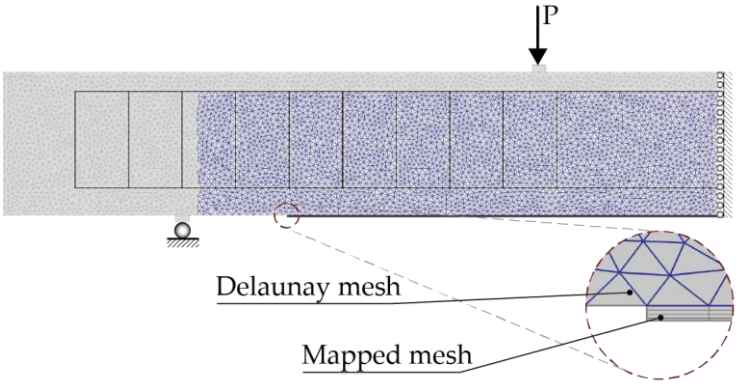

Figure 4.9. Mesh configurations for the plated RC beam (the embedded cohesive interface elements are highlighted in blue).

boundaries (see Figure 4.9). It is worth noting that, since concrete crushing is not observed in the experimental results reported in (Gao et al., 2004) and due to the fact that the adopted cohesive traction-separation law is not able to describe in a satisfactory manner the compressive behavior of the concrete, as already done in the analysis of RC beam, the cohesive interface elements have been inserted prior to the numerical simulations over a suitably chosen critical region, dominated by a combined tension-shear stress state. Moreover, no cohesive elements have been inserted at the inter-element boundaries superposed to the existing truss elements, in order to avoid possible preferential crack paths induced by the 2D representation of the actual 3D failure mechanism occurring in the neighborhood of the steel/concrete interface. All the embedded interface elements are characterized by the cohesive parameters listed in Table 4.5, suitably calibrated to

Table 4.5. Material parameters for the cohesive interfaces.

K_n^0 [N/mm³]	K_s^0 [N/mm³]	$\sigma_{\max}$ [MPa]	$\tau_{\max}$ [MPa]	G_{Ic} [N/m]	G_{IIc} [N/m]	α
4.214e5	3.161e5	2.1	4.2	125	1250	5

match the failure properties of the given concrete material. In particular, the mode-II cohesive parameters, i.e. the maximum shear stress $\tau_{\max}$ and the mode-II fracture energy G_{IIc} of concrete, are additional parameters, not reported in (Gao et al., 2004) but required to correctly analyze mixed-mode failure. Coherently with what suggested in Section 3.3, the parameter whilst G_{IIc} has been chosen ten times bigger than G_{Ic}, whilst $\tau_{\max}$ has been set equal to about 1.4 times larger than $\sigma_{\max}$, this value being consistent with typical cohesion values for concrete material.

Furthermore, both the CFRP-plate and the adhesive layer have been discretized by using four-node quadrilateral elements arranged in a mapped (i.e. structured) mesh, as shown at the bottom side of Figure 4.9. Additional cohesive elements have been inserted all along the physical adhesive/concrete (A/C) interface, to take into account also potential debonding mechanisms in the numerical model. As cohesive parameters, the values reported in Table 4.5 have been chosen, implicitly assuming that the failure occurs at the concrete side of the material interface.

The subsequent numerical computations are conducted by using a novel hybrid path-following scheme, obtained from the synergistic combination of a classical displacement control and a

newly proposed continuation strategy for capturing the unstable branches of the equilibrium path. Such a strategy adopts as a continuation parameter the average value of the normal displacement jump over all the cohesive interfaces, i.e.:

$$\frac{1}{\left|\Gamma_d\right|}\int_{\Gamma_d}\delta_n \, d\Gamma \tag{2.52}$$

strictly related to the dissipated cohesive energy, assumed to be a monotonically increasing quantity during the propagation of cover separation. The switching criterion between the two adopted path-following schemes is based on the number of Newton-Raphson iterations.

4.2.2 Results and discussion of the concrete cover separation analysis

In Figure 4.10, the numerically predicted structural response for the plated beam, in terms of load versus mid-span deflection curve, together with the reference experimental results obtained in (Gao et al., 2004), is reported. The numerical loading curve appears to be very close to that obtained in the experiments. In particular, the notable points of this curve, coinciding with the nucleation of main cracks in concrete (point A) and the yielding of steel reinforcing bars (point B) are well predicted by the present numerical simulations, even if a slightly stronger response is found for the equilibrium branch comprised between points A and B, governed by stabilized flexural/shear crack propagation.

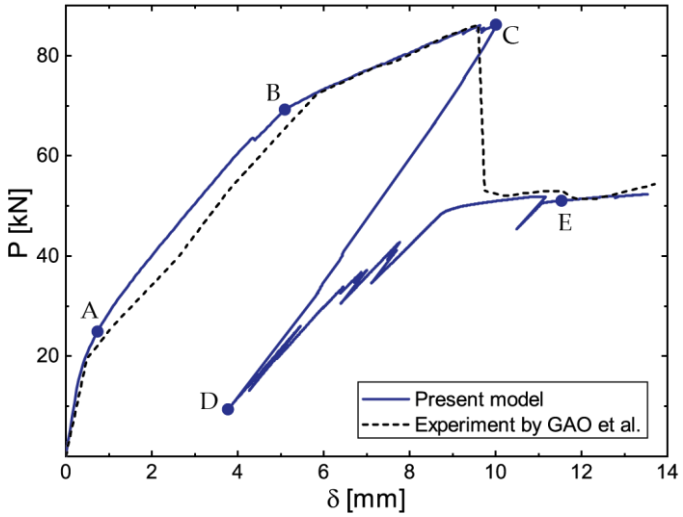

Figure 4.10. Comparison between experimental and numerical results in terms of the load versus mid-span deflection curve for the FRP-plated RC beam.

This is probably due to artificial strengthening/toughening effects induced by the mesh, as already discussed in Section 4.1. Nevertheless, the predicted ultimate load, associated with the concrete cover separation failure (point C), is of about 85.2 kN, very close to that measured experimentally (86.4 kN), with a percentage relative error of only 1.43%. The predicted mid-span deflection at failure, 9.44 mm, is also in perfect accordance with the measured value, 9.50 mm (with a percentage relative error of only 0.63%). It is worth noting that, until the peak load (point C) is reached, the numerical results have been obtained by means of a classical displacement control, being the structural response stable. At point C (coinciding with the onset of cover separation), once the number of Newton-Raphson iterations has reached a

critical threshold, the proposed hybrid path-following scheme switches from the displacement control to the previously mentioned average displacement jump control. In this way, it is possible to follow the snap-back branch of the equilibrium path, characterized by a severe reduction of both the load-carrying capacity and the beam deflection (up to the limit point E). After this, a strength recovery is experienced up to the achievement of its final residual value, coinciding with the ultimate strength of the beam without the FRP system (in good agreement with that obtained in (Gao et al., 2004)).

The deformed configurations, the damage variable maps and the main crack patterns of the plated beam for the simulation steps A, B, C and E of Figure 4.10 are reported in Figure 4.11. As can be deduced from the numerically predicted crack pattern, crack initiation occurs at the adhesive/concrete (A/C) interface. After that, a diffuse cracking is experienced in the tensile region of the beam, characterized by a rather uniform distribution of the main propagating cracks, up to the FRP cut-off section (see Figure 4.11a).

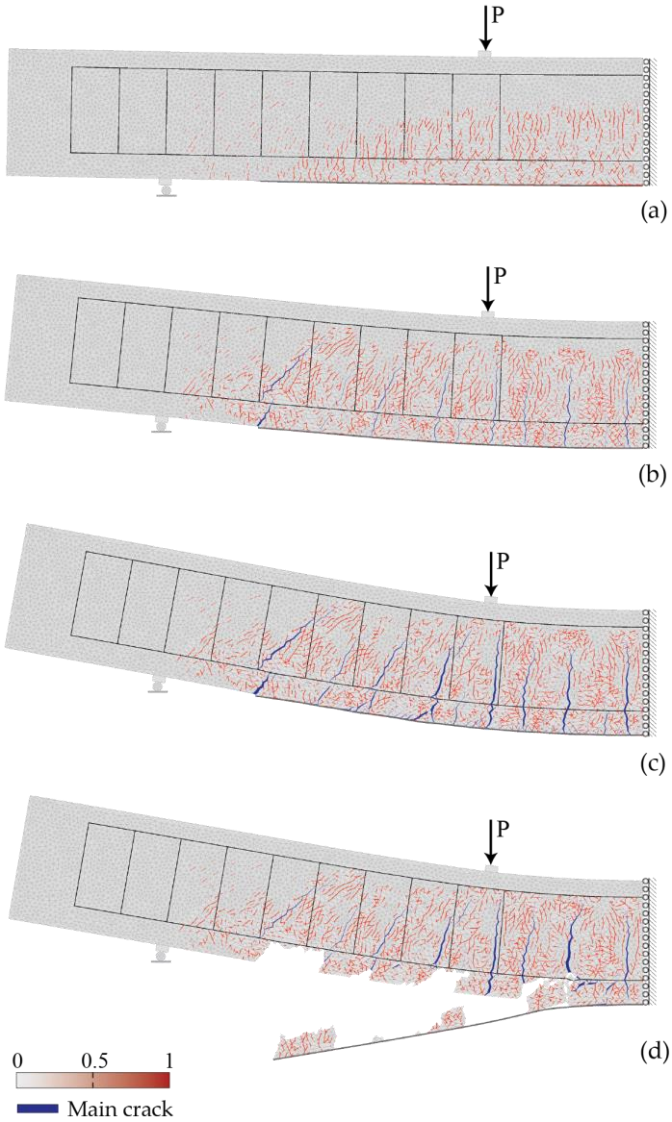

Figure 4.11. Deformed configuration (magnified by a scale factor of 10), damage variable map and main crack pattern for the FRP-plated RC beam at the different simulation steps highlighted in Figure 4.10: a) point A; b) point B; c) point C; d) point E.

As the load is further increased, the shear crack initiated at

the plate end tends progressively to become a major crack with the greatest width among all the existing cracks (see Figure 4.11b). At the intersection between this crack and the tensile reinforcing bars, a new horizontal crack is predicted to initiate as concrete cover separation when the peak load is reached (see Figure 4.11c). Finally, it is found that the numerically predicted failure pattern shown in Figure 4.11d, in which the evolution of concrete cover separation is accompanied by the FRP/concrete interfacial delamination, is fully consistent with the experimental observations made in (Gao et al., 2004).

The adopted formulation to simulate the interaction between concrete and rebars, based on a bond-slip relation, allow the main cracks to pass across the tensile steel reinforcements, thus avoiding artificial propagation constraints or, even worse, crack arrests, thus highlighting the importance of the embedded truss model (ETM) in these types of numerical simulations. In order to better clarify all the local failure mechanisms associated with cover separation, the stress distribution along the tensile reinforcement bars at different load levels is plotted in Figure 4.12, together with the corresponding crack pattern at the peak load. The reported oscillations, showing a decrease of the stress within each concrete tooth comprised between two adjacent main cracks, are due to the tension stiffening phenomena, which are well captured by the adopted local bond-slip model. The steel tensile stress gradually decreases as the distance from the nearest crack increases, due to development of bond stress at the

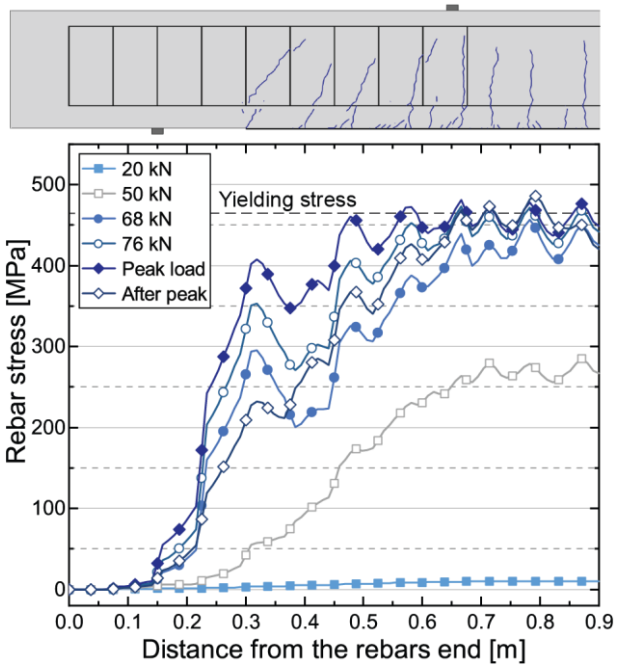

Figure 4.12. Longitudinal stresses along the tensile reinforcement bars for different loading levels (the first yielding stress level for steel rebars is indicated by σ_y).

steel/concrete interface, reaching a minimum mid-way between the two adjacent cracks. After the load level of 68 kN is reached, the first yielding in the constant moment span is experienced, coherently with what observed at point B of Figure 4.10. It is worth noting that a well predicted tension stiffening is able to correctly simulate steel yielding in the neighborhood of the primary cracks.

Moreover, from a deeper analysis of Figure 4.12, it can be observed that concrete cover separation has a direct effect of the stress levels at the reinforcing bars. Indeed, at small load levels

(see 20 kN and 50 kN curves), such longitudinal stresses globally exhibit a linear trend within the shear span, followed by a constant distribution within the constant moment span, meaning that the associated damage does not have a significant influence in the stress redistribution along the longitudinal direction, whereas at larger load levels (see 68 kN, 76 kN and peak load curves), the nucleation and subsequent propagation of the concrete cover separation (accompanied by shear cracking) at the FRP cut-off section causes a high stress concentration in the neighboring steel bars, leading to a sudden increase of stress above the separating concrete layer. Finally, after the concrete cover separation failure is occurred (see after peak curve), the longitudinal stress decreases in the shear span and the local peak in the neighborhood of the plate end becomes less evident, due to the sudden energy releases associated with the cover failure.

Even if the FRP rupture is not reported in (Gao et al., 2004), the longitudinal stresses on the lower surface of the FRP plate for different loading levels have been probed during the numerical simulation to estimate the safety level of the tested beam in regards to the plate failure (see Figure 4.13). At small load levels (see 20 kN and 50 kN curves), such longitudinal stresses increase rapidly from zero at the plate end and assume an approximately constant value in the constant bending moment zone. At larger load levels (see 68 kN, 76 kN and peak load curves), the global trend is similar to the previous one, but greater oscillations appear, reflecting the stress redistribution in the beam due to

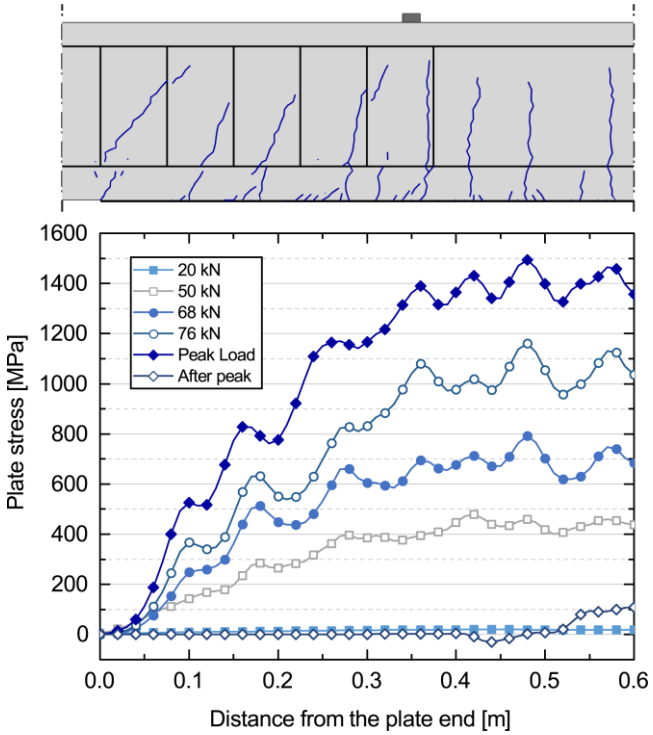

Figure 4.13. Longitudinal stresses on the lower surface of the FRP plate for different loading levels.

rapid crack development. The existing peak stresses in the FRP are associated with the stress concentration experienced at the location of major cracks. After the peak load, the concrete cover is subjected to an abrupt failure, such that the FRP plate experiences an elastic unloading, as confirmed by the extended vanishing behavior of the longitudinal stress distribution (see after peak curve). A maximum residual tensile stress of about 100 MPa in the FRP plate is recorded at the beam mid-span location, remaning the central part of the plate attached to the beam, allowing the interfacial shear stresses to be still transferred.

Finally, it can be noted that the maximum stress monitored in the FRP plate during the entire loading history, occurring at incipient cover separation failure, is of about 1500 MPa. This value is much below the FRP tensile strength, equal to 4200 MPa, resulting in a safety factor prediction, computed as the ratio between these values, of about 2.8.

4.3 Numerical application to steel bar-reinforced nano-enhanced UHPFRC elements

In this Section, the proposed integrated fracture model has been employed to perform failure analysis of ultra high-performance fiber-reinforced concrete (UHPFRC) structures.

In order to capture all the microscopic fracture mechanisms, including cement paste micro-cracking, matrix/aggregate debonding and fiber pull-out, the intrinsic exponential cohesive law, reported in Section 2.2.1 and used in the previous simulations, has been replaced by a suitable trilinear traction-separation law and described in Section 4.3.1.

Subsequently, the main applications of the proposed fracture approach to plain nano-enhanced UHPFRC are presented for both validation and parameter calibration of the trilinear cohesive models. Suitable comparisons with the available experimental results, reported in Section 4.3.2, are provided to show the accuracy of the proposed diffuse interface approach involving a four-point bending test on small-sized UHPFRC beams

with different volume fractions of graphite nanoplatelets (GNPs).

The proposed integrated numerical framework is also employed to simulate the mechanical behavior of steel bar-reinforced nano-enhanced UHPFRC structures. The main numerical outcomes, presented in Section 4.3.3 in terms of both global structural response and final crack pattern, show the ability of the proposed approach to predict the load-carrying capacity of such structures and assess the role of the embedded nano-reinforcement in the crack width control.

4.3.1 Traction–Separation Law for Nano-Enhanced UHPFRC Structures

The traction-separation law (TSL) implemented in the proposed diffuse interface model to describe the nonlinear fracture process in (eventually nano-enhanced) UHPFRC is here presented. This is a trilinear softening model able to capture the tensile failure of fiber-reinforced concretes, initially proposed in (Park et al., 2010) for functionally graded FRC and here adapted to the specific case of UHPFRC. In particular, all the microscopic fracture mechanisms of FRCs are taken into account, including cement paste micro-cracking, matrix/aggregate debonding and fiber pull-out.

The adopted model considers, in addition to the fracture resistance offered by the aggregate interlocking, also the additional

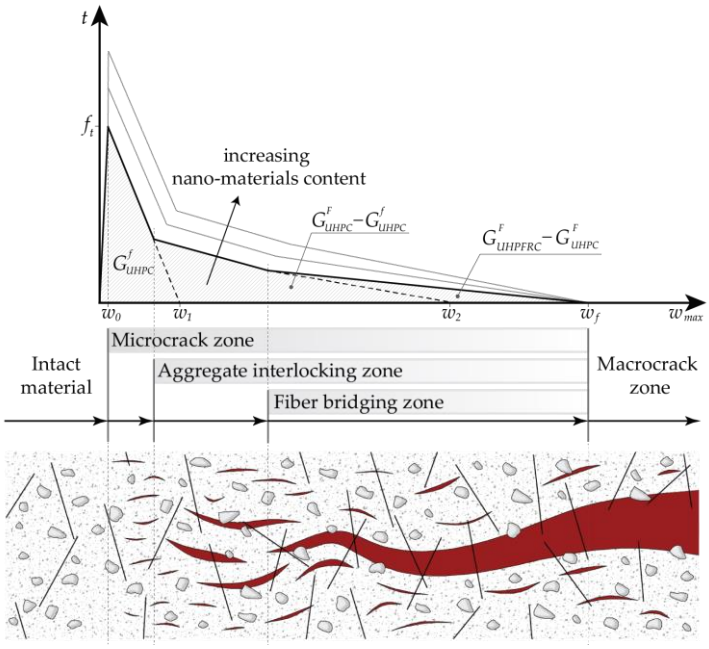

Figure 4.14. Traction-separation law for UHPFRC with a trilinear softening model, and microscopic fracture mechanisms corresponding to each linear descending branch.

toughening effect of embedded discrete fibers, which is associated with a sensible enlargement of the fracture process zone size in UHPFRC with respect to UHPC without reinforcement. The first two linear descending branches of the adopted trilinear softening model for UHPFRC are associated with the initial and total fracture energies of UHPC, respectively, whereas the last descending slope is related to the additional energy required to debond and pull-out the fibers from the cement paste, corresponding to the difference between the total fracture energy of

UHPFRC and the total fracture energy of UHPC, as shown in Figure 4.14.

The numerical calibration of this softening model requires the determination of the following six fracture parameters: tensile strength f_t, initial fracture energy G_{UHPC}^{f} and total fracture energy G_{UHPC}^{F} of the plain UHPC, critical crack tip opening displacement CTOD_c, total fracture energy G_{UHPFRC}^{F} of UHPFRC, and final crack opening width w_f. The first four parameters refer to the bilinear softening model of the plain UHPC, whereas the two latter ones define the last descending branch of UHPFRC.

The horizontal axis intercepts of the first and second softening slopes are expressed as:

$$w_1 = \frac{2G_{\mathrm{UHPC}}^{f}}{f_t} \tag{2.53}$$

and:

$$w_2 = \frac{\dfrac{2G_{\mathrm{UHPC}}^{F}}{f_t} - \mathrm{CTOD}_c}{1 - \dfrac{\mathrm{CTOD}_c f_t}{2G_{\mathrm{UHPC}}^{f}}} \tag{2.54}$$

respectively, where the expression for w_2 is derived assuming that the kink point between the first and second descending branches of the TSL is characterized by a crack opening width w (i.e. its abscissa in Figure 4.14) coinciding with the CTOD_c, supposed to be a known material property (for additional detail about the derivation of Equation (5), please see (Park et al., 2008)

and references cited therein). Finally, w_f is estimated as $L_f/4$, L_f being the fiber length. Such a value corresponds to the estimated pull-out length for randomly distributed short fibers (see (Park et al., 2010) for additional details).

The associated complete mixed-mode intrinsic-type interface constitutive behavior, including the damage irreversibility and the frictionless unilateral contact conditions, reads as:

$$t_n = \begin{cases} K^0 w_n & w_n < 0 \\ \dfrac{t\left(w_{\max}\right)}{w_{\max}} w_n & w_n \geq 0 \end{cases}, \quad t_s = \frac{t\left(w_{\max}\right)}{w_{\max}} w_s \tag{2.55}$$

where w_n and w_s denote the normal and tangential components of the displacement jump vector, the initial stiffness K^0 is used to enforce in an approximated manner the non-interpenetration condition in compression (i.e. for $w_n < 0$), and the function $t(w_{\max})$ represents the TSL shown in Figure 4.14, t being the effective traction and $w_{\max}$ the maximum value of the effective displacement jump w attained over the entire deformation history.

This traction-separation law has been applied to both normal and nano-enhanced UHPFRC (with special reference to UHPFRC with embedded graphite nanoplatelets). The effect of diffuse nano-reinforcement on the nonlinear softening response of the conglomerate consists in sensible increase of both tensile strength f_t and fracture energies G^f_{UHPC}, G^F_{UHPC} and G^F_{UHPFRC}, due to the improved bond within the cement paste as well as at the cement paste/aggregate and cement paste/fiber interfaces. As a

consequence, the resulting softening curve of nano-enhanced UHPFRC is entirely above that of UHPFRC without nano-enhancement, as depicted in the same Figure 4.14. Moreover, the final crack opening width w_f is assumed to be insensitive to the incorporation of nanoplatelets within the concrete matrix, the fiber/matrix bond-slip behavior occurring at higher spatial scales, which are not interacting with the nanoscale level.

Finally, it is worth noting that the above-described interface model is not suitable for hooked fibers and/or high fiber volume fractions, which are usually associated with a strain hardening behavior in the post-cracking stage, even accompanied with a secondary peak in the global traction-separation response (Fantilli et al., 2009; Suárez et al., 2019; Zhan and Meschke, 2016). However, such a behavior is not considered here, being outside of the scopes of the present work, but could be object of future investigations involving a wider class of UHPFRCs.

4.3.2 Numerical calibration and validation of the trilinear cohesive model

Here, the main numerical results obtained via the adopted diffuse cohesive interface model for plain UHPFRC are presented, with reference to a simulated flexural test which involves structural elements containing different volume fractions of graphite nanoplatelets (GNPs). The proposed numerical applications have the twofold role of calibrating the inelastic parameters of embedded interfaces and of assessing the numerical accuracy

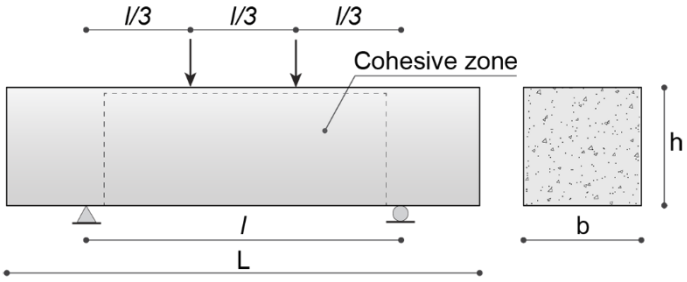

Figure 4.15. UHPFRC beam geometry and boundary conditions of the four-point bending test.

of the adopted fracture model, via suitable comparisons with available experimental results.

The present numerical simulations involve small-sized UHP-FRC beam specimens subjected to a four-point bending test, analyzed in (Meng and Khayat, 2016) from an experimental point of view, whose geometry and boundary conditions are depicted in Figure 4.15. The geometric parameters of the cross section are $b = 76\ mm$ and $h = 76\ mm$, whereas the total length and the span length of the beam are equal to $L = 305\ mm$ mm and $l = 203\ mm$, respectively. Three mixtures of UHPFRC, containing 0.5% by volume of steel fibers with length $L_f = 13\ mm$, have been used for the specimens considered in the next simulations: one mixture without nano-enhancement, which is taken as the control one and named as UHPFRC, and two mixtures containing 0.05% and 0.1% of GNP reinforcements, referred to as UHPFRC GNP 0.05% and UHPFRC GNP 0.1%, respectively.

Table 4.6. Inelastic parameters of embedded cohesive interfaces for the three UHPFRC mixtures.

	f_t (MPa)	G^f_{UHPC} (N/m)	G^F_{UHPC} (N/m)	G^F_{UHPFRC} (N/m)	$CTOD_c$ (mm)	w_f (mm)
UHPFRC	5.71	40	350	1800	0.005	3.25
UHPFRC GNP 0.05%	6.14	50	375	2800	0.005	3.25
UHPFRC GNP 0.1%	6.81	60	400	3800	0.005	3.25

The elastic bulk material parameters have been set equal for all the three concrete mixtures, being assumed to be almost independent of GNP embedding at lower volume fractions. In particular, the adopted Young's modulus is $E = 40\ GPa$, taken from the uniaxial tensile test results reported in (Meng and Khayat, 2016), whereas the Poisson's ratio is $\nu = 0.2$, as usually assumed for uncracked normal concretes.

The adopted values of the inelastic constitutive parameters introduced in Section 4.3.1 are shown in Table 4.6 for all the considered mixtures. The tensile strength values f_t are directly taken from the uniaxial tensile test responses reported in (Meng and Khayat, 2016), whereas the fracture energies G^f_{UHPC}, G^F_{UHPC} and G^F_{UHPFRC} as well as the CTOD_c values are obtained by means of a fitting procedure of the experimental load-displacement curves obtained for the four-point bending test analyzed in (Meng and Khayat, 2016) and reported in Figure 4.16 for comparison purposes. As constraints introduced to simplify the calibration procedure, the CTOD_c is assumed to be constant for all

the mixtures, and the fracture energy values are adjusted to enforce a linear variation with the nanoplatelet content. As expected, the estimated fracture energies G^{f}_{UHPC}, G^{F}_{UHPC} and G^{F}_{UHPFRC} increase for increasing values of the nanoplatelet volume fraction (at least within the considered range of variations). It is worth noting that these fracture energy values are intended not to be valid in general, but rather as reasonable estimates, providing enough accurate predictions for the investigated cases.

To reduce the computational effort of the numerical analyses, the cohesive interface elements have been inserted only within the rectangular area, which is dominated by a combined tension-shear stress state. Here, a suitably refined triangular tessellation has been generated by using an isotropic Delaunay algorithm and imposing a maximum element size of 4 mm, which corresponds to an average length of interface elements of about 2.93 mm. The resulting mesh is composed of 3890 three-node bulk elements and 5903 four-node zero-thickness interface elements. The subsequent numerical computations have been conducted under quasi-static loading conditions via a displacement-controlled path-following scheme, by adopting a constant vertical displacement increment of 5×10^{-3} mm for the extrados point of the mid-span section. Moreover, all the numerical simulations have been performed under a plane stress assumption.

The structural responses numerically derived for the different UHPFRC mixtures, depicted in (Biernacki et al., 2017) Figure

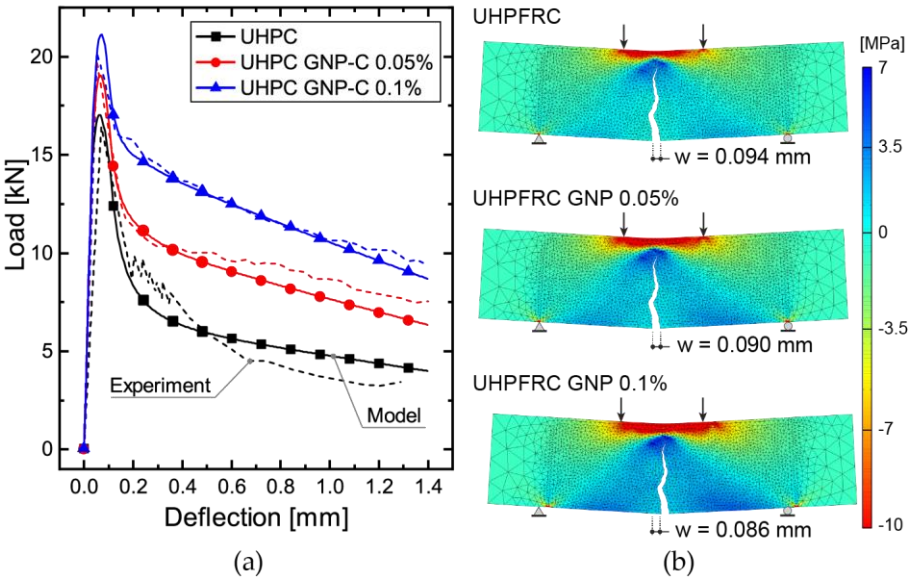

Figure 4.16. Global structural response for the three considered UHP-FRC mixtures: (a) comparison between numerical and experimental results in terms of load versus mid-span deflection curves; (b) deformed configurations (magnified by a scale factor of 25), horizontal stress maps and main crack paths at a beam deflection of 0.2 mm.

4.16a, have been compared with the experimental results reported in (Biernacki et al., 2017). The load versus mid-span deflection curves, can be schematized with three clearly detectable branches for each concrete mixture: the first one corresponds to the elastic regime in which the load level increases almost linearly up to the nucleation of the main crack, occurring at the mid-span section due to the symmetric geometry and boundary conditions. After the peak load, which is associated with the early stage of crack propagation, a fast crack growth characterizes the second branch of the numerically derived curve, along which the

load level decrease until the main crack arrest occurs, due to the steel fiber bridging effect. Then, in the final part of the softening branch, owing to the activation of the fiber pull-put forces, the load level does not drop to zero but remains at (slowly decreasing) residual values.

It is worth noting that the adopted diffuse cohesive methodology allows both nucleation and propagation of the main crack to be naturally predicted, as shown in Figure 4.16b, without assuming the preexistence of weak zones nor requiring the introduction of an initial stress-free crack.

The good agreement between the experimental and numerical loading curves for each investigated UHPFRC mixture underlines that the adopted traction-separation law, if suitably calibrated in terms of inelastic cohesive parameters, is reliable for determining the structural behavior of both normal and nano-enhanced UHPFRC elements with lower nanoparticle contents (up to 0.1% by volume). The percentage errors on the predicted load peak with respect to the experimental values are fully acceptable from an engineering point of view, being of 3.62%, 3.58% and 4.51%, for the three mixtures UHPFRC, UHPFRC GNP 0.05% and UHPFRC GNP 0.1%, respectively. Moreover, a slight local divergence between numerical and experimental results can be observed in the softening branch of the curves referring to the case of UHPFRC without nano-reinforcement, probably due to the occurrence of an unstable structural response in the experimental test, being associated with the appearance of

dynamic effects (totally neglected in the numerical simulations), characterized by very high speeds of the main crack propagation.

The numerical outcomes clearly demonstrate the ability of the proposed diffuse cohesive model for UHPFRC in capturing the effectiveness of the embedded reinforcement in the form of graphite nanoplatelets on the mechanical performances of small-scale structural elements, in terms of cracking resistance and fracture toughness. As a matter of fact, as known from the experiments and confirmed by numerical results, an increase in the GNP fraction leads to an increase of both the peak load and the energy absorption capacity, due to the increase in the bond strength between cement paste and steel fibers and between cement paste and fine aggregates, guaranteed by the additional work-of-fracture provided by embedded nanoplatelets. On the other hand, as illustrated in Figure 4.16b, in the presence of nano-enhancements, significant beneficial effects can be observed in terms of more controlled crack patterns, associated with an increased apparent ductility in the post-peak stage. Indeed, the inclusion of graphite nanoplatelets in the concrete matrix inhibits the nucleation of micro-cracks, reducing at the same time the (macroscopic) crack width. In particular, percentage reductions in the main crack width of about 4% and 8% are obtained for UHPFRC GNP 0.05% and 0.1% cases, respectively, both compared to the control UHPFRC mixture (without nano-reinforcement).

4.3.3 Failure analysis of steel bar-reinforced nano-enhanced UHPFRC beams

Here, the load-carrying capacity of steel bar-reinforced UHPFRC elements enhanced with graphite nanoplatelets (GNPs) has been investigated by means of the diffuse interface model enriched by the trilinear softening model described in Section 4.3.1, and by the embedded truss model (ETM), describe in Section 2.2.2, able to capture the diffuse damage processes which are typical of UHPFRC structures, and to simulate the steel/concrete interactions, respectively.

4.3.3.1 Geometric and material properties

The numerical application of the proposed integrated framework for steel bar-reinforced UHPFRC consists in the simulation of four-point bending tests performed on different medium-sized steel bar-reinforced beams made with the UHPFRC mixtures already adopted in Section 4.3.2, characterized by the same steel fiber content and geometry, and three different GNP contents (0%, 0.05% and 0.1%). The related geometric configuration, loading conditions and constraints, are taken from the experimental tests performed on normal RC beams found in (Gao et al., 2004), and already considered as reference data for the numerical simulations in Sections 4.2 and 4.3, (see Figure 4.1). The main mechanical parameters of both UHPFRC and steel materials are listed in Table 4.7. In particular, the UHPFRC elastic properties are the same as those considered in Section 4.3.2, whereas the

Table 4.7. Main elastic and strength properties of materials.

Material	Young's modulus (GPa)	Poisson's ratio	Yield strength (MPa)	Tangent modulus (GPa)	Compressive strength (MPa)
Steel	200	0.3	460	2.0	-
UHPRFC	40	0.2	-	-	174
UHPRFC GNP 0.05%	40	0.2	-	-	176
UHPRFC GNP 0.1%	40	0.2	-	-	178

UHPFRC compressive strength, required for the computation of the maximum concrete/steel shear stress according to the bond-slip model described in Section 2.2.2, is directly taken from (Meng and Khayat, 2016).

The bond stress-slip relation, adopted to capture the interaction between steel and surrounding nano-enhanced concrete, is a modification of that proposed by CEB-FIP Model Code 2010 (Fib, 2013), obtained by assuming, for UHPFRC, $\tau_{b,\max} = 3.9\sqrt{f_c}$ (f_c being its mean compressive strength), $s_1 = 0.1\ mm$ and $s_2 = 0.6\ mm$. The remaining parameters are taken from the original Model Code formula, thus $\tau_{b,f} = 0.4\tau_{b,\max}$ and $s_3 = 10\ mm$, coinciding with the distance between ribs. The interface behavior is completed by assuming a perfect steel/concrete bond in the normal direction, so that only the interfacial slip is regarded as an active degree of freedom.

The computational mesh, consisting of 17346 triangular elements with a maximum element size of 10 mm, has been generated by using a Delaunay triangulation algorithm to avoid any

preferential crack path direction. In order to preserve a significant computational efficiency, the extension of the cohesive insertion zone has been limited to the region comprised between the supports (see Figure 4.1), being the only susceptible to be cracked due to the presence of completely free boundary conditions outside of this region. Moreover, the embedded cohesive elements lying along the steel reinforcements are excluded from the numerical model. The inelastic cohesive parameters required by the adopted interface constitutive law are the same as those used in the previous numerical application and listed in Table 4.6, being already calibrated in Section 4.3.2 for the considered UHPFRC mixtures.

Finally, all the steel reinforcements (i.e. both longitudinal bars and stirrups) are modeled as one-dimensional two-node elastic-plastic truss elements connected to concrete elements via special zero-thickness four-node bond elements, according to the embedded truss model described in Section 2.2.2. The following numerical simulations have been performed under plane stress and quasi-static assumptions, adopting a displacement-control solution scheme with constant increments of the mid-span deflection equal to 5×10^{-2} mm.

4.3.3.2 Numerical results and discussion

The presentation and subsequent discussion of the numerically predicted structural response of the considered steel bar-reinforced GNP-enhanced UHPFRC beams are here reported.

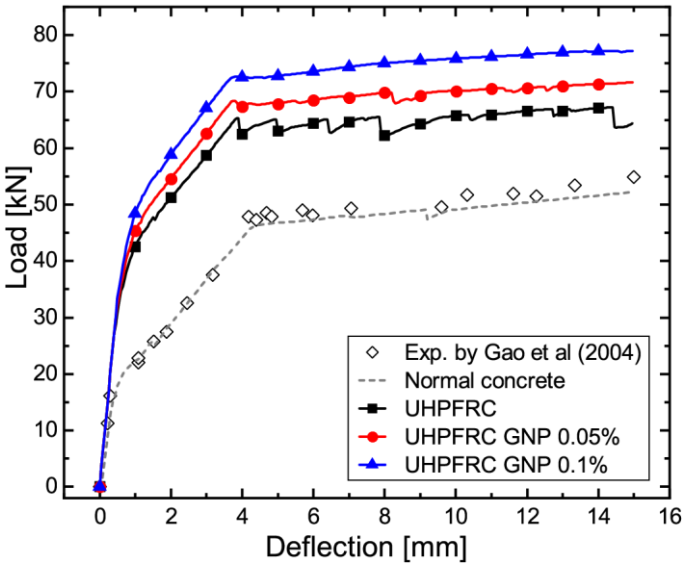

Figure 4.17. Numerically predicted load versus mid-span deflection curves of steel bar-reinforced UHPFRC beams enhanced with different content of GNPs (0%, 0.05% and 0.1%).

Such a response in terms of total load versus mid-span deflection curves is reported Figure 4.17 in for all the three concrete mixtures. The total load is measured as the sum of applied concentrated forces on the upper side of the beams.

For comparison purposes, this figure also shows the experimental results reported in (Gao et al., 2004) and in Section 4.1 represented as scattered points, together with the related numerical results obtained for a normal concrete (i.e. without steel fibers), represented by a dotted line. The latter results have been derived by performing an additional simulation introduced only for verification purposes. To this end, the trilinear softening

model discussed in Section 4.3.1 has been adapted to normal concrete, neglecting the third descending branch of Figure 4.14 and assuming the following concrete properties, coherent with the well-known softening model proposed by Petersson (Petersson, 1981): Young's modulus E = 31 GPa, Poisson's ratio ν = 0.2, tensile strength f_t = 2.1 MPa, initial fracture energy G_f = 75 N/m, total fracture energy G_F = 125 N/m, and critical crack tip opening displacement CTOD$_c$ = 0.048 mm. The excellent agreement between the experimental and numerical results further confirms the reliability of the proposed numerical framework for the failure prediction of both RC and FRC structural elements.

As expected, the loading curves referring to steel bar-reinforced UHPFRC beams (with and without GNP enhancement) show greater load-carrying capacities with respect to the conventional RC beam, with increasing strength values for increasing contents of embedded graphite nanoplatelets (from 0% to 0.1%).

In particular, the typical trilinear behavior of steel bar-reinforced structural elements has been observed for all the analyzed cases. The first slope change coincides with the occurrence of early nonlinear phenomena, consisting in coalescence of concrete microcracks and subsequent macrocrack nucleation. After this, the second linear branch with reduced stiffness initiates after the crack saturation state is reached, being associated with multiple macrocrack propagation toward the upper side of the RC beam. Finally, the second slope change corresponds to the initiation of the yielding phase for lower steel rebars, after which a slight

hardening is kept without the occurrence of any collapse until the end of simulation, stopped as the deflection reaches a prescribed value of 15 mm.

The numerical results clearly show that the combination of micro- and nano-reinforcements (in the form of steel fibers and graphite platelets, respectively) significantly improves the flexural behavior of UHPFRC beams, in terms of ultimate load and energy absorption. In particular, increments of 11% and 20% in the absorbed energy (computed as the area under each load-displacement curve reported in Figure 4.16), as well as increments of 4.8% and 11% in the first yielding load level, with respect the UHPFRC case, are reached with contents of nano-reinforcement equal to 0.05% and 0.1%, respectively. Such an increased strength at both peak and post-peak stages is essentially due to the concurrence of two phenomena. The first one consists in a stronger crack bridging effect of steel microfibers promoted by the high reactivity of embedded interacting nanomaterials, which allows macrocrack propagation to be retarded, thus leading ultimately to a stronger bond between steel reinforcing bars and surrounding concrete (see, for instance, (Qasem et al., 2020) and references cited therein). The second one is the additional crack bridging effect at the nanoscopic scale within the cement paste, responsible for an increase in the tensile strength of UHPFRC material.

Both phenomena, considered individually and/or in synergy, contribute to amplify the significance of the well-known tension

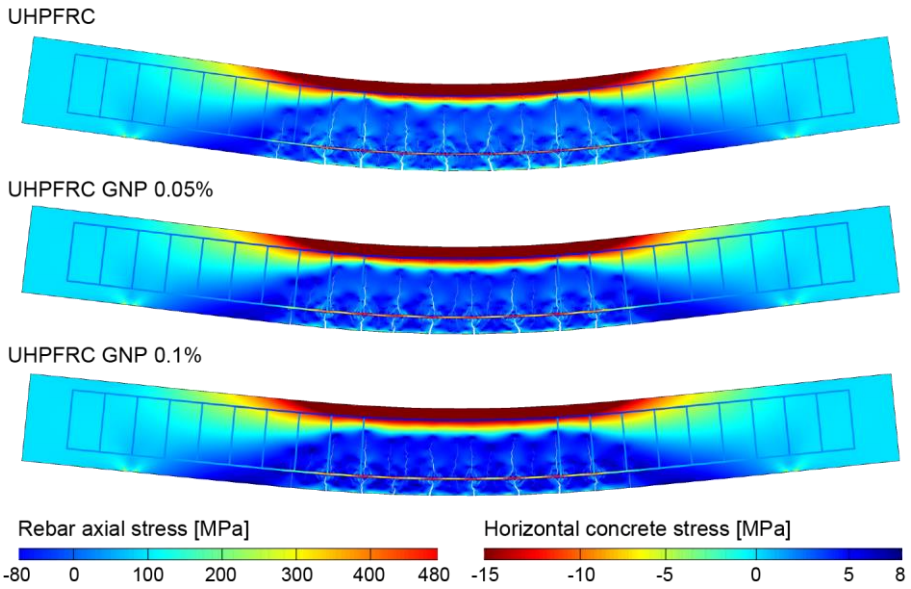

Figure 4.18. Deformed configurations (magnified by a multiplicative factor equal to 20) and stress maps for the three simulated steel bar-reinforced GNP-enhanced UHFRC beams at a load level of 65 kN.

stiffening effect characterizing the interaction between steel reinforcing bars and surrounding concrete layers.

The role of GNPs on the tension stiffening effect can be better highlighted by analyzing the numerically predicted cracking patterns clearly visible in the deformed configurations reported in Figure 4.18, as obtained for the three investigated concrete mixtures at the same load level of 65 kN (corresponding to the first yielding of tensile reinforcing bars of the UHPFRC beam without GNPs). It can be noted that a decrease in both average crack depth and crack spacing has been observed as the value of the GNP content increases. Indeed, it is worth noting that, owing

to the higher fracture toughening effect provided by the embedded nano-reinforcement, a significant reduction in the crack pattern development for the concrete mixture with the highest GNP volume fraction is experienced, compared to the other cases.

Specifically, by restricting the cracking analysis within the constant bending moment region, the average crack width values of 0.079 mm and 0.063 mm can be measured for the cases with GNP addition of 0.05% and 0.1%, respectively, corresponding to crack width reductions of 14% and 31%, respectively, compared to the case of UHPFRC without nano-enhancement (exhibiting an average crack width of 0.093 mm). In addition, the crack spacing for the three different mixtures has been measured at the same fixed load level of 65 kN, obtaining a mean value of 91 mm for the case without nano-enhancement and of 84 mm for both the nano-enhanced mixtures. A crack spacing reduction of 7.32% has been achieved with the introduction of nano-enhancement, while a non-relevant crack spacing reduction is observed for a GNP volume fraction equal to 0.1%, due to the fact that, for the analyzed configuration, such content of nano-reinforcement is associated with a diffuse micro-cracking within the concrete teeth between existing macro-cracks, without leading to the onset of new macro-cracks. Moreover, compared to the case without nano-enhancement, a beam deflection reduction equal to 13.2% and 27.7% has been achieved for the cases with GNP addition of 0.05% and 0.1%, respectively, highlighting an improve-

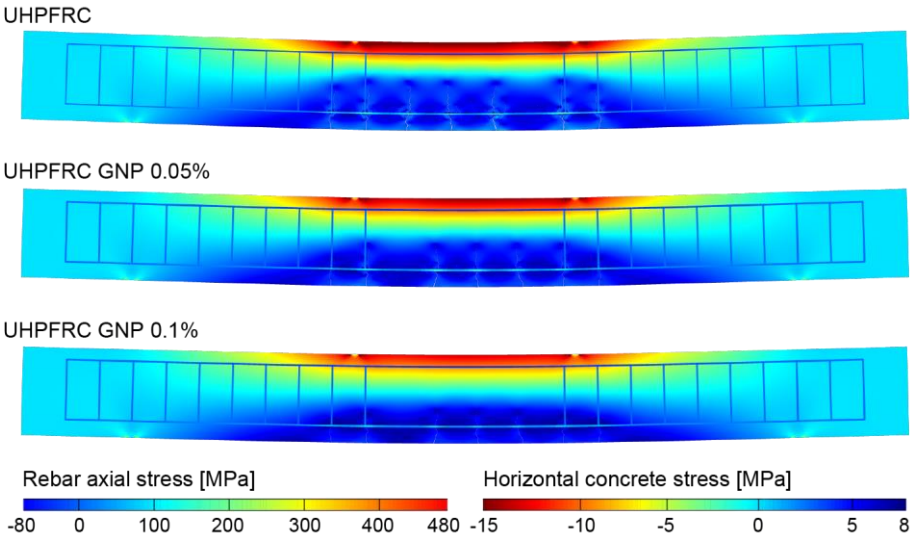

Figure 4.19. Deformed configurations (magnified by a multiplicative factor equal to 15) and stress maps for the three simulated steel bar-reinforced GNP-enhanced UHFRC beams at a load level of 45 kN.

ment of the overall mechanical performances in terms of increasing bending stiffness as the nano-reinforcement content increases. With the aim to investigate the cracking phenomenon under service conditions, in Figure 4.19, the deformed beam configurations for the three investigated concrete mixtures have been reported at a load level of 45 kN, corresponding to the early stage of crack propagation at the bottom of the beams. Moreover, the average crack width, crack spacing and beam deflection at the same load level have been reported in Table 4.8. In Figure 4.19, it can be seen that the cracking patterns are not completely developed, compared to those obtained at a load level of 65 kN, the further cracks being visible in Figure 4.18 in an incipient

Table 4.8. Average crack width, crack spacing, and beam deflection of the simulated beams at a load level of 65 kN.

Material	Average Crack Width (mm)	Crack Spacing (mm)	Beam Deflection (mm)
UHPFRC	0.093	91	3.80
UHPFRC GNP 0.05 %	0.080	84	3.30
UHPFRC GNP 0.1%	0.064	84	2.75

propagation stage at service conditions. More specifically, the crack spacing at service conditions, as reported in Table 4.8, is not influenced by the presence of nano-reinforcements, resulting in being equal to 100 mm for all the investigated mixtures. Contrary to what happens for the crack spacing, the average crack width is strongly influenced by the nano-reinforcement, which results in being equal to 0.019 mm and 0.012 mm for the cases with GNP addition of 0.05% and 0.1%, respectively, corresponding to a crack width reduction, compared to the case without nano-reinforcement, equal to 30.1% and 55.7%, respectively. The obtained crack width reduction at service condition reached by the addition of GNP results in being almost doubled compared to the one reached at a load level equal to 65 kN, highlighting a better fracture toughening effect provided by nano-reinforcements at service conditions. In addition, in Table 4.8, the beam deflection at service conditions has been also reported for the three investigated mixtures, highlighting a beam deflection re-

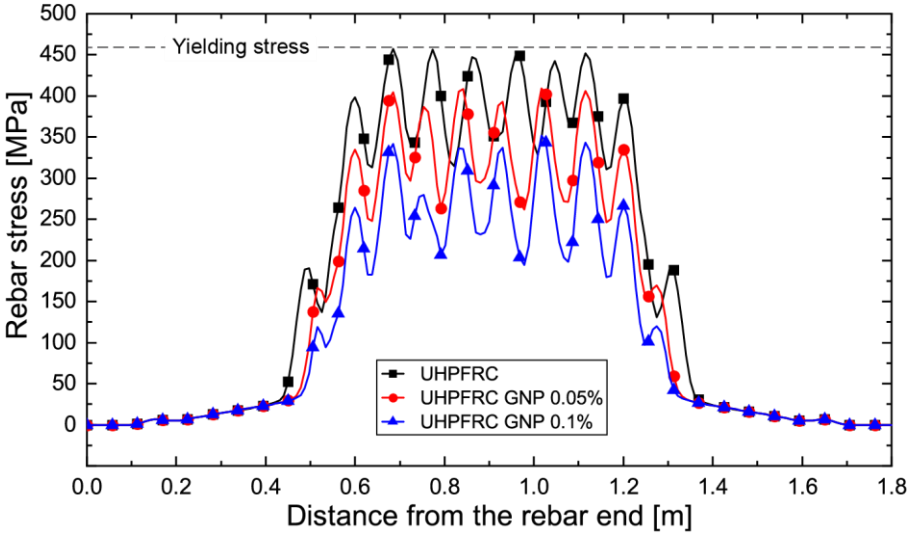

Figure 4.20. Axial stress distribution along the tensile longitudinal reinforcement bars of the three considered UHFRC beams with different contents of GNPs, for a load level of 65 kN.

duction equal to 16.7% and 29.2% for the cases with GNP addition of 0.05% and 0.1%, respectively, compared to the case without nano-enhancement. As a consequence, not relevant changes in the beam deflection reduction have been observed compared to those evaluated at a load level equal to 65 kN, and, generally speaking, also at service conditions, the bending stiffness increases as the nano-reinforcement content increases. The numerically predicted crack width and crack spacing reductions for GNP-enhanced concrete highlights the reliability of the proposed numerical framework for UHPFRCs in capturing the additional crack bridging effect provided by nanoparticles inserted into the concrete mixture, and, ultimately, its beneficial influence

on the ductility properties of structural elements, being intimately related to their macro-cracking behavior. Furthermore, in Figure 4.20, the axial stress distribution along the tensile reinforcement bars of the three simulated UHPFRC beams has been reported for the same load level (65 kN). The reported trends, characterized by lower values of the average rebar stress (and strain) for higher values of the GNP content, confirm the increase in the tension stiffening effect for increasing fractions of nano-reinforcement (at least within the considered range of variation). In particular, the reductions in the (global) maximum stress associated with 0.05% and 0.1% of GNPs with respect to the UHPFRC without nano-enhancement are of about 11% and 23%, respectively.

Finally, the reported oscillating behavior of such stresses, with local maxima in proximity of fully developed cracks and local minima between two contiguous cracks, demonstrates the capability of the adopted embedded truss model as well as of the proposed steel/UHPFRC bond-slip model to correctly capture the stress transfer between steel and concrete phases, which is of fundamental importance for the accurate numerical simulation of tension stiffening phenomena.

Conclusions

In this thesis the fracture phenomena in quasi-brittle materials like concrete have been widely investigated from a numerical point of view, by means of newly proposed discrete modeling techniques based on a cohesive fracture approach. Such advanced fracture methods constitute an efficient numerical framework for the simulation of the complex fracture behavior of concrete structures under general loading conditions, including multiple crack initiation, propagation and coalescence. The basic concepts of fracture mechanics have been critically discussed, together with a complete overview of the principal fracture models proposed in the past literature. In particular, the main goal of the present thesis is to propose a novel inter-element fracture model,

here called Diffuse Interface Model (DIM), based on a cohesive/volumetric finite element formulation, for the nonlinear analysis of both plain and reinforced concrete structures subjected to diffuse cracking. Such a formulation, based on the insertion of cohesive interface elements along all the internal mesh boundaries within a standard displacement-based finite element setting, is capable to simulate multiple crack nucleation and propagation under mixed-mode loading in a very accurate and computationally efficient manner. In detail, the adoption of a diffuse interface model dramatically simplifies the prediction of complex fracture phenomena in reinforced concrete elements, including crack branching and coalescence, allowing single crack paths and/or patterns to be obtained in an automatic manner, without any additional insertion criterion and/or complicated remeshing. The adopted inter-element cohesive approach possesses some advantages over most of the existing fracture approaches, since it preserves the discrete nature of cracking phenomena, unlike smeared crack and damage models, and, at the same time, does not require a great implementation effort, unlike the X-FEM technique and other sophisticated intra-element approaches.

The proposed fracture model exploits a novel calibration methodology for the elastic constitutive response of embedded cohesive interfaces, relying on a numerical micromechanical model, able to extend some previous results found in the litera-

ture, based on analytical or semi-empirical approaches. The proposed calibration approach leads to obtain invisible cohesive interfaces in the elastic range, with the final aim of reducing the well-known artificial compliance issues, while keeping the well-conditioning of the resulting numerical problem.

The adopted fracture model has been used in combination with an Embedded Truss Nodel (ETM), developed to taking into account the bond-slip effect between the steel reinforcing bars and the surrounding concrete, as well as its interaction with the neighboring propagating cracks, during the cracking analysis of reinforced concrete elements. Such a model, equipped with an elastoplastic constitutive behavior, and suitably connected via a bond-slip interface, is conceived to allow the reinforcing bars to be crossed by the neighboring propagating cracks, so that no artificial crack arrest is experienced during the associated numerical simulations.

Moreover, to take into account the possible damage phenomena which may occur along the existing interfaces during the numerical analysis of reinforced concrete structures externally strengthened with FRP systems, a Single cohesive Interface Model (SIM), is incorporated into the proposed numerical framework. This model consists in the insertion of mixed-mode cohesive elements along the material interfaces, i.e. adhesive/concrete (AC) and adhesive/plate (AP) interfaces, able to simulate multiple interfacial debonding initiation and propagation.

The proposed integrated fracture model, composed by DIM, ETM, and SIM approaches, has been developed in a 2D finite element setting and implemented within a commercial software, allowing to automatically simulate multiple discrete crack onset and propagation in concrete structures during the whole loading process until the final collapse, in a very accurate and efficient manner.

In the first part of the results, with reference to Chapter 3, the calibration and validation of the proposed fracture model is reported. The micromechanics-based calibration approach has provided some interesting general results. In particular, two charts are obtained for calibrating the normal and tangential elastic stiffness coefficients of the embedded cohesive interfaces, as functions of both the Poisson's ratio of the bulk and the admitted reduction in the overall Young's modulus after the insertion of such interfaces. These charts have been constructed by performing several analyses on a suitably defined representative volume element (RVE), consisting in a 2D cohesive finite element assemblies arranged according to an isotropic and homogeneous Delaunay tessellation, and subjected to the three in-plane pure loading modes assuming uniform traction BCs. The above-mentioned results are valid for any kind of isotropic material with positive Poisson's ratio and quasi-brittle behavior, whose nonlinear response can be effectively modeled with any cohesive approach. This represents an important aspect of the proposed fracture model, confirming its versatility and direct applicability to

a very large class of real-life materials, including those encountered in usual engineering applications.

A preliminary numerical validation for the proposed diffuse interface model (DIM) in plain concrete has been performed by investigating its capability to predict self-similar crack propagation under pure mode-I loading conditions. To this end, a novel comparison model has been introduced, named controlled diffuse interface model (CDIM), obtained by imposing an additional constraint during the mesh generation, which guarantees the insertion of cohesive elements along a straight-line coinciding with the a priori known propagation direction. The numerical results have demonstrated that, although the well-known lack of crack path convergence is experienced, only a little overestimation of the predicted crack length is found, of about 5%, strictly related to the fractal dimension of the distances measured along the edges of an isotropic and homogeneous Delaunay mesh. Such an overestimation still leads to acceptable values (from the engineering point of view) for both the numerically obtained peak load and dissipated energy, thus confirming the reliability of the proposed methodology.

A further validation of the DIM approach has been provided for plain concrete structures subjected to general mixed-mode loading conditions. The attention has been devoted to the calibration of mode-II inelastic parameters (i.e. tangential critical stress and mode-II fracture energy) for the embedded cohesive interfaces. In particular, with the aim of investigating the role of

such parameters, two sensitivity analyses have been performed by alternately varying one parameter while keeping fixed the other. The related numerical simulations have shown that reliable results can be obtained by choosing for the mode-II fracture energy values greater than the mode-I counterpart, without the need of calibrating it from ad-hoc experimental tests. On the contrary, a stronger restriction has been found for calibrating the tangential critical stress, which possesses a more precise physical meaning, being strictly related to the cohesion of the material. Indeed, the nonlinear response obtained by mans of the present diffuse interface approach has been shown to be insensitive to this parameter only in a limited range, outside of which erroneous damage patterns are numerically predicted.

In the second part of the results, with reference to Chapter 4, the integrated fracture model is used to perform complete failure analyses in different reinforced concrete structures, i.e.: normal-strength reinforced concrete (RC) elements, FRP-plated RC beams and steel bar-reinforced nano-enhanced ultra-high-performance fiber-reinforced concrete (UHPFRC) members. However, common failures in these structural elements are usually associated with complex mechanical phenomena, including not only tensile and shear concrete cracking (and eventually concrete crushing in compression), but also debonding at steel/concrete interfaces, yielding of reinforcing bars, debonding phenomena, and concrete cover separation.

Different simulations performed on real-scale RC beams by using the above-described model have provided numerical results which are fully consistent with the experiments, in terms of both load-carrying capacity and associated failure pattern, thus confirming the reliability of the adopted discrete fracture approach, as a rigorous and powerful numerical tool for both design and assessment of real-life concrete structures.

The proposed integrated fracture approach has been applied to the analysis of concrete cover separation failure in externally strengthened RC structures. Such a failure is usually associated with complex mechanical phenomena, including tensile cracking and compressive crushing of concrete, debonding at both FRP/concrete and steel/concrete interfaces, and yielding of reinforcing bars, thus leading to a highly nonlinear problem to be solved. The proposed model has been shown capable to accurately predict all these failure mechanisms, by performing suitable comparisons with experimental outcomes, with reference to real-scale RC beams retrofitted with an externally bonded CFRP plate. Both the numerically obtained load-carrying capacity and the associated failure pattern are fully consistent with the experiments, showing the superiority of the present approach over most of existing simplified stress- or fracture-based approaches for the cover separation analysis.

Finally, the proposed fracture model has been employed for tracing the structural response of steel bar-reinforced UHPFRC structures enhanced with nanomaterials.

Various numerical simulations have been performed to investigate the role of the content of embedded graphite nanoplatelets (GNPs) on its load-carrying capacity at both peak and post-peak stages, with reference to simply supported beams subjected to a four-point bending test. All the numerical outcomes have been validated by performing suitable comparisons with the available experimental results. A good accordance between numerical and experimental loading curves has been found, with a mean absolute percentage error on the peak load of only about 4%, by virtue of a proper calibration of the inelastic parameters of the embedded cohesive interfaces. Moreover, additional computations have been performed to investigate the mesh dependency effects on the global structural response and crack pattern. The related results have shown that, despite the (local) mesh-dependency of the numerically predicted crack paths, that is related to the unavoidable randomness in the mesh generation procedures, the (global) load-displacement curves are substantially independent of the adopted discretization.

Further numerical simulations have been performed to investigate the effect of nano-enhancement in steel bar-reinforced UHPFRC structures. A simulated four-point bending test on three medium-sized beams with different volume fractions of GNPs has been considered. The numerical outcomes have demonstrated the reliability and the accuracy of the proposed model in predicting both the strengthening and toughening ef-

fects of embedded nanomaterials, in terms of global load-deflection responses and associated crack patterns. In particular, increases in the first yielding load level and absorbed energy up to 11% and 20%, respectively, are numerically predicted for hybrid micro/nano-reinforcements with the highest considered GNP content (i.e. 0.1% by volume). Furthermore, the role of nanomaterials on the tension stiffening effect have been demonstrated, by analyzing both final crack patterns and associated stress distribution maps. From the numerical analyses, the addition of 0.05% and 0.1% of GNPs has led to crack width reductions of 14% and 31%, respectively, as well as to maximum axial stress reductions along steel rebars of about 11% and 23%, respectively, thus confirming the increased ductility of the enhanced UHP-FRC, at least for small volume contents of nano-reinforcement.

In conclusion, the fundamental strengths of the proposed inter-element fracture model can be summarized in the two following points: (i) comprehensiveness, here standing for the fully possibility of investigating all the main damage mechanisms in plain and reinforced concrete in a unified manner, either at the ultimate state (i.e. at complete failure) or under in-service loading conditions (e.g. for crack width control); and (ii) ease of implementation, essentially related to the capability of the principal modern commercial finite element environments to embed the well-established cohesive interface elements within a standard displacement-type finite element mesh, without any in-depth programming skills.

As future perspectives of this work, the following research directions could be explored:

- Extension of the proposed fracture approach, implicitly assuming only through-width surface cracks, to the more appealing 3D case, being needed in the presence of complex triaxial stress states, as in structural problems involving torsional loads. This point could be addressed in a straightforward manner with simple modifications of the adopted cohesive traction-separation law, while keeping the present variational framework by virtue of its general validity.
- Development of new strategies, alternative to the present diffuse interface model, for the adaptive insertion or activation of cohesive elements placed at the inter-element boundaries of a given bulk mesh, so that the inactive cohesive interfaces have no influence on the overall elastic properties.
- Incorporation of the proposed numerical model for RC structures within a general adaptive concurrent multiscale approach, to improve the related overall computational performances, similarly to what recently suggested for the failure analysis of lightweight aggregate concrete (Feo et al., 2015) and masonry structures (Greco et al., 2017; Leonetti et al., 2018).

Bibliography

Aprile, A., Feo, L., 2007. Concrete cover rip-off of R/C beams strengthened with FRP composites. Composites Part B: Engineering 38, 759–771. https://doi.org/10.1016/j.compositesb.2006.07.015

Arici, Y., 2011. Investigation of the cracking of CFRD face plates. Computers and Geotechnics 38, 905–916. https://doi.org/10.1016/j.compgeo.2011.06.004

Barenblatt, G.I., 1962. The Mathematical Theory of Equilibrium Cracks in Brittle Fracture, in: Advances in Applied Mechanics. Elsevier, pp. 55–129. https://doi.org/10.1016/S0065-2156(08)70121-2

Barenblatt, G.I., 1959. The formation of equilibrium cracks during brittle fracture. General ideas and hypotheses. Axially-symmetric cracks. Journal of Applied Mathematics and Mechanics 622–636.

Barsom, J.M., Rolfe, S.T., 1999. Fracture and fatigue control in structures: applications of fracture mechanics, 3rd ed. ed. ASTM, West Conshohocken, PA.

Bažant, Z.P., 1984. Size Effect in Blunt Fracture: Concrete, Rock, Metal. Journal of Engineering Mechanics 110, 518–535. https://doi.org/10.1061/(ASCE)0733-9399(1984)110:4(518)

Bažant, Z.P., 1976. Instability, Ductility, and Size Effect in Strain-Softening Concrete. ASCE J Eng Mech Div 102, 331–344.

Bažant, Z.P., Belytschko, T.B., 1985. Wave Propagation in a Strain-Softening Bar:Exact Solution. Journal of Engineering Mechanics 111, 381–389. https://doi.org/10.1061/(ASCE)0733-9399(1985)111:3(381)

Bažant, Z.P., Cedolin, L., 1983. Finite Element Modeling of Crack Band Propagation. Journal of Structural Engineering 109, 69–92. https://doi.org/10.1061/(ASCE)0733-9445(1983)109:1(69)

Bažant, Z.P., Cedolin, L., 1979. Blunt Crack Band Propagation in Finite Element Analysis. ASCE J Eng Mech Div 105, 297–315.

Bažant, Z.P., Di Luzio, G., 2004. Nonlocal microplane model with strain-softening yield limits. International Journal of Solids and Structures 41, 7209–7240. https://doi.org/10.1016/j.ijsolstr.2004.05.065

Bažant, Z.P., Lin, F., 1988. Nonlocal Smeared Cracking Model for Concrete Fracture. Journal of Structural Engineering 114, 2493–2510. https://doi.org/10.1061/(ASCE)0733-9445(1988)114:11(2493)

Bažant, Z.P., Ožbolt, J., 1990. Nonlocal Microplane Model for Fracture, Damage, and Size Effect in Structures. Journal of Engineering Mechanics 116, 2485–2505.

https://doi.org/10.1061/(ASCE)0733-9399(1990)116:11(2485)

Bažant, Z.P., Planas, J., 1998a. Fracture and Size Effect in Concrete and Other Quasibrittle Materials, 1st ed. Routledge. https://doi.org/10.1201/9780203756799

Bažant, Z.P., Planas, J., 1998b. Fracture and Size Effect in Concrete and Other Quasibrittle Materials, 1st ed. Routledge. https://doi.org/10.1201/9780203756799

Belytschko, T., Moës, N., Usui, S., Parimik, C., 2001. Arbitrary discontinuities in finite elements. International Journal for Numerical Methods in Engineering 50, 993–1013.

Biernacki, J.J., Bullard, J.W., Sant, G., Brown, K., Glasser, F.P., Jones, S., Ley, T., Livingston, R., Nicoleau, L., Olek, J., Sanchez, F., Shahsavari, R., Stutzman, P.E., Sobolev, K., Prater, T., 2017. Cements in the 21 st century: Challenges, perspectives, and opportunities. J Am Ceram Soc 100, 2746–2773. https://doi.org/10.1111/jace.14948

Blal, N., Daridon, L., Monerie, Y., Pagano, S., 2012. Artificial compliance inherent to the intrinsic cohesive zone models: criteria and application to planar meshes. Int J Fract 178, 71–83. https://doi.org/10.1007/s10704-012-9734-y

Bocca, P., Carpinteri, A., Valente, S., 1991. Mixed mode fracture of concrete. International Journal of Solids and Structures 27, 1139–1153. https://doi.org/10.1016/0020-7683(91)90115-V

Bolander, J.E., Le, B.D., 1999. Modeling crack development in reinforced concrete structures under service loading. Construction and Building Materials 13, 23–31. https://doi.org/10.1016/S0950-0618(99)00005-7

Bruno, D., Greco, F., Lo Feudo, S., Nevone Blasi, P., 2016. Multi-layer modeling of edge debonding in strengthened beams using interface stresses and fracture energies. Engineering Structures 109, 26–42. https://doi.org/10.1016/j.engstruct.2015.11.013

Bruno, D., Greco, F., Lonetti, P., Nevone Blasi, P., 2008. Influence of micro-cracking and contact on the effective properties of composite materials. Simulation Modelling Practice and Theory 16, 861–884. https://doi.org/10.1016/j.simpat.2008.05.006

Burdekin, F.M., Stone, D.E.W., 1966. The crack opening displacement approach to fracture mechanics in yielding materials. Journal of Strain Analysis 1, 145–153. https://doi.org/10.1243/03093247V012145

Buyukozturk, O., Gunes, O., Karaca, E., 2004. Progress on understanding debonding problems in reinforced concrete and steel members strengthened using FRP composites. Construction and Building Materials 18, 9–19. https://doi.org/10.1016/S0950-0618(03)00094-1

Camacho, G.T., Ortiz, M., 1996. Computational modelling of impact damage in brittle materials. International Journal of Solids and Structures 33, 2899–2938. https://doi.org/10.1016/0020-7683(95)00255-3

Carol, I., Prat, P.C., López, C.M., 1997. Normal/Shear Cracking Model: Application to Discrete Crack Analysis. Journal of Engineering Mechanics 123, 765–773. https://doi.org/10.1061/(ASCE)0733-9399(1997)123:8(765)

Carpinteri, A., 1990. A catastrophe theory approach to fracture mechanics. Int J Fract 44, 57–69. https://doi.org/10.1007/BF00012552

Carpinteri, A., 1989a. Decrease of apparent tensile and bending strength with specimen size: Two different explanations based on fracture mechanics. International Journal of Solids and Structures 25, 407–429. https://doi.org/10.1016/0020-7683(89)90056-5

Carpinteri, A., 1989b. Post-peak and post-bifurcation analysis of cohesive crack propagation. Engineering Fracture Mechanics 32, 265–278. https://doi.org/10.1016/0013-7944(89)90299-3

Carpinteri, A., 1989c. Cusp catastrophe interpretation of fracture instability. Journal of the Mechanics and Physics of Solids 37, 567–582. https://doi.org/10.1016/0022-5096(89)90029-X

Carpinteri, A., Colombo, G., 1989. Numerical analysis of catastrophic softening behaviour (snap-back instability). Computers & Structures 31, 607–636. https://doi.org/10.1016/0045-7949(89)90337-4

Cedolin, L., Dei Poli, S., Iori, I., 1983. Experimental determination of the fracture process zone in concrete. Cement and Concrete Research 13, 557–567. https://doi.org/10.1016/0008-8846(83)90015-7

Cendón, D.A., Gálvez, J.C., Elices, M., Planas, J., 2000. Modelling the fracture of concrete under mixed loading. International Journal of Fracture 103, 293–310. https://doi.org/10.1023/A:1007687025575

Ceroni, F., Pecce, M., 2007. Cracking behaviour of RC beams externally strengthened with emerging materials. Construction and Building Materials 21, 736–745. https://doi.org/10.1016/j.conbuildmat.2006.06.013

Červenka, J., Červenka, V., Laserna, S., 2018. On crack band model in finite element analysis of concrete fracture in engineering practice. Engineering Fracture Mechanics 197, 27–47. https://doi.org/10.1016/j.engfracmech.2018.04.010

Chen, Y.Z., 1989. Weight function technique in a more general case. Engineering Fracture Mechanics 33, 983–986. https://doi.org/10.1016/0013-7944(89)90113-6

Comi, C., Perego, U., 2001. Fracture energy based bi-dissipative damage model for concrete. International Journal of Solids and Structures 38, 6427–6454. https://doi.org/10.1016/S0020-7683(01)00066-X

Comsol AB, 2018. Comsol Multiphysics Physics Builder Manual.

de Borst, R. de, Gutiérrez, M.A., Wells, G.N., Remmers, J.J.C., Askes, H., 2004. Cohesive-zone models, higher-order continuum theories and reliability methods for computational failure analysis: COMPUTATIONAL FAILURE ANALYSIS. Int. J. Numer. Meth. Engng. 60, 289–315. https://doi.org/10.1002/nme.963

de Borst, R., 1991. SIMULATION OF STRAIN LOCALIZATION: A REAPPRAISAL OF THE COSSERAT CONTINUUM. Engineering Computations 8, 317–332. https://doi.org/10.1108/eb023842

de Borst, R., Remmers, J.J.C., Needleman, A., 2006. Mesh-independent discrete numerical representations of cohesive-zone models. Engineering Fracture Mechanics 73, 160–177. https://doi.org/10.1016/j.engfracmech.2005.05.007

de Vree, J.H.P., Brekelmans, W.A.M., van Gils, M.A.J., 1995. Comparison of nonlocal approaches in continuum damage mechanics. Computers & Structures 55, 581–588. https://doi.org/10.1016/0045-7949(94)00501-S

Dienes, J.K., 1986. Comments on "a generalized griffith criterion for crack propagation" by L. G. Margolin. Engineering Fracture Mechanics 23, 615–617. https://doi.org/10.1016/0013-7944(86)90165-7

Dolbow, J., Moës, N., Belytschko, T., 2000. Discontinuous enrichment in finite elements with a partition of unity method. Finite Elements in Analysis and Design, Robert J. Melosh Medal Competition, Duke University, Durham NC, USA, March 1999 36, 235–260. https://doi.org/10.1016/S0168-874X(00)00035-4

Dugdale, D.S., 1960. Yielding of steel sheets containing slits. Journal of the Mechanics and Physics of Solids 8, 100–104. https://doi.org/10.1016/0022-5096(60)90013-2

Elices, M., Guinea, G.V., Gómez, J., Planas, J., 2002. The cohesive zone model: advantages, limitations and challenges. Engineering Fracture Mechanics 69, 137–163. https://doi.org/10.1016/S0013-7944(01)00083-2

Erdogan, F., Sih, G.C., 1963. On the Crack Extension in Plates Under Plane Loading and Transverse Shear. Journal of Basic Engineering 85, 519–525. https://doi.org/10.1115/1.3656897

Erigen, A.C., 1983. Theories of nonlocal plasticity. International Journal of Engineering Science 21, 741–751.

Espinosa, H.D., Zavattieri, P.D., 2003. A grain level model for the study of failure initiation and evolution in polycrystalline brittle materials. Part I: Theory and numerical implementation. Mechanics of Materials 35, 333–364. https://doi.org/10.1016/S0167-6636(02)00285-5

Evans, R.H., Marathe, M.S., 1968. Microcracking and stress-strain curves for concrete in tension. Materials and Structures 1, 61–64.

Falk, M.L., Needleman, A., Rice, J.R., 2001. A critical evaluation of cohesive zone models of dynamic fractur. J. Phys. IV France 11, Pr5-43-Pr5-50. https://doi.org/10.1051/jp4:2001506

Fanning, P.J., Kelly, O., 2001. Ultimate Response of RC Beams Strengthened with CFRP Plates. J. Compos. Constr. 5, 122–127. https://doi.org/10.1061/(ASCE)1090-0268(2001)5:2(122)

Fantilli, A.P., Mihashi, H., Vallini, P., 2009. Multiple cracking and strain hardening in fiber-reinforced concrete under uniaxial tension. Cement and Concrete Research 39, 1217–1229. https://doi.org/10.1016/j.cemconres.2009.08.020

Fantuzzi, N., Leonetti, L., Trovalusci, P., Tornabene, F., 2018. Some Novel Numerical Applications of Cosserat Continua. Int. J. Comput. Methods 15, 1850054. https://doi.org/10.1142/S0219876218500548

Feo, L., Greco, F., Leonetti, L., Luciano, R., 2015. Mixed-mode fracture in lightweight aggregate concrete by using a moving mesh approach within a multiscale framework. Composite Structures 123, 88–97. https://doi.org/10.1016/j.compstruct.2014.12.037

Fib, 2013. CEB-FIP Model Code for concrete structures 2010.

Frosch, R.J., 1999. Another Look at Cracking and Crack Control in Reinforced Concrete. SJ 96. https://doi.org/10.14359/679

Fu, X., Chung, D.D.L., 1997. Effect of corrosion on the bond between concrete and steel rebar. Cement and Concrete Research 27, 1811–1815.

Gálvez, J.C., Cendón, D.A., Planas, J., 2002a. Influence of shear parameters on mixed–mode fracture of concrete. International Journal of Fracture 118, 163–189. https://doi.org/10.1023/A:1022883132117

Gálvez, J.C., Červenka, J., Cendón, D.A., Saouma, V., 2002b. A discrete crack approach to normal/shear cracking of concrete. Cement and Concrete Research 32, 1567–1585. https://doi.org/10.1016/S0008-8846(02)00825-6

Gálvez, J.C., Elices, M., Guinea, G.V., Planas, J., 1998. Mixed mode fracture of concrete under proportional and nonproportional loading. International Journal of Fracture 94, 267–284. https://doi.org/10.1023/A:1007578814070

Gao, B., Kim, J.-K., Leung, C.K.Y., 2004. Experimental study on RC beams with FRP strips bonded with rubber modified resins. Composites Science and Technology 64, 2557–2564. https://doi.org/10.1016/j.compscitech.2004.05.016

Gasser, T.C., Holzapfel, G.A., 2006. 3D Crack propagation in unreinforced concrete. Computer Methods in Applied Mechanics and Engineering 195, 5198–5219. https://doi.org/10.1016/j.cma.2005.10.023

Gasser, T.C., Holzapfel, G.A., 2005. Modeling 3D crack propagation in unreinforced concrete using PUFEM. Computer

Methods in Applied Mechanics and Engineering 194, 2859–2896. https://doi.org/10.1016/j.cma.2004.07.025

Gee, B., Parchei-Esfahani, M., Gracie, R., 2020. XFEM simulation of a mixed-mode fracture experiment in PMMA. Engineering Fracture Mechanics 229, 106945. https://doi.org/10.1016/j.engfracmech.2020.106945

Geers, M.G.D., de Borst, R., Brekelmans, W.A.M., Peerlings, R.H.J., 1998. Strain-based transient-gradient damage model for failure analyses. Computer Methods in Applied Mechanics and Engineering 160, 133–153. https://doi.org/10.1016/S0045-7825(98)80011-X

Gerstle, W.H., Xie, M., 1992. FEM Modeling of Fictitious Crack Propagation in Concrete. Journal of Engineering Mechanics 118, 416–434. https://doi.org/10.1061/(ASCE)0733-9399(1992)118:2(416)

Grassl, P., Johansson, M., Leppänen, J., 2018. On the numerical modelling of bond for the failure analysis of reinforced concrete. Engineering Fracture Mechanics 189, 13–26. https://doi.org/10.1016/j.engfracmech.2017.10.008

Greco, F., Leonetti, L., Luciano, R., 2015. A multiscale model for the numerical simulation of the anchor bolt pull-out test in lightweight aggregate concrete. Construction and Building Materials 95, 860–874. https://doi.org/10.1016/j.conbuildmat.2015.07.170

Greco, F., Leonetti, L., Luciano, R., Trovalusci, P., 2017. Multiscale failure analysis of periodic masonry structures with traditional and fiber-reinforced mortar joints. Composites Part B: Engineering 118, 75–95. https://doi.org/10.1016/j.compositesb.2017.03.004

Greco, F., Lonetti, P., 2009. Mixed mode dynamic delamination in fiber reinforced composites. Composites Part B: Engineering 40, 379–392. https://doi.org/10.1016/j.compositesb.2009.03.003

Greco, F., Lonetti, P., Zinno, R., 2002. An analytical delamination model for laminated plates including bridging effects. International Journal of Solids and Structures 39, 2435–2463. https://doi.org/10.1016/S0020-7683(02)00118-X

Griffith, A.A., 1921. The Phenomena of Rupture and Flows in Solids. Phil. Trans. Royal Soc. 221, 163–167.

Hillerborg, A., Modéer, M., Petersson, P.-E., 1976. Analysis of crack formation and crack growth in concrete by means of fracture mechanics and finite elements. Cement and Concrete Research 6, 773–781. https://doi.org/10.1016/0008-8846(76)90007-7

Inglis, C.E., 1913. Stresses in a Plate due to the Presence of Cracks and Sharp Corners. Trans. Institute of Naval Architecture 55, 219–241.

Ingraffea, A.R., 1990. Case studies of simulation of fracture in concrete dams. Engineering Fracture Mechanics 35, 553–564. https://doi.org/10.1016/0013-7944(90)90230-E

Ingraffea, A.R., Gerstk, W.H., Gergely, P., Saouma, V., 1984. Fracture Mechanics of Bond in Reinforced Concrete. Journal of Structural Engineering 110, 871–890. https://doi.org/10.1061/(ASCE)0733-9445(1984)110:4(871)

Ingraffea, A.R., Gerstle, W.H., 1984. Nonlinear fracture models for discrete crack propagation. Proceedings of the NATO Advanced Workshop on Application of Fracture Mechanics to Cementitious Composites 171–209.

Irwin, G.R., 1960. Plastic zone near a crack tip and fracture toughness. Proceedings of the Seventh Sagamore Ordnance Material Conference IV, 63–78.

Irwin, G.R., 1958. Fracture. Handbuch der Physik VI, Flügge Ed 551–590.

Irwin, G.R., 1957. Analysis of stresses and strains near the end of a crack traversing a plate. J. Appl. Mech. 24, 361–364.

Issa, M.A., 1999. Investigation of Cracking in Concrete Bridge Decks at Early Ages. Journal of Bridge Engineering 4, 116–124. https://doi.org/10.1061/(ASCE)1084-0702(1999)4:2(116)

Jäger, P., Steinmann, P., Kuhl, E., 2008. Modeling three-dimensional crack propagation-A comparison of crack path tracking strategies. Int. J. Numer. Meth. Engng 76, 1328–1352. https://doi.org/10.1002/nme.2353

Jirásek, M., 2004. Non-local damage mechanics with application to concrete. Revue Française de Génie Civil 8, 683–707. https://doi.org/10.1080/12795119.2004.9692625

Jirásek, M., Patzák, B., 2002. Consistent tangent stiffness for nonlocal damage models. Computers & Structures 80, 1279–1293. https://doi.org/10.1016/S0045-7949(02)00078-0

Jirásek, M., Zimmermann, T., 1998. Rotating Crack Model with Transition to Scalar Damage. Journal of Engineering Mechanics 124, 277–284. https://doi.org/10.1061/(ASCE)0733-9399(1998)124:3(277)

Kachanov, L.M., 1986. Introduction to continuum damage mechanics, Mechanics of elastic stability. M. Nijhoff, Dordrecht ; Boston.

Khor, W., Moore, P.L., Pisarski, H.G., Haslett, M., Brown, C.J., 2016. Measurement and prediction of CTOD in austenitic stainless steel: CTOD in Austenitic Stainless Steel. Fatigue Fract Engng Mater Struct 39, 1433–1442. https://doi.org/10.1111/ffe.12487

Klein, P.A., Foulk, J.W., Chen, E.P., Wimmer, S.A., Gao, H.J., 2001. Physics-based modeling of brittle fracture: cohesive formulations and the application of meshfree methods. Theoretical and Applied Fracture Mechanics 37, 99–166. https://doi.org/10.1016/S0167-8442(01)00091-X

Krajcinovic, D., Fonseka, G.U., 1981. The Continuous Damage Theory of Brittle Materials, Part 1: General Theory. Journal of Applied Mechanics 48, 809–815. https://doi.org/10.1115/1.3157739

Kuhl, E., Ramm, E., 1999. Simulation of strain localization with gradient enhanced damage models. Computational Materials Science 16, 176–185. https://doi.org/10.1016/S0927-0256(99)00060-9

Kupfer, H., Hilsdorf, H.K., Rusch, H., 1969. Behavior of Concrete Under Biaxial Stresses. Journal of the American Concrete Institute 66, 656–666.

Kuutti, J., Kolari, K., 2012. A local remeshing procedure to simulate crack propagation in quasi-brittle materials. Engineering Computations 29, 125–143. https://doi.org/10.1108/02644401211206025

Lemaitre, J., Chaboche, J.-L., Shrivastava, B., 2002. Mechanics of solid materials, 1. paperback ed., repr.transferred to digital print. ed. Cambridge Univ. Press, Cambridge.

Leonetti, L., Fantuzzi, N., Trovalusci, P., Tornabene, F., 2019. Scale Effects in Orthotropic Composite Assemblies as Micropolar Continua: A Comparison between Weak- and Strong-Form Finite Element Solutions. Materials 12, 758. https://doi.org/10.3390/ma12050758

Leonetti, L., Greco, F., Trovalusci, P., Luciano, R., Masiani, R., 2018. A multiscale damage analysis of periodic composites using a couple-stress/Cauchy multidomain model: Application to masonry structures. Composites Part B: Engineering 141, 50–59. https://doi.org/10.1016/j.compositesb.2017.12.025

Li, S., Wang, G., Morgan, E., 2004. Effective elastic moduli of two dimensional solids with distributed cohesive microcracks. European Journal of Mechanics - A/Solids 23, 925–933. https://doi.org/10.1016/j.euromechsol.2004.07.002

López-González, J.C., Fernández-Gómez, J., González-Valle, E., 2012. Effect of Adhesive Thickness and Concrete Strength on FRP-Concrete Bonds. J. Compos. Constr. 16, 705–711. https://doi.org/10.1061/(ASCE)CC.1943-5614.0000303

Lu, X.Z., Teng, J.G., Ye, L.P., Jiang, J.J., 2007. Intermediate Crack Debonding in FRP-Strengthened RC Beams: FE Analysis and Strength Model. J. Compos. Constr. 11, 161–174. https://doi.org/10.1061/(ASCE)1090-0268(2007)11:2(161)

Maalej, M., Bian, Y., 2001. Interfacial shear stress concentration in FRP-strengthened beams. Composite Structures 54, 417–426. https://doi.org/10.1016/S0263-8223(01)00078-2

Machida, S., Miyata, T., Toyosada, M., Hagiwara, Y., 1990. Study of Methods for CTOD Testing of Weldments, in:

Potter, J., McHenry, H. (Eds.), Fatigue and Fracture Testing of Weldments. ASTM International, 100 Barr Harbor Drive, PO Box C700, West Conshohocken, PA 19428-2959, pp. 142-142–15. https://doi.org/10.1520/STP24094S

Maiti, S., Rangaswamy, K., Geubelle, P.H., 2005. Mesoscale analysis of dynamic fragmentation of ceramics under tension. Acta Materialia 53, 823–834. https://doi.org/10.1016/j.actamat.2004.10.034

Margolin, L.G., 1984. A generalized Griffith criterion for crack propagation. Engineering Fracture Mechanics 19, 539–543. https://doi.org/10.1016/0013-7944(84)90010-9

Matallah, M., La Borderie, C., Maurel, O., 2010. A practical method to estimate crack openings in concrete structures. International Journal for Numerical and Analytical Methods in Geomechanics 34, 1615–1633.

Mazars, J., 1986. A description of micro- and macroscale damage of concrete structures. Engineering Fracture Mechanics 25, 729–737. https://doi.org/10.1016/0013-7944(86)90036-6

Mazars, J., 1984. Application de la mecanique de l'endommagement au comportement non lineaire et a la rupture du beton de struc-ture (Thèse de doctorat d'Etat). Université Paris VI, France.

Meng, W., Khayat, K.H., 2016. Mechanical properties of ultra-high-performance concrete enhanced with graphite nanoplatelets and carbon nanofibers. Composites Part B: Engineering 107, 113–122. https://doi.org/10.1016/j.compositesb.2016.09.069

Mergheim, J., Kuhl, E., Steinmann, P., 2005. A finite element method for the computational modelling of cohesive cracks. Int. J. Numer. Meth. Engng 63, 276–289. https://doi.org/10.1002/nme.1286

Moës, N., Belytschko, T., 2002. Extended finite element method for cohesive crack growth. Engineering Fracture Mechanics 69, 813–833. https://doi.org/10.1016/S0013-7944(01)00128-X

Needleman, A., 1990. An analysis of decohesion along an imperfect interface. Int J Fract 42, 21–40. https://doi.org/10.1007/BF00018611

Obaidat, Y.T., Heyden, S., Dahlblom, O., 2010. The effect of CFRP and CFRP/concrete interface models when modelling retrofitted RC beams with FEM. Composite Structures 92, 1391–1398. https://doi.org/10.1016/j.compstruct.2009.11.008

Oliver, J., 1989. A consistent characteristic length for smeared cracking models. Int. J. Numer. Meth. Engng. 28, 461–474. https://doi.org/10.1002/nme.1620280214

Ortiz, M., Pandolfi, A., 1999. Finite-deformation irreversible cohesive elements for three-dimensional crack-propagation analysis. International Journal for Numerical Methods in Engineering 44, 1267–1282.

Ortiz, M., Suresh, S., 1993. Statistical Properties of Residual Stresses and Intergranular Fracture in Ceramic Materials. Journal of Applied Mechanics 60, 77–84. https://doi.org/10.1115/1.2900782

Otsuka, K., Date, H., 2000. Fracture process zone in concrete tension specimen. Engineering Fracture Mechanics 65, 111–131. https://doi.org/10.1016/S0013-7944(99)00111-3

Pan, J., Leung, C.K.Y., Luo, M., 2010. Effect of multiple secondary cracks on FRP debonding from the substrate of reinforced concrete beams. Construction and Building Materials 24, 2507–2516. https://doi.org/10.1016/j.conbuildmat.2010.06.006

Papoulia, K.D., Vavasis, S.A., Ganguly, P., 2006. Spatial convergence of crack nucleation using a cohesive finite-element model on a pinwheel-based mesh. Int. J. Numer. Meth. Engng 67, 1–16. https://doi.org/10.1002/nme.1598

Park, K., Choi, H., Paulino, G.H., 2016. Assessment of cohesive traction-separation relationships in ABAQUS: A comparative study. Mechanics Research Communications 78, 71–78. https://doi.org/10.1016/j.mechrescom.2016.09.004

Park, K., Paulino, G.H., 2011. Cohesive Zone Models: A Critical Review of Traction-Separation Relationships Across Fracture Surfaces. Applied Mechanics Reviews 64, 060802. https://doi.org/10.1115/1.4023110

Park, K., Paulino, G.H., Roesler, J., 2010. Cohesive fracture model for functionally graded fiber reinforced concrete. Cement and Concrete Research 40, 956–965. https://doi.org/10.1016/j.cemconres.2010.02.004

Park, K., Paulino, G.H., Roesler, J.R., 2008. Determination of the kink point in the bilinear softening model for concrete. Engineering Fracture Mechanics 75, 3806–3818. https://doi.org/10.1016/j.engfracmech.2008.02.002

Paulino, G.H., Jin, Z.-H., Dodds, R.H., Sahu, S.K., Badgayan, N.D., Rama Sreekanth, P.S., 2017. Failure of Functionally Graded Materials, in: Reference Module in Materials Science and Materials Engineering. Elsevier, p. B9780128035818009000. https://doi.org/10.1016/B978-0-12-803581-8.00875-4

Peerlings, R.H.J., de Borst, R., Brekelmans, W.A.M., Geers, M.G.D., 1998. Gradient enhanced damage modelling of concrete fracture. Mechanics of Cohesive-Frictional Materials 3, 323–342.

Perera, R., Bueso-Inchausti, D., 2010. A unified approach for the static and dynamic analyses of intermediate debonding in FRP-strengthened reinforced concrete beams. Composite Structures 92, 2728–2737. https://doi.org/10.1016/j.compstruct.2010.04.006

Petersson, P.E., 1981. Crack growth and development of fracture zone in plain concrete and similar materials (No. TVBM-100). Lund Institute of Technology.

Pijaudier-Cabot, G., Bažant, Z.P., 1987. Nonlocal Damage Theory. Journal of Engineering Mechanics 113, 1512–1533. https://doi.org/10.1061/(ASCE)0733-9399(1987)113:10(1512)

Planas, J., Elices, M., 1993. Asymptotic analysis of a cohesive crack: 2. Influence of the softening curve. International Journal of Fracture 64, 221–237.

Planas, J., Elices, M., 1992. Asymptotic analysis of a cohesive crack: 1. Theoretical background. Int J Fract 55, 153–177. https://doi.org/10.1007/BF00017275

Planas, J., Elices, M., 1991. Nonlinear fracture of cohesive materials. Int J Fract 51, 139–157. https://doi.org/10.1007/BF00033975

Prasad, M.V.K.V., Krishnamoorthy, C.S., 2002. Computational model for discrete crack growth in plain and reinforced concrete. Computer Methods in Applied Mechanics and Engineering 191, 2699–2725. https://doi.org/10.1016/S0045-7825(02)00210-4

Qasem, A., Sallam, Y.S., Hossam Eldien, H., Ahangarn, B.H., 2020. Bond-slip behavior between ultra-high-performance concrete and carbon fiber reinforced polymer bars using a pull-out test and numerical modelling. Construction and Building Materials 260, 119857. https://doi.org/10.1016/j.conbuildmat.2020.119857

Quantrill, R.J., Hollaway, L.C., Thorne, A.M., 1996. Experimental and analytical investigation of FRP strengthened beam response: Part I. Magazine of Concrete Research 48, 331–342. https://doi.org/10.1680/macr.1996.48.177.331

Radfar, S., Foret, G., Saeedi, N., Sab, K., 2012. Simulation of concrete cover separation failure in FRP plated RC beams. Construction and Building Materials 37, 791–800. https://doi.org/10.1016/j.conbuildmat.2012.08.020

Rahimi, H., Hutchinson, A., 2001. Concrete Beams Strengthened with Externally Bonded FRP Plates. J. Compos. Constr. 5, 44–56. https://doi.org/10.1061/(ASCE)1090-0268(2001)5:1(44)

Rahulkumar, P., Jagota, A., Bennison, S.J., Saigal, S., 2000. Cohesive element modeling of viscoelastic fracture: application to peel testing of polymers. International Journal of

Solids and Structures 37, 1873–1897. https://doi.org/10.1016/S0020-7683(98)00339-4

Raoof, M., El-Rimawi, J.A., Hassanen, M.A.H., 2000. Theoretical and experimental study on externally plated R.C. beams. Engineering Structures 22, 85–101. https://doi.org/10.1016/S0141-0296(98)00056-X

Rashid, Y.R., 1968. Analysis of prestresse concrete pressure vessels. Nucl. Eng. Design 7, 334–55.

Remmers, J.J.C., Borst, R. de, Needleman, A., 2003. A cohesive segments method for the simulation of crack growth. Computational Mechanics 31, 69–77. https://doi.org/10.1007/s00466-002-0394-z

Rice, J.R., 1968a. A Path Independent Integral and the Approximate Analysis of Strain Concentration by Notches and Cracks. Journal of Applied Mechanics 35, 379–386. https://doi.org/10.1115/1.3601206

Rice, J.R., 1968b. Mathematical analysis in the mechanics of fracture. Fracture: an advanced treatise 2, 191–311.

Rice, J.R., 1968c. Fracture an Advanced Treatise, Academic Press. ed. H. Liebowitz, New York.

Rose, J.H., Ferrante, J., Smith, J.R., 1981. Universal Binding Energy Curves for Metals and Bimetallic Interfaces. Phys. Rev. Lett. 47, 675–678. https://doi.org/10.1103/PhysRevLett.47.675

Rots, J.G., 1988. Computational modeling of concrete fracture (PhD Thesis). Delft Univeristy of Technology, Delft.

Ruiz, G., Pandolfi, A., Ortiz, M., 2001. Three-dimensional cohesive modeling of dynamic mixed-mode fracture. Int. J.

Numer. Meth. Engng. 52, 97–120. https://doi.org/10.1002/nme.273

Rusch, H., Hilsdorf, H., 1963. Deformation characteristics of concrete under axial tension. Voruntersuchungen, 44.

Sancho, J.M., Planas, J., Cendón, D.A., Reyes, E., Gálvez, J.C., 2007. An embedded crack model for finite element analysis of concrete fracture. Engineering Fracture Mechanics 74, 75–86. https://doi.org/10.1016/j.engfracmech.2006.01.015

Sancho, J.M., Planas, J., Gálvez, J.C., Reyes, E., Cendón, D.A., 2006. An embedded cohesive crack model for finite element analysis of mixed mode fracture of concrete. Fat Frac Eng Mat Struct 29, 1056–1065. https://doi.org/10.1111/j.1460-2695.2006.01076.x

Scanlon, A., 1971. Time-dependent deflection of reinforced concrete slabs (PhD Thesis). University of Alberta, Edmonton, Canada.

Shardakov, I.N., Shestakov, A.P., Glot, I.O., Bykov, A.A., 2016. Process of cracking in reinforced concrete beams (simulation and experiment). Frattura ed Integrità Strutturale 10, 339–350. https://doi.org/10.3221/IGF-ESIS.38.44

Simo, J.C., Ju, J.W., 1987a. Strain- and stress-based continuum damage models—I. Formulation. International Journal of Solids and Structures 23, 821–840. https://doi.org/10.1016/0020-7683(87)90083-7

Simo, J.C., Ju, J.W., 1987b. Strain- and stress-based continuum damage models—II. Computational aspects. International Journal of Solids and Structures 23, 841–869. https://doi.org/10.1016/0020-7683(87)90084-9

Simo, J.C., Oliver, J., Armero, F., 1993. An analysis of strong discontinuities induced by strain-softening in rate-independent inelastic solids. Computational Mechanics 12, 277–296. https://doi.org/10.1007/BF00372173

Słowik, M., 2019. The analysis of failure in concrete and reinforced concrete beams with different reinforcement ratio. Arch Appl Mech 89, 885–895. https://doi.org/10.1007/s00419-018-1476-5

Smith, S.T., Teng, J.G., 2002a. FRP-strengthened RC beams. I: review of debonding strength models. Engineering Structures 24, 385–395.

Smith, S.T., Teng, J.G., 2002b. FRP-strengthened RC beams. II: assessment of debonding strength models. Engineering Structures 24, 397–417.

Song, J.-H., Areias, P.M.A., Belytschko, T., 2006. A method for dynamic crack and shear band propagation with phantom nodes. Int. J. Numer. Meth. Engng 67, 868–893. https://doi.org/10.1002/nme.1652

Stolarska, M., Chopp, D.L., Moës, N., Belytschko, T., 2001. Modelling crack growth by level sets in the extended finite element method. Int. J. Numer. Meth. Engng. 51, 943–960. https://doi.org/10.1002/nme.201

Suárez, F., Gálvez, J.C., Enfedaque, A., Alberti, M.G., 2019. Modelling fracture on polyolefin fibre reinforced concrete specimens subjected to mixed-mode loading. Engineering Fracture Mechanics 211, 244–253. https://doi.org/10.1016/j.engfracmech.2019.02.018

Teng, J.G., Smith, S.T., Yao, J., Chen, J.F., 2003. Intermediate crack-induced debonding in RC beams and slabs. Construction and Building Materials 17, 447–462. https://doi.org/10.1016/S0950-0618(03)00043-6

Tijssens, M.G.A., Sluys, L.J., van der Giessen, E., 2001. Simulation of fracture of cementitious composites with explicit modeling of microstructural features. Engineering Fracture Mechanics 68, 1245–1263. https://doi.org/10.1016/S0013-7944(01)00017-0

Tomar, V., Zhai, J., Zhou, M., 2004. Bounds for element size in a variable stiffness cohesive finite element model. Int. J. Numer. Meth. Engng. 61, 1894–1920. https://doi.org/10.1002/nme.1138

Toutanji, H., Zhao, L., Anselm, E., 2006. Verifications of Design Equations of Beams Externally Strengthened with FRP Composites. J. Compos. Constr. 10, 254–264. https://doi.org/10.1061/(ASCE)1090-0268(2006)10:3(254)

Turon, A., Camanho, P.P., Costa, J., Dávila, C.G., 2006. A damage model for the simulation of delamination in advanced composites under variable-mode loading. Mechanics of Materials 38, 1072–1089. https://doi.org/10.1016/j.mechmat.2005.10.003

Turon, A., Dávila, C.G., Camanho, P.P., Costa, J., 2007. An engineering solution for mesh size effects in the simulation of delamination using cohesive zone models. Engineering Fracture Mechanics 74, 1665–1682. https://doi.org/10.1016/j.engfracmech.2006.08.025

Tvergaard, V., Hutchinson, J.W., 1992. The relation between crack growth resistance and fracture process parameters in elastic-plastic solids. Journal of the Mechanics and

Physics of Solids 40, 1377–1397. https://doi.org/10.1016/0022-5096(92)90020-3

von Mises, R., 1913. Mechanik der festen Körper im plastisch-deformablen Zustand. Nachrichten von der Gesellschaft der Wissenschaften zu Göttingen, Mathematisch-Physikalische Klasse 1913, 582–592.

Wang, K., Jansen, D.C., Shah, S.P., Karr, A.F., 1997. Permeability study of cracked concrete. Cement and Concrete Research 27, 381–393. https://doi.org/10.1016/S0008-8846(97)00031-8

Wang, Q., Guo, Z., Hoogenboom, P.C.J., 2005. Experimental investigation on the shear capacity of RC dapped end beams and design recommendations. Structural Engineering and Mechanics 21, 221–235.

Wells, A.A., 1965. The application of fracture mechanics to yielding materials. Proc. R. Soc. Lond. A 285, 34–45. https://doi.org/10.1098/rspa.1965.0087

Westergaard, H.M., 1937. Bearing pressures and cracks. Journal of Applied Mechanics - ASME 6, 49–53.

Westergaard, H.M., 1934. Stresses at a crack, size of the crack and the bending of reinforced concrete. Prooceding American Concrete Institute 30, 93–102.

Wittmann, F.H., Eidgenössische Technische Hochschule Zürich, International Union of Testing and Research Laboratories for Materials and Structures, International Conference on Fracture Mechanics of Concrete Structures (Eds.), 1995. Fracture mechanics of concrete structures: proceedings of the Second International Conference on Fracture Mechanics of Concrete Structures (FRAMCOS 2) held at

ETH Zurich, Switzerland, July 25 - 28, 1995. Presented at the International Conference on Fracture Mechanics of Concrete Structures (FRAMCOS), Freiburg, AEDIFICATIO Publishers.

Wittmann, F.H., Hu, X., 1991. Fracture process zone in cementitious materials. Int J Fract 51, 3–18. https://doi.org/10.1007/BF00020849

Xie, M., Gerstle, W.H., 1995. Energy-Based Cohesive Crack Propagation Modeling. Journal of Engineering Mechanics 121, 1349–1358. https://doi.org/10.1061/(ASCE)0733-9399(1995)121:12(1349)

Xu, X.-P., Needleman, A., 1994. Numerical simulations of fast crack growth in brittle solids. Journal of the Mechanics and Physics of Solids 42, 1397–1434. https://doi.org/10.1016/0022-5096(94)90003-5

Yang, Y., Xue, Y., Yu, Y., Ma, N., Shao, Y., 2017. Experimental study on flexural performance of partially precast steel reinforced concrete beams. Journal of Constructional Steel Research 133, 192–201. https://doi.org/10.1016/j.jcsr.2017.02.019

Yang, Z.J., Chen, J., 2005. Finite element modelling of multiple cohesive discrete crack propagation in reinforced concrete beams. Engineering Fracture Mechanics 72, 2280–2297. https://doi.org/10.1016/j.engfracmech.2005.02.004

Yang, Z.J., Chen, J.F., Proverbs, D., 2003. Finite element modelling of concrete cover separation failure in FRP plated RC beams. Construction and Building Materials 17, 3–13. https://doi.org/10.1016/S0950-0618(02)00090-9

Yu, J., Tan, K.-H., 2013. Experimental and numerical investigation on progressive collapse resistance of reinforced concrete beam column assemblages. Engineering Structures 55, 90–106. https://doi.org/10.1016/j.engstruct.2011.08.040

Zararis, P.D., Papadakis, G.Ch., 2001. Diagonal Shear Failure and Size Effect in RC Beams without Web Reinforcement. J. Struct. Eng. 127, 733–742. https://doi.org/10.1061/(ASCE)0733-9445(2001)127:7(733)

Zavattieri, P.D., Espinosa, H.D., 2001. Grain level analysis of crack initiation and propagation in brittle materials. Acta Materialia 49, 4291–4311. https://doi.org/10.1016/S1359-6454(01)00292-0

Zhan, T., Wang, Z., Ning, J., 2015. Failure behaviors of reinforced concrete beams subjected to high impact loading. Engineering Failure Analysis 56, 233–243. https://doi.org/10.1016/j.engfailanal.2015.02.006

Zhan, Y., Meschke, G., 2016. Multilevel Computational Model for Failure Analysis of Steel-Fiber–Reinforced Concrete Structures. J. Eng. Mech. 142, 04016090. https://doi.org/10.1061/(ASCE)EM.1943-7889.0001154

Zhang, S.S., Teng, J.G., 2014. Finite element analysis of end cover separation in RC beams strengthened in flexure with FRP. Engineering Structures 75, 550–560. https://doi.org/10.1016/j.engstruct.2014.06.031

Zhang, W., François, R., Cai, Y., Charron, J.-P., Yu, L., 2020. Influence of artificial cracks and interfacial defects on the corrosion behavior of steel in concrete during corrosion initiation under a chloride environment. Construction and Building Materials 253, 119165. https://doi.org/10.1016/j.conbuildmat.2020.119165

Zhang, Z. (Jenny), Paulino, G.H., Celes, W., 2007. Extrinsic cohesive modelling of dynamic fracture and microbranching instability in brittle materials. Int. J. Numer. Meth. Engng 72, 893–923. https://doi.org/10.1002/nme.2030

Zhou, W., Zhao, J., Liu, Y., Yang, Q., 2002. Simulation of localization failure with strain-gradient-enhanced damage mechanics. Int. J. Numer. Anal. Meth. Geomech. 26, 793–813. https://doi.org/10.1002/nag.225

Zi, G., Belytschko, T., 2003. New crack-tip elements for XFEM and applications to cohesive cracks. Int. J. Numer. Meth. Engng. 57, 2221–2240. https://doi.org/10.1002/nme.849

Zidani, M.B., Belakhdar, K., Tounsi, A., Adda Bedia, E.A., 2015. Finite element analysis of initially damaged beams repaired with FRP plates. Composite Structures 134, 429–439. https://doi.org/10.1016/j.compstruct.2015.07.124